

The activity and evolution of low-mass young stellar objects

Ana Catarina da Silva Rei

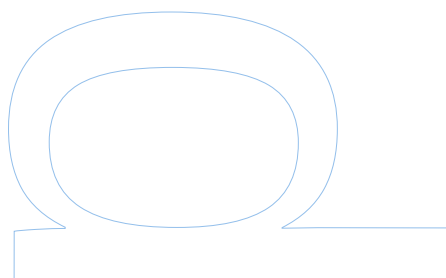
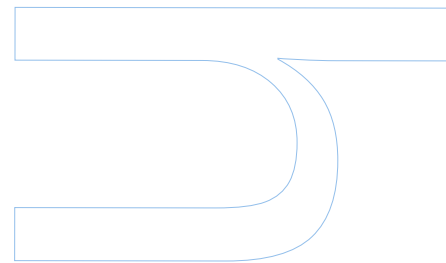
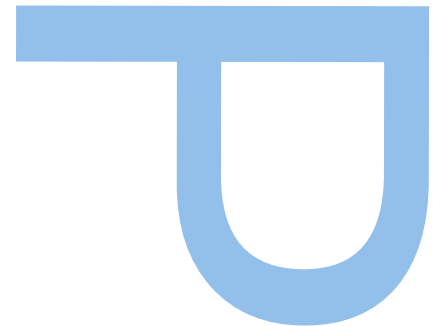
Doutoramento em Astronomia
Departamento de Física e Astronomia
2018

Orientador

Jorge Filipe da Silva Gameiro,
Professor Auxiliar, Faculdade de Ciências da Universidade do Porto

Coorientador

Sílvia Helena Paixão Alencar,
Profesora associada, Universidade Federal de Minas Gerais





Todas as correções determinadas pelo júri, e só essas, foram efetuadas.

O Presidente do Júri,

Porto, ____ / ____ / ____

U

U

U

Acknowledgements

First I want to thank Mario João Monteiro, for accepting me at the Doctoral Program in Astronomy at Faculdade de Ciências da Universidade do Porto and allow me to take all the opportunities to finish it. Secondly I want to thank my Jorge Filipe Gameiro and Sílvia Alencar for accompanying my work, and in particular I am very thankful to Filipe for all his patience, reviews, help and insight.

As important, I want to thank a lot my mother, Isabel Coentro, my stepfather, Milton Monteiro, and my twin soul Tiago Soares, for all the financial and emotional support. Without you three I would never be able to follow my dreams. Thank you for all the hands that you stretch for me to grab and get up from the ground every time I struggled. I also can not forget all the support my family gave me during this journey. Obrigada!

I want to thank my two collaborators: Peter Petrov and Guilherme Teixeira. This work is also yours, I am very thankful to all the help, knowledge and insight that you both shared with me.

Last, but not least, I want to express my thanks to all my colleagues, for all the good moments, and in particular to Ângela Santos, for all the help, good conversation and company at lunch!

Ana Rei

Resumo

A melhor forma que temos de saber como se formou o sistema solar é através do estudo de estrelas jovens de baixa massa ($0.1 M_{\odot}$ - $2.5 M_{\odot}$). Estas estrelas, conhecidas por estrelas T Tauri, são na realidade sistemas formados por uma estrela jovem e um disco circumestelar. Em algumas das estrelas T Tauri, chamadas de T Tauri clássicas, ainda está a ocorrer acreção de matéria do disco para a estrela, através de canais criados por campos magnéticos. Acredita-se que este processo é responsável pelas várias características espectrais e fotométricas observadas nas estrelas T Tauri clássicas.

No entanto, existe uma outra classe de estrelas jovens de baixa massa, que é bastante menos activa do que as clássicas: as estrelas T tauri com riscas de emissão fracas. Pensa-se que estas sejam a evolução natural das clássicas, quando a estrela já cessou o processo de acreção de matéria e está perto de atingir a sequência principal. Nestas estrelas observam-se riscas de emissão fracas, que se acredita estarem relacionadas com actividade cromosférica.

Nesta tese são estudados tópicos associados a cada uma das classes de estrelas T Tauri. No caso das T Tauri clássicas, são analisados espectros de três estrelas muito activas, com o objectivo de melhor compreender os efeitos produzidos na atmosfera da estrela devido à acreção de matéria. No caso das T Tauri de riscas fracas, utilizamos síntese espectral para determinarmos parâmetros estelares para uma amostra de 24 estrelas com espectros de resolução intermédia obtidos pelo espectrógrafo VLT/GIRAFFE, na configuração HR15N.

Ao mesmo tempo que procuramos respostas para o que acontece na região central do sistema estrela-disco, tentamos fornecer alternativas para a análise espectral de T Tauris de riscas fracas que poderão ajudar na análise das T Tauri clássicas.

Abstract

The study of low-mass ($0.1 M_{\odot}$ - $2.5 M_{\odot}$) young stellar objects offers the possibility to understand how our own solar system was formed. These stars, also known as T Tauri stars, are star-disk systems, formed by a young stars surrounded by a circumstellar disk. In some of these stars, called classical T Tauri stars, matter is being accreted from the disk to the star via magnetically driven channels. It is believed that this process is responsible for the several spectroscopic and photometric features observed in the classical T Tauri stars.

At the same time, there is another class of low-mass young stars, much less active than the classical T Tauri stars: the weak-line T Tauri stars. Most probably, these stars are the natural evolution of classical T Tauri stars, when there is no longer accretion ongoing and the star is almost reaching the main sequence phase. The weak emission lines present in the spectra of weak-line T Tauri stars may be related with chromospheric activity.

In this thesis, we study issues related with each class of T Tauri stars. We analyse three very active classical T Tauri stars, aiming to better understand the effects of accretion on the atmosphere of the stars. On the other hand, we use the spectral synthesis method to determine fundamental stellar parameters for a sample of 24 stars spectra of intermediate-resolution, obtained by the VLT/GIRAFFE spectrograph, HR15N mode.

While we search for answers to what is happening in the inner-disk region of the star-disk systems, we try to offer a different approach to the analysis of the weak-line T Tauri stars, that may be helpful future analysis of classical T Tauri stars.

Key-words

Young stellar objects, Low-mass, Pre-main sequence, T Tauri stars, Classical T Tauri stars, Weak-line T Tauri stars, Star formation, NGC 2264, LKH α 321, V1331 Cyg, AS 353A, Veiling, Stellar parameters, Spectral synthesis.

Contents

1	Introduction	25
1.1	T Tauri Stars and where to find them	26
1.1.1	Low-mass star formation	27
1.1.2	T Tauri Stars classes	31
1.2	Classical T Tauri Stars	33
1.2.1	Observational features	34
1.3	Magnetospheric accretion model	39
1.3.1	Mass-accretion	39
1.3.2	Outflows and winds	42
1.4	Weak-line T Tauri Stars	43
1.5	Extreme TTS: FUor and EXor outbursts	43
1.6	Open questions	46
1.7	Objectives of this work	47
2	CTTS veiling nature	49
2.1	Line-dependent veiling in very active cTTS	49
2.2	Observational data	52
2.3	Analysis of cTTS spectra	52
2.3.1	Templates	52
2.3.2	Determination of spectral type	55
2.3.3	Measurement of equivalent widths	57
2.3.4	Sources of uncertainty	58
2.4	CTTS spectra analysis	61
2.4.1	AS 353A	61
2.4.2	V1331 Cyg	68
2.4.3	LkH α 321	77
2.5	Analysis of the results	84
2.5.1	Veiling continuum determination	84

2.5.2	Accretion luminosity determination	85
2.5.3	Mass-accretion rates and filling factor	88
2.6	Discussion	90
3	Fundamental stellar parameters of wTTS	95
3.1	Fundamental stellar parameters determination	95
3.1.1	GIRAFFE HR15N spectra	96
3.2	Observational data: TTS from NGC 2264	98
3.2.1	WTTS classification	98
3.3	Method: Spectral synthesis	104
3.3.1	SME setup for GIRAFFE HR15N spectra	104
3.3.2	Sources of uncertainties	108
3.4	Testing SME with synthetic and real stars spectra	109
3.4.1	SME synthetic spectra	109
3.4.2	Real stars	119
3.4.3	Internal comparison	124
3.5	Analysis of wTTS from NGC 2264	127
3.5.1	SME results	127
3.5.2	The Spectral Indices method results	132
3.5.3	Influence of v_{mic} and v_{mac} on the results	132
3.5.4	Mass and age determination	137
3.5.5	Fixing [Fe/H]	141
3.5.6	WTTS metallicity issue	143
3.5.7	NGC 2264 cluster metallicity	144
3.6	Discussion	144
3.6.1	The method	145
3.6.2	NGC 2264 wTTS	146
4	Conclusion	149
4.1	Activity: classical T Tauri Stars	149
4.2	Evolution: weak-line T Tauri Stars	151
4.3	Activity is linked to evolution	152
4.4	Questions answered?	153
4.5	What lies in the future?	154
A	WTTS Hα plots	163

B Publications

List of Tables

2.1	Literature data for the three cTTS	53
2.2	Common parameters for all synthetic spectra	56
2.3	Template synthetic spectra parameters for each star	57
2.4	Derived stellar parameters	61
2.5	Photospheric line pairs used in the spectral type determination of As 353A	64
2.6	Photospheric line pairs used in the spectral type determination of V1331 Cyg	74
2.7	Photospheric line pairs used in the spectral type determination of LkH α 321	80
2.8	Accretion luminosity and mass accretion rates determination.	88
3.1	WTTS sample: identification and raw measurements.	100
3.2	WTTS sample: photometry derived parameters from Venuti et al. (2014) (V_14).	102
3.3	WTTS sample: spectroscopy data from from Bouvier et al. (2016) (B_16) and Spina et al. (2017)(S_17).	103
3.4	SME wavelength intervals and fitted lines	106
3.5	SME initial parameters	107
3.6	SME synthetic spectra grid: SME_A.	110
3.7	Average differences between reference values and SME results for SME_A_1 and SME_B	113
3.8	SME synthetic spectra samples B description	114
3.9	SME accuracy and precision considering different spectral resolutions	116
3.10	SME accuracy and precision considering different S/N	117
3.11	Benchmark and FGK stars samples description.	119
3.12	Benchmark stars stellar parameters from literature (Lit.) and determined by SME.	121
3.13	Average differences between literature values and SME results for BenS and FGK samples.	121
3.14	SME results for the wTTS sample.	128

3.15 WTTS parameters determination using the Spectral Indices method. 133

3.16 WTTS mass and age estimates. 138

List of Figures

1.1	T Tauri star and Hind's Nebula.	26
1.2	Rho Ophiucus star forming region.	28
1.3	Orion Nebula seen by Spitzer.	29
1.4	Positions of some cTTS and wTTS in the Hertzsprungel-Russel diagram. . .	30
1.5	Empirical division between cTTS and wTTS	33
1.6	Example of cTTS optical spectra.	35
1.7	Spectral energy distributions of the four TTS from 3600 Å to 100 μm. . . .	35
1.8	Hα model profiles obtained by Kurosawa et al. (2006).	37
1.9	Magnetospheric accretion model	39
1.10	Shock region and heated stellar atmosphere	40
1.11	Spectrum of classical T Tauri BP Tau	40
1.12	Herbig-Haro 24 object	44
1.13	FUor and EXor outbursts	45
2.1	Veiling factor (VF) versus wavelength for BPTau and AATau	50
2.2	EW ratio versus line strength for the Sun and a G7IV star.	58
2.3	EW ratio versus wavelength for the Sun and a G7IV star.	59
2.4	EW ratio versus excitation potential of the lower level for the Sun and a G7IV star.	59
2.5	AS 353A Digital Sky Survey image	62
2.6	Hubble image of HH 32	62
2.7	P Cygni profiles of the Hα and Hβ lines in the AS 353A HIRES spectrum .	63
2.8	Fragment of AS 353A spectrum	64
2.9	Fragments of AS 353A spectrum used to estimate spectral type	65
2.10	AS 353A veiling as a function of line strength	66
2.11	AS 353A veiling as a function of wavelength	67
2.12	AS 353A veiling as a function of line excitation potential of the lower level .	67
2.13	V1331Cyg Digital Sky Survey image	69

2.14	P Cygni profiles of the H α and H β lines in the V1331 Cyg HIRES spectrum	69
2.15	V1331 Cyg forbidden line observations	70
2.16	Fragment of V1331 Cyg spectrum	71
2.17	Fragment of V1331 Cyg spectrum used to estimate spectral type	72
2.18	Fragments of V1331 Cyg spectrum used to estimate spectral type (cont.)	73
2.19	Fragments of V1331 Cyg spectrum used to estimate spectral type (cont.)	74
2.20	V1331 Cyg veiling as a function of line strength	75
2.21	V1331 Cyg veiling as a function of wavelength	76
2.22	V1331 Cyg veiling as a function of line excitation potential of the lower level	76
2.23	LkH α 321 Digital Sky Survey image in the optical	77
2.24	P Cygni profiles of the H α and H β lines in the LkH α 321 HIRES spectrum	78
2.25	LkH α 321 forbidden line observations	78
2.26	Effects of LkH α 321 rotation on the photospheric lines	79
2.27	Fragment of spectra of LkHa 321	80
2.28	Fragments of LkH α 321 spectrum used to estimate spectral type	81
2.29	LkH α 321 veiling as a function of line strength	82
2.30	LkH α 321 veiling as a function of wavelength	83
2.31	LkH α 321 veiling as a function of line excitation potential	83
2.32	CTTS He I line at 5876 Å	87
3.1	NGC 2264 WFI image	99
3.2	SME line mask	108
3.3	SME_A_1 sample results	112
3.4	SME_B results	115
3.5	SME resolution test	117
3.6	SME S/N test	118
3.7	BenS sample results	122
3.8	FGK sample results	123
3.9	Compilation of synthetic and real stars spectra T_{eff} determinations	125
3.10	Compilation of synthetic and real stars spectra $\log g$ determinations	126
3.11	Compilation of synthetic and real stars spectra [Fe/H] determinations	127
3.12	WTTS SME results versus literature values for T_{eff} and $\log g$	129
3.13	WTTS SME results versus literature values for [Fe/H] and $v \sin i$	130
3.14	WTTS T_{eff} versus [Fe/H]	131
3.15	WTTS SME results versus SI method	134

3.16 Influence of v_{mic} on the wTTS results	135
3.17 Influence of v_{mac} on the wTTS results	136
3.18 Temperature versus $\log g$ diagrams for the wTTS	139
3.19 WTTS EW(Li) versus age	140
3.20 WTTS T_{eff} versus EW(Li)	140
3.21 Influence of [Fe/H] fixed on the results	142
3.22 Temperature versus $\log g$ diagram for the wTTS with [Fe/H] fixed	143
A.1 WTTS H α line and σ	164
A.2 WTTS H α line and σ (cont.)	165
A.3 WTTS H α line and σ (cont.)	166
A.4 WTTS H α line and σ (cont.)	167
A.5 WTTS H α line and σ (cont.)	168

List of Abbreviations

CTTS	Classical T Tauri Stars
EW	Equivalent width
IR	Infrared
LTE	Local Thermodynamical Equilibrium
MS	Main-sequence
NLTE	Non Local Thermodynamical Equilibrium
PMS	Pre-main sequence
SME	Spectroscopy Made Easy
S/N	Signal-to-noise ratio
TTS	T Tauri Stars
UV	Ultraviolet
VALD	Vienna Atomic Line Data
WTTS	Weak-line T Tauri Stars
VF	Veiling Factor
YSO	Young Stellar Objects
ZAMS	Zero-age main sequence

Chapter 1

Introduction

Every time we turn our face to the night sky and look at the stars, we are seeing the past. The light coming from the star closest to us, the Sun, arrives at the Earth 8 minutes and 19 seconds after leaving its surface. In fact, when we observe the Sun we are seeing it as it was more than 8 minutes ago. This happens because the light travels at a constant speed. Nowadays, we can even prospect the first moments of the formation of the Universe and the vastness of space. While we can not see how the Universe is at this instant, we are also unable to witness the formation of our own Solar System.

Centuries of astronomical breakthroughs showed us that our Sun is just an ordinary dwarf star in its middle age, similar to the majority of stars in our Galaxy, the Milky Way. The Sun is a G2V star. Its spectral type tell us that it is a star with an effective temperature (hereafter T_{eff}) of around 5770 K and a logarithmic surface gravity (hereafter, $\log g$) of 4.44 dex, which classifies it as a dwarf star. The surface gravity of a star is defined by:

$$g = g_{\odot} \frac{M_*}{R_*^2}, \quad (1.1)$$

where g_{\odot} is the surface gravity of the Sun, M_* and R_* are the mass and radius of the star, in solar units. But it is its temperature that is mainly responsible for the G2 classification, since this parameter is mostly responsible for the environmental conditions that constrain the photospheric lines formation (absorption lines) (Gray, 2005).

The Sun is a main-sequence (hereafter, MS) star also known to have mass $M_{\odot} = 1.989 \times 10^{30}$ kg, radius $R_{\odot} = 6.959 \times 10^8$ m and a luminosity L_{\odot} (total power emitted by the star) of 3.845×10^{26} W. The luminosity (bolometric, i.e., for the entire wavelength range) of a star (L_*), can be determined if both radius (R_*) and effective temperature (T_{eff}) of a star are known:

$$L_* = 4\pi R_*^2 \sigma T_{\text{eff}}^4, \quad (1.2)$$

where σ is the Stefan-Boltzmann constant.



Figure 1.1: T Tauri star and Hind's Nebula. T Tauri is the yellow star located in the middle of the image, while the Hind's Nebula is the yellowish dust cloud next to T Tauri. Credits: Don Goldman & APOD/NASA.

Compared to other stars in the Galaxy, our Sun is considered a low-mass star. Dwarf low-mass stars are also known as solar type stars, since they share similar characteristics. In order to understand how our solar system formed, we need to look at the formation of low-mass stars, located in star forming regions. These low-mass young stellar objects (hereafter, YSO) are also known as T Tauri Stars. Contrary to our rather quiet Sun, T Tauri stars are identified as variable stars, with peculiar spectra.

1.1 T Tauri Stars and where to find them

The first star discovered with the spectral and photospheric characteristics today associated with T Tauri stars was the star T Tauri. T Tauri was first identified by Russel Hind in 1852 as a variable star located in the Taurus constellation (Figure 1.1). Stars that share similar characteristics with T Tauri are also known as T Tauri Stars (hereafter TTS)

While T Tauri was discovered in the middle of the XIX century, the first astrophysicist that recognized similarities between the T Tauri star spectrum and that of the Sun's chromosphere was Alfred Joy, almost one century later (Joy, 1945, 1949). By that time, TTS were categorized as irregular variables associated with dark clouds and reflection nebulae and with emission spectrum similar to that of the Sun's chromosphere (Bertout, 1989).

Ambartsumyan was the first to associate T Tauri stars with OB associations and

star forming processes (Ambartsumian , 1947). He advanced with the idea that TTS were young low-mass stars, grouped in T-associations, and often found near O stars associations.

Not long after, Herbig (1962) reinforced the young age argument and in the following years made systematic studies of TTS with major contributions to our current knowledge of these objects. One of his studies associated the kinematics of TTS with those of their molecular cloud maternity (Herbig, 1977; Jones & Herbig, 1979).

Studies regarding TTS strongly evolved in the last decades. Nowadays it is known that TTS are not stars but systems constituted by a still forming star surrounded by a circumstellar disk from which the star is still accreting matter via magnetically driven channels. Studying TTS means studying the star-disk system interaction and evolution.

1.1.1 Low-mass star formation

Stars with all types of masses and sizes are born in the same places: clouds of molecular gas. These clouds can also range from structures with less than $100 M_{\odot}$ and smaller than 1 parsec to giant complexes with $10^6 M_{\odot}$ and 100 parsec in extension (Hartmann, 2009) . Gas in molecular clouds has typical temperatures between 10-20 K.

Some of the most studied and closest star forming regions are the Taurus, Ophiuchus (Figure 1.2) and Orion. NGC 2264, as well as Lupus and Chamaeleon, have gained relevance with the advance of instrumentation on the last decade.

For star formation to occur it is necessary that gravity overcomes any resisting forces, including those of turbulent motions, thermal gas pressure and magnetic fields. The regions of the cloud with higher instability are the places where we can find the dense cores of collapsing material, giving origin to new stars. These condensations of gas have densities higher than 10^3 cm^{-2} (Petrov, 2003). On the other hand, some more turbulent phenomenon, like supernova or radiation pressure from OB type stars, can exert pressure on the surrounding cloud material and trigger star formation.

Stars in their earliest stages of formation are not visible in the optical, but can be observed in the infrared (IR), where they glow as bright sources (Figure 1.3). Pre-main sequence (hereafter, PMS) stars¹ can be classified according to their IR data. Infrared sources can be divided into four classes, according to their spectral energy distribution (Lada, 1987). Class 0 and I of infrared sources are typically associated with protostars candidates, still embedded within the parent cloud and only visible at IR wavelengths.

¹Pre-main sequence stars are young stars with ongoing formation. They are still contracting and the temperature at their core did not reach the hydrogen burning temperature, that marks the beginning of their “adulthood”. With the ignition of hydrogen burning, they reach the MS phase of their lives.

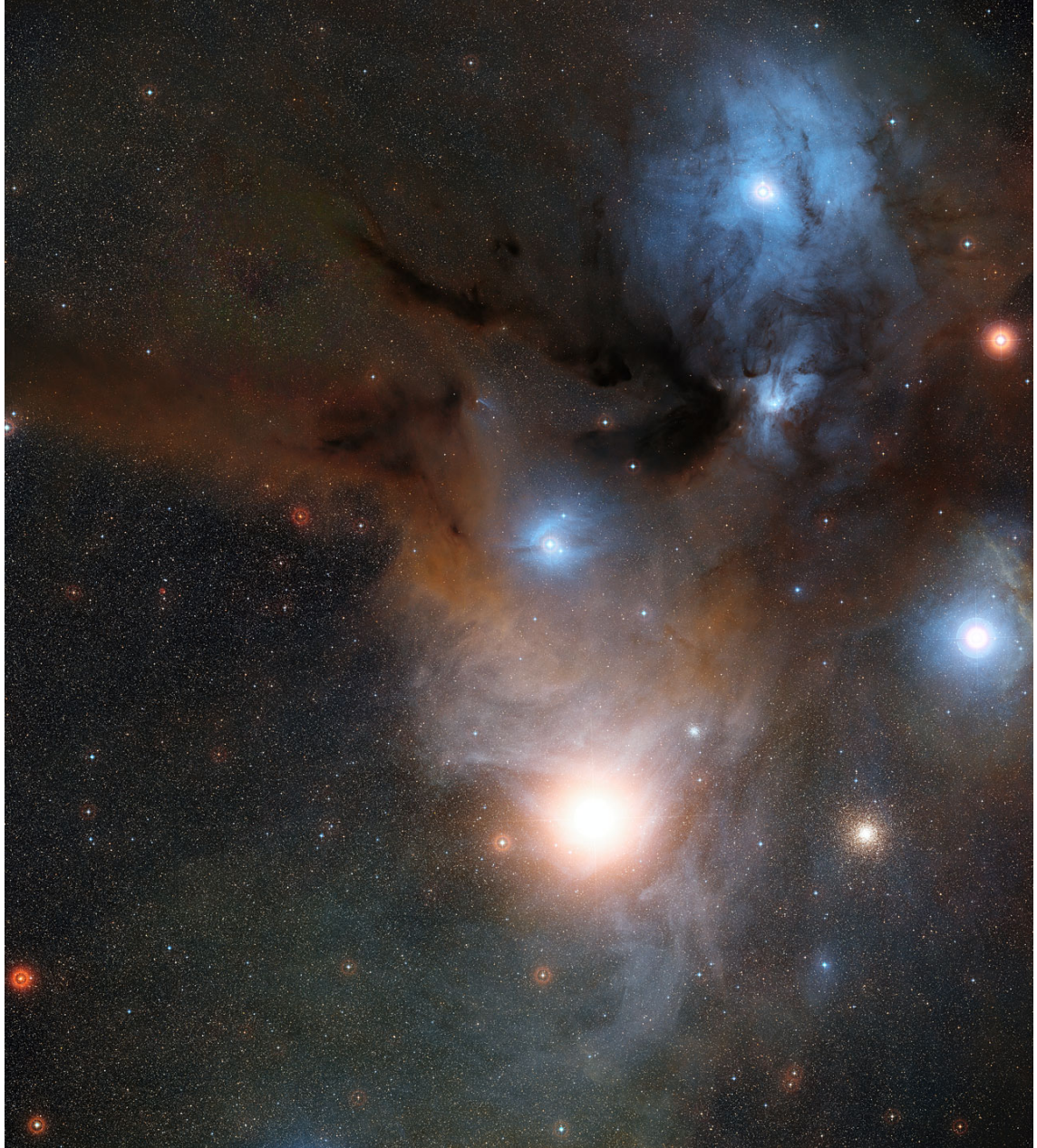


Figure 1.2: Rho Ophiucus star forming region. This star forming region is located in the Serpens constellation. Image in the visible created from Digitalized Sky Survey 2 data. Credits: ESO/Digitalized Sky Survey 2.



Figure 1.3: False image of the Orion Nebula made of Spitzer Space Telescope infrared data. Protostars are seen in red. Credits: NASA.

Class II and III IR sources have been mostly associated with visible YSO. T Tauri stars fall within the class II and III of IR sources, showing an excess of IR radiation, although inferior to those of Class 0 and I.

With the knowledge about PMS stars temperature, luminosity or surface gravity, it is possible to place these stars in a Hertzsprung-Russell diagram. Evolutionary models for the pre-main sequence stage, like the ones from Siess et al. (2000), give us an idea about the mass, radius and age of PMS stars, as well as their stage of stellar evolution (Figure 1.4). Stars that fall along the vertical line of the evolutionary track (Hayashi track) are still slowly contracting, at a roughly constant temperature, and totally convective (Hayashi, 1961). After the development of the radiative zone, the PMS stars follow the Henyey track (Henyey et al., 1955), with an increase of temperature and luminosity, until the hydrogen burning starts. These tracks positions depend on the metallicity of the star, since the chemical composition of a star affects the gas opacities.

Not all stars are easy to study in their PMS stages. In fact, the low-mass stars are the ones that allow us to better study this stage, with optical observations. Our current knowledge from the low-mass stars PMS stage of stellar evolution enables the connection between low-mass and intermediate-mass star formation. Nevertheless, high-mass star formation is still the hardest to study due to their fast evolution. When high-mass stars finally dissipate the surrounding cloud material they are already in their MS phase. This means that these stars become visible when they are already converting hydrogen into

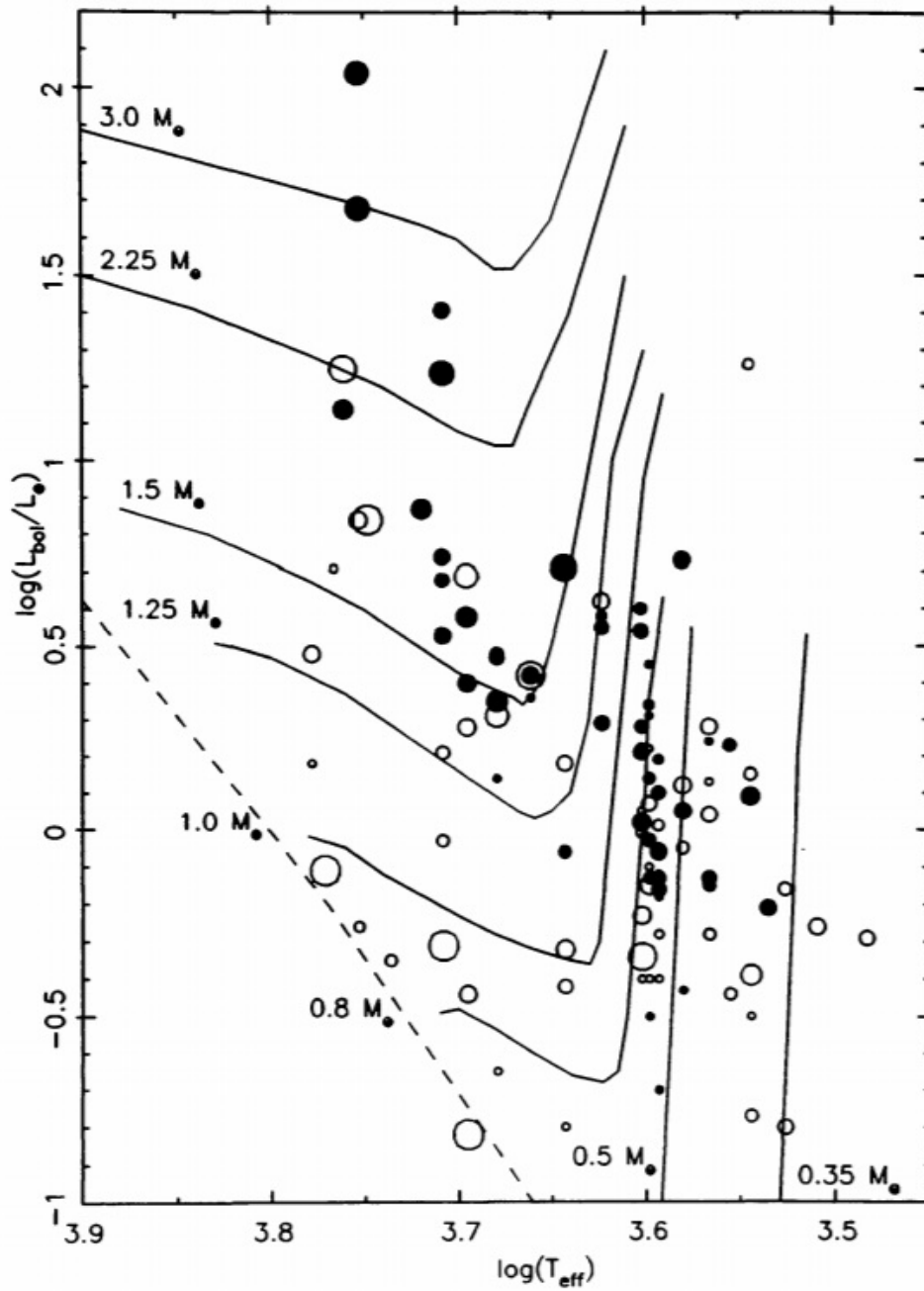


Figure 1.4: Positions of some cTTS and wTTS in the Hertzsprung-Russel diagram. CTTS are represented by filled circles and wTTS by open circles. The different sizes of the symbols represent different projected rotational velocity values. The dashed line represents the zero age main sequence (ZAMS). Credits: Bertout (1989).

helium at their cores.

1.1.2 T Tauri Stars classes

Most TTS have been discovered in H α line (6562.8 Å) surveys, due to their strong H α line emission, but since then many characteristics of TTS have been unveiled. TTS typically share the following features:

- Spectroscopic and photometric variability (e.g. Johns & Basri (1995), Venuti et al. (2014));
- Emission line spectra, with both narrow and broad emission lines. Broad emission of Balmer lines is characteristic, with H α line being one of the most important lines to study TTS (e.g. Finkenzeller & Basri (1987), Ingleby et al. (2013), Sicilia-Aguilar et al. (2015));
- Excess of continuum emission that causes the veiling of the photospheric lines (e.g. Basri & Batalha (1990), Stempels & Piskunov (2002), Stempels & Piskunov (2003), Dodin & Lamzin (2012));
- P Cygni and inverse P Cygni line profiles (e.g. Petrov et al. (2014));
- Excess of infrared radiation, associated with the presence of a circumstellar disk (e.g. Bertout et al. (1988), Cody et al. (2014));
- Magnetic phenomena (e.g. Johns-Krull et al. (1999));
- Association with molecular and dark clouds and OB associations (star forming regions) (e.g. Joy (1949), Dahm & Simon (2005));
- Association with Herbig-Haro objects: jets and outflows originated within the system and interacting with the surrounding cloud material (ex. Reiter et al. (2017));
- Low mass, typically between 0.1 and 2.5 M $_{\odot}$ (e.g. Bertout (1989));
- Young age, indicated by the presence of Lithium absorption line at 6707.8 Å, typically with equivalent widths above 100 mÅ. Typical ages between 1 to 10 Myrs (e.g. Bertout (1989), Basri et al. (1991));

Although these features are observed for TTS, not all share the same observational peculiarities. TTS can, in fact, be divided into two classes, according to their emission line spectrum (Bertout, 1989). Stars that show observational features similar to those of

T Tauri, with broad emission lines and that match Herbig (1962) definition, are known as classical T Tauri stars (hereafter cTTS). Low-mass PMS stars with weak, narrow emission lines are known as weak-line T Tauri stars (hereafter wTTS). Also, wTTS do not show veiled spectra, caused by the excess of continuum emission, like cTTS. Accordingly to the magnetospheric accretion model, the excess of continuum emission that causes the veiling of photospheric lines in cTTS is produced by the shock region, where the matter coming from the disk via magnetically driven channels encounters the stellar atmosphere (Dodin & Lamzin, 2012).

The criterium that distinguishes between cTTS and wTTS has evolved since Herbig's studies and nowadays the most widely used has been established by White & Basri (2003). According to their study on low-mass stars and brown dwarfs in the Taurus-Auriga star forming region, cTTS and wTTS distinction can be made based on the equivalent width of the $H\alpha$ line ($EW(H\alpha)$) and the width at 10% of the peak intensity of the $H\alpha$ line ($width_{10\%}$) (Figure 1.5).

One can classify a TTS as a cTTS if:

- $width_{10\%} \geq 270 \text{ km s}^{-1}$ (stronger criteria);
- $EW(H\alpha) \geq 3\text{\AA}$ for K0-K5 stars;
- $EW(H\alpha) \geq 10\text{\AA}$ for K7-M2.5 stars;
- $EW(H\alpha) \geq 20\text{\AA}$ for M2-M5.5 stars;
- $EW(H\alpha) \geq 40\text{\AA}$ for M6-M7.5 stars.

This type of division is empirical and so one can say that there is a “gray” region between cTTS and wTTS at the boundaries of each criteria. The classification of stars in this condition needs to be assisted by other criteria than the analysis of the $H\alpha$ line alone.

wTTS do not show IR excess as strong as cTTS and their projected rotational velocity (hereafter, $v \sin i$) is typically higher than that of cTTS. The interaction between disk and star, mostly by magnetic braking, may seem responsible for slowing down the star rotation (e.g. Bertout (1989)).

At the same time, when placed in the Hertzsprung-Russell diagram, cTTS and wTTS coexist for the same masses and ages (based on the simple PMS stellar evolution models) (Figure 1.4). This indicates that, although related, the star-disk interaction evolution might occur at different rates than the stellar evolution, predicted by the models. Some recent studies also point out that the average age of wTTS is higher than that of cTTS

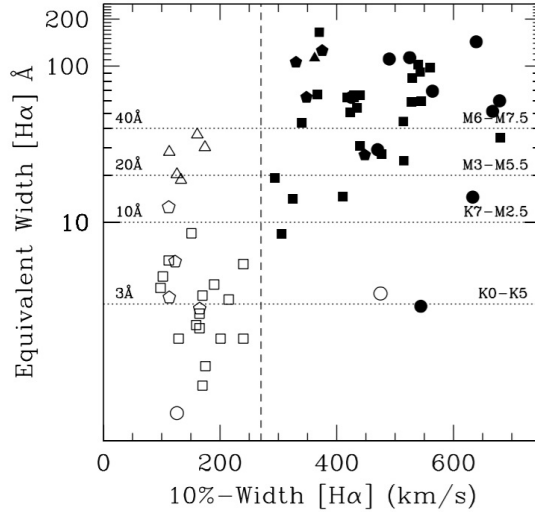


Figure 1.5: Empirical division between cTTS (filled symbols) and wTTS (open symbols). The distinction is done based on the equivalent widths and width at 10% peak of maximum intensity of the H α line. The filled symbols represent the optically veiled TTS, while the unveiled TTS are represented by the unfilled symbols. The vertical dashed line represents the value $\text{width}_{10\%} = 270 \text{ km s}^{-1}$. Credits: White & Basri (2003).

(Galli et al., 2015). Nevertheless, in the current paradigm, wTTS are the natural evolution of cTTS.

1.2 Classical T Tauri Stars

Classical T Tauri Stars are, from the two classes, the systems whose study is probably the most difficult. The way we see TTS has evolved since the beginning of their study. The increasing instrumentation capability allows us to probe deeper into these systems, more advanced theoretical models can be developed. Nevertheless, a model capable of explaining all observed spectroscopic and photometric features is yet to appear.

Different topics have been addressed in different time periods, as a reflex of the advance of technology. Chromospheric activity was a main research topic back in 1960, followed by the magnetic activity subject. The observations in the ultra-violet (UV) were important to explain the high fluxes of the H α line, as well as the broadening of Balmer lines, were not explained by the previous chromospheric models (e.g. Walter et al. (1987)). These observations showed that the chromospheric activity in TTS is similar to that of the Sun's chromosphere. X-ray emission, as well as polarization and observation of Zeeman broadening of some lines, made it clear that magnetic fields on the order of kilogauss are present at the surface of TTS.

Also, observations in the IR with the Infrared Astronomical Satellite (IRAS) were determinant to confirm the existence of circumstellar disks. The high IR luminosity can be associated with a disk from which matter is being accreted onto the star (e.g. Bouvier et al. (2007)). The disk activity is believed to be the main difference between cTTS and wTTS. In wTTS the lack of IR excess indicates a lack of circumstellar disk.

At the same time, models of TTS with stellar winds were able to explain part of the observed emission lines, but not all (Shu et al., 1994). The magnetospheric accretion models (see Section 1.3) are able to explain most of the observational features of TTS.

1.2.1 Observational features

In this subsection we will look into more detail, although briefly, the observational features that makes the cTTS such unique objects.

Spectral type

TTS are the infants of solar type stars and their spectral energy distribution is typically that of dwarf stars with spectral types that range from late F to M. CTTS are still contracting, so they are typically better modeled by a sub-giant star (lower $\log g$), instead of a dwarf.

CTTS spectrum

The spectrum of a cTTS (Figure 1.6) seems to be formed by contributions of three components:

- a photospheric spectrum emitted by the central star;
- a continuum and emission line spectra due to the presence of hot gas;
- an IR spectrum due to the presence of dust (Figure 1.7).

The photospheric spectrum itself is similar to that of a MS star with the same spectral type. Still, the lithium absorption line (Li I) at 6707.8 \AA is much deeper than for MS stars with spectral types earlier than K7. The presence and intensity of the Li I line is seen as an indication of youth ($\text{EW}(\text{Li}) \geq 100 \text{ m\AA}$). Since these stars are very young, they did not have enough time to burn all the lithium content present in the initial clump of gas material (e.g. Bertout (1989)).

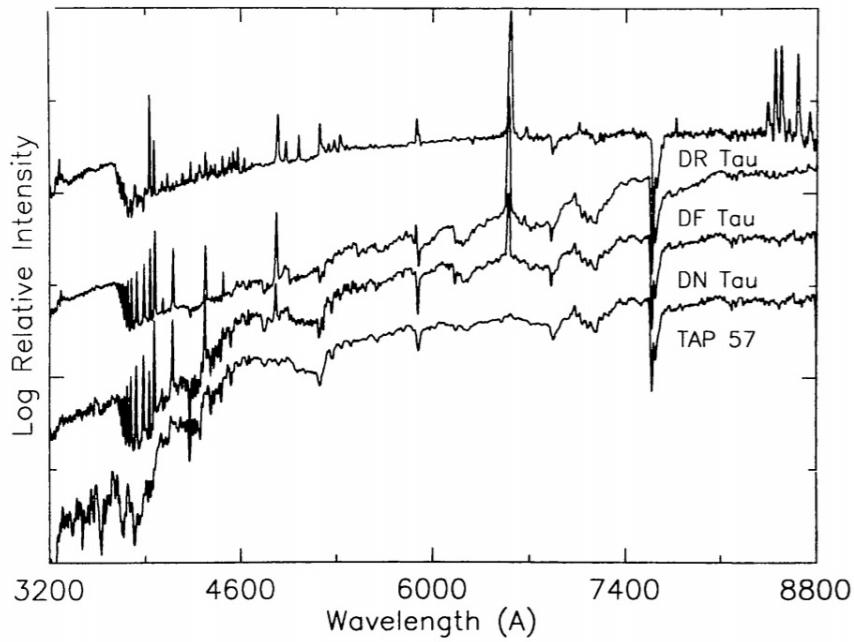


Figure 1.6: Example of cTTS optical spectra. The four stars are shown in order of increase emission level. Emission lines, in special $H\alpha$ line at 6563 \AA , are visible. The stars with higher emission level show less photospheric lines. TAP 57 is a wTTS, while DR Tau, DF Tau and DN Tau are cTTS. Credits: Bertout (1989).

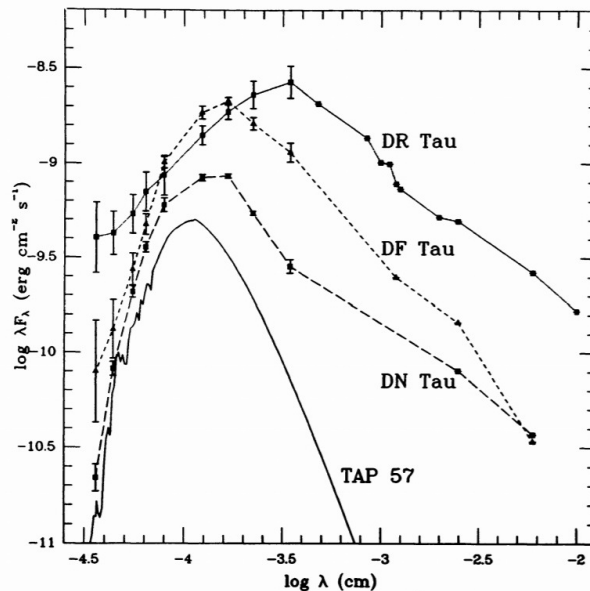


Figure 1.7: Spectral energy distributions of the four TTS from 3600 \AA to $100 \mu\text{m}$. Star TAP 57 is a wTTS and it is possible to see the differences in IR and UV emissions between wTTS and the three cTTS. Credits: Bertout (1989).

Veiling

One of the major difficulties when it comes to study the cTTS is the fact that the photospheric lines spectra are shallower than those of a MS star with the same spectral type. In some cases the photospheric spectrum is so weak that the weakest lines or even entire parts of the spectrum become invisible (Figure 1.6). This is caused by an excess of continuum emission that affects the spectrum from the UV to the IR, being more intense in the blue part of the spectrum (Basri & Batalha, 1990). This effect is known as *veiling* and has an origin that is non-photospheric.

Since the *veiling continuum* is stronger at the shorter wavelengths, this indicates that its origin is associated with a hot region, typically hotter than that of the star's photosphere. Also, the veiling intensity can vary in time periods of hours to days (e.g. Gahm et al. (1989)).

Recent studies also shown that there are other sources of veiling, contributing not with a continuum emission, but a discrete one. Broad emission (Sicilia-Aguilar et al., 2015) as well as line emission (Gahm et al., 2008) can contribute with filling-in emission of some photospheric lines. The resultant veiling is a combination of emission coming from several sources in the vicinity of the star.

Rotation

Another feature that comes into play while analysing TTS spectra is the projected rotational velocity parameter ($v \sin i$) obtained from the measurement of the broadening of the photospheric lines.

From the theory that stars form from gravitational collapse, they should rotate at velocities close to critical due to angular momentum conservation (Hartmann, 2009). The first studies on low-resolution spectra of cTTS indicated $v \sin i$ values up to 100 km s⁻¹, that were consistent with the star formation theory. On the other hand, the following studies with high resolution spectroscopy revealed that, in fact, TTS rotate at much slower velocities (e.g. Bouvier et al. (1986), Hartmann & Stauffer (1989)). On average, for solar masses and inferior, they rotate at 10% of the initially measured values and estimated from theory. In average, cTTS rotate more slowly than wTTS, which is explained by the interaction between stars and disk due to magnetic braking (Bouvier, 1993).

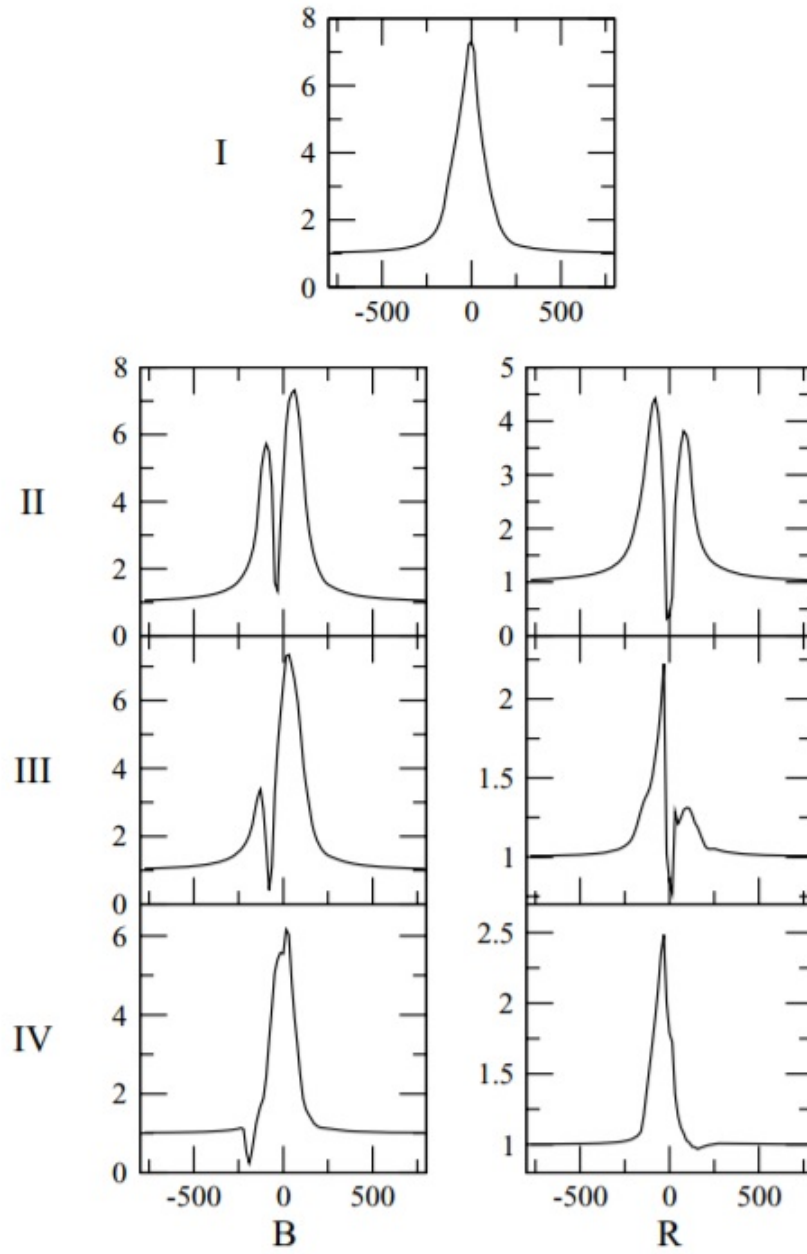


Figure 1.8: $H\alpha$ model profiles obtained by Kurosawa et al. (2006). These models reproduce the classification made by Reipurth et al. (1996) based on a sample of real cTTS spectra. Credits: Kurosawa et al. (2006).

Emission line spectrum

One of the key features of TTS is their emission line spectrum, that is typically populated by broad emission lines in cTTS ($\text{FWHM} \geq 200 \text{ km s}^{-1}$) (Bertout, 1989). This emission spectrum includes the Balmer series and lines of both neutral and ionized metals. Some of the most intense emission lines, besides the Balmer lines, are lines of Ca II, He I, Mg II, Fe I, Fe II. The fluorescent FeI emission lines, in particular those at 4048 Å and 4132 Å, are also important features of cTTS spectra. At the same time, many forbidden emission lines are observed in cTTS, like [O I] and [S II]. Nevertheless, the most prominent emission line for the TTS study is the H α line.

From the H α line it is possible to extract several information about both geometry and activity of the star-disk system. The inclination of the system plays an important role in the emission line profiles. According to the magnetospheric accretion model (see section 1.3), the H α emission line is originated at the hot accreting gas in the inner disk region.

Reipurth et al. (1996) studied the H α line in a relatively large sample of cTTS and attributed a type of profile morphology to the H α line. Kurosawa et al. (2006) used a simple model of the magnetospheric accretion model with stellar winds to study which condition (mass-accretion rates, inclination of the system) produced each type of H α profile previously classified by Reipurth et al. (1996). Figure 1.8 shows the different types of H α line profiles.

The classical P-Cygni profiles are also classified as type IV-B, with absorption at the blue part of the line. This type of morphology typically associated with strong wind features is not easily reproduced by magnetospheric accretion plus disk wind models (Kurosawa et al., 2006). Also, inverse P-Cygni profiles (type IV-R, absorption on the red part of the line) have a very low occurrence rate in H α line. In this case the observer is viewing the gas that is being accreted through the magnetically driven channels, so the angle range is very small. At the same time, inverse P-Cygni profiles are common in other lines, such as the HeI at 1 micron (Edwards et al., 2006).

Variability

CTTS do show both spectroscopic and photometric variability, most of the times irregular in terms of periodicity. It was this variability that made these stars known as irregular variables before their classification as TTS.

This variability can be caused by:

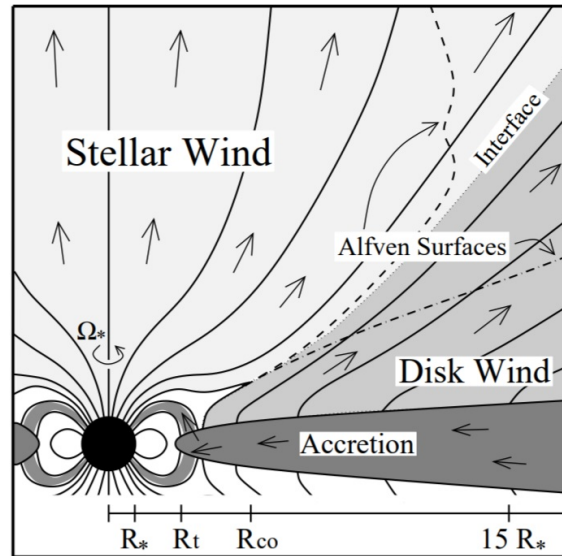


Figure 1.9: Schematic representation of the magnetospheric accretion model. This model includes disk and stellar winds. R_* is the stellar radius, R_t is the distance from the star at which the inner disk region is located and R_{co} is the co-rotation radius. Ω represents the angular spin rate of the star. Credits: Matt & Pudritz (2005).

- Cold spots on the surface of the star, that cause typical periodicity of few days, as well as flares (e.g. Barsunova et al. (2016));
- Variable mass-accretion rate, as well as hot spots with long lifetimes on the stellar surface (e.g. Alencar et al. (2012));
- Occultation of the star by the dust clouds from the circumstellar disk. In this case, the decrease in the brightness is accompanied by an increase in linear polarization and reddening (e.g. Rice et al. (2015)).

1.3 Magnetospheric accretion model

1.3.1 Mass-accretion

Even though there is no single model able to explain all the observed features in all T Tauri stars, the magnetospheric accretion model provides an explanation to several of these features (e.g. Bouvier et al. (2007) and references therein). According to this model, the young star is surrounded by a dusty gas disk, truncated at few stellar radii, from which gas is transported via magnetically driven channels onto the star (Figure 1.9).

In this scenario, dust and gas travel from the outer parts of the disk inwards, until a point in the vicinity of the star where the temperature starts to sublimate the dust. Normally in cTTS the dust extends down to the truncation radius (Bodman et al., 2017).

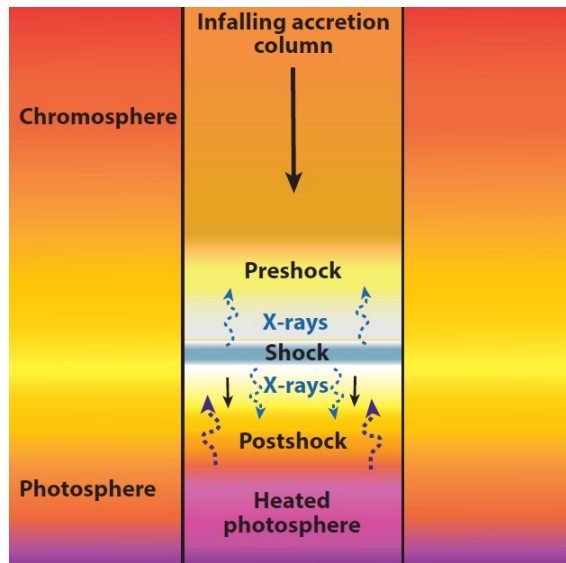


Figure 1.10: Shock region and heated stellar chromosphere and photosphere. The high-energy emission generated at the shock region flows up and down, to the pre-shock and post-shock regions. Below the shock region, this energy causes the heat of the photosphere around and from the hot spot region. Credits: Hartmann et al. (2016).

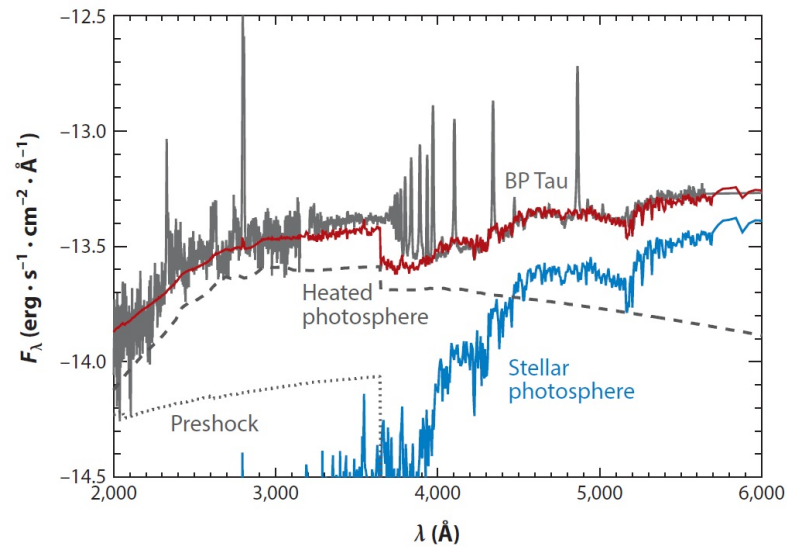


Figure 1.11: Spectrum of classical T Tauri BP Tau. The observed spectrum can be synthesized with a combination of radiation from a stellar photosphere with the same spectral type as the star, ultraviolet radiation from the pre-shock region and continuum radiation from a heated photosphere. Credits: Hartmann et al. (2016).

At this point the disk is truncated by the magnetic field. The truncation radius depends on the strength on the magnetic field, mass-accretion rate, as well as the mass and radius of the star. It can range from around 4 to 6 stellar radii (Hartmann et al., 2016). The truncation radius corresponds to the point where the disk matter stress equals the magnetic stress, so that motion becomes energetically favorable along magnetic field lines.

The ionized gas from the inner disk is then channelled by magnetic field lines onto the star atmosphere, forming the so called accretion columns. In these columns, the moving gas is heated up to temperatures above 8000 K. It is within the accretion columns that most of the observed broad permitted emission lines are presumed to be formed (e.g. Sicilia-Aguilar et al. (2015)).

Another important region contributing to emission line formation and to the excess of continuum emission affecting the spectra of cTTS is the shock region. The shock region is located at the base of the accretion column, where the gas, moving at free falling velocities around 300 km s^{-1} , hits the stellar atmosphere, in a region somewhere between the stellar chromosphere and photosphere (Figure 1.10).

Below the shock region, the gas can be heated up to temperatures of the order of 10^6 K due to the production of high energy radiation at the shock region that is transmitted to both pre-shock and post-shock regions. It is believed that the radiation coming from the shock region is responsible for the formation of hot spots in the stellar photosphere, whose radiation of $\sim 10^4$ K contribute to the veiling continuum observed on the cTTS spectra.

The energy that penetrates into the star's photosphere also causes a heating up of the region below the shock region. This energy is absorbed and re-emitted, with narrow emission that can fill-in some photospheric lines (e.g. Gahm et al. (2008)). Also, as the gas goes into the stellar photosphere, it starts to move slower, cooling down and getting denser, mixing with the already existing gas (Hartmann et al., 2016). On the other hand, the broad emission lines, like the Balmer series and other elements, such as Fe and Ca, must be formed within the accretion column and pre-shock region, where the hot gas is moving towards the star (e.g. Calvet & Gullbring (1998), Sicilia-Aguilar et al. (2015)).

Figure 1.11 shows an example of a comparison of a real spectrum of BP Tau with simulated spectra resulting from the sum of the stellar photosphere with radiation from the pre-shock region and the heated photosphere (Hartmann et al., 2016). These very simple elements resulting from the magnetospheric accretion model can reproduce the majority of the observed spectra of cTTS, mainly in the ultraviolet and optical regions of the electromagnetic spectrum.

1.3.2 Outflows and winds

The magnetospheric accretion model implies that during the transport of matter, angular momentum is transferred from the disk to the star (Hartmann, 2009). While the accretion is ongoing, the star rotation should increase. However, since the early observations of TTS one of the key features of cTTS is their slow rotation. Somehow, cTTS systems do conserve their angular momentum during the accretion process, while keeping the inner star as a slow rotator. At the same time, the magnetospheric accretion model predicts that part of the angular momentum is lost at the accretion channels.

Models with stellar and disk winds, like that proposed by (Shu et al., 1994), were created to justify the conservation of angular momentum (Figure 1.9) (Ferreira et al., 2006). After several years of observations of jets and outflows directly associated with YSO of low and intermediate masses, winds, jets and outflows are today known to be the key for the angular momentum conservation in the magnetospheric accretion model (Bouvier et al., 2007). The evolution of a cTTS system is the evolution of this process of energy transfer between disk, star and environment.

Although the rapid developments on the last few decades regarding mass-loss processes, how both winds and jets form and how the accretion and outflows are regulated are still unknown. Increasing computational capabilities and theoretic improvements are allowing the modeling of accretion and outflows altogether (e.g. Romanova et al. (2012), Zanni & Ferreira (2013), Dyda et al. (2015)).

The presence of outflows is also detected in the broad emission lines present in the cTTS spectra. As mentioned before, the P Cygni profiles of the Balmer series, like the $H\alpha$ and $H\beta$ lines, as well as Ca II and Na I D lines, are evidence of material moving outwards. The HeI at 1 micron is an excellent diagnostic of both inflow and outflow (e.g. Edwards et al. (2006)).

Another evidence of jets and outflows is the presence of low excitation forbidden lines of certain elements, like the [OI], [NII], [SII] and [FeII] lines. Analysis to the forbidden lines indicate that the outflows are constituted by a low velocity component ($\leq 50 \text{ km s}^{-1}$) and a high velocity component ($\geq 100 \text{ km s}^{-1}$). This is compatible with a disk wind and a collimated jet, respectively (Nisini et al., 2018).

Estimations for the ratio between mass-loss and mass-accretion rates for the jets are between 0.01 and 0.4, with an average of around 0.1 for most cTTS (e.g. Hartigan et al. (1995), Nisini et al. (2018)). So typically, the mass that is ejected from the system by the jets corresponds to around 10 % of the mass transported from the disk to the star. At the

same time, mass is also being lost by the stellar and disk winds.

Optical observations of jets and outflows in YSO show that these are typically bipolar and perpendicular to the disk. The interaction of these with their surroundings, due to collisional excitation of nebular material, produces the so called Herbig-Haro objects (Figure 1.12). The outflows have extensions that can exceed 1 parsec (e.g. Bally & Devine (1994)).

1.4 Weak-line T Tauri Stars

In the current paradigm, wTTS are the evolution of cTTS (Bertout, 1989). Contrary to the cTTS, the wTTS spectra only show narrow and weak emission lines, in accordance with an enhanced chromospheric activity and consistent with a young age. At the same time, their IR emission is compatible with a non-accreting and sometimes dissipative disk, probably with planet formation ongoing.

On the other hand, wTTS and cTTS coexist for the same masses and ages. The distinction between the two classes is closely related with the star-disk interaction evolution. In fact, it is the lifetime of the circumstellar disk that dictates for how long accretion will be occurring.

Recent studies, like the one from Galli et al. (2015), showed that, in average, cTTS are younger than wTTS. Also, there is evidence that the average lifetime of circumstellar disks is not the same for stars in different star forming regions. It is highly probable that the environment conditions constrain the star-disk system interaction and lifetime of the disks.

Since wTTS spectra are not affected by veiling, their spectra are easier to analyse with traditional methods used for MS stars. With knowledge of fundamental stellar parameters, like T_{eff} and $\log g$, it is possible to use these stars as templates for the analysis of cTTS with the same spectral type, forming from the same cloud material.

1.5 Extreme TTS: FUor and EXor outbursts

Even though cTTS are already very extravagant objects, there are few YSO with rather extreme behaviours: FUor and EXor objects. Both classes of objects display a rapid and dramatic change in magnitude and spectral type for a certain period of time, followed by a slow decay (Figure 1.13).

FUor stars are the most dramatic of the two, following its prototype, the FU Orionis star, still one of the most studied FUor objects. The true cause for these phenomena



Figure 1.12: Herbig-Haro 24 (HH24) object. This object is located 400 parsecs away, in the star forming region Orion B. This image, made with Hubble Space Telescope data shows the effects on the surrounding cloud material of two collimated jets perpendicular to the young star-disk system, that is obscured by the cloud. Credits: Nasa, Esa, Hubble Heritage (STScI/AURA).

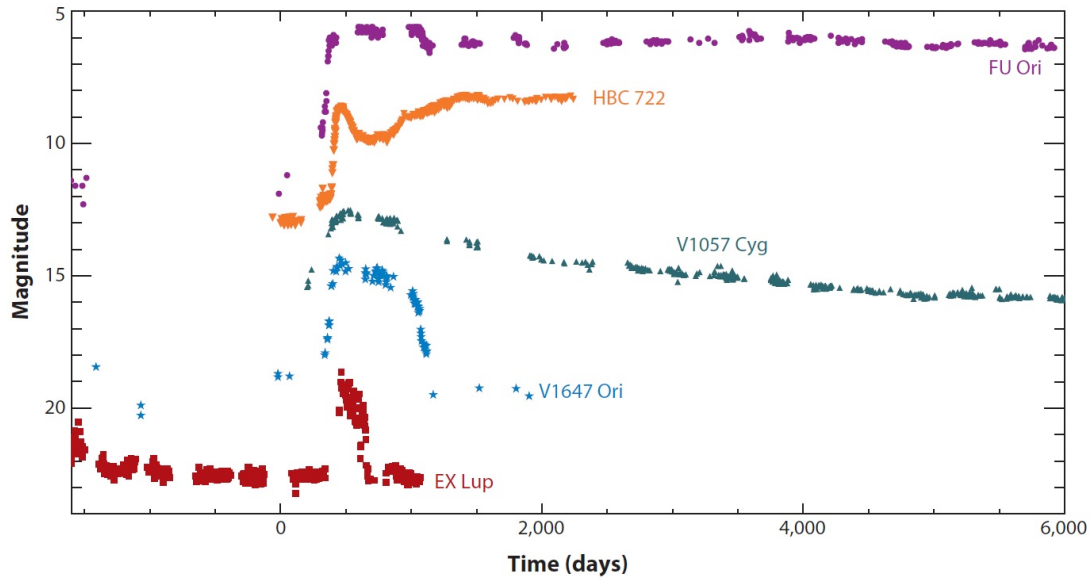


Figure 1.13: Changes in visual magnitude of FUor and EXor objects during several years. Credits: Hartmann et al. (2016).

is still unknown, although the current explanation lies on a sudden increase of the mass accretion rate, leading to a high luminosity phase, most probably caused by instability in the circumstellar disk (Hartmann & Kenyon, 1985). Recent studies support the idea that the FUor outbursts can occur at any time during the transition between Class I and II of TTS (Hartmann et al., 2016). The FUor objects have disks that are more massive than those of TTS of Classes I and II, as well as mass accretion rates that are two orders of magnitude higher than standard cTTS (Gramajo et al., 2014).

Thanks to the FUor star V1057 Cyg, it was possible to document the spectra before, during and after the FUor phase (Herbig et al., 2003). Before its outburst, in 1971, the spectrum of this star was like that of a cTTS with features of very powerful winds (Herbig, 2009; Petrov&Herbig, 2008). It is highly probable that cTTS showing features of high mass-loss processes are the progenitors of FUors (Petrov et al., 2014). TTS that show spectra compatible with the presence of very high wind activity (emission lines displaying P Cyg profiles) are candidates to be pre-FUori stars. Studying the conditions of the pre-outburst phase can enlighten our knowledge about the FUori phenomenon.

On the other hand, the EX Lup star (prototype of EXor objects) display outbursts with a shorter duration than those of FUor objects. Contrary to the latest, EXor objects spectra are populated by a large quantity of emission lines, that are present both during the outburst and during the quiescence phase (Sicilia-Aguilar et al., 2015).

Lorenzetti et al. (2012) demonstrated that EXor phenomena can be just a more intense

and less frequent manifestation of mass accretion events seen in any cTTS.

1.6 Open questions

Our knowledge about TTS has increased tremendously in the past few decades, due to the major improvements in instrumentation. Still, many questions remain unanswered and many more are formulated each time a new study is done. Nevertheless, some questions are still more relevant to the overall picture than others:

- **Accretion and stellar atmosphere.** What are the effects of accretion on the stellar atmosphere? At what extent does the accretion shock affect the star's photosphere and chromosphere? How does the accretion process influence the overall activity of cTTS?
- **Outflows/winds/jets.** How does the jets observed in several cTTS/Herbig-Haro objects form? What are the physical mechanisms responsible for the jets collimation? An interesting fact is that this issue is also an open question for the extragalactic cases of active galactic nuclei (AGN).
- **Relationship between accretion and mass-loss processes.** Accretion and outflows are clearly associated phenomena, but how do they relate with each other? What physical processes/mechanisms trigger each one? Which one regulates the other? How is the mass-accretion and mass-loss rates established?
- **CTTS and wTTS.** CTTS and wTTS coexist for the same stellar masses and the same ages, accordingly to the current PMS models. This implies that the PMS evolution of TTS is not only stellar, but regulated by the activity of the star-disk system. Which process/mechanisms regulate the evolution of the system from cTTS to wTTS? How can we improve our PMS models in order to take into account the star-disk system evolution?
- **Extreme TTS.** According to our current knowledge and TTS paradigm, cTTS are the evolution of class II IR objects, that will evolve to wTTS until reaching the MS phase. But there are some extreme TTS, like FU Orionis and EX Lupi, that still challenge our knowledge. Do all cTTS pass through a time in their evolution of such high activity? Or is the environment the major influence on the extreme accretion rates of these special types of YSO?

- **Multiplicity in TTS.** Many TTS are grouped in binaries and even multiple systems of 3 or more low-mass stars. Some of these systems are constituted by both cTTS and wTTS. How does the accretion processes regulate in these cases? If stars are too far away from each other (while still orbiting around a common center of mass), each star should have its own disk. In cases when stars are too close to each other they can accrete from the same disk. But what happens in those cases when each star has a disk that is interacting with the other one? And in more complex scenarios?

1.7 Objectives of this work

This doctoral thesis studies the activity and evolution of low-mass YSO. Therefore, it is divided into two works that offer new knowledge and further insight regarding both TTS classes. The two following chapters describe in detail each work and in the last chapter we summarize and highlight the most important conclusions of both works.

Chapter 2: Activity

In Chapter 2 we study three very active cTTS with the objective of understanding how the accretion of matter influences the stellar atmosphere. With this work we hope to bring some insight to the first open question written in the previous section: *how does the accretion process affect the stellar atmosphere?*

We analyse the way that photospheric lines are differently veiled: stronger lines are more veiled than weaker lines. We conclude that the effects of the accretion process on the star's atmosphere must be more extended and deep than the area occupied by the hot spot created due to the accretion shock. We observe this effect for stars with relatively high mass-accretion rates and powerful outflows/winds processes. We also noticed that for the three cases, the veiling continuum due to the hot spot was not the main source of veiling.

While our study shows that the accretion process does influence the star's atmosphere, more questions are raised.

Chapter 3: Evolution

In Chapter 3 we study the class of wTTS, that represents the evolution of cTTS towards the MS. We are looking for answers to the following questions: *what information about the PMS evolution can wTTS give us? Can we improve the cTTS studies from wTTS spectral analysis?*

This study aims to offer a simple way to quickly derive fundamental stellar parameters from intermediate resolution spectra for the wTTS that have been observed with the multi-object spectrographs FLAMES/GIRAFFE, operating at the Very Large Telescope. GIRAFFE produces narrow band, intermediate resolution spectra for more than 100 stars simultaneously when the multi-mode MEDUSA is used. It is one of the instruments used in the Gaia-ESO Survey to obtain spectra of young stars in several star forming regions.

In this work we use spectral synthesis to derive fundamental stellar parameters for a sample of wTTS from the star forming region NGC 2264. The spectra were obtained during a two month campaign, in 2012, that produced around 20 spectra per star. We adapted a line list and developed a script to automatically analyse large amount of spectra with the IDL package Spectroscopy Made Easy.

Since wTTS spectra are not veiled, traditional methods can be used to obtain effective temperature, surface gravity, metallicity and the projected rotational velocity. The knowledge of the stellar parameters allows one to estimate the mass and age, as well as use these stars as templates for the analysis of cTTS in the same star forming region. It also allows us to constrain global cloud parameters, like metallicity, that should be similar for stars forming in the same birthplace.

The several tests done using synthetic spectra and MS star templates produce results showing that the developed methodology can be used for the analysis of GIRAFFE spectra. But wTTS are not MS stars and their spectra are still affected by some degree of chromospheric activity, that might influence the determination of stellar parameters by spectral synthesis. Also, the inadequacy of the line list and atmospheric models used in the analysis can be responsible for the obtained results.

Chapter 2

CTTS veiling nature

2.1 Line-dependent veiling in very active cTTS

It is nowadays accepted that the concept of magnetospheric accretion must represent a close approximation to the reality of the accretion process in cTTS (e.g. Basri & Batalha, 1990; Hartigan et al., 1991, 1995; Valenti et al., 1993; Calvet et al., 2004; Bouvier et al., 2007; Hartmann et al., 2016). In accordance with this scenario, matter is transported from the inner-disk region onto the stellar surface via magnetically driven channels. The material that collides with the star atmosphere produces a region of shock-heated gas, called *hot spot*. This hot spot region typically has temperatures several thousand kelvins higher than the star effective temperature and its hot continuum emission superposes that of the stellar continuum (Calvet & Gullbring, 1998). This excess of continuum emission makes the photospheric lines shallower than those of a MS star with the same spectral type. This effect observed on the spectra of moderately active cTTS is known as veiling. The shock region is also responsible for the presence of several broad and narrow emission lines.

In this concept, a variation on the mass-accretion rate must directly affect the amount of veiling observed in cTTS spectra and so the veiling has been considered as a way to measure mass-accretion rates. Nevertheless, there are other indicators for the mass-accretion, like the equivalent widths¹ of the H α line (6563 Å) in emission, as well as other emission lines (e.g. Muzerolle et al., 1998; Herczeg & Hillenbrand, 2008; Dahm, 2008; Fang et al., 2009; Rigliaco et al., 2012; Mendigutía et al., 2015).

¹By definition (Gray, 2005), the equivalent width of an absorption line is the total absorption in the line expressed as a fraction of the continuum:

$$EW = \int_{-\infty}^{+\infty} \frac{F_c - F_\nu}{F_c} d\nu \quad (2.1)$$

where EW is the equivalent width of the line, F_c is the flux in the continuum and F_ν is the flux in the line.

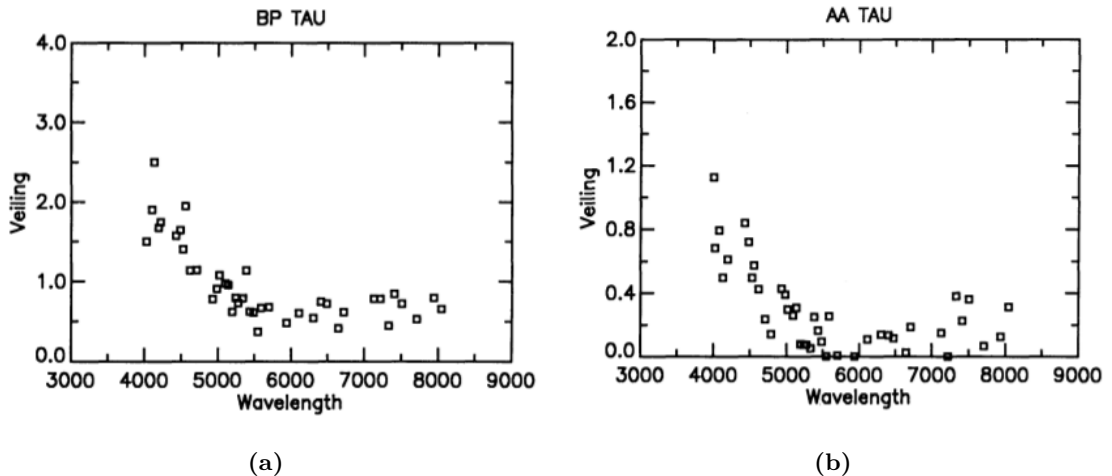


Figure 2.1: Veiling factor (VF) versus wavelength for BPTau and AATau. Credits: (Basri & Batalha, 1990).

In the most recent years, more careful studies of high resolution spectra of very active cTTS raised some doubts about the nature of the veiling effect. In some cases, the expected correlation between veiling and brightness was not found. RW Aur A is a clear case, with a veiling that is highly variable from night-to-night, but no correlation with brightness in V band was found from both photometric and spectroscopic monitoring (Petrov et al., 2001). Other cases are those of RU Lup and S Cra SE, where the large veiling correlates weakly with brightness (Gahm et al., 2008).

For the case of S Cra SE, Gahm et al. (2008) noticed the appearance of narrow emission cores at the bottom of the photospheric absorptions at the times when the activity of the star was more intense (higher mass-accretion rates). Also, studies on DR Tau (Petrov et al., 2011), V1331 Cyg (Petrov et al., 2014) and EX Lup (Sicilia-Aguilar et al., 2015) have shown that when the veiling is measured for each photospheric line from their equivalent widths (compared with a template of the same spectral type), the veiling is dependent on the strength of the line. Stronger lines are considerably more veiled than weaker lines, with the weakest remaining unveiled in some cases. A similar effect was noticed earlier in DI Cep (Gameiro et al., 2006). This type of veiling effect is known as line-dependent veiling.

Up to now there are three possible origins pointed out in literature for the line-dependent veiling: narrow emission lines formed at the post-shock region (Gahm et al., 2008), broad emission lines formed at the pre-shock region (Sicilia-Aguilar et al., 2015) and an accretion enhanced chromosphere (Petrov et al. (2011, 2014)).

The veiling of the stellar photospheric lines of cTTS can be expressed by the veiling

factor (VF) as:

$$VF = \frac{EW(template)}{EW(TTS)} - 1 \quad (2.2)$$

where $EW(template)$ and $EW(TTS)$ are the equivalent widths of the photospheric lines on the template² and TTS spectra, respectively. According to equation 2.2, a veiling factor higher than 0 means that the equivalent widths of the lines in the TTS are reduced by an additional non-photospheric continuum (known as veiling continuum). In that sense, the veiling factor measures the continuum excess in units of the photospheric continuum.

The veiling continuum is traditionally associated with the presence of a hot spot, where the accretion column shocks on the stellar surface. Due to the involved energies, the hot spot must be two or three times hotter than the stellar photosphere. So the hot spot produces radiation (approximated to a black body) that has its peak at shorter wavelengths. This is indicated by the observed rise of the veiling factor towards the blue region of the optical spectrum of some cTTS (Basri & Batalha, 1990; Calvet & Gullbring, 1998). On cTTS spectra where the veiling continuum is the dominant source of veiling, a simple plot of the veiling versus wavelength can show this effect (Figure 2.1).

In this work we are investigating the fraction of the veiling that is not due to the veiling continuum but due to the line-dependent veiling and its nature. To do this we will analyse the ratio of equivalent widths between template and cTTS. In the cTTS spectra, for most of the photospheric lines this ratio is larger than unity, although for the weakest lines it may be less than unity because of the errors of measurements and continuum estimation. Since we are assuming a spectral type for each star that is also subject to uncertainty, it might also result in some additional bias.

We have analysed three very active cTTS: LkH α 321 (=V1980 Cyg), AS 353 A (=V1352 Aql) and V1331 Cyg and further investigate the line-dependent veiling origin. These stars have spectra populated by strong emission lines, photospheric lines that are highly affected by veiling and they also display spectral features associated with strong mass-loss activity (like winds and outflows).

This work was done in collaboration with Doctor Peter Petrov, that gently provided the spectra of these three stars.

²A template spectrum is a spectrum with photospheric characteristics as similar as possible to those of the TTS, but without the effects induced by the accretion process (veiling, emission lines, etc.). A detailed explanation about template spectra is given in subsection 2.3.1.

2.2 Observational data

We analysed two sets of optical spectra obtained with two instruments at different times.

The first set of spectra used here was obtained by George Herbig with the High Resolution Echelle Spectrograph (HIRES) at the Hawaiian telescope Keck-1³(Vogt et al., 1994). These spectra have spectral resolution $R \sim 50\,000$ and a wavelength range within $4350 - 6750 \text{ \AA}$. There are some gaps between spectral orders from $\lambda = 4350 \text{ \AA}$ to $\lambda = 5000 \text{ \AA}$. Spectral resolution was derived from weak telluric lines prior to this work.

The spectra of LkH α 321 and V1331 Cyg were obtained in December 2002 and 24 July of 2004, respectively. The average signal-to-noise ratio (S/N) per resolution element is $S/N \sim 170$ at 5000 \AA and $S/N \sim 400$ at 6500 \AA . The spectrum of AS 353A was obtained in July 2003 and has an average $S/N \sim 200$ at 5000 \AA and $S/N \sim 350$ at 6500 \AA .

The second set of spectra used here was obtained by the Utrecht Echelle Spectrograph (UES), previously operating at the William Herschel Telescope. The observation of these three stars were done in November of 1998. The UES spectra has a resolution similar to that of HIRES, but with a much lower S/N ($S/N \leq 100$). For this reason these spectra were not used to derive the equivalent widths of the photospheric lines, but as an auxiliary to studies regarding changes of radial velocity within the range of few years.

Both sets of spectra have been normalized previously to this work. Since we do not have detailed information about the normalization process in each case, the definition of continuum in both sets of spectra is indeed one source of uncertainty.

Particular information about each stars spectra can be found in section 2.4. Table 2.1 summarizes the information available in the literature for the three stars: distance, visual magnitude (V), spectral type (SpT), visual extinction (A_v) and the logarithm of the bolometric luminosity (L_*).

2.3 Analysis of cTTS spectra

2.3.1 Templates

Traditional spectroscopy methods for the determination of fundamental stellar parameters can not be used for cTTS, due to the presence of veiling and emission lines. Instead, the use of template spectra for the analysis of cTTS is a common procedure, namely for the determination the spectral type and other stellar properties of these stars.

³The W. M. Keck Observatory is operated as a scientific partnership among the California Institute of Technology, the University of California, and the National Aeronautics and Space Administration. The Observatory was made possible by the generous financial support of the W. M. Keck Foundation.

Table 2.1: Literature data for the three cTTS

Star	Distance (pc)	V (mag)	SpT	Av (mag)	log(L _*) (L _⊙)
AS 353A	150 ± 50 ^h	12.21	K2 - K5 ^e		1.32 ^d
V1331 Cyg	550 ± 50 ^a	11.7 - 12.5 ^a	G7 - K0 IV ^e	1.4 ^f	0.4 ^g
LkHa 321	550 ± 50 ^a	12.25 - 12.44 ^b	G1 ^c	2.23 ^c	1.42 ^d

^a Shevchenko et al. (1991), ^b Grankin et al. (2007), ^c Cohen & Kuhn (1979), ^d From photometry data, ^e Petrov & Babina (2014); Petrov et al. (2014), ^f Hamann & Persson (1992), ^g Tokunaga et al. (2004), ^h Prato et al. (2003).

There are two types of template spectra that can be used for this purpose: real stellar spectra (from MS stars, sub-giant stars⁴ or wTTS) and synthetic spectra. Real stars spectra, in particular those of wTTS located in the same star forming region, are more appropriate than the synthetic ones to compare with cTTS. Nevertheless, each real star is an individual with its own peculiarities and it is not easy to find MS and wTTS stars of all spectral types with well determined stellar parameters and none or very low levels of activity. Another difficulty is that of finding high resolution, high S/N spectra of MS and sub-giant stars for a wide range of temperatures.

On the other hand, the available synthetic spectra are built based on models for MS stars and using line parameters information whose source is mostly theoretical. Although these might introduce some uncertainties, they are much smaller and easy to control than those from a real spectra. In section 2.3.4 this issue is explored in more detail. Given the type of study we performed on these three cTTS is related with activity, we decided to use synthetic spectra as template spectra instead those of real stars.

The grids of synthetic spectra were obtained with the software package Spectroscopy Made Easy (hereafter, SME) (Valenti & Piskunov, 1996). SME allows us to create high resolution spectra with no noise and with no constraints to the combination of stellar parameters. One advantage of synthetic spectra is the well defined continuum level, that makes the measurement of equivalent widths more accurate. Another advantage is the creation of synthetic spectra with projected rotational velocity ($v \sin i$) values similar to those of the analysed stars. This was very helpful to measure the equivalent widths of lines for the case of LkH α 321. While rotation does not change the equivalent widths of the

⁴Since cTTS are still ongoing contraction, the radius is still expanded. For this reason, their surface gravity ($\log g$) is lower than that of a MS dwarf star, so the spectra of sub-giant stars are more adequate to be used as template for cTTS spectra ($\log g \sim 3.5 - 4$ dex).

lines, for high values of $v \sin i$ ($\geq 30 \text{ km s}^{-1}$ for the LkH α 321) some lines are completely blended, so instead of lines we are, in some cases, measuring line profiles resulting from line blending).

We produced synthetic spectra with SME to fulfill the following tasks:

- determination of spectral type and estimation of $v \sin i$ and radial velocity (v_{rad}) for each cTTS;
- measurement of equivalent widths of lines to compare with the equivalent widths of the corresponding lines on the cTTS spectra.

In the first task, to determine the spectral type of our three cTTS we need information about T_{eff} , $\log g$ and metallicity expressed in terms of iron content ($[\text{Fe}/\text{H}]$). For the second task we created synthetic spectra with the same parameters as those of the cTTS, estimated in the first task. These are considered the template spectra for each of the three cTTS.

These stars are affected by veiling, both from a continuum source and emission filling-in the stronger lines with several origins (Gahm et al., 2008; Petrov et al., 2011, 2014; Sicilia-Aguilar et al., 2015). We can overcome this by analysing the ratios of close by weak photospheric lines, since the veiling continuum can be considered constant on small wavelength intervals. Also, the veiling continuum does not discriminate weak from stronger lines. All lines in a small wavelength interval must be affected by the same amount of veiling continuum. This means that the ratios of nearby photospheric lines must be conserved, since they are being reduced by the same amount. So, we can use the ratios of lines to estimate T_{eff} , since some lines are much more sensitive to changes on temperature than others (see section 2.3.2). On the other hand, the presence of veiling makes the determination of $\log g$ and $[\text{Fe}/\text{H}]$ a very difficult task.

Depending on the temperature of the star, the $\log g$ can be estimated by several indicators. One of these indicators on cooler stars are the wings of several lines (like Ca II H and K lines, Na I D lines, Mg I b lines), that are strongly affected by the surface gravity (Gray, 2005). Sadly, these lines are not available on our spectra. Another common way to measure $\log g$ is by comparison of weak lines in different ionized stages (Gray, 2005). Since we do not know how the line-dependent veiling affects the lines of different ionization stages this method must be avoided. For the $\log g$ we decided to adopt a typical value for cTTS: $\log g = 3.75$ dex. This value is that of a sub-giant star and is also concordant with $\log g$ values derived from T_{eff} and stellar bolometric luminosity (L_*) using the PMS tracks

from Siess et al. (2000). A difference in 0.25 dex in $\log g$ does not affect significantly our results.

The same is also true for the case of metallicity, since the line-dependent veiling affects lines differently. TTS are the PMS counterparts of solar type stars. In a rough approximation we can assume that they have $[\text{Fe}/\text{H}]$ similar to that of the Sun. Also, several low-mass star forming regions in our Galaxy share an average $[\text{Fe}/\text{H}]$ close to solar (Spina et al., 2017). In this analysis we are assuming a solar metallicity for our stars: $[\text{Fe}/\text{H}] = 0.0$ dex.

Besides $\log g$ and $[\text{Fe}/\text{H}]$, there are few parameters shared by all the synthetic spectra created to execute the two tasks: spectral resolution, microturbulence (v_{mic}), macroturbulence (v_{mac}) and wavelength range. The value for the spectral resolution is the same as that of the HIRES spectra. Both parameters share similar effects on the photospheric lines with other stellar parameters, like with $v \sin i$, and are not significant in our analysis. For this reason we decided to keep them as fixed parameters, with equal values for the three stars.

We assume that $v_{mic} = 1.0 \text{ km s}^{-1}$, a typical value for cool stars and wTTS (e.g. Padgett, 1996; Rojas et al., 2008; James et al., 2006; Taguchi et al., 2009). The v_{mac} value is estimated using equation 1 from Valenti & Fischer (2005) taking an average $T_{eff} = 5000$ K: $v_{mac} = 2.8 \text{ km s}^{-1}$. This value is obtained taking in account the spectral types found in literature: between G5 IV and K2 IV, corresponding to temperatures between 4800 K and 5500 K. Due to strong veiling it is not possible to measure the stellar parameters with high accuracy and precision, so we can use an average value of v_{mac} for the construction of the synthetic spectra with no loss of precision.

The synthetic spectra are based on the Kurucz (Castelli & Kurucz, 2003) grids of stellar atmospheric models, considering Local Thermodynamical Equilibrium (LTE). A line list extracted from the Vienna Atomic Line Database (VALD)⁵ (Ryabchikova et al., 2015), using the option “Extract stellar”, was also used to create the synthetic spectra. The values for each of these parameters are presented in Table 2.2.

2.3.2 Determination of spectral type

Due to the presence of veiling it is very difficult to estimate $[\text{Fe}/\text{H}]$ and $\log g$ for our very active cTTS. And for this reason we decided to assume a solar metallicity and a $\log g$ value of a sub-giant star ($\log g = 3.75$ dex). So our determination of T_{eff} will define the spectral

⁵VALD database is operated at Uppsala University, the Institute of Astronomy RAS in Moscow, and the University of Vienna.

Table 2.2: Common parameters for all synthetic spectra

Spectral resolution	[M/H] (dex)	$\log g$ (dex)	v_{mic} (km s ⁻¹)	v_{mac} (km s ⁻¹)	λ Å
50 000	0.0	3.75	1.0	2.8	[4500, 7000]

type of each star.

Photospheric lines are sensitive to different conditions of temperature inside the stellar atmosphere. Lines of different elements form at different depths and their strength and shape is affected by the intrinsic properties of the star. At the same time, it is possible to use the lines more sensitive to changes of a certain parameter to estimate a value of that particular parameter.

To estimate T_{eff} for each star we analyse the ratios of relatively weak close by lines at wavelength intervals free of emission. Weak single line profiles of photospheric lines were selected according to their sensitiveness to changes in T_{eff} . This selection was made using the grids of synthetic spectra and afterwards each pair of lines was compared with the corresponding pairs on each cTTS spectra. Figures and tables with the pairs of lines used to determine T_{eff} hence, spectral type of each star will be presented in section 2.5.

The value of T_{eff} for each star was chosen based on the similarity between the ratios of the lines in the real spectrum and in the synthetic spectra. For each star there is an uncertainty of less than 250 K.

Regarding the determination of $v \sin i$, artificial veiling was added to the synthetic spectra, so that we can do a proper fit between template and real spectra to estimate this parameter. Synthetic spectra with different values of $v \sin i$ and veiling were simulated and adjusted to the weak lines, until a good match between real and synthetic spectra was achieved. Both AS 353A and V1331 Cyg have $v \sin i$ values below 6 km s⁻¹. Since we were not able to see major differences between any value of $v \sin i$ from 1 to 6 km s⁻¹ for both stars, we decided to use the minimum value of 1 km s⁻¹ in our templates, in order to improve the continuum level determination while measuring the equivalent widths.

As for the determination of v_{rad} we cross correlated our cTTS spectra with that of the Sun. After the determination of the equivalent widths for each star we used the information about the difference in wavelength between the real and the synthetic spectra to re-determine v_{rad} and confirm the determination by cross correlation.

In Table 2.3 we summarize the values used to construct each synthetic template based on the spectral type, $v \sin i$ and v_{rad} determinations for each star.

Table 2.3: Template synthetic spectra parameters for each star

Template for	T_{eff} (K)	$\log g$ (dex)	[M/H] (dex)	$v \sin i$ (km s ⁻¹)	v_{rad} (km s ⁻¹)	v_{mic} (km s ⁻¹)	v_{mac} (km s ⁻¹)
AS 353A	5000	3.75	0.0	1	-11	1.0	2.8
V1331 Cyg	5000	3.75	0.0	1	-15	1.0	2.8
LkH α 321	5250	3.75	0.0	32	-16	1.0	2.8

2.3.3 Measurement of equivalent widths

The aim of this study is the comparison between the equivalent widths of the same photospheric lines in the cTTS and the template spectra. If continuum veiling is the main source of veiling in the photospheric lines then we should observe a variation of the veiling with wavelength and no dependence on the line strength. On the other hand, if line-dependent veiling is a significant contributor to the total veiling, we should observe a variation in veiling from line to line, even within a small wavelength region.

To perform this study, hundreds of lines were measured on both cTTS and synthetic templates. We made use of the software package IRAF⁶ to perform this task.

Only the single line profiles clearly identified on both real and synthetic spectra were measured. We avoided regions with broad emission, even if there were photospheric lines visible on top of that emission. A detailed description of the measured lines for each star will be reported in Section 2.4.

It is also important to show that for a normal MS star we do not observe any trend of the equivalent widths ratio with strength of the line, wavelength or excitation potential. Also, if no veiling is present on the spectrum of a star, then when compared with a template with the same spectral type it is expected that the average of equivalent widths ratio will be around 1. This means that the equivalent width of the photospheric lines in the star is similar to that of the template. This study with MS stars will also shed some light on the uncertainties associated with the equivalent width measurement, mainly due to the continuum level estimation.

Real spectra of the Sun and a G7 IV star (HD190248) were used to study the equivalent widths ratio versus line strength, wavelength and excitation potential on non-active, non-veiled stars and evaluate the uncertainties due to the equivalent width measurements.

⁶IRAF is distributed by the National Optical Astronomy Observatories, which are operated by the Association of Universities for Research in Astronomy, Inc., under cooperative agreement with the National Science Foundation.

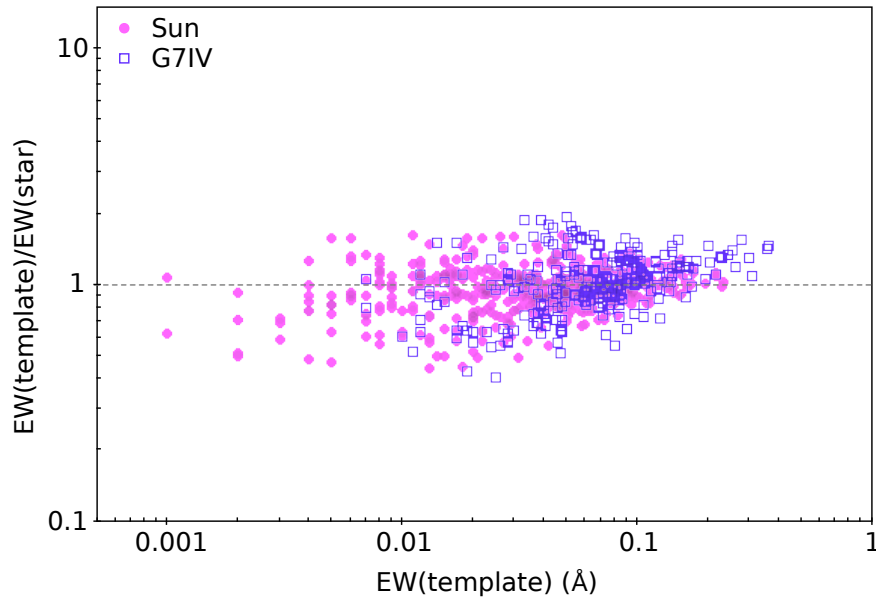


Figure 2.2: Equivalent widths ratio versus line strength for the Sun (filled pink dots) and a G7IV (open blue squares) star. The ratio is centered around the veiling factor = 0. No dependency of veiling with line strength is observed.

The Sun spectrum⁷ was obtained by the High Accuracy Radial velocity Planet Searcher (HARPS) and has a $S/N \geq 500$ (Blanco-Cuaresma et al., 2014). The G7 IV star spectrum was extracted from the ESO Archive⁸. We assigned a synthetic template with $T_{\text{eff}} = 5000$ K and $\log g = 3.75$ dex to the G7 IV star⁹ and a template with $T_{\text{eff}} = 5750$ K and $\log g = 4.4$ dex to the Sun, both with solar metallicity.

The equivalent widths of the same lines were measured on both real and synthetic spectra and the ratio $EW(\text{template})/EW(\text{star})$ was analysed, in terms of line strength, wavelength and excitation potential of low level of the transition. More than 500 lines were measured in each case. There is no dependence of $EW(\text{template})/EW(\text{star})$ on line strength of the photospheric lines (Figure 2.2), wavelength (Figure 2.3) and excitation potential (Figure 2.4).

2.3.4 Sources of uncertainty

From the analysis of Figure 2.2 we can observe that there is line-to-line scatter of the equivalent widths ratio, more evident for the weaker lines. As mentioned previously, the normalization of the spectra was done previously to this work and we do not have informa-

⁷Obtained from <https://www.blancocuaresma.com/s/benchmarkstars>

⁸Obtained from http://www.eso.org/sci/observing/tools/uvespop/field_stars_uptonow.html

⁹Considering the relationship between spectral type and effective temperature as presented in Gray (2005).

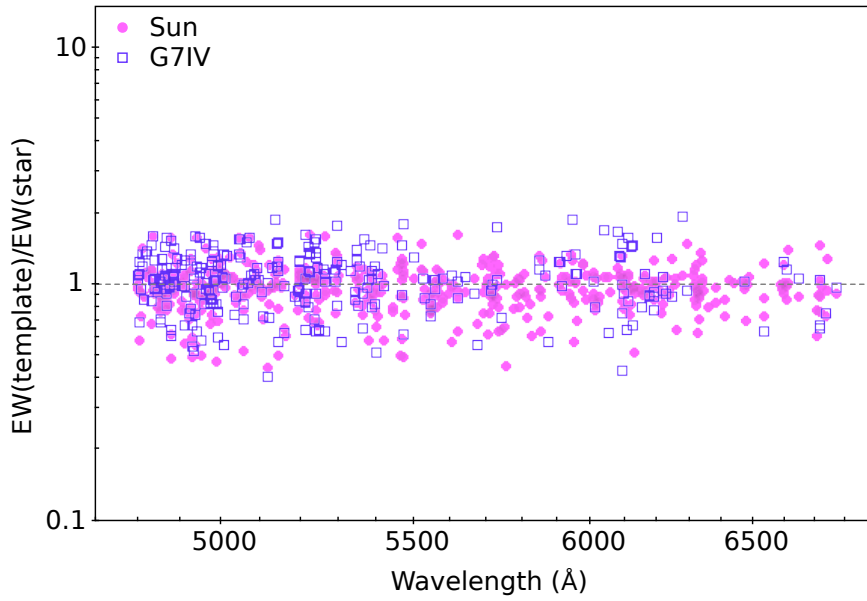


Figure 2.3: Equivalent widths ratio versus wavelength for the Sun (filled pink dots) and a G7IV (open blue squares) star. The ratio is centered around the veiling factor = 0. No dependency of veiling with wavelength is observed.

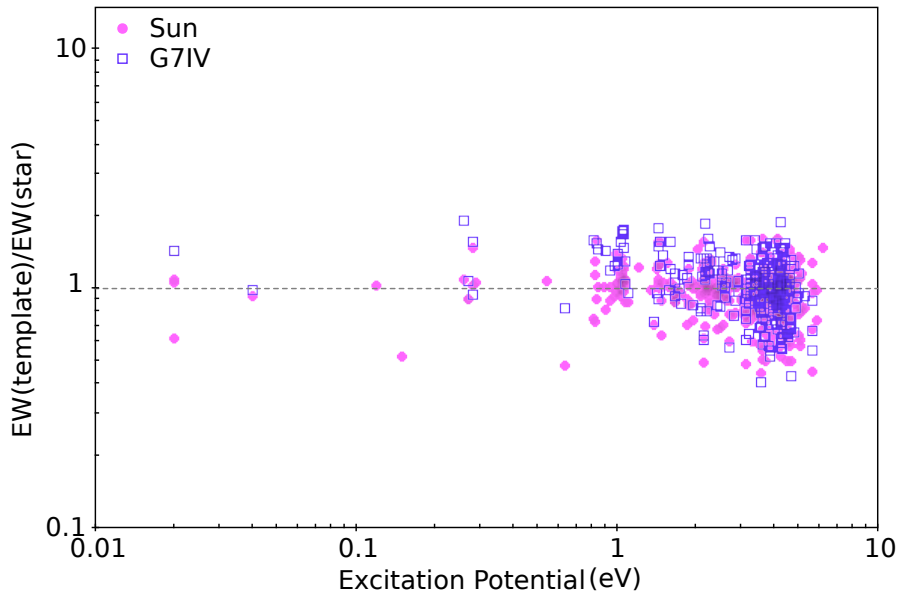


Figure 2.4: Equivalent widths ratio versus excitation potential of the lower level for the Sun (filled pink dots) and a G7IV (open blue squares) star. The ratio is centered around the veiling factor = 0. No dependency of veiling with excitation potential is observed.

tion about the normalization process. The way the spectra was normalized can influence the determination of the continuum level. The observed scatter is mainly caused by the incorrect determination of the continuum level and can be quantified with a standard deviation from the average. For the weakest lines, with $EW \leq 50 \text{ m\AA}$ the sample standard deviation is about 0.2 - 0.3 dex, while for the stronger lines is 0.1 - 0.2 dex.

There is another source of error that can be pointed out since we are using synthetic spectra as templates in our analysis. This second source of error is the lack of correction for the $\log gf$ and van der Waals damping parameters in the synthetic templates.

For this study we did not calibrate the values of $\log gf$ and van der Waals damping parameters for the astrophysical case. This type of correction is done to obtain a higher accuracy when determining fundamental stellar parameters with SME. It is usually done using high resolution spectrum of the Sun, that is the star with most accurate stellar parameters. Since we are not correcting these line parameters, some lines can show significant differences when comparing the synthetic spectra with that of real MS stars. These differences in equivalent widths produces a scatter. But in the case of cTTS, they do not seem to be as affected by it as the MS stars, most probably due to the veiling effect on the photospheric lines. Applying this type of correction to all of the analysed lines for the three different templates would also be very time consuming. For these reasons, we decided to not apply any $\log gf$ and van der Waals damping parameters correction to the line list.

On the cTTS spectra, the measurements of the equivalent widths have an uncertainty associated that depends on both the S/N of the spectra and on the determination of the local continuum level, that can be affected by the blending of photospheric lines and broad emission lines. The latest is the main source of error in this case, since we are dealing with considerably high S/N spectra (from 100 in the blue up to 400 in the red part of the spectrum). We made use of the synthetic spectra to define the continuum level on both sides of each photospheric line. With this information it was easier to find the continuum level at each side of the photospheric lines on the cTTS spectra.

The synthetic spectra were also used to estimate an average uncertainty on the determination of the equivalent widths of the lines. To do this we applied different values of random noise to a synthetic spectrum created with similar parameters to those used as templates for the cTTS. A synthetic spectrum with the same parameters and no noise was also created. Then we measured few hundreds of lines in the synthetic spectra with noise and in the one without noise. To evaluate the influence of random noise and continuum level values on our determinations, we compared the equivalent widths ratio of the lines

Table 2.4: Derived stellar parameters

Star	Sp.Type	T_{eff} (K)	M_* (M_{\odot})	R_* (R_{\odot})	$v \sin i$ (km s^{-1})	v_{rad} (H) (km s^{-1})	v_{rad} (U) (km s^{-1})	EW(H α) (\AA)	EW(HeI) (\AA)
LkHa 321	G5-G7	5500-5250	2.9	5.3	32	-16 \pm 0.5	-14.4 \pm 1.0	30	0.08
V1331 Cyg	G7-K1	5250-5000	2.9	5.5	\leq 6	-15.0 \pm 0.3	-16.8 \pm 0.3	53	0.22
AS 353A	K1-K2	5000-4800	1.6	2.1	\leq 6	-10.4 \pm 0.2	-8.0 \pm 0.2	58	1.30

Note: v_{rad} (H) is the radial velocity measured from the HIRES spectra, while v_{rad} (U) is the radial velocity measures from the UES spectra.

against line intensity. From our analysis we consider an error between 5 to 12 %, being higher for the weaker lines.

Although the line-to-line scatter of the EW(synthetic)/EW(real) ratio is relatively large, it does not affect our results due to the large number of lines used in the analysis.

2.4 CTTS spectra analysis

In this section we analyse in detail each star, presenting information extracted from the literature (background), the analysis of each star spectrum, including the estimation of spectral type, and the results from the veiling analysis through the equivalent widths measurements (results). Table 2.4 resumes information about these stars resulting from our spectral analysis described in the following sub-sections.

2.4.1 AS 353A

Background

AS 353A is a cTTS that belongs to a multiple T Tauri stars system. AS 353B has been considered a wTTS until recently, when it was resolved into a subarcsecond binary and AS 353Ba has been reclassified as a cTTS (Tokunaga et al., 2004). AS 353 system belongs to the Aquila star forming region and has an estimated distance of 150 ± 50 pc (Prato et al., 2003; Rice et al., 2006) (Figure 2.5).

Associated with AS 353 is the Herbig-Haro object HH 32 (Figure 2.6) (Herbig & Jones, 1983). AS 353A has a rich emission lines spectrum and the Balmer lines do show strong blue-shifted absorption (Figure 2.7). The P Cygni profiles of the Balmer lines indicates the presence of powerful mass-loss processes, that is confirmed by the direct observations of its jet.

Previous estimations of spectral type for AS 353A from Basri & Batalha (1990) in the optical pointed out for a K2 star, later confirmed from K-band spectroscopy by Tokunaga

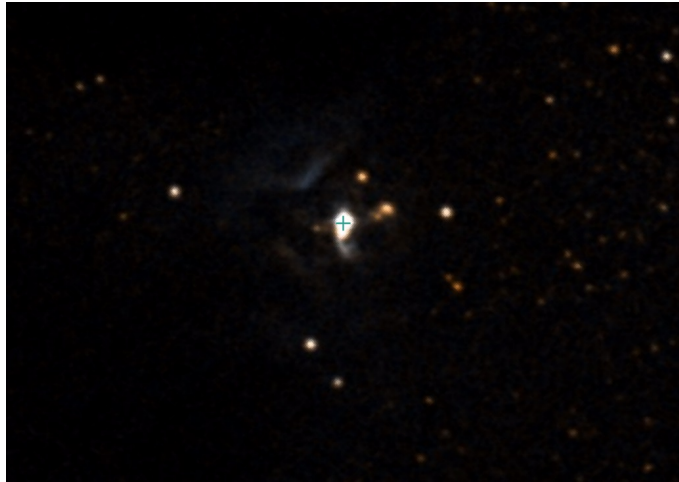


Figure 2.5: AS 353A Digital Sky Survey image (optical). Credit: Simbad (Wenger et al., 2000).

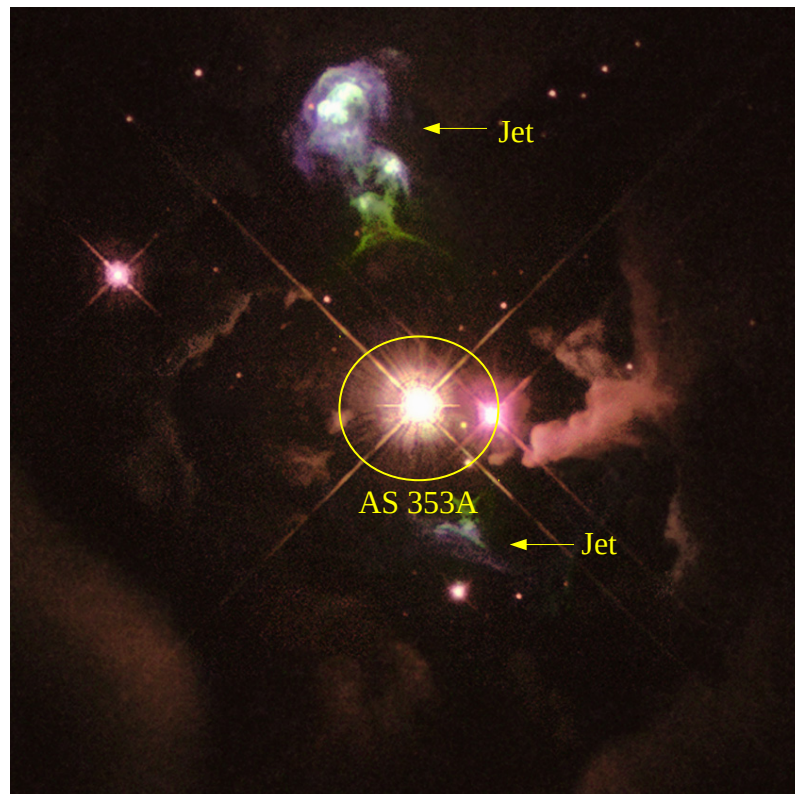


Figure 2.6: Hubble image of HH 32 (optical). AS 353A is the driving source of the jet. Credits: NASA/ESA/The Hubble Heritage Team (AURA/STScI)

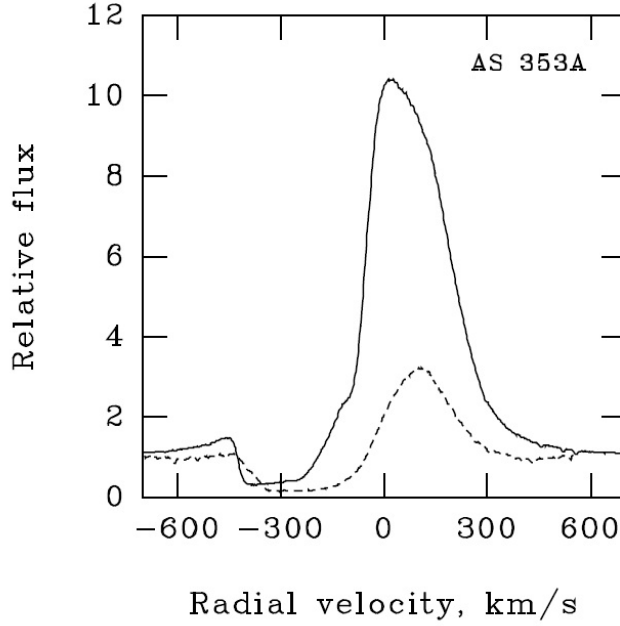


Figure 2.7: P Cygni profiles of the $H\alpha$ (solid line) and $H\beta$ (dashed line) lines in the AS 353A HIRES spectrum (Rei et al., 2018).

et al. (2004). A stellar bolometric luminosity $\log(L^*/L_{\odot}) = 0.4$ was also estimated by Tokunaga et al. (2004). Later, Rice et al. (2006) used H-band spectroscopy and derived a spectral type K5, $v \sin i = 10 \text{ km s}^{-1}$ and $v_{rad} = -11.4 \pm 1.1 \text{ km s}^{-1}$. This star shows photometric variability within 0.86 mag in the V band (Fernandez & Eiroa, 1996).

Table 2.1 summarizes data collected from the literature for AS 353A.

Spectral analysis

The spectrum of AS 353A is populated by very broad emission lines, on top of which it is possible to observe photospheric lines (Figure 2.8). From the three stars, the spectrum of AS 353A is the only one that allowed the largest amount of equivalent widths measurement of the photospheric lines. One of the reasons for this is its slow rotation: $v \sin i \leq 6 \text{ km s}^{-1}$.

Figure 2.7 show the $H\alpha$ and $H\beta$ lines in the HIRES spectrum of AS 353A. The equivalent widths of the $H\alpha$ and He I lines (in emission) were also measured: $EW(H\alpha) = -58 \text{ \AA}$ and $EW(\text{He I}) = -1.30 \text{ \AA}$.

Figure 2.9 shows the fragments of AS 353A spectrum used to determine the spectral type. In these plots are over-plotted synthetic spectra with two different values of T_{eff} (4600 K and 5400 K). The uncertainty associated is of approximately 250 K. The synthetic spectrum chosen as template for AS 353A has $T_{\text{eff}} = 5000 \text{ K}$, $\log g = 3.75 \text{ dex}$, $[\text{Fe}/\text{H}] =$

Table 2.5: Photospheric line pairs used in the spectral type determination of AS 353A

Line 1			Line 2		
λ (\AA)	Ele.	Exc. Pot. (eV)	λ (\AA)	Ele.	Exc. Pot. (eV)
6111.070	Ni I	4.09	6111.651	V I	1.04
6116.180	Ni I	4.27	6116.990	Co I	1.79
6116.180	Ni I	4.27	6119.528	V I	1.06
6146.207	Ti I	1.87	6147.834	Fe I	4.08
6151.617	Fe I	2.18	6152.292	Si I	5.96
6154.225	Na I	2.10	6155.134	Si I	5.62
6156.023	Ca I	2.52	6157.727	Fe I	4.08

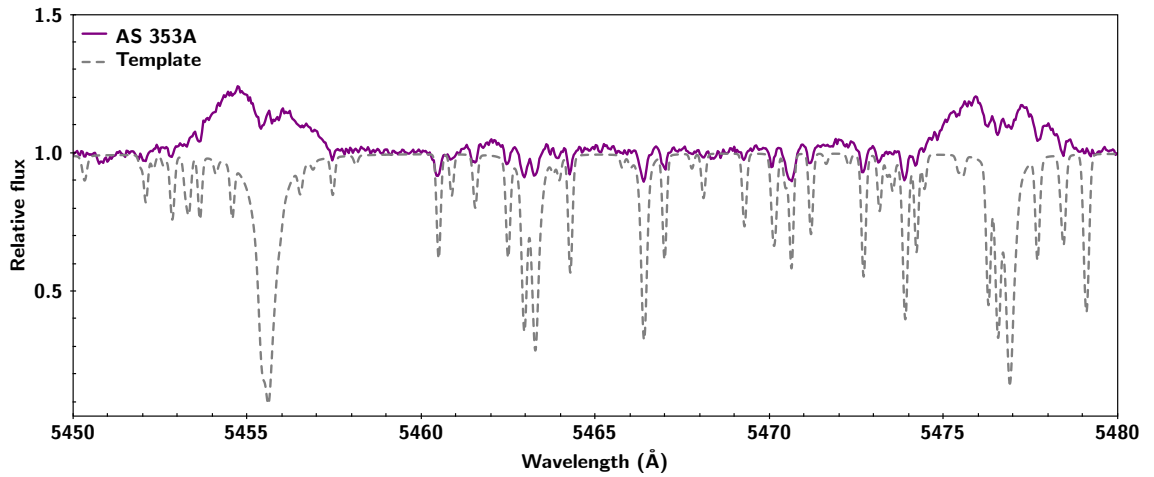


Figure 2.8: Fragment of AS 353A spectrum. The dashed gray line represents the synthetic template for this star. It is possible to observe photospheric lines on top of the broad emission.

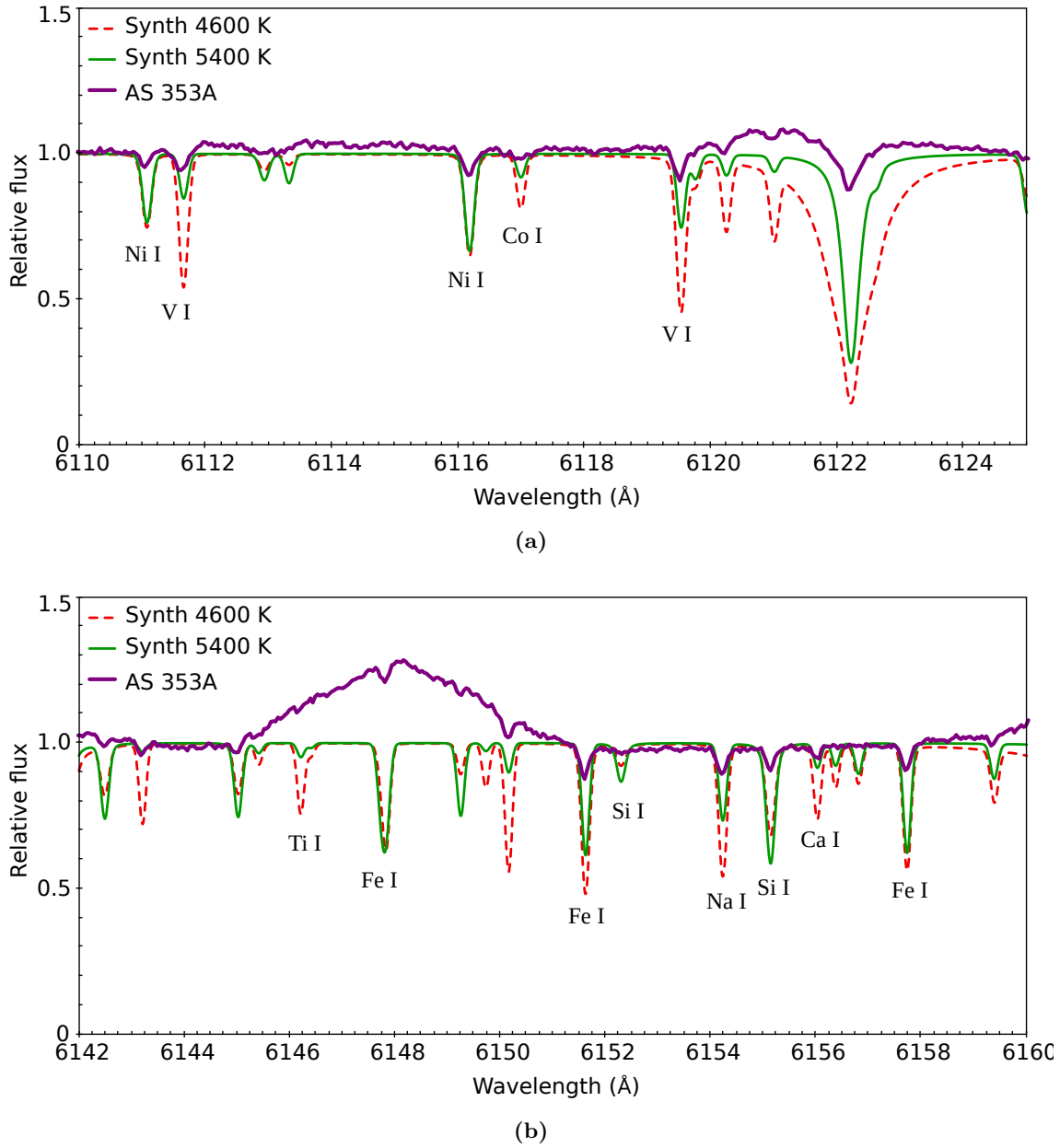


Figure 2.9: Fragments of AS 353A spectrum used to estimate spectral type. The pairs were chosen due to their dependence on T_{eff} , as illustrated by the synthetic spectra with different values of T_{eff} : 4600 K (red dashed line) and 5400 K (green solid line).

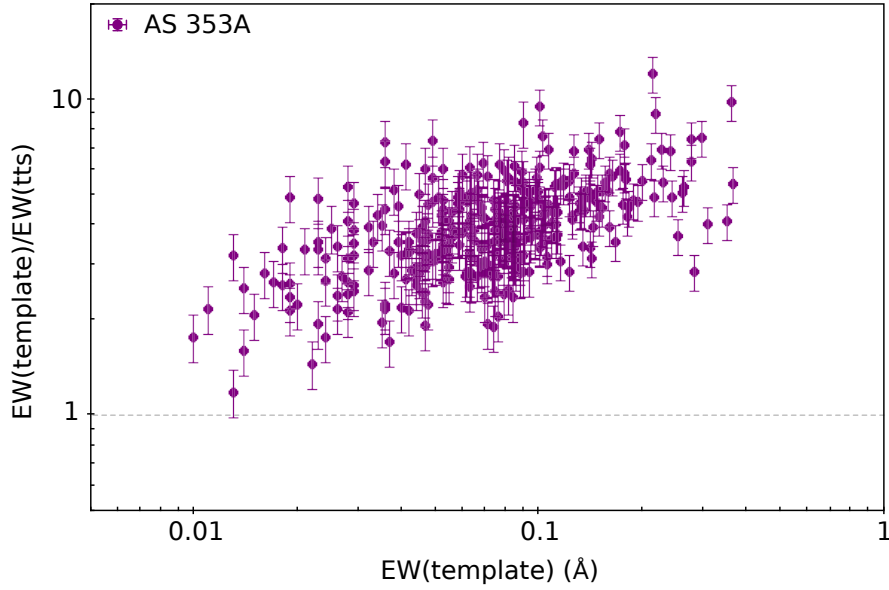


Figure 2.10: AS 353A veiling as a function of line strength (template with $T_{\text{eff}} = 5000$ K).

0.0 dex and $v \sin i = 1 \text{ km s}^{-1}$ (Table 2.3). From our spectral type analysis we concluded that AS 353A has T_{eff} between 4900 K and 5100 K, corresponding to a K0 IV – K1 IV star¹⁰.

The value for the v_{rad} estimated from the HIRES spectra is $v_{\text{rad}} = -10.4 \pm 0.2 \text{ km s}^{-1}$. This value is similar to that derived by Rice et al. (2006): -11.4 km s^{-1} . From the UES spectra we derived a value $v_{\text{rad}} = -8.0 \pm 0.2 \text{ km s}^{-1}$. This value is slightly different from the HIRES one, but still similar to the radial velocities of other stars belonging to the Aquila star forming region (Rice et al., 2006).

Table 2.4 summarizes the stellar parameters and equivalent widths of H α and He I lines derived in this work.

Results

Although AS 353A spectrum is populated by broad emission lines, it has several spectral regions without emission, where photospheric lines are easily identified. Moreover, its low $v \sin i$ makes the measurement and identification of each line easier. For this star we measured 354 photospheric lines. Most of this lines are Fe I lines (192 lines). Other elements are: Al I (1 line), Ca I (9 lines), Co I (4 lines), Cr I (29 lines), Cu I (1 line), Mg I (2 lines), Mn I (6 lines), Na I (2 lines), Ni I (38 lines), Sc I (3 lines), Sc II (3 lines), Si I (6 lines), Ti I (40 lines), Ti II (2 lines), V I (14 lines), Y II (1 line) and Zr I (1 line). The corresponding equivalent widths on the synthetic template for this star were

¹⁰Considering the relationship between T_{eff} and spectral type found in Gray (2005).

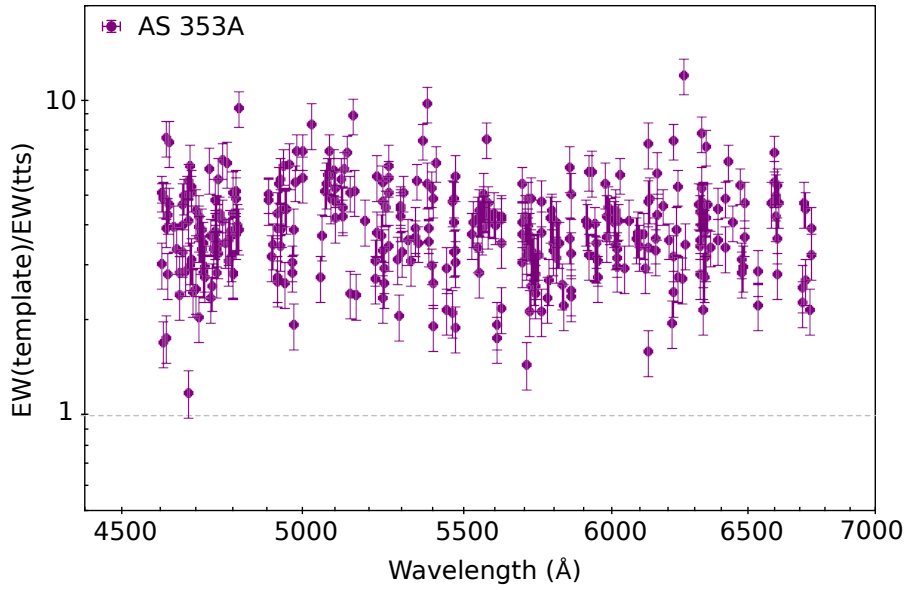


Figure 2.11: AS 353A veiling as a function of wavelength (template with $T_{\text{eff}} = 5000$ K).

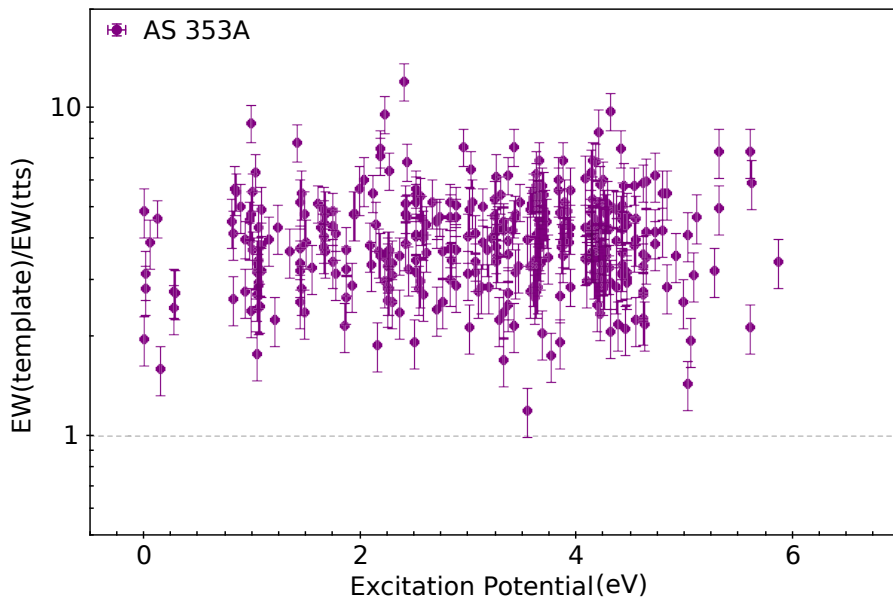


Figure 2.12: AS 353A veiling as a function of line excitation potential of the lower level (template with $T_{\text{eff}} = 5000$ K).

also measured.

Figure 2.10 shows the ratio between the equivalent widths of lines on the template and on the star versus line strength on template. Even though there is a high dispersion of values, the correlation between $EW(\text{template})/EW(\text{tts})$ and $EW(\text{template})$ is clear, with higher veiling for the stronger lines. On the other hand, as for $\text{LkH}\alpha$ 321, it is not dependent on wavelength (Figure 2.11) or excitation potential (Figure 2.12), so the veiling origin is different than that of the veiling continuum. Also, a template with a slightly different spectral type than that of the star does not affect the correlation.

In the case of AS 353A, the photospheric lines on top of broad emission are clearly visible (Figure 2.8) and also do not show more veiling than that of photospheric lines at the continuum level. Narrow emission cores on the photospheric lines are also not observed.

2.4.2 V1331 Cyg

Background

V1331 Cyg is located in the dark cloud LDN 981 (Figure 2.13), with an estimated distance of 550 ± 50 pc (Shevchenko et al., 1991). This star has been on the focus in the last years (e.g. Petrov et al. (2014), Choudhary et al. (2016)) due to its not commonly powerful mass-loss features, shown by the well defined P Cygni profiles of the Balmer lines and rich emission lines spectrum (Figure 2.14).

The V1331 Cyg spectrum is similar to that of the pre-outburst spectrum of FUori V1057 Cyg, making it a pre-FUori candidate (Welin, 1976). Another interesting feature of this star is the ring-like nebula that surrounds it (Figure 2.15). This structure might be caused by past mass-loss events, while the rich emission line spectrum is due to the almost exactly pole on orientation of the star-disk system (Petrov et al., 2014).

V1331 Cyg has a photometric variability of almost 1 mag, varying from $V = 11.7$ mag to $V = 12.5$ mag (Kolotilov, 1983; Shevchenko et al., 1991). From the photometric data, this star has an estimated stellar bolometric luminosity of $L = 21 L_{\odot}$, with a stellar extinction $A_V = 1.4$ mag.

The spectra of V1331 Cyg that is used on this work has been previously analysed by Petrov & Babina (2014) and Petrov et al. (2014). Table 2.1 summarizes data collected from the literature for V1331 Cyg.

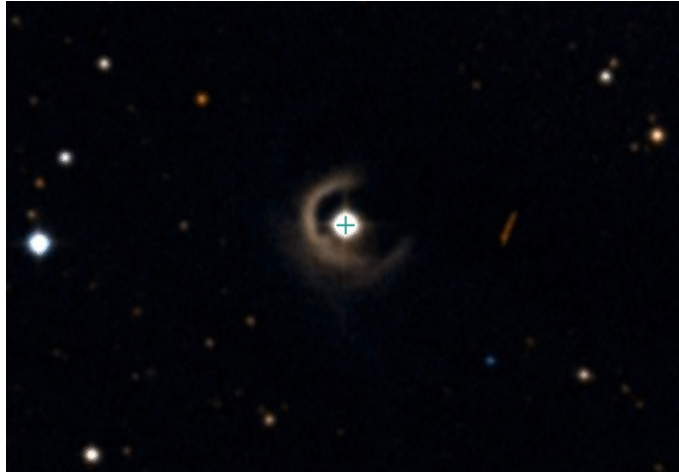


Figure 2.13: V1331Cyg Digital Sky Survey image (optical). Credit: Simbad (Wenger et al., 2000).

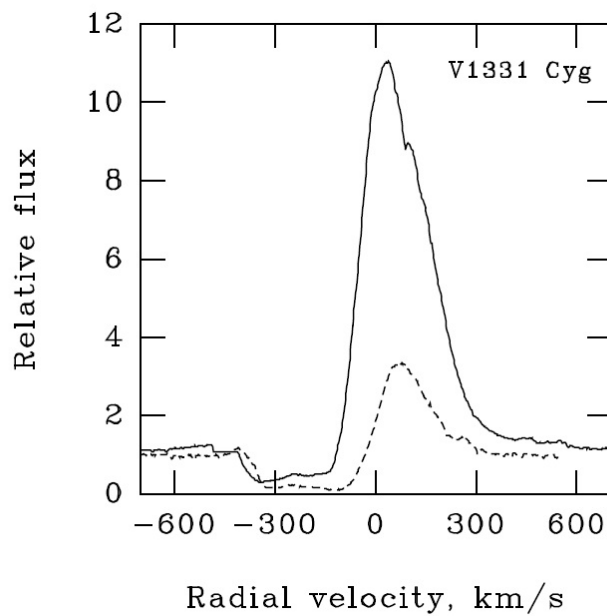


Figure 2.14: P Cygni profiles of the H α (solid line) and H β (dashed line) lines in the V1331 Cyg HRES spectrum (Rei et al., 2018).

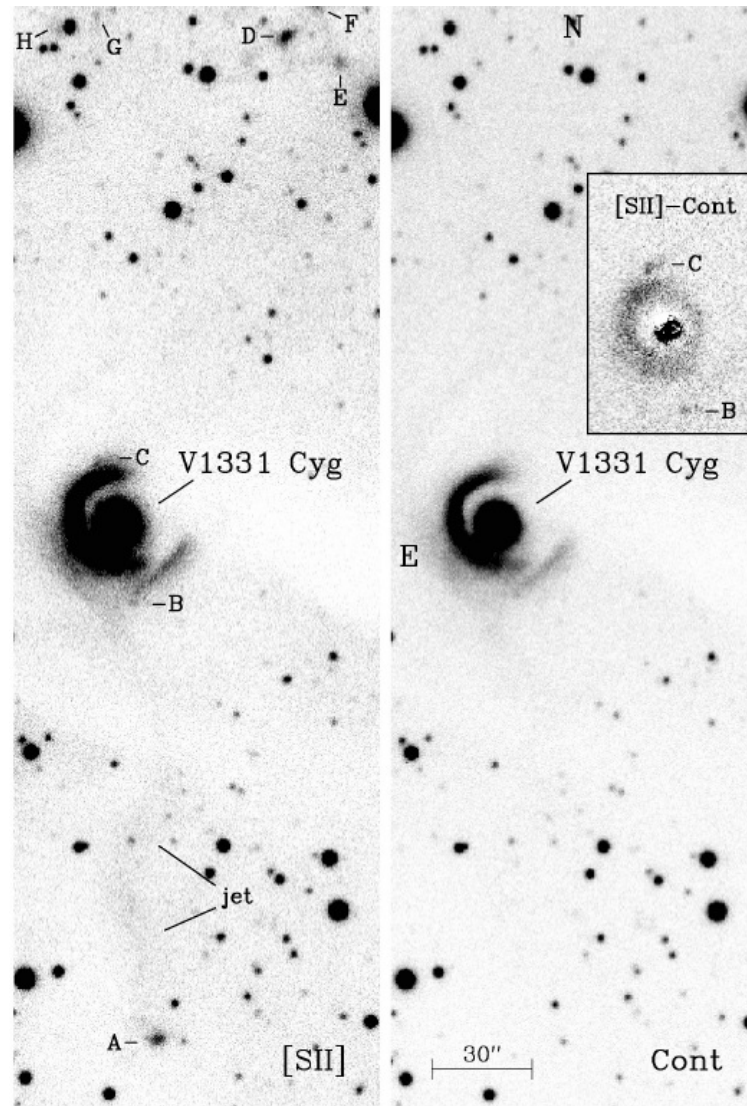


Figure 2.15: V1331 Cyg [S II] forbidden line observation. The [S II] forbidden line observations (left image) allows the detection of the jet and structures when the continuum is extracted (right image). Credits: Mundt & Eisloffel (1998).

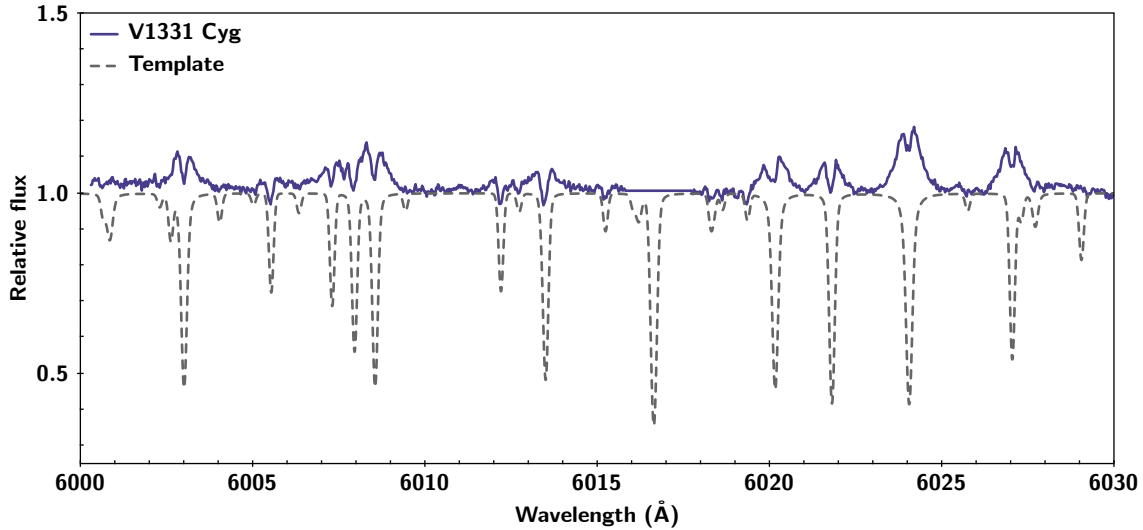


Figure 2.16: Fragment of V1331 Cyg spectrum. The dashed gray line represents the synthetic template for this star. It is possible to observe photospheric lines on top of the broad emission.

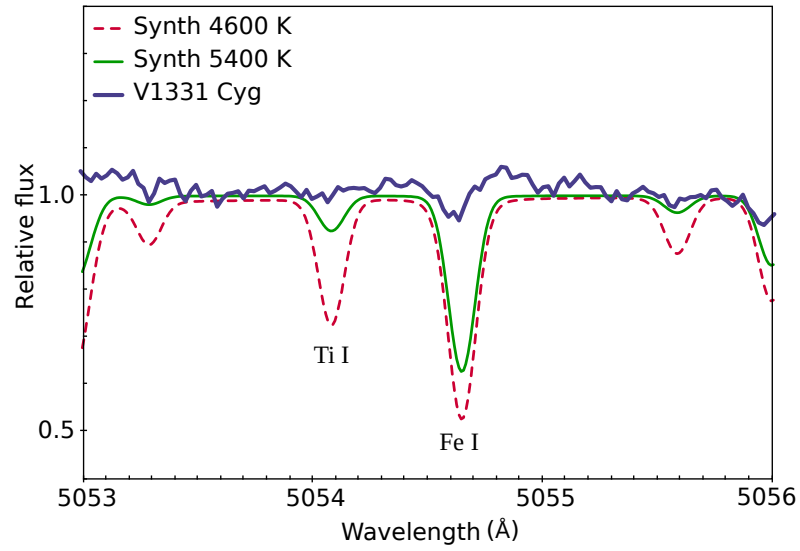
Spectral analysis

V1331 Cyg spectrum is of the three stars the one that has more emission line features, both narrow and broad. These features might not be only associated with the accretion process, but also with the fact that the jet is in the direction of the observer (Petrov et al., 2014). Still, it is possible to use some regions rich in narrow photospheric lines at some “spectral valleys”, between emission lines, to estimate the spectral type and measure the equivalent widths of those lines. Figure 2.16 shows a spectral region of V1331 Cyg with broad emission lines, where the photospheric lines are visible on top of the broad emission.

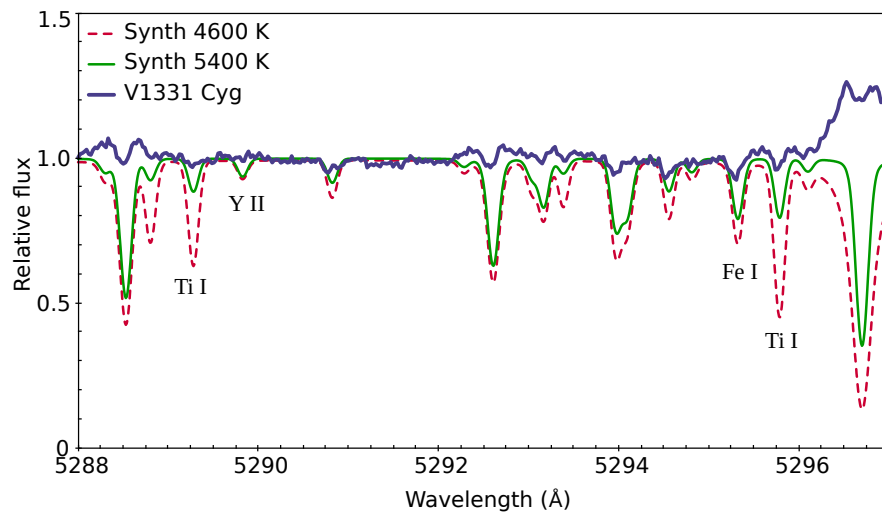
Like AS 353A, this star has a low value of $v \sin i$ ($\leq 6 \text{ km s}^{-1}$). For the same reasons pointed out for AS 353A, we opted to consider $v \sin i = 1 \text{ km s}^{-1}$ when computing the template for V1331 Cyg.

Figure 2.14 show the $H\alpha$ and $H\beta$ lines in the HIRES spectrum of V1331 Cyg, respectively. The equivalent widths of the $H\alpha$ and He I lines (in emission) were also measured: $EW(H\alpha) = -53 \text{ \AA}$ and $EW(\text{He I}) = -0.22 \text{ \AA}$.

Figures 2.17, 2.18 and 2.19 show the fragments of V1331 Cyg spectrum used to determine the spectral type (Table 2.6). In these plots are also shown synthetic spectra with two different values of T_{eff} (4600 K and 5400 K). The uncertainty associated is of approximately 250 K. The synthetic spectrum chosen as template for V1331 Cyg has $T_{\text{eff}} = 5000 \text{ K}$, $\log g = 3.75 \text{ dex}$, $[\text{Fe}/\text{H}] = 0.0 \text{ dex}$ and $v \sin i = 1 \text{ km s}^{-1}$. From our spectral type analysis we concluded that V1331 Cyg has T_{eff} between 5250 K and 5000 K, corresponding

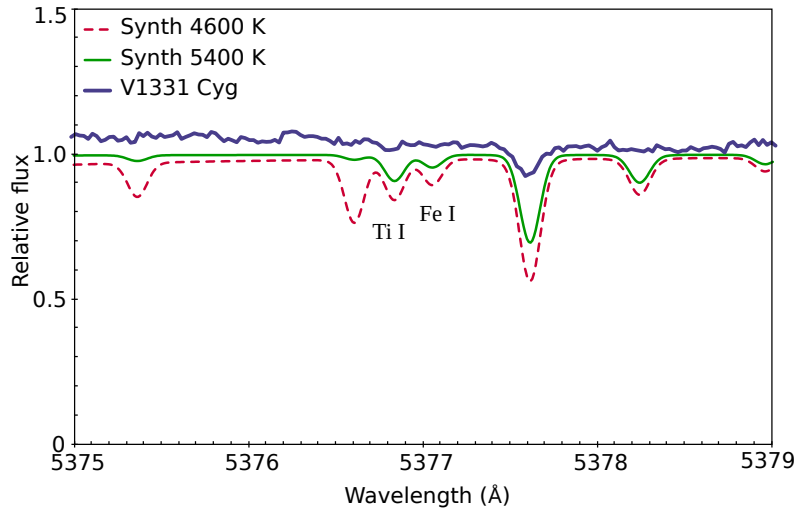


(a)

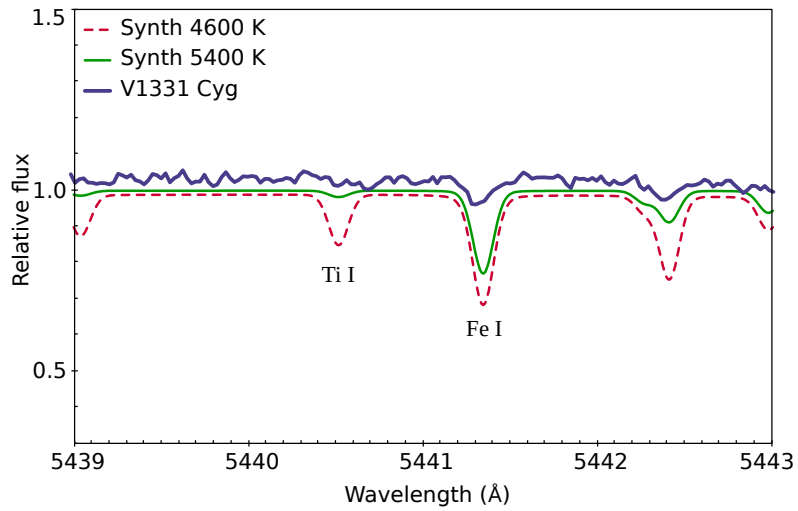


(b)

Figure 2.17: Fragment of V1331 Cyg spectrum used to estimate spectral type. The pairs were chosen due to their dependence on T_{eff} , as illustrated by the synthetic spectra with different values of T_{eff} : 4600 K (red dashed line) and 5400 K (green solid line).



(a)

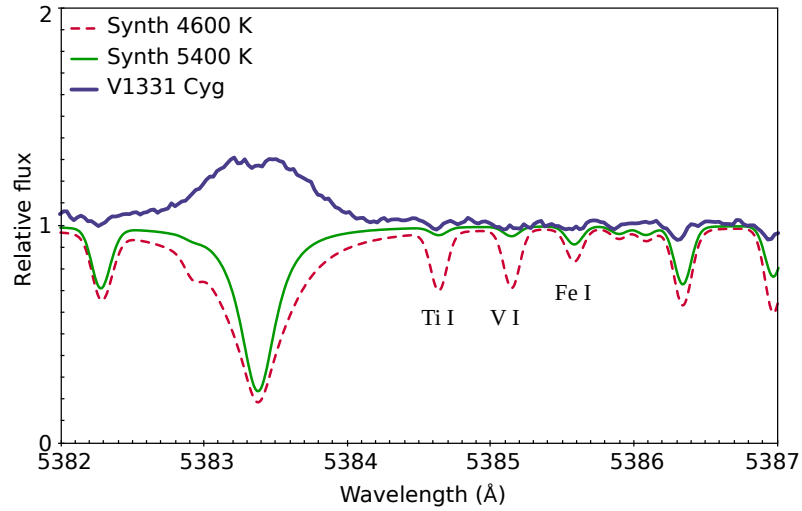


(b)

Figure 2.18: Fragments of V1331 Cyg spectrum used to estimate spectral type (cont.). The pairs were chosen due to their dependence on T_{eff} , as illustrated by the synthetic spectra with different values of T_{eff} : 4600 K (red dashed line) and 5400 K (green solid line).

Table 2.6: Photospheric line pairs used in the spectral type determination of V1331 Cyg

Line 1			Line 2		
λ (\AA)	Ele.	Exc. Pot. (eV)	λ (\AA)	Ele.	Exc. Pot. (eV)
5054.074	Ti I	2.68	5054.642	Fe I	3.64
5289.269	Ti I	0.84	5289.817	Y 2	1.03
5295.312	Fe I	4.42	5295.776	Ti I	1.07
5376.599	Ti I	0.00	5376.830	Fe I	4.29
5384.630	Ti I	0.83	5385.575	Fe I	3.69
5385.133	V I	2.61	5385.575	Fe I	3.69
5440.509	Ti I	1.43	5441.339	Fe I	4.31
5460.499	Ti I	0.05	5461.549	Fe I	4.45
5465.773	Ti I	1.07	5466.987	Fe I	3.57



(a)

Figure 2.19: Fragments of V1331 Cyg spectrum used to estimate spectral type (cont.). The pairs were chosen due to their dependence on T_{eff} , as illustrated by the synthetic spectra with different values of T_{eff} : 4600 K (red dashed line) and 5400 K (green solid line).

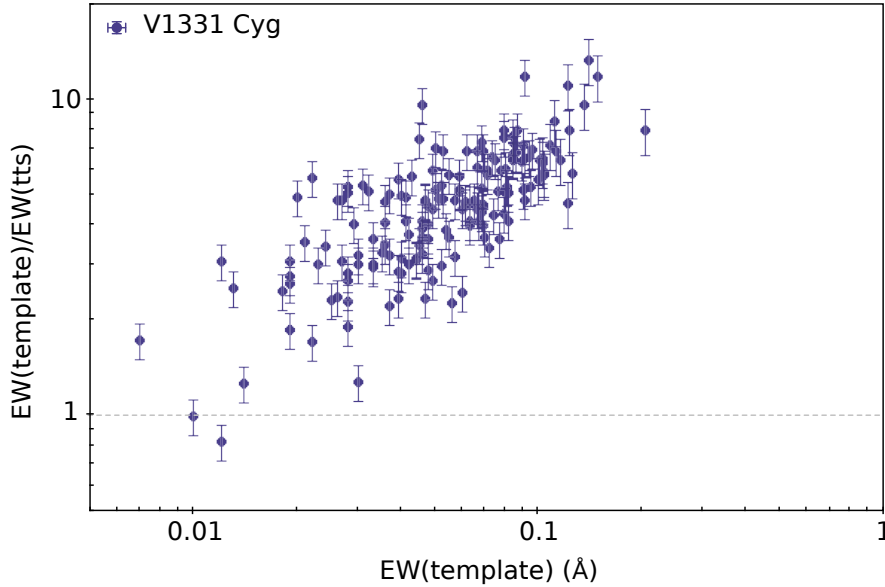


Figure 2.20: V1331 Cyg veiling as a function of line strength (template with $T_{\text{eff}} = 5000$ K).

to a G7 IV – K1 IV star¹¹.

The value for the v_{rad} estimated from the HIRES spectra is $v_{\text{rad}} = -15.0 \pm 0.3$ km s⁻¹. From the UES spectra we derived a value $v_{\text{rad}} = -16.8 \pm 0.3$ km s⁻¹. Table 2.4 summarizes the stellar parameters and equivalent widths of H α and He I lines derived in this work.

Results

V1331 Cyg is, of the three stars, the one with more emission lines on its spectrum. This might be caused by the pole-on orientation of the system, so that we observe the emission lines produced by the outflow/jet (Petrov et al., 2014). Nevertheless, some spectral regions are free from emission and we were able to measure the equivalent widths of 162 photospheric lines. This star has a low $v \sin i$, expected from its pole-on orientation, making its lines narrow and relatively easy to identify. Most of the measured lines are of Fe I (96 lines), with the other lines being of the following elements: Ca I (1 line), Co I (9 lines), Cr I (8 lines), Mn I (1 line), Na I (2 lines), Nd 2 (1 line), Ni I (19 lines), Si I (3 lines), Ti I (14 lines), V I (8 lines). The equivalent widths of the same lines were measured on the appropriated synthetic template.

In Figure 2.20 we plot the ratio between the equivalent widths of the lines on the synthetic template and the star versus the line strength on template lines. The correlation between veiling and line strength for V1331 Cyg is the strongest among the three stars. It is clear that the veiling on the photospheric lines on V1331 Cyg is stronger for the

¹¹Considering the relationship between T_{eff} and spectral type found in Gray (2005).

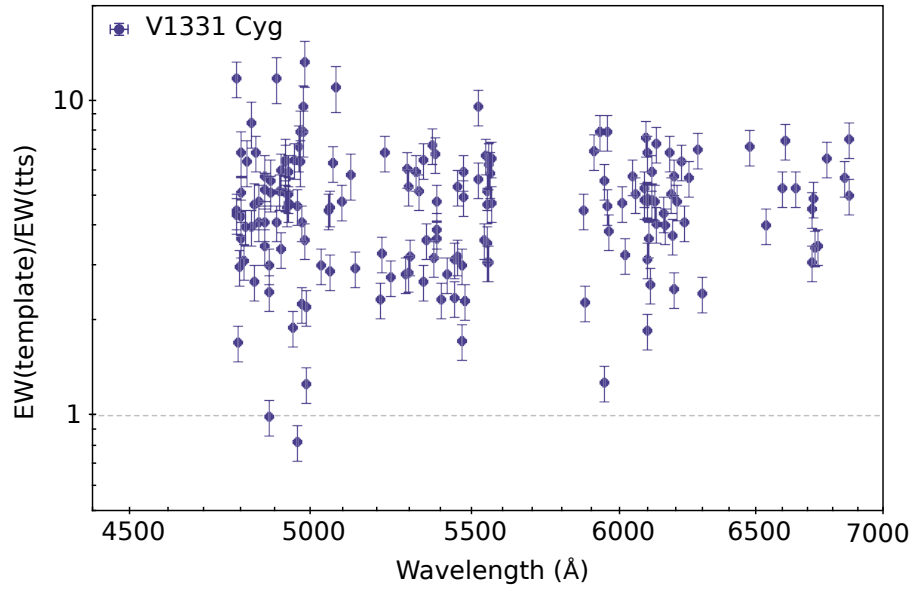


Figure 2.21: V1331 Cyg veiling as a function of wavelength (template with $T_{\text{eff}} = 5000$ K).

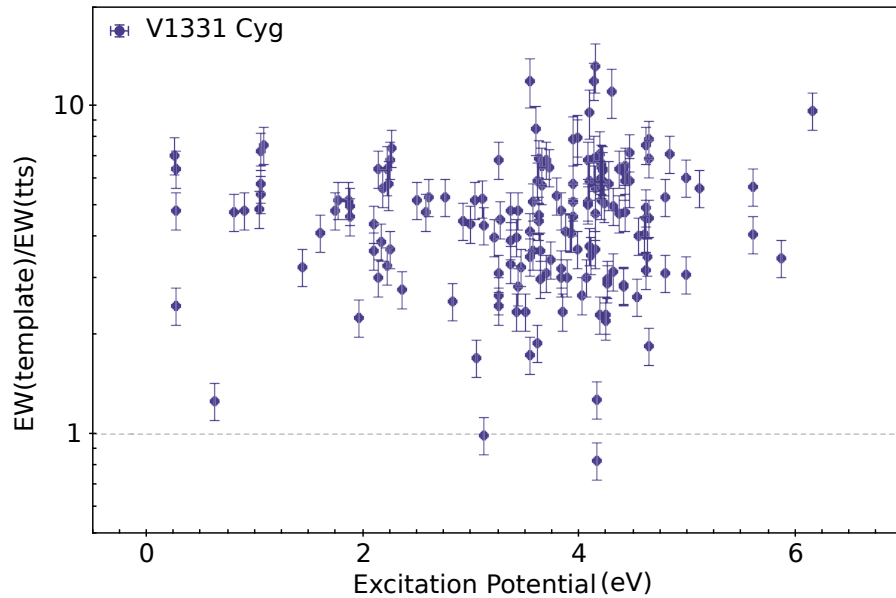


Figure 2.22: V1331 Cyg veiling as a function of line excitation potential of the lower level (template with $T_{\text{eff}} = 5000$ K).



Figure 2.23: LkH α 321 Digital Sky Survey image (optical). Credit: Simbad (Wenger et al., 2000).

stronger lines. Again, a small change on template spectral type does not change this correlation. Also in this case, there is no dependence of veiling on wavelength (Figure 2.21) or excitation potential (Figure 2.22).

2.4.3 LkH α 321

Background

LkH α 321 is a T Tauri star located in a dark cloud in the Cygnus constellation, near the star forming region NGC 7000/IC 5070 (Figure 2.23). The distance to this star has been estimated to be 550 ± 50 pc by Shevchenko et al. (1991).

This star has been studied for more than three decades and is well known for its permanently strong wind features associated with P Cygni profiles of the Balmer lines (Figure 2.24).

Also, [SII] forbidden line images reveal a jet with an extension of 22 arcseconds (Mundt & Eisloffel, 1998). Figure 2.25 shows the knotty structure of the jet when the continuum is subtracted to the [SII] line image.

Despite its strong mass-loss features, this star shows low photometric variability, with visual magnitude $V = 12.25 - 12.44$ (Grankin et al., 2007). Back in 1979, Cohen & Kuhl estimated a spectral type G1 and an interstellar extinction $A_V = 2.23 \pm 0.3$ mag for this star.

Table 2.1 summarizes data collected from the literature for LkH α 321.

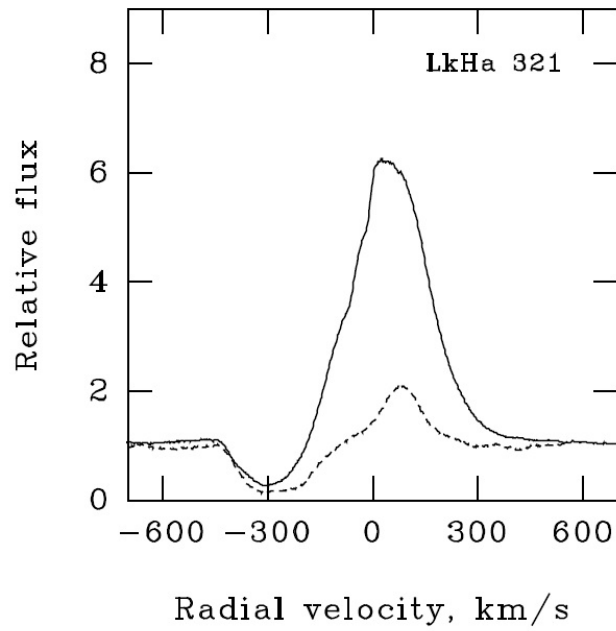


Figure 2.24: P Cygni profiles of the H α (solid line) and H β (dashed line) lines in the LkH α 321 HIRES spectrum (Rei et al., 2018).

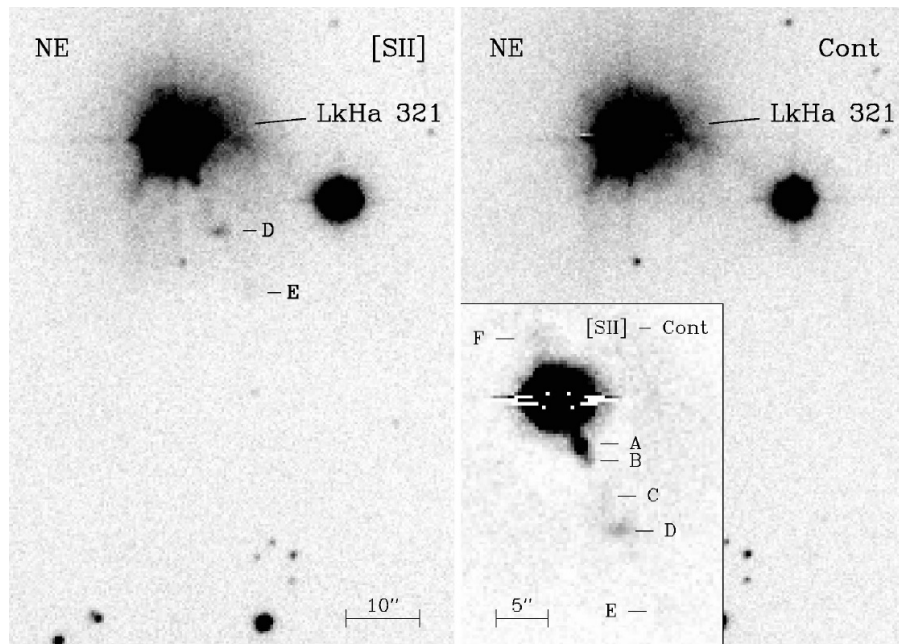


Figure 2.25: LkH α 321 [SII] forbidden line observations. The [SII] forbidden line observations (left image) allows the detection of a jet whose structure can be analysed when the continuum is extracted. Credits: Mundt & Eisloffel (1998).

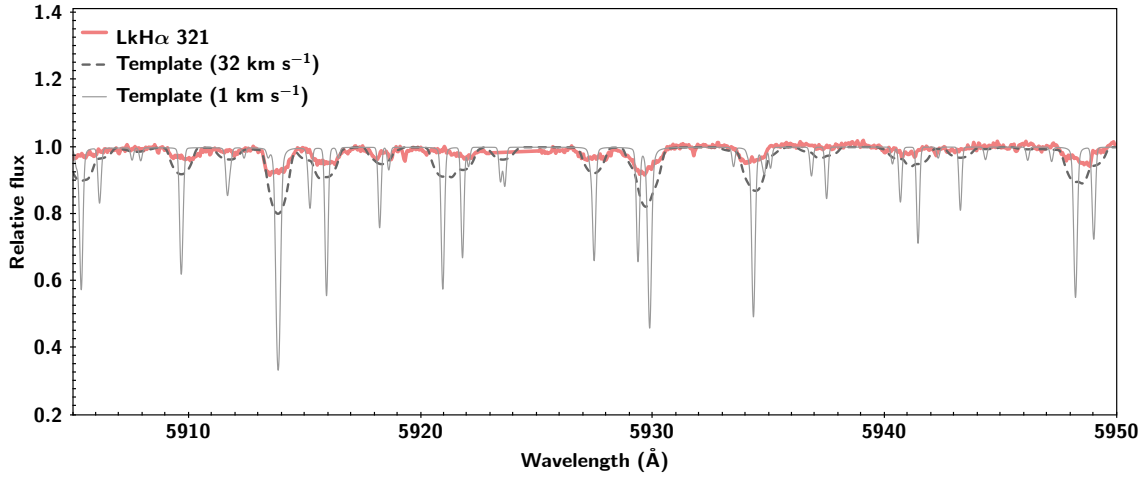


Figure 2.26: Effects of LkH α 321 rotation on the photospheric lines. A fragment of spectrum with no broad emission is compared with two fragments of synthetic spectra with the same spectral type and instrumental resolution. The dashed gray line represents the synthetic spectrum with the same $v \sin i$ of the star (32 km s^{-1}), while the solid gray line corresponds to synthetic spectrum with $v \sin i = 1 \text{ km s}^{-1}$.

Spectral analysis

LkH α 321 spectrum is different from that of AS 353A and V1331 Cyg due to its high value of $v \sin i$. The Doppler effect due to the high velocity of rotation of this star is responsible for the broadening of the photospheric lines. Figure 2.26 shows a fragment of the spectrum of LkH α 321 compared with two synthetic spectra with the same spectral type and instrumental resolution. One has the same $v \sin i$ as the star (32 km s^{-1}), while the other has $v \sin i = 1 \text{ km s}^{-1}$. The effect of rotation on the broadening of the photospheric lines is very clear in this picture. Due to the large value of $v \sin i$, some of the photospheric line profiles on the star's spectrum are in fact blends of two or more lines. Because of this, the amount of single line profiles measured is less than two hundred lines. The same is true for the amount of ratios of weak lines used to determine the spectral type.

LkH α 321 spectrum is also populated by broad emission lines, whose broadening is not caused by the rotation of the star, but by the mass-accretion and mass-loss processes. Figure 2.27 shows a fragment of the spectrum of LkH α 321 where it is possible to observe two broad emission Fe I lines. On top of these emission lines, the photospheric lines are also visible.

Figure 2.24 shows the H α and H β lines in the HIRES spectrum of LkH α 321. The

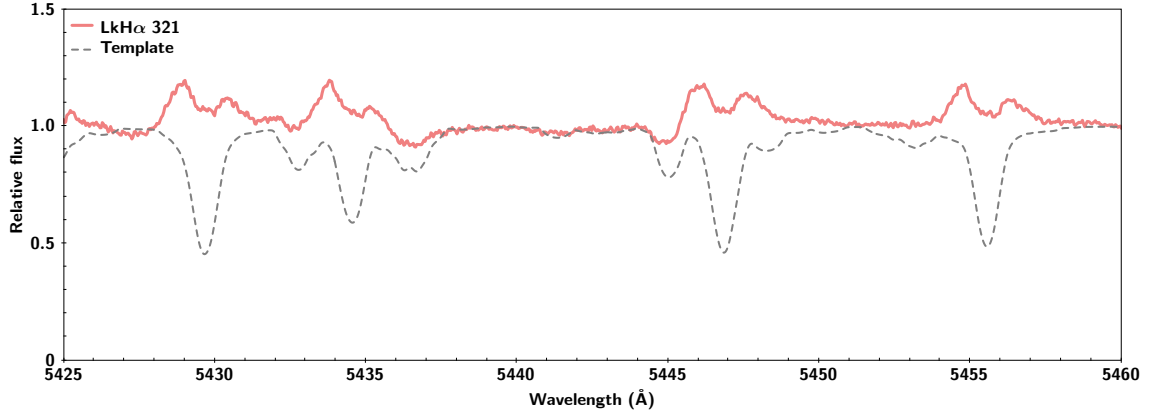


Figure 2.27: Fragment of spectra of LkHa 321. The dashed gray line represents the synthetic spectrum with the same $v \sin i$ of the star (32 km s^{-1}). In this fragment it is possible to observe emission lines of Fe I. It is also possible to observe photospheric lines on top of the broad emission.

Table 2.7: Photospheric line pairs used in the spectral type determination of LkHa 321

Line 1			Line 2		
λ (Å)	Ele.	Exc. Pot. (eV)	λ (Å)	Ele.	Exc. Pot. (eV)
6013.416	Ti I	1.07	6016.605	Fe I	3.55
6039.729	V I	1.06	6041.950	Fe I	4.96
6325.164	Ti I	0.02	6327.599	Ni I	1.68
6469.193	Fe I	4.48	6471.662	Ca I	2.53

equivalent widths of the $H\alpha$ and lines (in emission¹²) were also measured: $EW(H\alpha) = -30 \text{ \AA}$ and $EW(\text{He I}) = -0.08 \text{ \AA}$.

Following the procedure described in section 2.3.2, for the determination of spectral type, we found that the most appropriated synthetic template for LkHa 321 is one with $T_{\text{eff}} = 5250 \text{ K}$, $\log g = 3.75 \text{ dex}$, $[\text{Fe}/\text{H}] = 0.0 \text{ dex}$ and $v \sin i = 32 \text{ km s}^{-1}$ (Table 2.3). The error in T_{eff} is around 250 K. This analysis places LkHa 321 between the spectral types G5 IV and G7 IV¹³.

Figure 2.28 shows the several fragments of LkHa 321 spectrum used to determine the spectral type. In these plots are also shown synthetic spectra with two different values of T_{eff} (4600 K and 5400 K). For the chosen pairs of lines (Table 2.7) there is a significant difference in the ratios of the lines for the two values of temperature. This makes the chosen ratios dependent on T_{eff} . These ratios of close by weak lines were compared with those of several synthetic spectra with different temperatures. The synthetic spectrum

¹²In case of emission it is convention to add a “-” sign to the value of the equivalent width of the line.

¹³Considering the relationship between T_{eff} and spectral type found in Gray (2005).

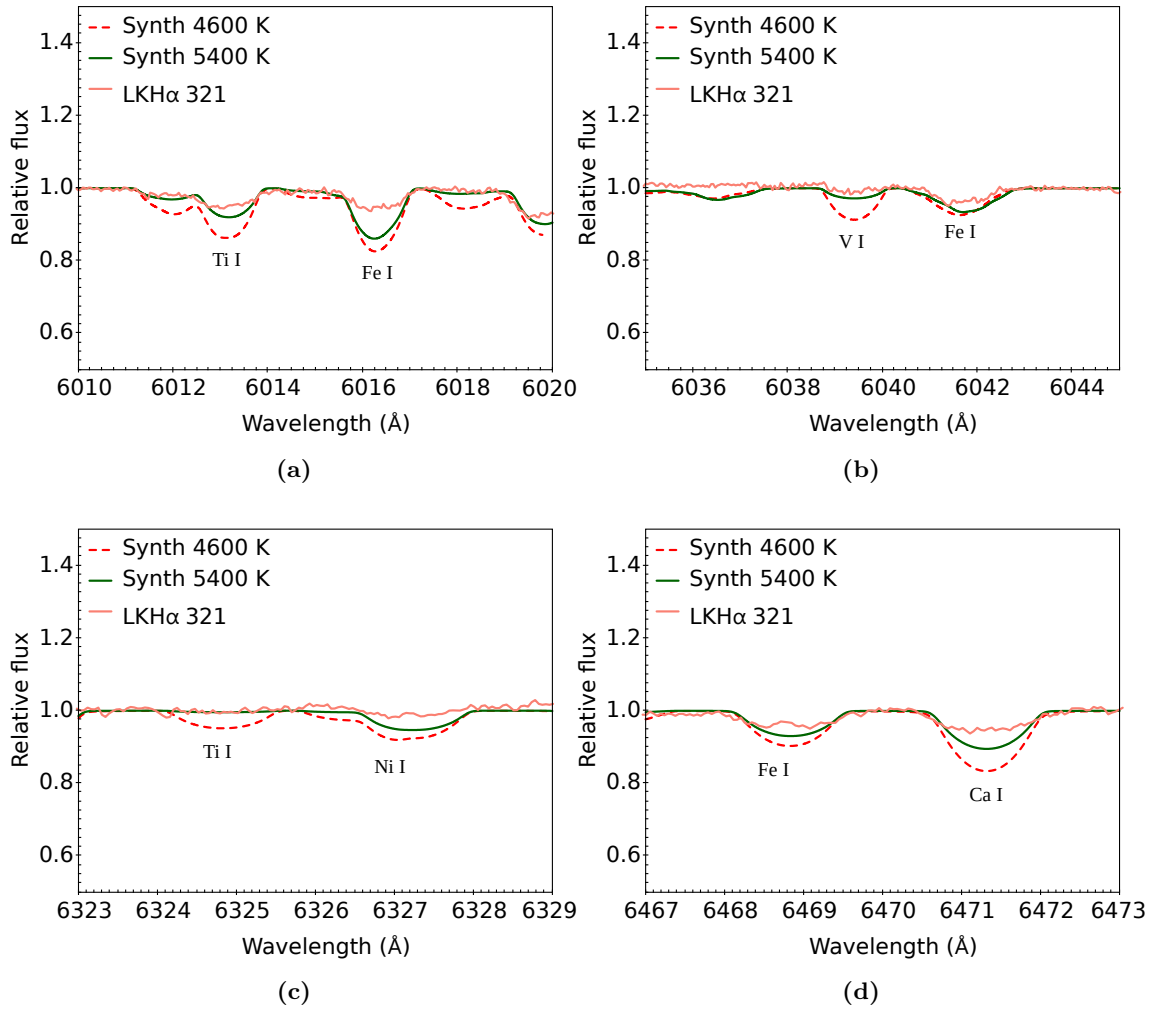


Figure 2.28: Fragments of LkH α 321 spectrum used to estimate spectral type. The pairs were chosen due to their dependence on T_{eff} , as illustrated by the synthetic spectra with different values of T_{eff} : 4600 K (red dashed line) and 5400 K (green solid line).

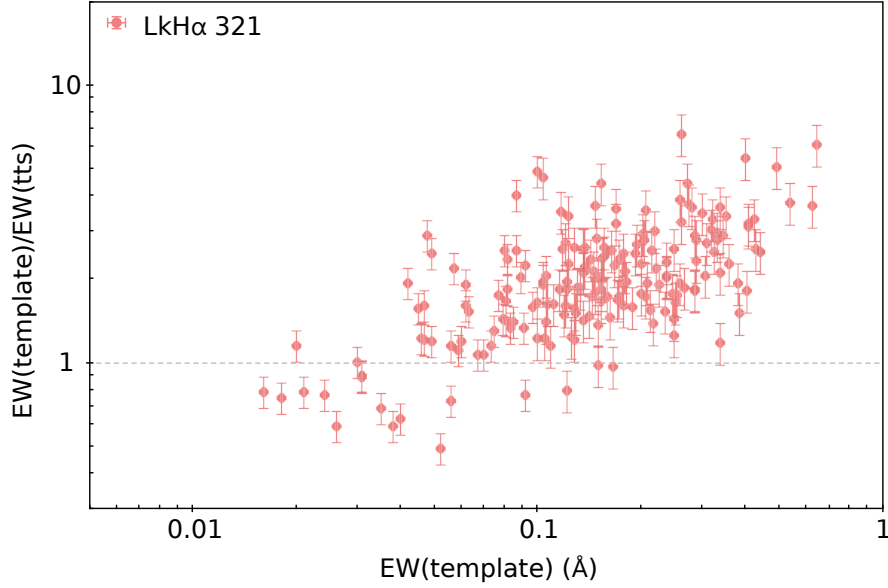


Figure 2.29: LkH α 321 veiling as a function of line strength (template with $T_{\text{eff}} = 5250$ K).

with ratios similar to those of the real spectrum was considered as template and its value of T_{eff} was adopted as the value of T_{eff} of LkH α 321. The uncertainty associated is of approximately 250 K.

We also estimated v_{rad} for this star from two different spectra: HIRES and UES. The measurements made using the UES spectra gave a value of $v_{\text{rad}} = -14.4 \pm 1.0$ km s $^{-1}$, while the value obtained from the HIRES spectra is $v_{\text{rad}} = -16.0 \pm 0.5$ km s $^{-1}$. No significant change is then observed between the radial velocity of the two spectra, taken with a difference of 4 years.

Table 2.4 summarizes the stellar parameters and equivalent widths of H α and He I lines derived in this work.

Results

Contrary to AS 353A and V1331 Cyg, LkH α 321 has a high $v \sin i$ (32 km s $^{-1}$). In this case, the photospheric lines are broad and most are the result of line blending (Figure 2.26). The element associated with each line is the one with the major contribution to the blending.

For this star, we were able to measure the equivalent widths of 186 lines, with the majority being of Fe I (116 lines). The other lines are dominated by the following elements: Al I (1 line), Ba II (2 lines), Ca I (9 lines), Co I (3 lines), Cr I (14 lines), Fe II (1 line), Mg I (1 line), Mn I (3 lines), Ni I (6 lines), Sc II (2 lines), Si I (2 lines), Ti I (15 lines, Ti II (1 line), V I (4 lines) and Y II (1 line). The same line profiles were measured on the

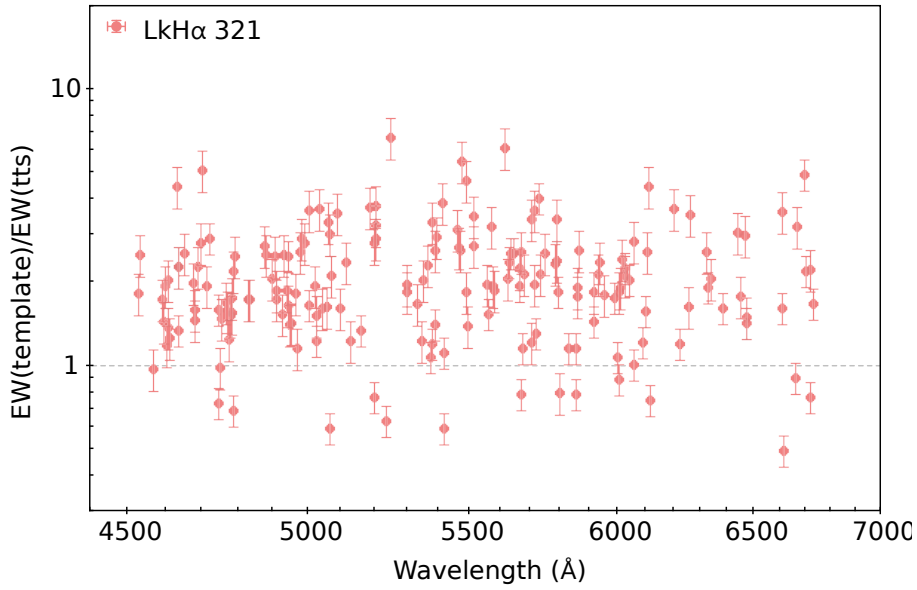


Figure 2.30: LkH α 321 veiling as a function of wavelength (template with $T_{\text{eff}} = 5250$ K).

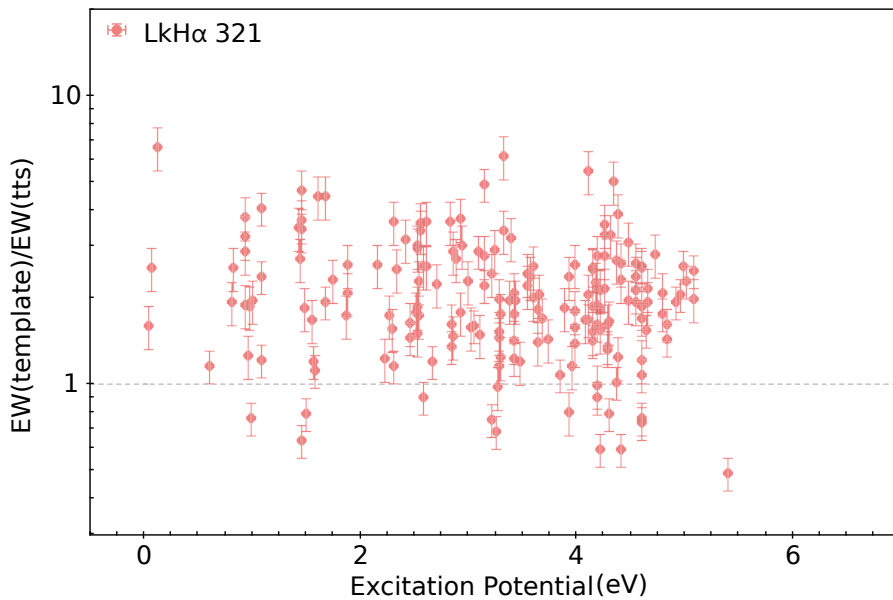


Figure 2.31: LkH α 321 veiling as a function of line excitation potential of the lower level (template with $T_{\text{eff}} = 5250$ K).

synthetic template with the same spectral type and $v \sin i$.

Figure 2.29 shows the ratio between equivalent widths on template and star in function of the line's strength on template. Although there is a high dispersion and we are dealing with line blending, the correlation between veiling and line strength is evident. Even if the spectral type of the template is slightly different from the estimated one, the correlation remains. Stronger lines are more veiled than weaker lines.

On the other hand, the veiling in this star is not dependent on wavelength (Figure 2.30) or excitation potential (Figure 2.31). Also, the photospheric lines on top of the broad emission are not differently veiled than those at the continuum level. This means that the broad emission is optically thin and is not contributing to the observed veiling. No narrow emission cores are observed inside the broad photospheric lines, so the veiling origin must not be so closely associated to the hot spot.

At the same time, veiling independent on wavelength is indicative that the veiling origin is not the same as that of the veiling continuum. Weak lines allowed the estimation of the veiling continuum value around 0. The veiling present in LkH α 321 spectrum does not have a significant contribution from the veiling continuum.

2.5 Analysis of the results

2.5.1 Veiling continuum determination

In the context of the magnetospheric accretion model, the observed veiling on the photospheric lines of cTTS is attributed to the hot spots created at the base of the accretion column, where the matter shocks on the stellar atmosphere.

Due to the amount of energy involved, the hot spots are hotter than the stellar photosphere and their emission superimposes that of the stellar continuum. The radiation emitted by the hot spot can be approximated to that emitted by a black body at a certain temperature. This radiation affects the photospheric lines as a *veiling continuum*, making the spectral lines on a cTTS shallower than those on a MS star with the same spectral type. The veiling continuum is more intense on the blue part of the spectrum, since typical hot spot temperatures range between 6 000 K and 8 000 K (Calvet & Gullbring, 1998) and its peak emission is at shorter wavelengths than that of the star.

Although varying in wavelength, the veiling continuum does not discriminate the weak from the strong photospheric lines. For a small range of wavelength, it affects both weak and strong lines in the same way. Our results for the three cTTS show that stronger lines are more affected by the veiling than the weaker lines. This means that we must

only use the weak lines to estimate the veiling continuum, since these do seem to be less affected by the line-dependent veiling. Weak lines form at the deeper layers of the stellar photosphere and are less affected by the changes on the stellar atmosphere due to the accretion process, that is more intense on the top of the star's atmosphere.

Our results also show that the measured veiling does not depend on the wavelength. This is another evidence that the line-dependent veiling does not share the same origin of the veiling continuum. On the other hand, a lower spectral resolution and/or poor S/N level affects more the measurement of the weak lines and thus can induce an overestimation of the veiling continuum.

For each star we analysed the $EW(\text{template})/EW(\text{tts})$ ratio results for the weakest lines in the nearest regions to the He I line at 5876 Å. This line appears in emission and is considered a reliable line to estimate the accretion luminosity (Alcalá et al., 2014). Also, from the Figures 2.29, 2.10 and 2.20 we estimated the following veiling continuum (VC) for each star: $VC \sim 0.0$ for LkH α 321, $VC \sim 0.1$ for V1331 Cyg and $VC \sim 0.6$ for AS 353A.

2.5.2 Accretion luminosity determination

The in falling gas releases continuum emission, formed at the hot spots, and line emission, produced also in the accretion column (narrow emission lines in the post-shock region and broad emission lines in the pre-shock region). This energy per unit time is denominated accretion luminosity, L_{acc} , and measures the released energy per unit time integrated over the entire spectrum.

CTTS have strong stellar magnetic fields that can truncate the circumstellar disk at the equilibrium point between ram and magnetic pressures (R_{in}). For typical magnetic field strengths, the truncation radius has values $R_{in} \sim 3 - 6 R_*$ (Johnstone et al., 2014; Hartmann et al., 2016). The accreting matter is channeled from the inner disk region onto the star at near free-fall velocities:

$$v_{ff} = \left(\frac{2GM_*}{R_*} \right)^{1/2} \left(1 - \frac{R_*}{R_{in}} \right)^{1/2}, \quad (2.3)$$

where R_* and M_* are the star radius and mass, respectively, G is the gravitational constant, and R_{in} is the inner disk radius or truncation radius. If we assume that all the kinetic energy is dissipated at the shock region, the accretion luminosity (L_{acc}) is:

$$L_{acc} = \frac{1}{2} \dot{M}_{acc} v_{ff}^2, \quad (2.4)$$

where \dot{M}_{acc} is the mass-accretion rate.

In the last decade an effort has been made in order to study the correlation between the accretion luminosity and the emission line luminosity for several lines (e.g Fang et al. (2009); Rigliaco et al. (2012); Alcalá et al. (2014, 2017)). These authors have shown that L_{acc} is well correlated with the line luminosity, L_{line} , of some emission lines. These includes lines of the Balmer series, as well as Ca II lines and the He I lines (Alcalá et al., 2014). Nevertheless, these relationships are empirical and affected by high uncertainties.

In this work we use the data provided by Alcalá et al. (2014) on these relationships. This is one of the most recent works on the subject and also the one that uses data for a wider range of stellar masses and larger amount of lines analysed simultaneously, hence avoiding problems of variability. These correlations are of the form:

$$\log\left(\frac{L_{acc}}{L_{\odot}}\right) = a \times \log\left(\frac{L_{line}}{L_{\odot}}\right) + b, \quad (2.5)$$

where L_{acc} and L_{line} are the accretion luminosity and line luminosity in units of solar luminosity (L_{\odot}), a and b are constants. For each of the analysed lines, Alcalá et al. (2014) provide the values for the a and b constants, with associated uncertainties and standard deviation from the linear fit.

For our wavelength range, from the Balmer series, only $H\alpha$ and $H\beta$ are available, but both show P Cygni profiles. In this case, part of the emission due to accretion might being reduced due to the outflow absorption. If we used these lines to estimate the accretion luminosity we would be estimating a minimum limit value. From the other available emission lines on our spectra, we decided to choose the He I line at 5876 \AA (Figure 2.32) line to estimate the accretion luminosity. For this line, the a and b constants have small associated uncertainties and standard deviation (Alcalá et al., 2014), making it a reliable line to use. For the He I line at 5876 \AA , $a = 1.13$ and $b = 3.51$ ¹⁴.

To determine L_{acc} from equation 2.3 it is necessary to calculate L_{line} . It can be determined through the equation:

$$\frac{L_{line}}{L_{star}} = EW \times (1 + VC) \frac{F_{cont}}{L_{star}}, \quad (2.6)$$

where L_{star} is the stellar bolometric luminosity, F_{cont} is the stellar continuum flux density at the wavelength of the He I line, EW is equivalent width of the He I emission, and VC is the veiling continuum (at the wavelength of He I line).

¹⁴From Alcalá et al. (2017), the a and b constants have been updated to the values $a = 1.15$ and $b = 3.67$. These small changes do not significantly affect our estimates of \dot{M}_{acc} .

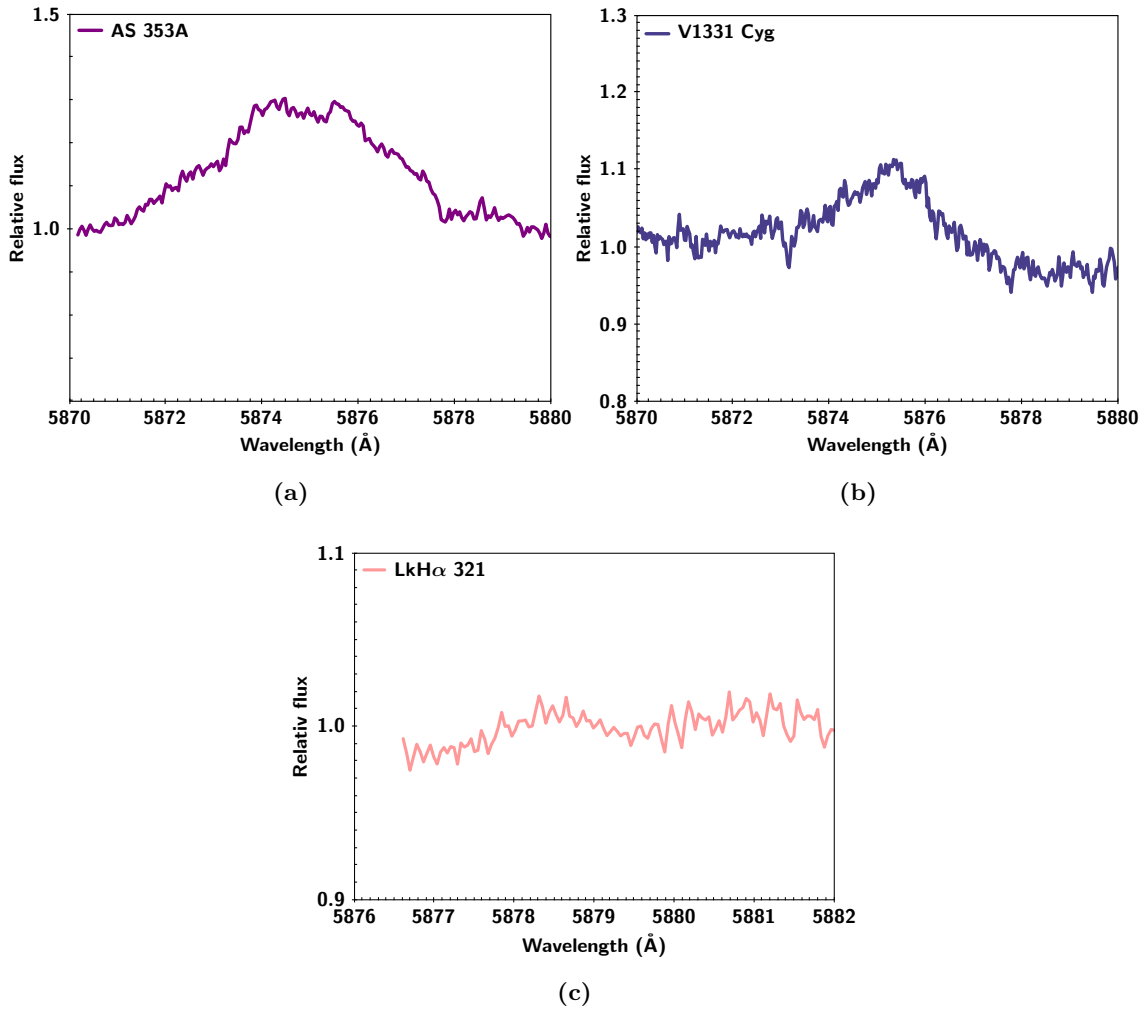


Figure 2.32: CTTS He I line at 5876 Å. Spectra in these plots is not in the star's reference frame.

Table 2.8: Accretion luminosity and mass accretion rates determination.

Star	VC	$\log(L_{He}/L_{star})$ (dex)	$\log(L_{acc}/L_{star})$ (dex)	$\log(\dot{M}_{acc})$ ($M_{\odot}yr^{-1}$)
LkH α 321	0.0	-4.97	-1.72	-7.4
V1331 Cyg	0.1	-4.51	-1.21	-6.9
AS 353A	0.6	-3.6	-0.31	-7.1

The ratio F_{cont}/L_{star} can be computed through the equation:

$$\frac{F_{cont}}{L_{star}} = \frac{\pi B(T_{eff}, \lambda)}{\sigma T_{eff}^4}, \quad (2.7)$$

where $B(T_{eff}, \lambda)$ is the Planck function for the black body radiation of a star with effective temperature, T_{eff} , at the wavelength λ . In this equation, T_{eff} takes the value determined for each cTTS (Table 2.4). Since the black body approximation for the radiation of a star is not always the most correct, we used template spectra from the stellar spectral flux library by Pickles (1998). The spectra in this library are flux-calibrated and are available for a wide range of spectral types and wavelength (1150 - 25000 Å).

2.5.3 Mass-accretion rates and filling factor

The mass-accretion rate (\dot{M}_{acc}) measures the amount of mass (in solar mass units) accreted from the disk per year. The mass-accretion rate can then be determined from equations 2.3 and 2.4:

$$\dot{M}_{acc} = \frac{L_{acc}R_*}{GM_*}(1 - R_*/R_{in})^{-1}, \quad (2.8)$$

In this work we consider $R_{in} = 3 R_*$ in our calculation (e.g. Johnstone et al. (2014)). If instead we had considered $R_{in} = 6 R_*$ in our calculation, we would obtain the following mass-accretion rates: $\log(\dot{M}_{acc})(\text{LkH}\alpha\ 321) = -7.53$ ($M_{\odot}yr^{-1}$), $\log(\dot{M}_{acc})(\text{V1331 Cyg}) = -7.05$ ($M_{\odot}yr^{-1}$) and $\log(\dot{M}_{acc})(\text{AS 353A}) = -7.21$ ($M_{\odot}yr^{-1}$). The assumed value for the truncation radius has no major influence on the results for the mass-accretion rates. In Table 2.8 are summarized the values of the veiling continuum (VC), He I line luminosity ($\log(L_{He}/L_{star})$), accretion luminosity ($\log(L_{acc}/L_{star})$) and mass-accretion rates derived for the three cTTS.

If we had considered the black body approximation instead of using the flux-calibrated spectra from Pickles (1998), we would obtain the following mass-accretion rates: $\log(\dot{M}_{acc})(\text{LkH}\alpha$

321) = $-7.78 (M_{\odot}yr^{-1})$, $\log(\dot{M}_{acc})(V1331 \text{ Cyg}) = -7.15 (M_{\odot}yr^{-1})$ and $\log(\dot{M}_{acc})(AS 353A) = -7.23 (M_{\odot}yr^{-1})$. With the black body approximation the obtained mass-accretion rates are slightly lower than those derived by using the flux-calibrated spectra. By using the black body approximation one might slightly underestimate the mass-accretion rates.

From the knowledge about the accretion luminosity, veiling continuum and effective temperature of the star it is possible to estimate the temperature (T_{spot}) and filling factor (f) of the possible hot spot(s).

Assuming that the hot spot radiates as a black body, the veiling continuum at any wavelength is proportional to the ratio of the Planck functions between the hot spot and the star radiation:

$$VC \sim f \frac{B(T_{spot}, \lambda)}{B(T_{star}, \lambda)}, \quad (2.9)$$

Also,

$$\frac{L_{acc}}{L_{star}} \sim f \left(\frac{T_{spot}}{T_{star}} \right)^4, \quad (2.10)$$

For these calculations we are considering the L_{acc} derived from the He I 5876 Å line, so we can compute f and T_{spot} considering $\lambda = 5876 \text{ Å}$. At the same time, T_{star} takes the value derived for each cTTS (Table 2.4).

On the other hand, the uncertainty on the determination of the veiling continuum is very high. Also, we do not see a clear dependency of the veiling with wavelength, which indicates that the hot spot temperatures must not be higher than 10 000 K. This increases the difficulty on estimating the temperature of the hot spot with accuracy. For this reason we decided to calculate the range of filling factors within the range of typical temperatures for the hot spots for cTTS: 6000 – 8000 K (Calvet & Gullbring, 1998).

LkHα 321 does not allow these type of calculations, since we obtained $VC \sim 0$ for this star in particular. In accordance with the hot spot hypothesis the filling factor for the hot spots on the surface of LkHα 321 should be not higher than 1%. For V1331 Cyg we obtained filling factors between 1% and 3% of the stellar surface. AS 353A is the star with the highest filling factors, between 7% and 20%, which seems to be unusually large. This can be caused by an overestimation of the veiling continuum.

These values are, of course, affected by several uncertainties, not only due to the difficulties in estimating the veiling continuum, but also due to the fact that we are estimating L_{acc}/L_{star} from empirical relations.

2.6 Discussion

The veiling of photospheric lines on the spectra of active low-mass young stars is one of the most relevant features of these objects. Since its identification, more than half a century ago, by Joy (1949), the veiling has been a matter of study on its own. Up until now, three possible origins for the veiling, all directly related with the accretion process, have been pointed out in the literature.

As explained before, the major source of veiling is the shocked gas region (hot spot) on the stellar atmosphere, created at the base of the accretion funnel(s) (e.g. Basri & Batalha (1990), Calvet & Gullbring (1998)). This type of veiling is due to the radiation emitted by the hot spot, that is at a temperature that can be twice higher than that of the star's photosphere, typically between 6000 K and 8000 K (Calvet & Gullbring, 1998). In result, the photospheric lines on the star's spectrum are shallower due to the excess of continuum emission: veiling continuum. Considering the emission from the hot spot well fitted by black body emission, the veiling continuum should be stronger on the blue, where the radiation from the hot spot has its emission peak. Basri & Batalha (1990) observed this phenomenon for several cTTS.

The two other possible veiling origins reside on emission lines produced before and after the shocked gas region. The post-shocked gas region is on the origin of narrow emission lines, that can fill in the photospheric lines (Dodin & Lamzin, 2012). This effect seems to be more relevant in cTTS with rich emission lines spectra and veiling factors higher than 3 (Gahm et al., 2008). On the other hand, the in falling pre-shocked gas is on the origin of broad emission lines, that can also contribute with emission to the photospheric lines, causing an extra veiling (Sicilia-Aguilar et al., 2015).

If the observed veiling in the optical is not only due to the excess of continuum emission from the hot spot, there are direct implications on the estimation of the mass-accretion rates. In fact, if we overlook veiling from other sources than the hot spot, we might be overestimating the mass-accretion rates.

Narrow emission lines as a veiling origin

Analysis of other very active cTTS, like RU Lup and S CrA, show that in periods of high activity the veiling rises up to values that seem to be unrelated with the veiling continuum. The veiling continuum is produced at the shock regions, so an increase in this type of veiling is directly related with an increase in mass-accretion rates. If the mass-accretion rates increase, as a consequence an increase in the brightness of the star should

also be observed.

From photometric and spectroscopic monitoring of four “extreme” cTTS, Gahm et al. (2008) report high variable veiling that are not be correlated with brightness. In fact, while the veiling factor changed by several magnitudes within the period of 4/5 years, there was a weak change in brightness of the star. So there must be other source of veiling for the line-dependent veiling.

While analysing the spectra of these four active stars, Gahm et al. (2008) noticed the presence of narrow emission cores within the absorption lines. This indicates that there is narrow emission filling in the absorption lines, with a variable behaviour. The fact that this emission is narrow is indicative of a chromospheric origin and changes over time on the atmosphere of the star caused by the accretion process (Gahm et al., 2008).

The three stars analysed in our work are also very active, with high-mass accretion rates and strong outflow activity. In our case we do not analyse the temporal variability of the veiling or brightness of the star. One of our objectives was to investigate if the line-dependent veiling reported by Petrov et al. (2014) for V1331 Cyg was present in comparable objects.

Contrary to the extreme stars analysed by Gahm et al. (2008), our three stars do not show narrow emission cores within the photospheric lines. LkH α 321 is the star where this type of filling-in of the lines should be more easily observed, due to its high $v \sin i$. But there is no sign of narrow emission cores on this star also. So LkH α 321, V1331 Cyg and AS 353A veiling must have other origin than that of the immediate post-shock region.

Broad emission lines as a veiling origin

Another spectral feature that can contribute to the veiling of photospheric lines on cTTS are the broad emission lines. As pointed out before, these lines are formed within the in falling gas, at the base of the accretion column.

Sicilia-Aguilar et al. (2015) studied the peculiar object EX Lup in its quiescence phase and noted that its spectrum was not reproduced by a synthetic spectrum with the same spectral type with added veiling continuum. While some lines were well fitted, other appeared shallower than supposed. This shows that these lines were more veiled than others, in the same wavelength region. One of the possibilities the authors advanced was a broad emission component, formed at the pre-shocked gas, contributing to the total veiling on these lines.

In our three stars spectra, the broad emission lines are broader than the corresponding

photospheric lines. Also, photospheric lines can be seen on top of that emission (Figures 2.27, 2.8 and 2.16). These lines are affected by the line-dependent veiling in the same way as the photospheric lines. The broad emission does not seem to contribute considerably to the observed veiling on these lines. What we see in these cases seems to be the sum of the photospheric spectrum with optically thin broad emission, with origin at regions of lower density (Kwan & Fischer, 2011).

One way that broad emission can affect the measurement of the equivalent widths of the photospheric lines is that the broad emission blends may form an additional pseudo-continuum. With that in mind we avoided the photospheric lines near regions with strong broad emission.

Veiling continuum produced at the hot spot

One of the characteristics of veiling continuum is its dependency on wavelength, being stronger for shorter wavelengths. Since we observe in our targets a veiling effect that depends on line strength, only weak lines can be used to evaluate the veiling continuum. The veiling continuum affects all lines in the same way in a small wavelength range. It does not discriminate between weak and strong lines. Since we believe that veiling with another origin than that of the hot spot is affecting more the stronger lines, only the weak ones can be used to estimate the veiling continuum. It is also noticeable from Figures 2.30, 2.11 and 2.21 that for the same wavelength intervals there is strong veiling variation.

As pointed out before, the veiling continuum can be correlated with the mass-accretion rate and accretion luminosity. Also, it has been shown that the accretion luminosity is well correlated with the line luminosity of several emission lines, via empirical relations (e.g. Fang et al. (2009); Rigliaco et al. (2012); Alcalá et al. (2014, 2017)). Some of these lines are emitted in the pre-shock gas, where the gas is optically thin, while others are produced in the optically thick post-shock gas. Also, Balmer lines, Ca II and He I lines originate in the accretion columns (Alcalá et al., 2014).

We used weak lines to estimate the veiling continuum: 0.6 for AS 353A, 0.1 for V1331 Cyg and around 0 for LkH α 321. With knowledge of the veiling continuum we were able to estimate the filling factor of the hot spots within a range of hot spot temperatures between 6000 K and 8000K. For AS 353A, we obtained filling factors between 7% and 20% of the stellar surface. For V1331 Cyg the filling factor is between 1% and 3% of the stellar surface, while for LkH α 321 is less than 1%.

Even though these calculations are subject to uncertainties, we do not expect hot

spot temperatures higher than 10 000 K. We also believe that the high values of filling factor for AS 353A are related with overestimation of the veiling continuum.

We conclude that, in general, the veiling continuum contribution to the total veiling is small in comparison to that of the line-dependent veiling.

Accretion powered chromosphere

What our observations tell us is that the layers of the stellar atmosphere where stronger lines are formed are more affected by the accretion process than the layers where weaker lines form.

Weaker lines are formed at the deepest layers of the stellar atmosphere, with lines of higher excitation potential forming deeper than those with lower excitation potentials. On the other hand, moderate and strong lines are formed at higher layers of the stellar atmosphere. Moderate lines with higher excitation potentials form deeper than those with lower excitation potentials. Also, in the solar spectrum, strong lines do not have high excitation potentials, so these lines have less energy requirements for formation than weaker lines (Gurtovenko & Sheminova, 2015).

We have shown that narrow or broad emission lines or veiling continuum can not justify the dependence of veiling on line strength that is observed for the three cTTS. In fact, these three types of veiling contribute very little or nothing to the observed veiling on AS 353A, LkH α 321 and V1331 Cyg. In the case of LkH α 321, the veiling continuum is mostly absent. However, we do observe a large veiling, that strongly depends on the strength of the lines.

The line-dependent veiling was also observed on DR Tau (Petrov et al., 2011). In this star, both veiling continuum and line-dependent veiling are variable, but at times when the veiling continuum disappears, the line-dependent veiling decreases but persists.

While we do not analyse the time-evolution of the line-dependent veiling on our objects, it is noticeable that its source is related with the accretion process, but not directly with the accretion columns and shock regions. It was proposed by Petrov et al. (2011), for the DR Tau, an interpretation for this type of veiling as the result of an “accretion powered chromosphere”. The upper layers of the atmosphere are heated by the accretion energy, creating a chromospheric effect that is in the origin of the line-dependent veiling. This means that the accretion process influences the stellar atmosphere to a greater extension than that of the confined area of the hot spots.

It is also possible that the stellar magnetic field structure is more complex than

assumed. Abramenko (2008) found that the solar magnetic field has a fractal structure. CTTS magnetic fields near the stellar surface are expected to be as complex as those in the Sun. This means that as the material from the accretion column approaches the stellar atmosphere, the magnetic field lines will split that material and channel it through accretion columns with lower filling factors. This might create a complex structure where in fact the atmosphere is affected in a wider region than that of a single hot spot created at the base of accretion column. How this heating structure might affect the stellar atmosphere is up to debate.

Another possibility is a more profound alteration of the stellar atmosphere due to the accretion process, with a change in the stellar atmosphere temperature profile. We know from the studies of the Sun atmosphere that there is a temperature profile, with a decrease in temperature towards the exterior, that rises again at the chromosphere and corona. In the Sun, this minimum is located at the transition point between the photosphere and the chromosphere. If in cTTS this temperature profile is altered and the minimum is set further deep into the atmosphere, the chromosphere will have a larger extension, where the higher temperatures are favorable for creating emission lines.

In conclusion, this work reinforces the message of precaution from previous works that one must be cautious while estimating the mass-accretion rates from the veiling alone. If only veiling continuum is considered and other sources of veiling are present in a particular cTTS, it can lead to overestimation of the mass-accretion rates, that can compromise further studies on cTTS models.

This work was accepted for publication in *Astronomy & Astrophysics* (see article in Appendix).

Chapter 3

Fundamental stellar parameters of wTTS

3.1 Fundamental stellar parameters determination

The spectrum of a star contains a wide range of information about that star. We can extract from it knowledge about the most fundamental stellar parameters, such as the effective temperature (T_{eff}), surface gravity ($\log g$), metallicity (typically expressed as $[\text{Fe}/\text{H}]^1$), projected rotational velocity ($v \sin i$), microturbulence velocity (v_{mic}), macroturbulence velocity (v_{mac}) and radial velocity (v_{rad}). Knowledge about these parameters allow us to estimate, from models, the mass and radius, as well as the age of stars.

Nowadays, there are several methods available in the literature that can help us in this task, most of them automatic and easy to use. These methods can be divided into two main types: spectral synthesis (e.g. Valenti & Piskunov (1996)) and equivalent widths (e.g. Sousa et al. (2012)) methods. Some routines and codes also combine the spectral synthesis with the equivalent widths methods to compute stellar parameters for a wider range of spectral types (e.g. Blanco-Cuaresma et al. (2014)). Most of the available methods are optimized for the analysis of high resolution spectra ($R \geq 50000$) of MS stars.

Unless a spectral analysis method takes into account the veiling factor, it can not be used to analyse cTTS. In Chapter 2 we described a way to estimate the spectral type of cTTS, using specific weak photospheric lines ratios that are very sensitive to temperature changes.

On the other hand, one of the key features of wTTS is the absence of veiling in their spectra. Contrary to cTTS, the wTTS show no signs of ongoing accretion, although their spectra is still populated by weak and narrow emission lines associated with chromospheric activity. For wTTS, the most common methods may be used to determine fundamental

1

$$[\text{Fe}/\text{H}] = \log_{10} \left(\frac{N_{\text{Fe}}}{N_{\text{H}}} \right)_{\text{star}} - \log_{10} \left(\frac{N_{\text{Fe}}}{N_{\text{H}}} \right)_{\text{Sun}}, \quad (3.1)$$

where N_{Fe} and N_{H} are the number of iron and hydrogen atoms, respectively, per unit of volume.

stellar parameters.

The spectral classification of wTTS in a wide sample of TTS can provide good input information regarding that population, if all stars are members of the same star forming region. It is also possible to trace some of the characteristics of the cloud itself if the TTS population is well characterized. At the same time, wTTS with well determined spectral types can be used as templates for the cTTS in the same population and improve their spectral type determination. For a given star forming region we do expect that some stellar atmospheric parameters, like the metallicity, are approximately the same for all TTS.

3.1.1 GIRAFFE HR15N spectra

As mentioned previously, TTS, as well as other PMS stars, can be found in young clusters located in star forming regions. The study of large samples of TTS allow statistical studies and possible establishment of empirical correlations between stellar and activity parameters. This is necessary for the development and improvement of PMS evolutionary models. One key interest in studying large samples of TTS is to understand the physical processes behind the dichotomy cTTS/wTTS.

Nowadays, the new generation of multi-target optical spectrographs allow the observation of more than one hundred objects simultaneously. The study of large sample of stars can grant us access to knowledge related with the accretion and mass-loss processes for TTS in similar environmental conditions.

The VLT-FLAMES spectrograph is a multi-object intermediate and high resolution spectrograph at the Very Large Telescope (VLT), that can be used to observe TTS. FLAMES is the Fiber Large Array Multi Element Spectrograph at the Very Large Telescope and feeds two different spectrographs.

One of these spectrographs is the Ultraviolet and Visual Echelle Spectrograph (UVES), a high resolution optical spectrograph mounted at Nasmyth B focus of the UT2. It is constituted by a blue and a red arm that can be used separated or simultaneously. The blue arm can cover the wavelength range 3000 to 5000 Å, whilst the red arm can cover the wavelength range from 4200 to 11000 Å. The maximum resolution of UVES for single target observations is $R \sim 110\,000$. When FLAMES is used while observing with UVES, 8 targets can be observed at the same time (usually one fiber is used to target the sky) and the spectral resolution will be of 47000 (corresponding to a fiber with 1" of aperture). The wavelength range of FLAMES/UVES is that of the red arm.

The second instrument is the GIRAFFE spectrograph, an intermediate to high resolution ($R = 5500 - 65100$) spectrograph that covers the whole visible range ($3700 - 9500 \text{ \AA}$). GIRAFFE spectrograph has a multi-object observational mode called MEDUSA. This mode allows the simultaneous observation of approximately 130 objects, that can include fibers targeting the sky/nebula. The fibers have pre-defined widths, which defines the resolution of the spectra in each setup.

From all the available modes of FLAMES/GIRAFFE, one of the most relevant for the observation of YSO is the HR15N mode, because such setup covers the $H\alpha$ line at 6563 \AA and the lithium (Li) resonance line at 6708 \AA . The spectra obtained with this mode ranges from 6470 to 6820 \AA and is centred at 6650 \AA . The resolution of the spectra with this mode is $R \sim 19000$, for observations done after February 2015, and $R \sim 17000$ for previous observations. This is considered intermediate resolution.

As pointed out before, the $H\alpha$ line is a very important line for the identification, classification and study of TTS. This line often appears in emission in TTS and because of that can not be used to perform determination of fundamental parameters. The Li line at 6708 \AA is an indicator of youth, since these TTS did not had enough time to consume the lithium present in the cloud material from which they are forming. This observation mode allows the identification and classification of TTS stars. If time-series observations are asked, it can also be used to monitor the $H\alpha$ variability of several TTS located in the same star forming region, simultaneously.

While GIRAFFE HR15N spectra can be used to study the $H\alpha$ line, it is not in the most adequate wavelength range to determine fundamental stellar parameters. The photospheric lines present in this range are rare, weak and mostly of neutral elements. The lack of lines of ionized elements is problematic for the determination of $\log g$ and $[\text{Fe}/\text{H}]$ (Gray, 2005).

One of the main reasons to insist on finding ways to obtain fundamental stellar parameters for stars observed with the GIRAFFE HR15N setup is the Gaia-ESO Survey (GES). The GES is a large public spectroscopic stellar survey intended to support the Gaia Mission. The aim of the Gaia satellite is to provide highly accurate astrometric measurements and radial velocity estimates for thousands of stars. However, the accuracy of the GAIA radial velocities may not be sufficient for many purposes. Therefore, in order to complement the GAIA radial velocities estimates, the GES is observing thousands of stars with the VLT/FLAMES spectrograph, providing radial velocities measurements with a higher precision than those of GAIA.

A significant amount of TTS observed by GES are faint targets with spectral types

later than F, that are being observed for the first time, mostly with the GIRAFFE spectrograph in the HR15N setup. GES spectra does offer the opportunity to find and select new TTS for further studies, so it is important to explore to the maximum the information that the GIRAFFE HR15N spectra provide.

3.2 Observational data: TTS from NGC 2264

The main focus of this work is the analysis of wTTS spectra from the star forming region NGC 2264 obtained with the GIRAFFE spectrograph in the HR15N setup (MEDUSA mode).

NGC 2264 is a star forming region located at about 800 parsecs away in the direction of Monoceros constellation (Dahm & Simon, 2005). Under this designation are also the Cone Nebula and the Christmas tree cluster (Figure 3.1). The cluster is located in front of an emission nebula, that contributes with emission in $H\alpha$, as well as some forbidden lines (like [NII] and [SII]), to the spectra of the stars (e.g. Sousa et al. (2015), McGinnis et al. (2015)). This region is populated by very young stars of various masses, making it of special interest to study the PMS stage of evolution. The mean age of the cluster is estimated to be around 3 Myrs (Dahm & Simon, 2005).

NGC 2264 is one of the most studied star forming regions in the latest years. The first studies related with this object started more than one hundred years ago, but in the last two decades it gained an increased interest, accompanying the improvement in sensibility of the new generation of instruments (e.g. Dahm & Simon, 2005; Alencar et al., 2010; Venuti et al., 2014; Sousa et al., 2015; Bouvier et al., 2016).

It consists of a series of 20 spectra for each of the ~ 160 stars divided into two fields of observation. The spectra was taken during the course of two months, between December 2011 and February 2012 (Sousa et al., 2015; McGinnis et al., 2015). The spectral resolution is $R \sim 17000$. The spectra was reduced with the GASGANO package available from ESO and as described by Sousa et al. (2015). Afterwards, all the analysed spectra were normalized. The normalization was done by continuum definition by eye on the original spectra. The radial velocity of each star was measured before setting each spectra in stellar rest frame, via cross-correlation with a solar spectrum.

3.2.1 WTTS classification

At a first moment we excluded the spectra with strong $H\alpha$ line absorption and few photospheric lines, most likely early spectral type stars. In a second step we removed from the



Figure 3.1: NGC 2264. In this image it is possible to see the Cone Nebula and Christmas tree cluster together. Image obtained by the Wide Field Imager instrument. Credits: ESO.

Table 3.1: WTTS sample: identification and raw measurements.

Corot ID	RA (deg)	Dec (deg)	S/N	RV (km s ⁻¹)	EW(Li) (Å)	EW(Hα) (Å)	w10%Hα (km s ⁻¹)
223989989	100.40100	9.65567	34	15.7 ± 0.5	0.43 ± 0.02	-2.48 ± 0.12	82 ± 1
500007458	100.18771	9.76161	40	20.5 ± 0.8	0.49 ± 0.02	-2.94 ± 0.17	107 ± 2
223985176	100.32471	9.56028	42	18.7 ± 0.3	0.42 ± 0.05	-2.48 ± 0.12	128 ± 4
223976494	100.18388	9.39871	44	13.8 ± 0.8	0.37 ± 0.04	-0.74 ± 0.06	91 ± 5
223971984	100.10942	9.63372	46	36.1 ± 0.4	0.51 ± 0.09	-1.71 ± 0.19	139 ± 3
500007276	100.17258	9.80267	46	19.7 ± 0.9	0.50 ± 0.01	-3.64 ± 0.15	105 ± 4
223973692	100.13667	9.85814	46	19.1 ± 0.4	0.48 ± 0.01	-3.10 ± 0.12	142 ± 5
500007330	100.27421	9.87994	47	22.3 ± 0.3	0.53 ± 0.02	-1.06 ± 0.10	96 ± 4
223972691	100.12063	9.70475	47	20.1 ± 0.2	0.48 ± 0.01	-1.53 ± 0.06	98 ± 4
223992383	100.43725	9.74453	49	17.3 ± 0.3	0.41 ± 0.04	-1.23 ± 0.04	96 ± 7
500007366	100.19733	9.81372	50	18.6 ± 0.5	0.44 ± 0.05	-1.98 ± 0.08	110 ± 6
500007298	100.15263	9.80636	50	19.6 ± 0.2	0.42 ± 0.01	-1.57 ± 0.06	88 ± 2
223991789	100.42808	9.71572	52	16.7 ± 0.7	0.46 ± 0.01	-1.61 ± 0.12	119 ± 5
500007248	100.27125	9.86236	56	21.4 ± 0.3	0.49 ± 0.01	-1.87 ± 0.19	118 ± 2
223988965	100.38542	9.63539	58	17.5 ± 0.6	0.45 ± 0.01	-1.71 ± 0.04	119 ± 2
223985845	100.33558	9.75986	64	16.8 ± 0.5	0.41 ± 0.01	-0.90 ± 0.05	86 ± 2
223988742	100.38171	9.80911	65	17.6 ± 0.3	0.48 ± 0.03	-1.67 ± 0.05	112 ± 2
500007176	100.26850	9.85725	70	25.8 ± 0.2	0.44 ± 0.01	-0.68 ± 0.02	104 ± 10
223972960	100.12454	9.83622	76	24.5 ± 0.2	0.44 ± 0.04	1.28 ± 0.05	
223980989	100.25704	9.80614	81	23.7 ± 0.6	0.52 ± 0.01	-0.94 ± 0.04	126 ± 3
223982535	100.28242	9.73417	102	22.7 ± 0.1	0.28 ± 0.01	1.83 ± 0.04	
223986498	100.34600	9.45740	104	17.9 ± 0.7	0.25 ± 0.02	0.98 ± 0.25	
223988099	100.37163	9.65997	122	19.9 ± 0.3	0.28 ± 0.01	1.16 ± 0.06	
500007051	100.25921	9.86442	137	37.4 ± 0.1	0.28 ± 0.02	1.60 ± 0.06	

sample all stars with equivalent width of Li line lower than 0.1 \AA , excluding the MS stars with spectral type later than G (Bertout, 1989). In a third step we applied the criteria defined by White & Basri (2003) for the classification of TTS into cTTS or wTTS. This selection criteria is based on the equivalent width of the $H\alpha$ line ($EW(H\alpha)$) and the width at 10% peak of maximum intensity of the $H\alpha$ line ($width10\%$).

As proposed by White & Basri (2003), we can consider as cTTS those stars with $width10\% \geq 270 \text{ km s}^{-1}$. At the same time, it is probable that stars with $EW(H\alpha) \geq 3 \text{ \AA}$ for K0-K5 stars or $EW(H\alpha) \geq 10 \text{ \AA}$ for K7 - M2.5 stars can also be considered cTTS (see Chapter 1).

We decided to select all the stars from the sample with $EW(H\alpha) \leq 10 \text{ \AA}$ and $width10\% \leq 270 \text{ km s}^{-1}$. With this criteria we are likely excluding any cTTS from our sample. At the same time, we take into account residual contamination due to nebular emission. Since there are 20 spectra for each star and photometric variability is not significant for these stars (based on the σ over the median spectra), we measured the equivalent widths of Li and $H\alpha$ lines and $width10\%$ of the $H\alpha$ line for each spectrum and averaged the results. The uncertainties are given by the standard deviation of the mean. The measurements were done using IDL routines developed by us. The values of equivalent widths have a minus sign in case of the line being in emission. The reason for the sign is just to distinguish between lines in emission and absorption.

Another selection criterion considered while defining our sample is associated with the signal-to-noise ratio (S/N) of the spectrum. The stars in each target field were observed all at the same time, with the same exposure time. This means that the fainter stars will have spectra with lower S/N than the brighter ones. While some stars in the sample have $S/N \geq 100$, the average S/N is ~ 50 and the faintest stars do have spectra with $S/N \leq 30$. While testing our methodology (see sections 3.3 and 3.4) we noticed that for those stars whose spectra had $S/N \leq 30$, the code was not always able to compute the stellar parameters. For this reason we decided to exclude those stars with $S/N \leq 30$.

Our final sample includes 24 wTTS. Table 3.1 summarizes each star Corot ID, coordinates (right ascension (RA) and declination (Dec), average S/N, radial velocity (RV), equivalent width of the Li line $EW(Li)$, $H\alpha$ line $EW(H\alpha)$ and $width10\%$ for each star.

The stars analysed in this work have been previously observed within photometric surveys and more recently by the GES. From Venuti et al. (2014) we have an indication about the spectral type for most stars, based on photometric data (Tables 3.2), while from Bouvier et al. (2016) and Spina et al. (2017) we have access to an estimation of T_{eff} from spectroscopic data (Tables 3.3). Bouvier et al. (2016) and Spina et al. (2017) share similar

Table 3.2: WTTS sample: photometry derived parameters from Venuti et al. (2014) (V_14).

Corot ID	T_{eff} (V_14) (K)	$\log g$ (V_14) (dex)	R mag.(V_14)	SpT (V_14)
223989989	3984	4.06	16.0	K7
500007458	3989	3.89	15.7	K7
223985176	3910	3.62	14.8	M0
223976494				
223971984	3914	3.3	14.3	M0
500007276	4389	3.99	15.1	K5
223973692	4194	3.82	15.3	K6
500007330	4002	3.8	15.2	K7
223972691	4184	3.96	15.0	K6
223992383	3994	3.93	15.1	K7
500007366	3682	3.46	15.4	M1
500007298	4383	4.12	15.1	K5
223991789	3194	3.49	18.2	M4:M4.5
500007248	4385	4.01	15.0	K5
223988965	4194	3.68	14.5	K6
223985845	3502	3.61	14.5	M2
223988742	4948	4.08	14.5	K2
500007176	4396	4.07	14.3	K5
223972960	4941	4.07	14.0	K2
223980989	4392	3.5	13.8	K5
223982535	6678	4.19	13.2	F2
223986498				
223988099	5661	3.91	12.8	G5
500007051	5223	3.82	12.6	K0

Table 3.3: WTTS sample: spectroscopy data from from Bouvier et al. (2016) (B.16) and Spina et al. (2017)(S.17).

Corot ID	T_{eff} (B.16) (K)	$v \sin i$ (B.16) (km s ⁻¹)	EW(Li)(B.16) (Å)	T_{eff} (S.17) (K)	[Fe/H] (S.17) (dex)	$\log g$ (S.17) (dex)
223989989	4225 ± 308	12.0 ± 0.5	0.5387 ± 0.0198	4225 ± 127	-0.09	
500007458	4888 ± 167	21.0 ± 0.5	0.5910 ± 0.0040			
223985176	4979 ± 190	15.0 ± 0.5	0.4712 ± 0.0135			
223976494						
223971984	4182 ± 345	28.0 ± 1.6	0.5890 ± 0.0171			
500007276	4443 ± 258	18.7 ± 1.5	0.5406 ± 0.0022	4443 ± 120	-0.10	
223973692	4769 ± 256	30.0 ± 0.5	0.5720 ± 0.0010			
500007330	4269 ± 324	22.2 ± 1.7	0.5999 ± 0.0034	4268 ± 117	-0.14	
223972691	4421 ± 276	15.0 ± 0.5	0.5250 ± 0.0063	4420 ± 122	-0.11	
223992383	4897 ± 167	12.0 ± 0.5	0.4565 ± 0.0063			
500007366	4172 ± 428	30.0 ± 0.5	0.5354 ± 0.0035			
500007298	4954 ± 206	12.0 ± 0.5	0.4597 ± 0.0071			
223991789	4474 ± 424	21.0 ± 0.5	0.5025 ± 0.0042	4473 ± 145	-0.09	
500007248	4417 ± 220	12.0 ± 0.5	0.5186 ± 0.0058			
223988965	4805 ± 95	15.0 ± 0.5	0.4828 ± 0.0008	4805 ± 95	-0.08	4.48
223985845	4932 ± 128	24.7 ± 1.2	0.4493 ± 0.0144	4932 ± 128	-0.12	4.46
223988742	4805 ± 107	21.0 ± 0.5	0.5073 ± 0.0026	4805 ± 107	-0.06	4.48
500007176	4650 ± 245	15.0 ± 0.5	0.4573 ± 0.0008	4650 ± 133	-0.02	
223972960				4865 ± 117	-0.17	4.00
223980989	4436 ± 264	22.0 ± 1.6	0.5670 ± 0.0036	4435 ± 119	-0.09	
223982535	5529 ± 188	13.0 ± 1.5	0.2870 ± 0.0015	5528 ± 82	0.01	
223986498	5480 ± 197	36.0 ± 0.5	0.2718 ± 0.0063	5479 ± 88	-0.08	
223988099	5626 ± 177	18.0 ± 0.5	0.2744 ± 0.0037			
500007051	5377 ± 177	10.4 ± 1.7	0.3121 ± 0.0057	5376 ± 85	-0.08	

T_{eff} values for the same stars, since both works are using the parameters derived by the GES consortium.

WTTS median spectra

A median spectrum was also created from the median of all the 20 spectra available for each star. The median spectrum eliminates cosmic rays that each spectrum might be affected with². For those stars with H α in emission we plot the median spectrum H α line and the standard deviation (σ) (see Appendix, Figures A.1, A.2, A.3, A.4 and A.5). There seem to be no significant photometric variability, either for the photospheric lines or H α line.

3.3 Method: Spectral synthesis

In this work we use the spectral synthesis code Spectroscopy Made Easy (SME), that was presented by Valenti & Piskunov (1996) as a user friendly IDL software package for the analysis of stellar spectra. SME can compute several fundamental stellar parameters. This method makes use of a library of atmospheric models and a line list to compute synthetic spectra, which is used to fit the real spectra.

One of the advantages of SME is that it takes into consideration the instrumental resolution and the S/N of the spectrum. This makes SME suitable for the analysis of GIRAFFE spectra.

In this work we follow the strategy adopted by Valenti & Fischer (2005) for the analysis of cool stars ($T_{\text{eff}} \leq 5000$ K). Our line mask takes into consideration the characteristics of both GIRAFFE HR15N wavelength band and the features associated with the young stars spectrum.

3.3.1 SME setup for GIRAFFE HR15N spectra

To analyse any spectrum, SME requires several input information, including the initial guess parameters, the wavelength intervals to be considered for the analysis, as well as an indication of the lines to fit (line mask). It also requires a line list extracted from VALD. When this work started, in 2013, very little was known about the reliability of fundamental stellar parameters determination from the GIRAFFE HR15N wavelength band. With the

²Changes in radial velocity can allow the identification of possible binary systems. Since that is not the objective of this work we did not analysed the radial velocity variability before creating the median spectrum of each star.

publications from the GES consortium (e.g. Damiani et al. (2014), Lanzafame et al. (2015)), some light started to be shed about the stellar parameters determination for this wavelength band.

Recently, an alternative method for the analysis of GIRAFFE HR15N was proposed by Damiani et al. (2014): the Spectral Indices (SI) method. From the work of Damiani et al. (2014) we can conclude that the determination of $\log g$ and $[\text{Fe}/\text{H}]$ have associated high uncertainties. So, when building our line mask we prioritized those lines that are more sensitive to T_{eff} changes.

To build the line mask and define the wavelength intervals adequate for the analysis of the GIRAFFE spectra, we used synthetic spectra with different values of T_{eff} , $\log g$ and $[\text{Fe}/\text{H}]$ to find which lines were more sensitive to each parameter changes. Our selection was based on the following criteria:

- small wavelength intervals (2 to 7 Å) with few lines to allow an accurate line modeling;
- preference for single line profiles, avoiding for most cases blending that could introduce a higher error when fitting;
- taking into consideration possible high $v \sin i$ (up to 40 km s⁻¹) of some wTTS, so relatively isolated lines profiles were preferred;
- the H α and Li lines were avoided, since H α line can be in emission and the Li line is typically not present in the models used by SME.

Then, using the solar spectrum, we tested several combinations of short wavelength intervals where the selected lines were included. We also used the spectra of the wTTS in our sample with the highest S/N to properly adjust the wavelength intervals. The combination of spectral lines that gave the best fit results for the Sun was used to build the line mask for the analysis of the wTTS sample. Our final line mask contains 24 spectral lines divided by 16 wavelength intervals (Table 3.6 and Figure 3.2).

SME allows the simultaneous determination of several parameters, set as variables, while others can be fixed as pre-defined values. Due to degeneracy in models caused by the inter-dependency in parameters, such as between $v \sin i$ and v_{mac} or between $[\text{Fe}/\text{H}]$ and v_{mic} (Valenti & Fischer, 2005; Tsantaki et al., 2014), when using SME some parameters must not be set as variables at the same time as others. Our main focus are the T_{eff} , $\log g$, $[\text{Fe}/\text{H}]$ and $v \sin i$ parameters. We decided to keep as fixed parameters both v_{mac} and v_{mic} . These two parameters are associated with small and large scale turbulence in stellar

Table 3.4: SME wavelength intervals and fitted lines

$\Delta\lambda$ (Å)	λ (Å)	Element
6545.00-6547.00	6546.238	FeI
6596.50-6598.20	6597.559	FeI
6607.00-6611.00	6608.025	FeI
	6609.110	FeI
6626.50-6628.50	6627.544	FeI
6632.80-6634.75	6633.749	FeI
6642.50-6649.00	6643.629	NiI
	6645.210	SiI
	6646.931	FeI
	6648.080	FeI
6653.00-6654.50	6653.851	FeI
6676.70-6679.70	6677.954	FeI
6702.50-6706.00	6703.566	FeI
	6705.101	FeI
6709.00-6711.00	6710.318	FeI
6724.50-6727.50	6726.666	FeI
6732.00-6734.00	6733.150	FeI
6741.00-6744.00	6741.628	SiI
	6743.122	TiI
6749.20-6751.00	6750.152	FeI
6752.00-6754.00	6752.707	NiI
6802.50-6811.50	6804.271	FeI
	6806.843	FeI
	6810.262	FeI

Table 3.5: SME initial parameters

Parameter	Value	
T_{eff} (K)	5000	Variable
$\log g$ (dex)	4.0	Variable
[Fe/H] (dex)	0.0	Variable
v_{mic} (km s ⁻¹)	0.85	Fixed
v_{mac} (km s ⁻¹)	2.8	Fixed
$v \sin i$ (km s ⁻¹)	0.0	Variable
v_{rad} (km s ⁻¹)	0.0	Fixed

atmospheres and are responsible for part of the spectral line broadening. The consequences of fixing v_{mic} and v_{mac} while computing the other four parameters are explored in Section 3.5.3.

The initial guess parameters, common to all analysed spectra, are presented in Table 3.11. The chosen initial values for T_{eff} , $\log g$ and [Fe/H] are typical values for wTTS: $T_{\text{eff}} \sim 5000$ K, $\log g \sim 4.0$ dex, [Fe/H] ~ 0.0 dex. The initial guess for the $v \sin i$ parameter is 0.0 km s^{-1} .

The v_{mac} value was computed using equation 1 from Valenti & Fischer (2005) for the T_{eff} value of 5000 K: $v_{\text{mac}} = 2.8 \text{ km s}^{-1}$. For the v_{mic} value we adopted the value used by Valenti & Fischer (2005), that is also adequate for wTTS (e.g. Padgett, 1996; Rojas et al., 2008; James et al., 2006; Taguchi et al., 2009): $v_{\text{mic}} = 0.85 \text{ km s}^{-1}$ (Valenti & Fischer, 2005). The radial velocity (v_{rad}) parameter was also kept fixed at 0.0 km s^{-1} , since all analysed spectra, both real and synthetic are in stellar rest frame.

We decided to use the Kurucz atmospheric models (Castelli & Kurucz, 2003) in this analysis, since their grid is available for a wider range of parameters, avoiding further extrapolation during the minimization process.

The line list for the parameters determination was extracted from VALD for a solar type star ($T_{\text{eff}} = 5770$ K, $\log g = 4.44$ dex). The reason for this choice of parameters while extracting the line list resides on the empirical line data correction applied to the oscillator strength values ($\log gf$) and van der Waals damping parameter, using a high resolution spectrum of the Sun. The reason behind the necessity of this correction lies with the lack of enough accurate theoretical line data (Valenti & Fischer, 2005). Other works related with fundamental stellar parameters determinations, mainly those using spectral synthesis, also perform this type of correction (e.g. Tsantaki et al. (2013)).

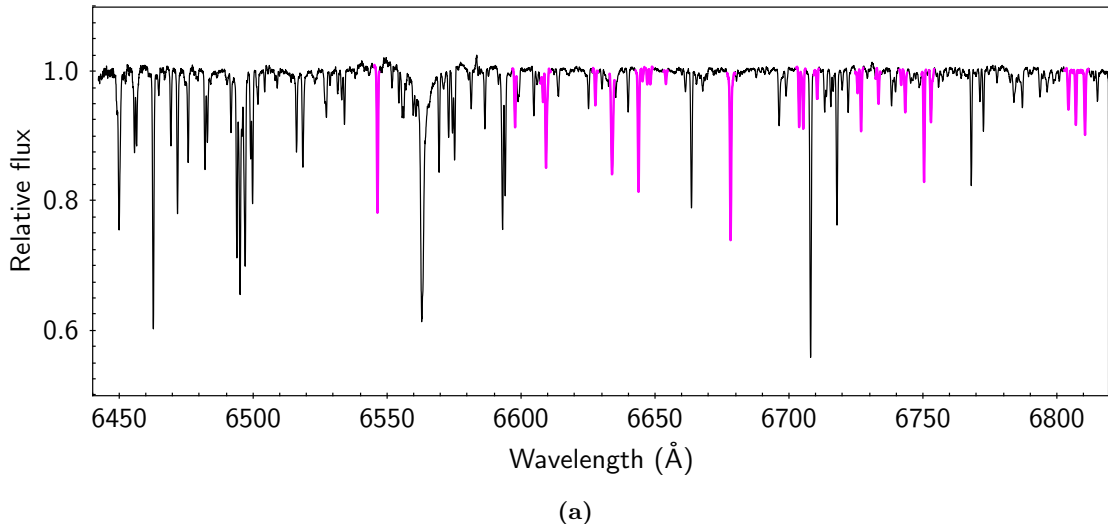


Figure 3.2: Plot of the spectrum of star 223988099 with the lines used in the SME line mask in evidence.

3.3.2 Sources of uncertainties

There are several sources of uncertainty while using SME to determine fundamental stellar parameters from the GIRAFFE HR15N spectra.

One source of uncertainty that is difficult to quantify is the lines choice present in our line mask. Different line combinations can lead to slightly different results, since some lines are more sensitive to a certain parameter than others. Even though we tried to select those lines that showed higher T_{eff} sensitivity and the best fit for the Sun, other combinations of lines can also be used. The same is true for our choice of initial guess parameters.

Another source of uncertainty is the inter-dependency of the parameters. A less accurate or wrong determination of one parameter can have a significant impact on the determination of one or more of the other parameters.

Another extra source of error is the choice of atmospheric models. Although one can choose from different grids of atmospheric models available in the literature, these models will always be an approximation to reality. For the case of young stars, this error source can be relevant, since, due to the lack of proper atmospheric models for PMS stars, we are using MS stars atmospheric models. The Kurucz atmospheric models assume LTE atmospheres, which might not be appropriated for young stars atmospheres.

In the case of a single spectrum, we can associate an uncertainty to the results computed by SME in two ways. One is by extracting the *sigma value* associated with each parameter from the co-variance matrix calculated by SME and provided in the output.

This uncertainty is a fitting error that takes into account both continuum and line fitting. The second way is related with the fact that SME gives slightly different results if different initial parameters are given. One can then run SME for the same spectrum with several different sets of initial guess parameters and estimate an uncertainty. This uncertainty is typically very small, as computed by (Valenti & Fischer, 2005): $\sigma(T_{\text{eff}}) = 33 \text{ K}$, $\sigma(\log g) = 0.06 \text{ dex}$, $\sigma([\text{Fe}/\text{H}]) = 0.021 \text{ dex}$, $\sigma(v \sin i) = 0.34 \text{ km s}^{-1}$.

The fact that we have more than 20 spectra for each star in the wTTS sample allows us to take into account the uncertainties associated with the spectra themselves, since these stars show very low spectral variability. Because these spectra were obtained in different nights during two months, spectra quality is different and averaging the results can help minimize the effects of bad observational conditions or residual nebular variability. We analysed the spectra of each star and averaged the results. The final parameters are the mean value of the ~ 20 spectra available for each star and the standard deviation of the sample.

3.4 Testing SME with synthetic and real stars spectra

In order to test the SME setup for the analysis of GIRAFFE spectra we used the following samples:

- five samples of synthetic spectra generated by SME;
- a sub-sample of 17 stars from the Gaia-ESO Survey Benchmark stars;
- a sample of 190 FGK stars.

In the following we describe each sample in detail, as well as the test results.

3.4.1 SME synthetic spectra

Synthetic spectra created with corrected line list

Four samples of synthetic spectra (SME_A_1 to SME_A_4) were created using SME providing the same atmospheric models and line list used to analyse the GIRAFFE spectra.

A detailed description of these samples is presented in Table 3.6. The first sample, SME_A_1, is used to test the SME setup regarding accuracy and precision of the determinations of T_{eff} , $\log g$, $[\text{Fe}/\text{H}]$. It is composed by 504 synthetic spectra with the parameters: $T_{\text{eff}} = [4000, 6000] \text{ K}$, $\log g = [3.0, 4.5] \text{ dex}$, $[\text{Fe}/\text{H}] = [-1.0, +4.0] \text{ dex}$ and $v \sin i = 10 \text{ km s}^{-1}$.

Table 3.6: SME synthetic spectra grid: SME_A.

Parameter	SME_A.1	SME_A.2	SME_A.3	SME_A.4
T_{eff} (K)	[4000, 6000]	[4000, 6000]	[4000, 6000]	[4000, 6000]
T_{eff} bin (K)	250	250	250	250
$\log g$ (dex)	[3, 4.5]	[3, 4.5]	[3, 4.5]	[3, 4.5]
$\log g$ bin (dex)	0.25	0.25	0.25	0.25
[Fe/H] (dex)	[-1.0, +0.4]	[-1.0, +0.4]	[-1.0, +0.4]	[-1.0, +0.4]
[Fe/H] bin (dex)	0.2	0.2	0.2	0.2
$v \sin i$ (km s ⁻¹)	10	[1, 30]	10	10
$v \sin i$ bin (km s ⁻¹)	-	5	-	-
Resolution	17000	17000	[5000, 50000]	17000
Resolution bin	-	-	5000	-
S/N	300	300	300	[25, 150]
S/N bin	-	-	-	25
Sample size	504	48	42	120

The second sample of synthetic spectra, SME_A.2, is used to test the restrictions to the determination of $v \sin i$. It is composed by 48 spectra of random stellar parameters within the same range as SME_A.1, with $v \sin i$ ranging from 1 to 30 km s⁻¹. The third and fourth samples of synthetic spectra, hereafter SME_A.3 and SME_A.4, are used to check the effects of spectral resolution and spectral noise, respectively, on accuracy and precision of the results. These samples are composed by spectra with random parameters within the same range as SME_A.1, but with different values of spectral resolution (from R=5000 to R=50000) and S/N (from 25 to 150), respectively.

Our choice for the range of T_{eff} , $\log g$, [Fe/H] and $v \sin i$ reflects the typical parameters of young low-mass stars (Bertout, 1989). The S/N is similar to that of the benchmark stars (see section 3.4.3): S/N = 300. These spectra also has $v_{\text{mic}} = 0.85$ km s⁻¹ and $v_{\text{mac}} = 2.8$ km s⁻¹.

The four samples were analysed with the SME setup described in section 3.3, with T_{eff} , $\log g$, [Fe/H] and $v \sin i$ as free parameters.

The values obtained for the four stellar parameters in sample SME_A.1 are plotted in Figure 3.3. In the plot we show the difference between the reference values and the values derived by SME ($\Delta = \text{reference} - \text{SME}$) versus the reference values.

Looking at the results for T_{eff} it is noticeable that for $T_{\text{eff}} \leq 5000\text{K}$ there is a systematic

underestimation of temperature of the order of 70 K. Although the accuracy is worse, we obtain better precision towards lower temperatures. For larger temperatures we notice a high dispersion of the values (Table 3.7). Several tests done to the SME_A.1 sample have shown that the observed underestimation of temperature is not due to the lower values of instrumental resolution and do not depend on S/N, $v \sin i$, $\log g$ or [Fe/H]. This effect is also present if all other parameters except T_{eff} are fixed while running SME. It is also not observed when real stars spectra are analysed with the same setup (see Sections 3.4.2, 3.4.3).

As for the [Fe/H] parameter, there is an increasing underestimation of [Fe/H] for reference values lower than -0.5 dex, with decreasing precision. Since our aim is the analysis of stars with [Fe/H] close to solar, the observed lack of precision and accuracy is not relevant for our work.

As expected, $\log g$ results do show a high dispersion for all reference values, but increasing towards lower reference values. Despite the low precision, in average the accuracy of the determinations is not as bad as for T_{eff} (Table 3.7).

In Figure 3.3 (d)) we plot the determinations for the $v \sin i$ parameter for samples SME_A.1 and SME_A.2. Sample SME_A.2 does not have the same diversity of parameters combinations as present in sample SME_A.1 and it might be for that reason that we do not observe a dispersion as high as for the SME_A.1 sample.

Frasca et al. (2015) performed Monte Carlo simulations on the $v \sin i$ parameter for stars with GIRAFFE spectra ($R \sim 17000$) and checked the results dependency on S/N and stellar spectral type. They found out that below $v \sin i = 7 \text{ km s}^{-1}$ it was not possible to accurately resolve the $v \sin i$ value. Figure 3.3 (d)) confirms the decrease of precision and accuracy for lower values of $v \sin i$.

The results reported in Figure 3.3 are obtained with the four parameters (T_{eff} , $\log g$, [Fe/H], $v \sin i$) set as variables. If any of these parameters is set as fixed the results might suffer changes that can be significant in terms of accuracy and precision of the determinations. Since we want to analyse a sample of real wTTS spectra whose parameters are mostly unknown we do not want to fix any of these four parameters. For this reason we have no major interest in checking the results of fixing individual parameters while testing the SME setup for synthetic spectra. But, as will be explained later in this section, it will be necessary to fix $v \sin i$ while analysing the real stars sample of benchmark stars and FGK stars, since their $v \sin i$ is lower than the spectral resolution of GIRAFFE spectra. For the $v \sin i$ parameter only, we found no effect caused by fixing it during SME computation on the determination of T_{eff} , $\log g$ or [Fe/H], since $v \sin i$ only contributes with broadening

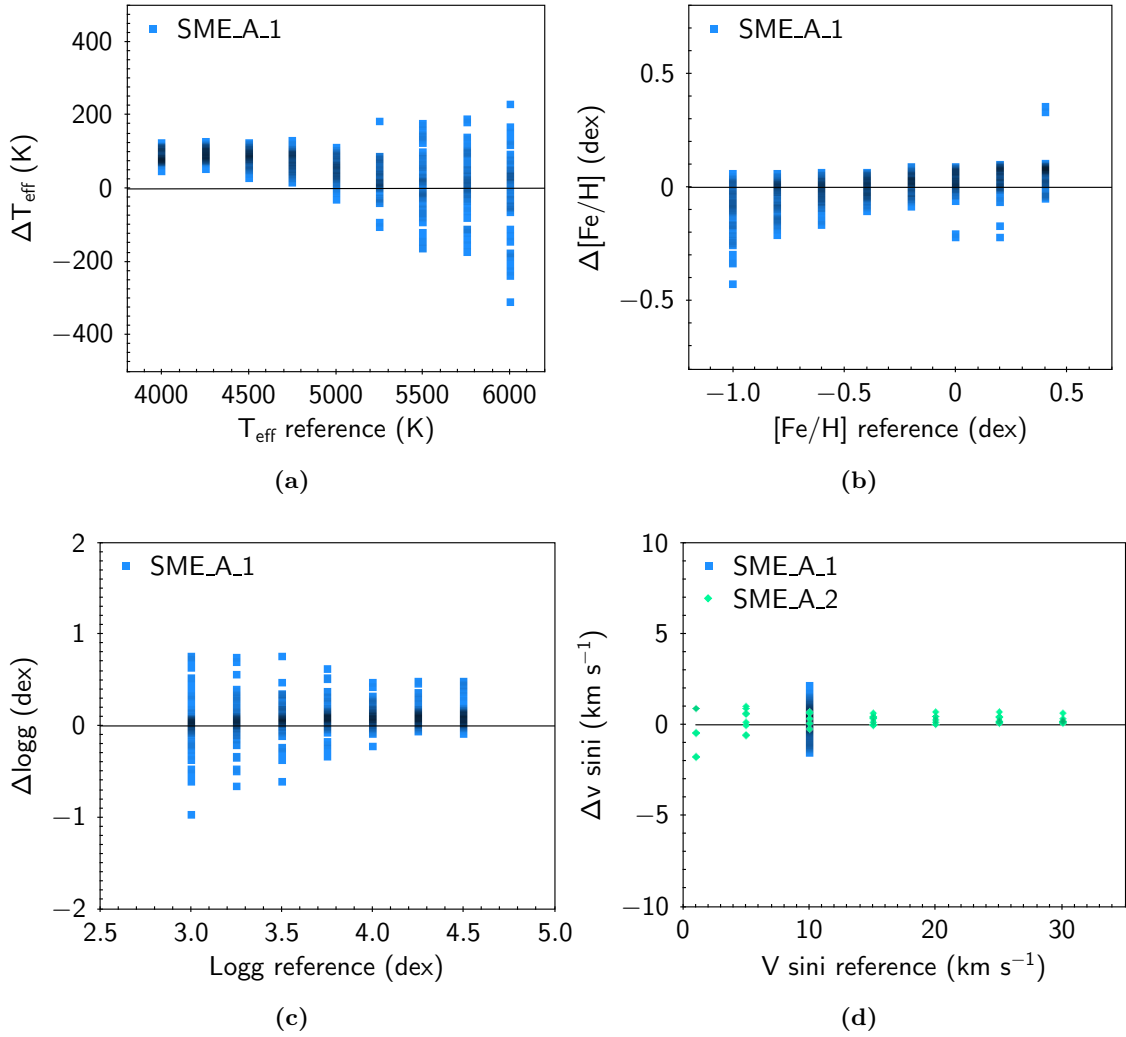


Figure 3.3: SME results from the analysis of SME_A.1 sample. Difference between the reference values and the SME results ($\Delta = \text{reference} - \text{SME}$) for T_{eff} (a), $[\text{Fe}/\text{H}]$ (b) and $\log g$ (c). SME results for $v \sin i$ from the analysis of SME_A.2 samples are also plotted (d).

Table 3.7: Average differences between reference values and SME results for SME_A.1 and SME_B

Parameter	SME_A.1	SME_A.1	SME_B	SME_B
	$T_{\text{eff}} \leq 5000 \text{ K}$		$T_{\text{eff}} \leq 5000 \text{ K}$	
$\langle \Delta T_{\text{eff}} \rangle$ (K)	49	78	2	7
σ	68	27	111	86
$\langle \Delta[\text{Fe}/\text{H}] \rangle$ (dex)	-0.004	0.02	-0.13	-0.19
σ	0.079	0.06	0.12	0.12
$\langle \Delta \log g \rangle$ (dex)	0.08	0.07	-0.62	-0.67
σ	0.18	0.07	0.37	0.36
$\langle \Delta v \sin i \rangle$ (km s ⁻¹)	0.25	0.29	0.02	0.87
σ	0.51	0.30	1.19	0.79

to the lines.

Synthetic spectra created with original line list from VALD

After the several tests with the SME_A.1 sample we conclude that the decrease in accuracy for T_{eff} lower than 5000 K should be intrinsic to the synthetic spectra. The problem might reside with the atmospheric models or with the line list used. A quick test showed that the chosen models were not the source of the problem. Using the MARCS models instead of the Kurucz we obtain the same results. So the problem should be related with the line list itself.

To create the SME_A samples we used as input the same line list used in the determination of stellar parameters. As will be shown in the following sections, the systematic underestimation of temperature for cool stars is not observed in the case of the real stars (benchmark and FGK stars).

In order to understand if the problem was really related with the line list given as input to create the synthetic spectra, we decided to create a small sample of synthetic spectra using a VALD line list for $T_{\text{eff}} = 4500 \text{ K}$ and $\log g = 4.0 \text{ dex}$. In this case no empirical correction to the $\log gf$ and van der Waals damping parameters was performed. The description of this sample, hereafter SME_B, can be found in table 3.8. The results of the analysis to this sample are shown in Figure 3.4.

Contrary to the results for the SME_A.1 sample, T_{eff} does not show the same underestimation for values lower than 5000 K. In fact, the behaviour is the opposite as for the SME_A.1 sample, showing a slight overestimation for the lower values of temperature.

Table 3.8: SME synthetic spectra samples B description

Parameter	SME_B
T_{eff} (K)	[4000, 5250]
T_{eff} bin (K)	250
$\log g$ (dex)	[3.0, 4.5]
$\log g$ bin (dex)	0.5
[Fe/H] (dex)	[-0.5, +0.25]
[Fe/H] bin (dex)	0.25
$v \sin i$ (km s ⁻¹)	10
$v \sin i$ bin (km s ⁻¹)	-
Resolution	17000
Resolution bin	-
S/N	300
S/N bin	-
Sample size	96

On the other hand, both [Fe/H] and $\log g$ show worse results than when considering the SME_A.1 sample. The $v \sin i$ parameter does not seem to be affected by the type of line list used to build the synthetic spectra.

Table 3.7 compares the average of the differences between the reference values and the SME results for both samples.

Starting with T_{eff} , it is evident that for the SME_B sample the results do not show the same systematic underestimation as for the SME_A.1 sample, for spectra cooler than 5000 K. On the other hand, the dispersion is higher. While there seems to be an increase in accuracy of the results, there is also an overall decrease in precision. At the same time, this analysis shows that the offset for $T_{\text{eff}} \leq 5000$ K for the SME_A.1 sample is indeed related with the line list provided as input. The main reason might be the temperature for which the line list given as input to create the SME_A sample was extracted from VALD (solar like temperature, 5770 K).

Regarding [Fe/H] and $\log g$, one can see that for the SME_B sample the determinations lack both accuracy and precision. This must be related with the fact that SME_B sample was created using a line list that does not have empirical adjustments for the $\log gf$ and van der Waals damping parameters of the analysed lines. At the same time, wrong determination of one parameter can lead to a significant decrease in accuracy in another

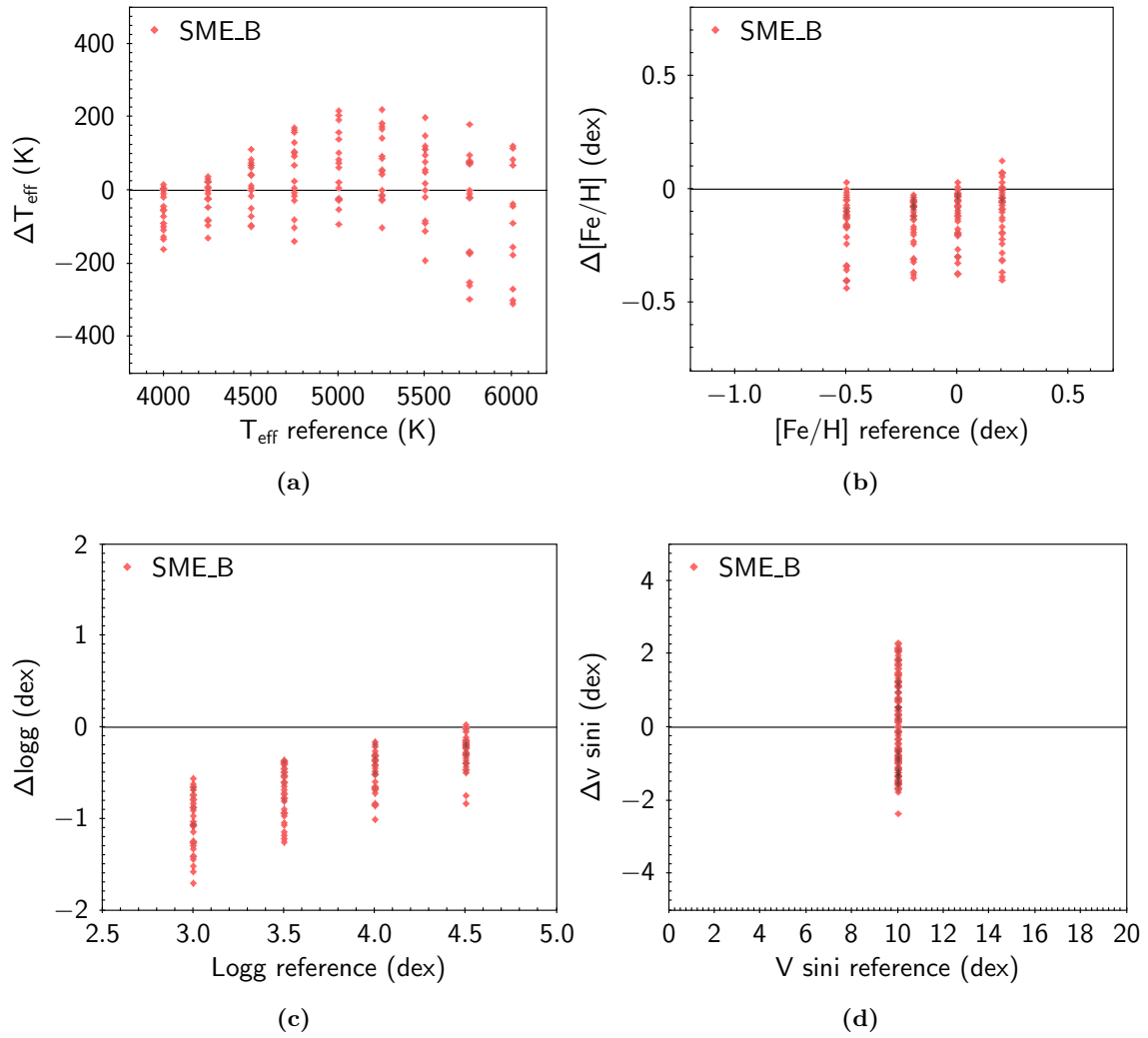


Figure 3.4: SME results from the analysis of SME_B sample. Difference between the reference values and the SME results ($\Delta = \text{reference} - \text{SME}$) for T_{eff} (a), $[\text{Fe}/\text{H}]$ (b), $\log g$ (c) and $v \sin i$ (d).

Table 3.9: SME accuracy and precision considering different spectral resolutions

Resolution (x1000)	ΔT_{eff} (K)		$\Delta \log g$ (dex)		$\Delta[\text{Fe}/\text{H}]$ (dex)		$v \sin i$ (km s^{-1})	
	Mean	σ	Mean	σ	Mean	σ	Mean	σ
5	191	46	0.17	0.06	0.18	0.09	-0.85	0.47
10	94	48	0.08	0.05	0.06	0.08	0.75	0.89
20	45	38	0.03	0.03	-0.01	0.06	0.11	0.26
25	38	39	0.02	0.03	-0.02	0.05	0.06	0.20
30	27	39	0.02	0.03	-0.03	0.05	0.04	0.18
50	30	46	0.01	0.03	-0.03	0.06	0.04	0.12

parameter. This does seem to be the case for $\log g$ and $[\text{Fe}/\text{H}]$.

Spectral resolution and signal-to-noise ratio analysis

To further test the effects of spectral resolution and S/N on the accuracy and precision of the developed SME setup we used two small samples of synthetic spectra: SME_A_3 and SME_A_4 (Table 3.6). Sample SME_A_3 is composed by synthetic spectra with random parameters, within the range of the SME_A_1 sample and with the same S/N (~ 300), to which we applied 6 different resolutions ($R = 2500, 10000, 20000, 25000, 30000, 50000$). SME_A_3 sample is composed by a total of 42 spectra. Sample SME_A_4 is composed by spectra with resolution $R \sim 17000$, with random combinations of parameters within the range of SME_A_1, and different values of S/N ($S/N = 25, 50, 75, 100, 125, 150$), with a total of 120 spectra.

The SME_A_3 sample results for several values of spectral resolution and the SME_A_4 sample results for several values of S/N are shown in Figures 3.5 and 3.6, respectively. In general, there is an increase of accuracy and precision with the increase in resolution and S/N for all the parameters (see Tables 3.9 and 3.10).

The results for the synthetic spectra sample with GIRAFFE resolution ($R \sim 17000$) were analysed in detail previously and are not shown in the Figure 3.5. Also, apart from $v \sin i$, whose accuracy and precision clearly improve for higher spectral resolutions, the other three parameters show no major differences in accuracy and precision for resolutions higher than 20000 (Table 3.9). At the same time, it is clear that the S/N of the spectra does affect the precision of the results, but not their accuracy. For spectra with $S/N \leq 75$, the precision can decrease in approximately half, while for spectra with $S/N \geq 75$ the precision does not vary significantly (Table 3.10).

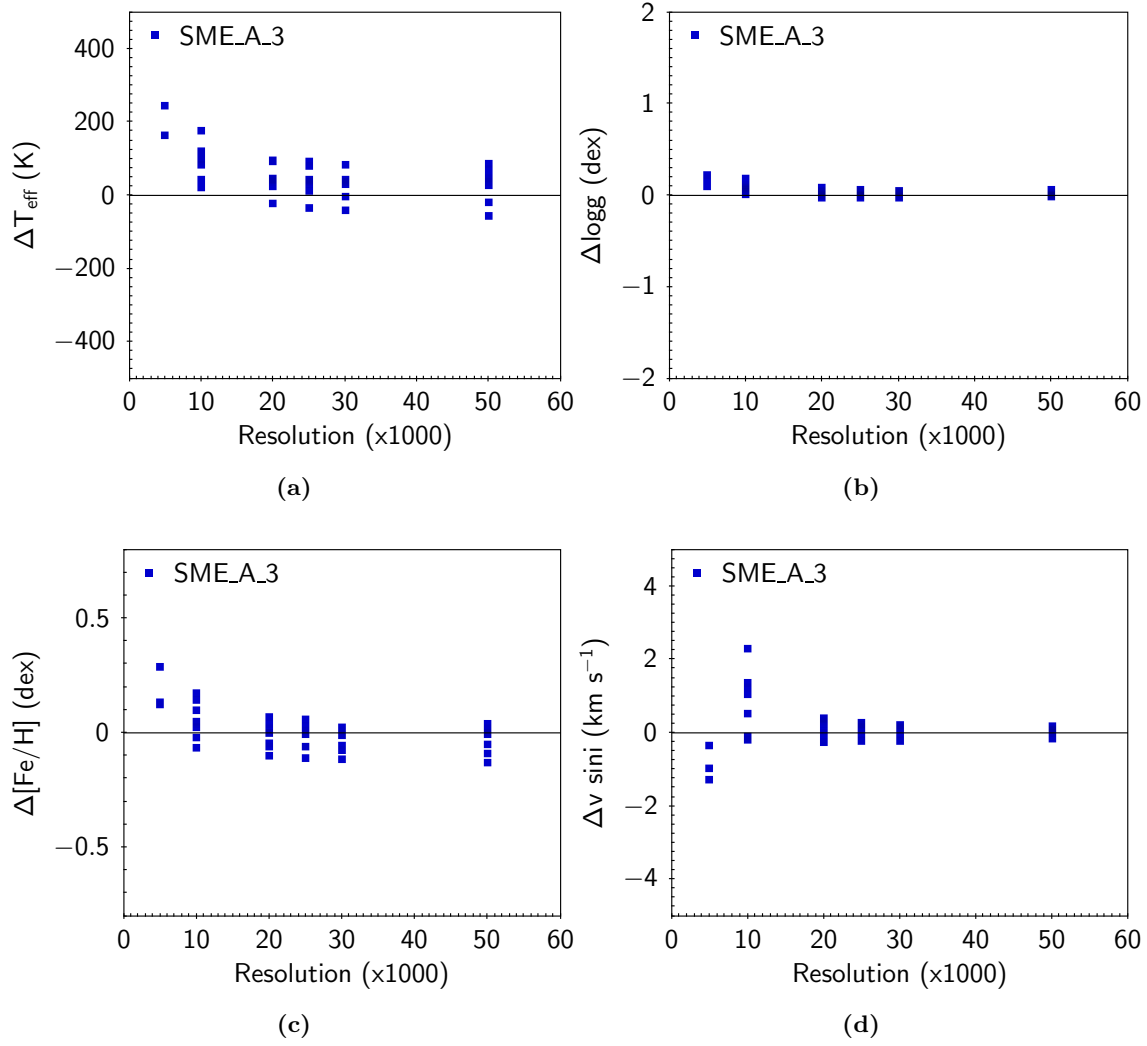


Figure 3.5: SME results for a sample of synthetic spectra with different spectral resolutions (SME_A_3). The plots show the difference between the reference value and the SME results ($\Delta = \text{reference} - \text{SME}$) versus spectral resolution for T_{eff} (a)), $\log g$ (b)), $[\text{Fe}/\text{H}]$ (c)) and $v \sin i$ (d)).

Table 3.10: SME accuracy and precision considering different S/N

S/N	ΔT_{eff} (K)		$\Delta \log g$ (dex)		$\Delta [\text{Fe}/\text{H}]$ (dex)		$v \sin i$ (km s $^{-1}$)	
	Mean	σ	Mean	σ	Mean	σ	Mean	σ
25	88	46	0.07	0.09	0.03	0.08	0.27	0.80
50	81	27	0.06	0.06	0.03	0.06	0.21	0.48
75	66	40	0.06	0.05	0.03	0.05	0.41	0.39
100	65	22	0.05	0.04	0.04	0.05	0.40	0.34
125	58	30	0.05	0.06	0.01	0.06	0.21	0.42
150	60	28	0.05	0.06	0.01	0.05	0.23	0.40

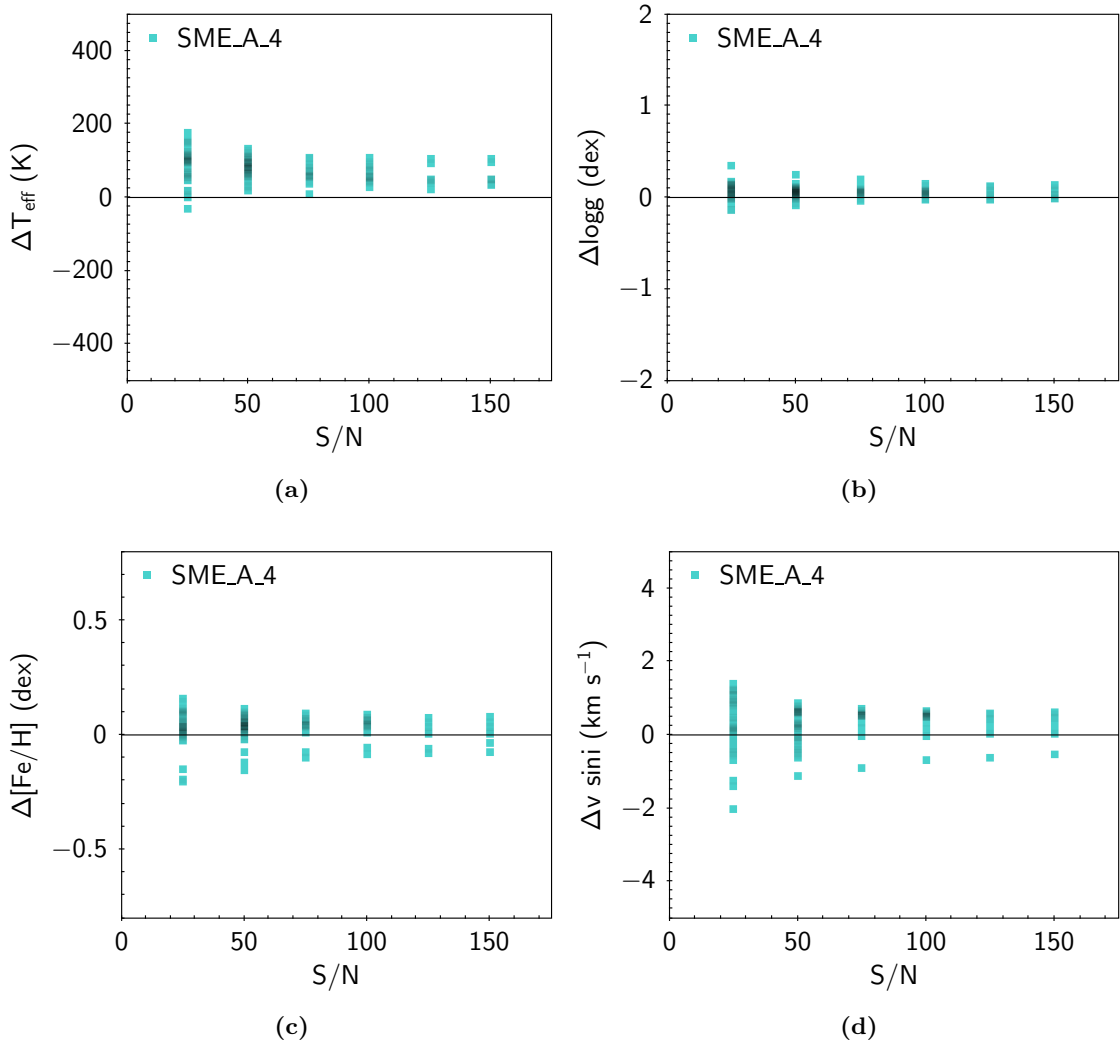


Figure 3.6: SME results for a sample of synthetic spectra with different values of S/N (SME_A_4). The plots show the difference between the reference value and the SME results ($\Delta = \text{reference} - \text{SME}$) versus S/N for T_{eff} (a)), $\log g$ (b)), $[\text{Fe}/\text{H}]$ (c)) and $v \sin i$ (d)).

Table 3.11: Benchmark and FGK stars samples description.

Parameter	BenS	FGK
T_{eff} (K)	[3900, 6000]	[4500, 5500]
T_{eff} bin (K)	-	-
$\log g$ (dex)	[3.0, 4.7]	[3.6, 4.6]
$\log g$ bin (dex)	-	-
[Fe/H] (dex)	[-1.0, +0.4]	[-0.9, 0.4]
[Fe/H] bin (dex)	-	-
$v \sin i$ (km s ⁻¹)	≤5	≤5
$v \sin i$ bin (km s ⁻¹)	-	-
Resolution	17000	17000
Resolution bin	-	-
S/N	⟨300⟩	≥100
S/N bin	-	-
Sample size	17	190

3.4.2 Real stars

Besides synthetic spectra we also used real stars spectra to test our SME setup and see the adequacy of the method to the determination of T_{eff} , $\log g$, [Fe/H] and $v \sin i$ for the wTTS. We used spectra of few stars from the GES Benchmark stars sample and a sample of 190 FGK stars observed with HARPS. The FGK stars spectra were kindly provided by Sérgio Sousa and Nuno Santos (Sousa et al., 2008).

Benchmark stars

The benchmark stars spectra³ were obtained with HARPS and with the NARVAL spectrograph with spectral resolution higher than 40000 (Blanco-Cuaresma et al., 2014). The spectra was degraded to the GIRAFFE HR15N resolution ($R \sim 17000$) by gaussian convolution. The average S/N of the spectra is ~ 300 . The stellar parameters for the benchmark stars spectra can be found in Jofré et al. (2014), Blanco-Cuaresma et al. (2014) and Heiter et al. (2015). We selected the stars with parameters typical of wTTS (Table 3.11). The analysed benchmark stars sample, hereafter BenS, includes 17 benchmark stars with $\log g \geq 3$ dex.

Due to the low values of $v \sin i$ (the vast majority presents $v \sin i \leq 5$ km s⁻¹) we

³Spectra downloaded from <https://www.blancocuaresma.com/s/benchmarkstars>

kept this parameter as constant ($v \sin i = 1 \text{ km s}^{-1}$) during the determination of stellar parameters with SME. Also, it must be noted that the Gaia Benchmark stars sample lacks sub-giant and dwarf stars with low values of temperature (below 4500 K). Since our SME line mask was not developed for stars with $\log g$ values below 3 dex, there are very few stars in our BenS sample with T_{eff} values below 5000 K and $\log g$ above 3 dex.

The stars are identified in Table 3.12, where we also show the stellar parameters obtained from the literature and determined by SME. On Figure 3.7 we plot the results for T_{eff} , $\log g$ and $v \sin i$ for the BenS sample.

There is one difference between the T_{eff} results for the synthetic spectra and for the BenS samples: no underestimation of T_{eff} is observed. For stars with temperatures below 5500 K we observe a slight overestimation, while for stars above 5500 K there is a predominant underestimation of T_{eff} . The dispersion is higher for the hottest stars (with ΔT_{eff} up to 380 K), like in the case of the SME_A sample.

The BenS T_{eff} results show that the observed systematic underestimation of T_{eff} for the SME_A sample for $T_{\text{eff}} \leq 5000 \text{ K}$ must have an intrinsic cause related with the construction of the synthetic spectra.

The $\log g$ results are relatively accurate, with $\langle \Delta \log g \rangle = 0.007 \text{ dex}$, similar to that of the synthetic spectra (Table 3.13). At the same time, the determinations show similar precision as for the SME_A sample, with $\Delta \log g \sim 1 \text{ dex}$ for only one star.

The accuracy of the $[\text{Fe}/\text{H}]$ determinations is reasonable, with $\langle \Delta [\text{Fe}/\text{H}] \rangle = -0.02 \text{ dex}$, although we only have very accurate results for few stars (Table 3.13). The dispersion is homogeneously distributed along the range the metallicity.

FGK stars

To further test our SME setup we also made use of a sub-sample of 190 stars, hereafter FGK (see Table 3.11), from a sample of 451 FGK stars previously analysed by Sousa et al. (2008) and revisited by Tsantaki et al. (2013) and Teixeira et al. (2016). The FGK stars stellar parameters can be found in Sousa et al. (2008). These values were obtained mainly with TMCalc (Sousa et al., 2007) and MOOG (Snedden, 1973).

The selected 190 stars are non-active (or with low chromospheric activity levels) MS dwarfs with $T_{\text{eff}} \leq 5500 \text{ K}$. The spectra present a S/N above 100 and were degraded to the GIRAFFE spectral resolution of 17000. Like we did for the BenS sample, the $v \sin i$ parameter was kept fixed to a constant value ($v \sin i = 1 \text{ km s}^{-1}$) while determining the other three parameters with SME, since these stars have $v \sin i$ values inferior to the

Table 3.12: Benchmark stars stellar parameters from literature (Lit.) and determined by SME.

Star	T_{eff} (K)		[Fe/H] (dex)		$\log g$ (dex)	
	Lit.	SME	Lit.	SME	Lit.	SME
EpsFor	5123	5060	-0.62	-0.53	3.52	3.54
HD140283	5522	6412	-2.43	-1.87	3.58	4.60
DelEri-w	4954	5216	0.06	0.26	3.76	4.14
EtaBoo	6099	6285	0.30	0.40	3.79	4.89
BetHyi-w	5873	5597	-0.07	-0.15	3.98	4.17
BetVir	6083	5948	0.21	0.34	4.10	4.08
HD22879	5868	5533	-0.88	-1.01	4.27	4.47
MuAra	5902	5691	0.33	0.36	4.30	4.36
AlfCenA	5792	5690	0.24	0.26	4.31	4.41
MuCas	5308	5322	-0.82	-0.74	4.41	4.40
18Sco	5810	5781	0.01	0.14	4.44	4.52
TauCet	5414	5097	-0.50	-0.46	4.49	3.82
Gmb1830	4827	5068	-1.46	-1.24	4.60	4.71
EpsEri-w	5076	5092	-0.10	-0.01	4.61	4.49
61CygA	4374	4464	-0.33	-0.41	4.63	4.31
AlfCenB-w	5231	5242	0.22	0.29	4.63	4.49
61CygB	4044	4149	-0.38	-0.62	4.67	4.16
Sun	5770	5813	0.02	0.10	4.44	4.54

Table 3.13: Average differences between literature values and SME results for BenS and FGK samples.

Parameter	BenS	FGK
$\langle \Delta T_{\text{eff}} \rangle$ (K)	27	46
σ	140	80
$\langle \Delta [\text{Fe}/\text{H}] \rangle$ (dex)	-0.02	-0.08
σ	0.12	0.10
$\langle \Delta \log g \rangle$ (dex)	0.007	0.070
σ	0.242	0.170

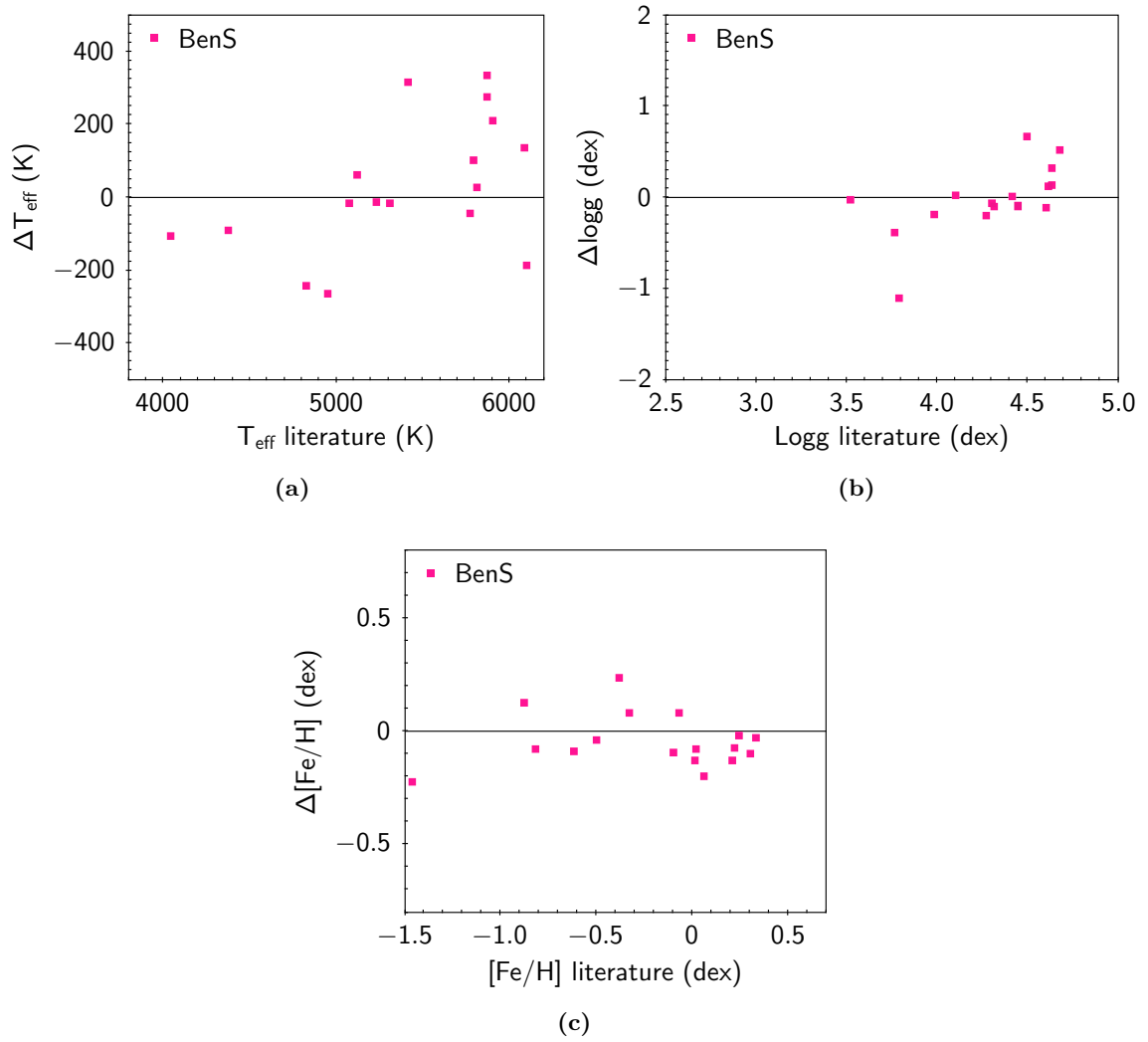


Figure 3.7: SME results for the BenS sample. The plots show the difference between the reference value and the SME results ($\Delta = \text{reference} - \text{SME}$) for T_{eff} (a), $\log g$ (b) and $[\text{Fe}/\text{H}]$ (c).

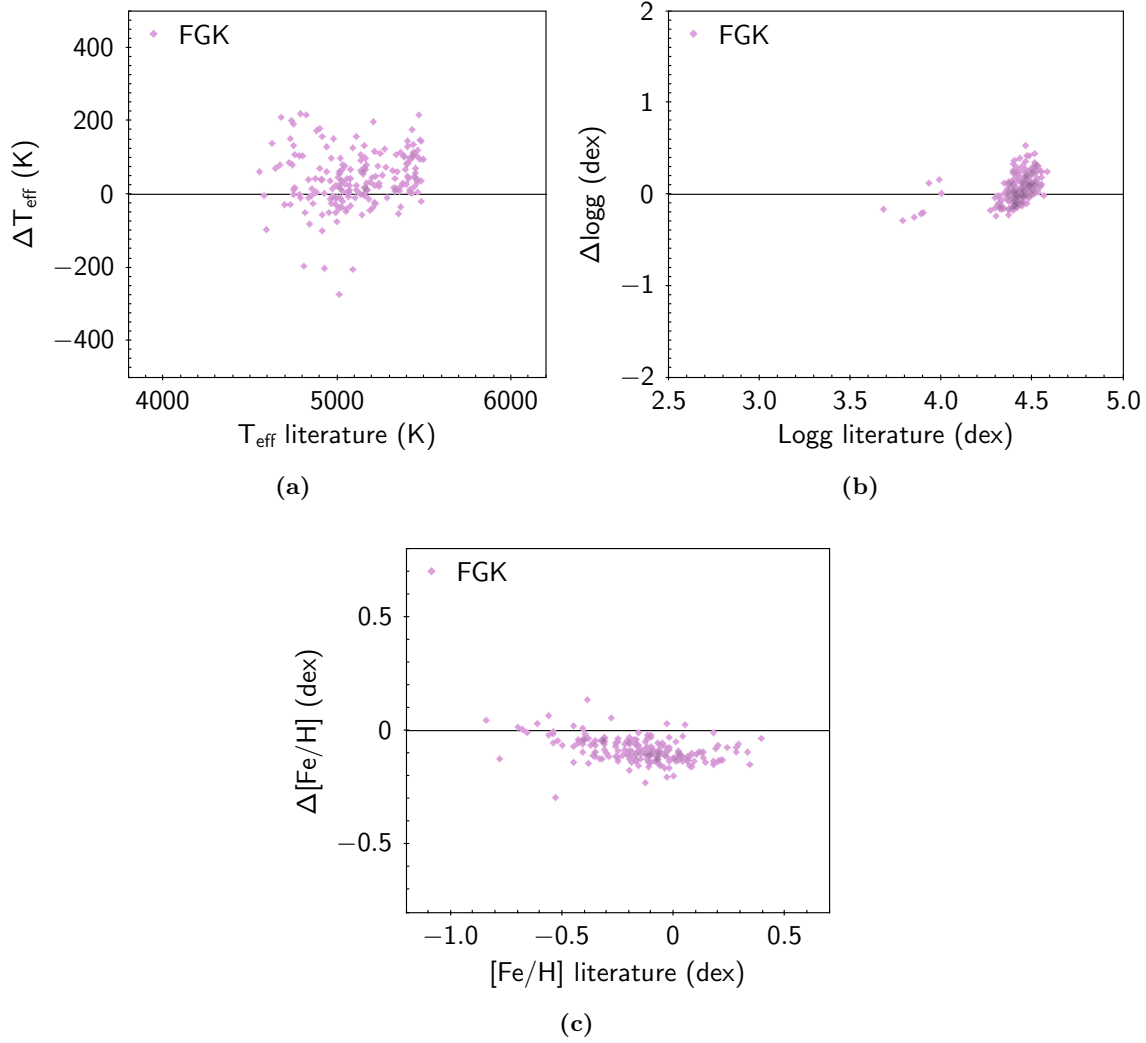


Figure 3.8: SME results for the FGK sample. The plots show the difference between the reference value and the SME results ($\Delta = \text{reference} - \text{SME}$) for T_{eff} (a), $\log g$ (b)) and $[\text{Fe}/\text{H}]$ (c)).

spectral resolution of the GIRAFFE spectra.

On Figure 3.8 we plot the results for T_{eff} , $\log g$ and $[\text{Fe}/\text{H}]$ for the FGK sample. On table 3.13 we present the average of the differences between the literature values and the SME determinations.

In this case we see that there is a slight underestimation of T_{eff} for this sample, but with no correlation with the temperature. At the same time, only for few stars the ΔT_{eff} does exceed 200 K. The dispersion is almost half that of the BenS sample (Table 3.13).

On the other hand, these stars have a very low range of $\log g$, since they are mostly dwarf stars, so the $\log g$ values are concentrated between 4.2 and 4.7 dex. We can also see a slight underestimation of $\log g$, but $\Delta \log g$ does not exceed 0.6 dex. In general, the accuracy is inferior to that of the BenS sample, but the dispersion is lower (Table 3.13).

A more clear overestimation of the results is present for the [Fe/H] parameter. In this case we obtain less accurate results than those of the BenS sample, with similar dispersion (Table 3.13). We have no clear explanation for the constant overestimation of [Fe/H] observed for this sample. One possibility might reside with our line list, since we only observed similar behaviour for the SME_B sample.

3.4.3 Internal comparison

An analysis of all samples used to test the SME setup described in section 3.3 has been done, in order to understand if this setup can be used in the analysis of the wTTS.

Figures 3.9, 3.10 and 3.11 compile the results obtained with the SME_A_1, BenS and FGK samples. In Figure 3.9 we plot the differences in temperature between the reference values and those derived by SME (ΔT_{eff}) for each sample. In overall, we observe a generalized slight underestimation of temperature. At the same time, the dispersion is higher for the hottest stars, with ΔT_{eff} rarely exceeding 200 K. Globally, we obtain $\langle \Delta T_{\text{eff}} \rangle \sim 48$ K and $\sigma \sim 100$ K.

In Figure 3.10 we compare the results obtained for the $\log g$ parameter. It is clear that for $\log g \leq 4$ there is an increasing loss of precision. Globally, $\langle \Delta \log g \rangle \sim 0.04$ dex and $\sigma \sim 0.5$ dex.

In Figure 3.11 we compare the determinations for the [Fe/H] parameter. Also in this case we observe a decrease in precision and accuracy for $[\text{Fe}/\text{H}] \leq -0.5$ dex. Globally, $\langle \Delta[\text{Fe}/\text{H}] \rangle \sim 0.02$ dex and $\sigma \sim 0.2$ dex.

As for the $v \sin i$ parameter we only have the results from the analysis of the SME_A_1 sample, that gives $\langle \Delta v \sin i \rangle \sim 0.25$ km s⁻¹ and $\sigma \sim 0.5$ km s⁻¹.

Although it can not be done for the synthetic spectra, we can compare our results to those of the other works for both BenS and FGK samples. There are few recent works done on the determination of parameters of the benchmark stars with intermediate resolution spectra (e.g. Lanzafame et al. (2015), Tsantaki et al. (2018)). But we can also compare our results with those obtained for the same stars with high resolution spectra by Blanco-Cuaresma et al. (2014) and Smiljanic et al. (2014). While in the first work they determine parameters for the benchmark stars with a method that combines spectral synthesis and equivalent widths (iSpec), the second resumes the determinations from several GES consortium working groups, where stellar parameters are determined using different methods.

From Blanco-Cuaresma et al. (2014) and Smiljanic et al. (2014), we conclude that

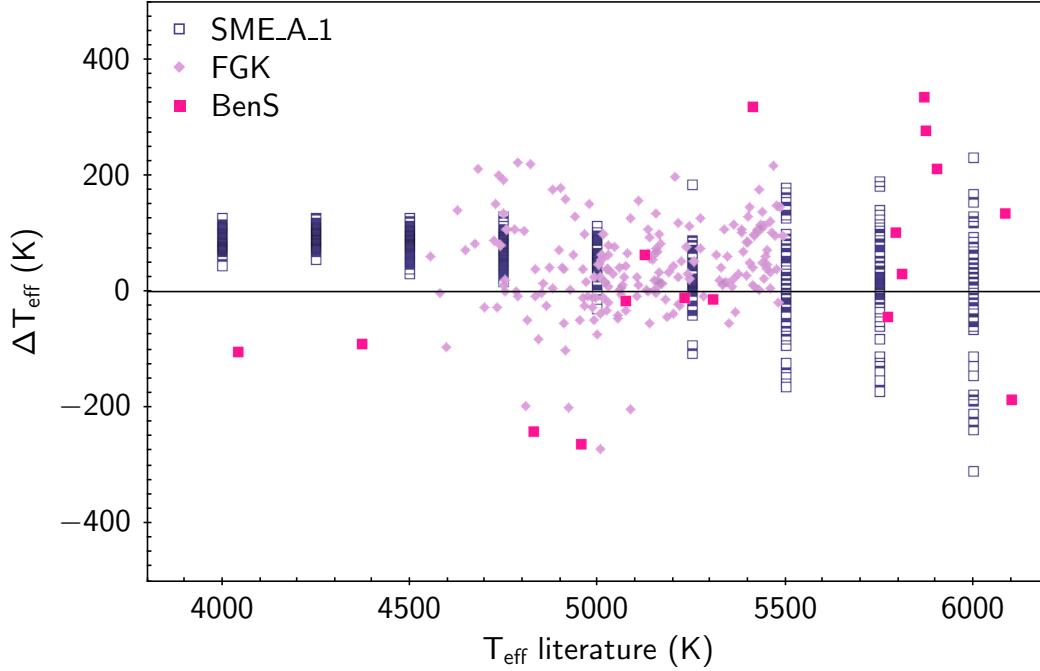


Figure 3.9: Compilation of SME T_{eff} results for the SME_A.1, BenS and FGK samples. The plots show the difference between the reference value and the SME results ($\Delta = \text{reference} - \text{SME}$) versus T_{eff} reference values.

our results are comparable to those obtained for high resolution spectra, both in terms of accuracy and precision. In fact, our results are in overall better than those obtained by Smiljanic et al. (2014) for the benchmark stars.

The same is true for the $\log g$ parameter. Apart from few exceptions, our determinations are within ± 0.5 dex, for the benchmark stars with $\log g \geq 3.0$ dex. These are comparable to the $\log g$ results derived by Blanco-Cuaresma et al. (2014) and Smiljanic et al. (2014). The differences between the reference values and our determinations for the $[\text{Fe}/\text{H}]$ parameter are also comparable to those of Blanco-Cuaresma et al. (2014) and Smiljanic et al. (2014), with few stars exceeding $\Delta[\text{Fe}/\text{H}] = \pm 0.2$ dex.

As for the intermediate resolution spectra studies, we can compare our results with those of Lanzafame et al. (2015) and Tsantaki et al. (2018). GES consortium uses different methods for the analysis of the GIRAFFE spectra, namely ROTFIT and the Spectral Indices method (Damiani et al., 2014). From Lanzafame et al. (2015) analysis of the same Gaia Benchmark stars sample we can conclude that our results for the BenS sample are comparable to those obtained by the groups analysing the GIRAFFE spectra.

Tsantaki et al. (2018) also uses the spectral synthesis method to obtain parameters for both medium and high resolution spectra for the benchmark stars and for the sample of 451 stars from where we selected the 190 FGK stars analysed with SME. Tsantaki et

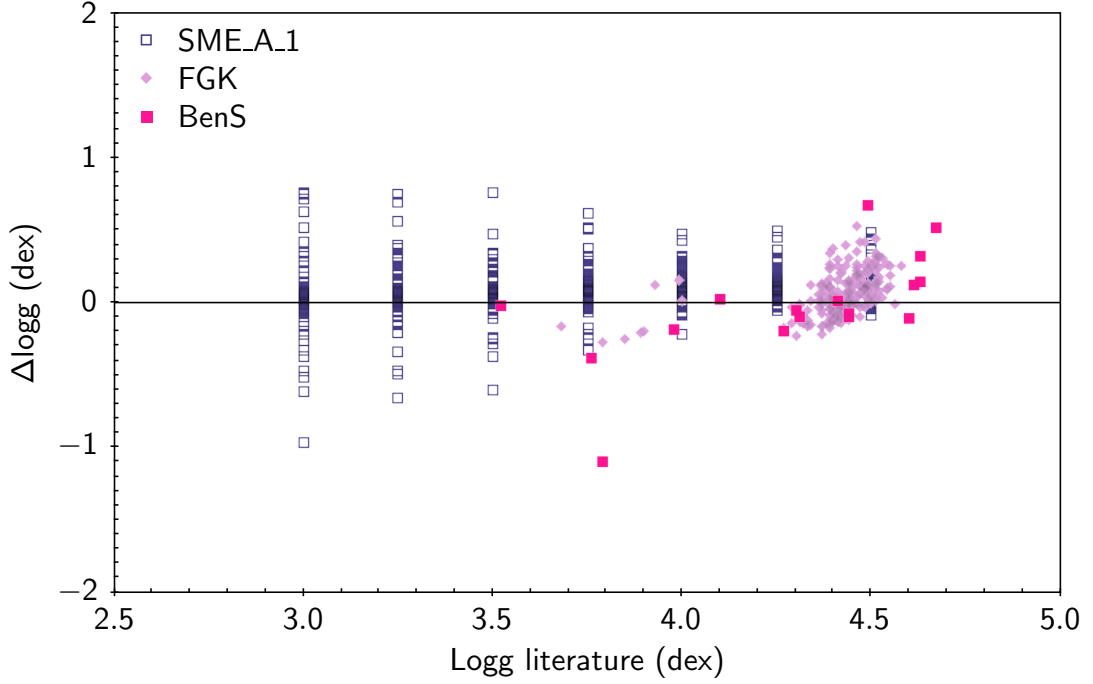


Figure 3.10: Compilation of SME $\log g$ results for SME_A.1, BenS and FGK samples. The plots show the difference between the reference value and the SME results ($\Delta = \text{reference} - \text{SME}$) versus $\log g$ reference values.

al. (2018) obtained less dispersion for temperatures above 5000 K, with similar accuracy for the high resolution spectra (451 FGK stars sample). On the other hand, they obtain similar accuracy and dispersion for intermediate resolution spectra (GIRAFFE HR15N spectra), for the benchmark stars.

We are overlooking effects like the non-LTE (NLTE) effects. These might become important if one desires high accuracy and high precision on the determinations of the stellar parameters. In our case we are dealing with intermediate resolution and low S/N spectra in a wavelength range with few appropriate lines for stellar parameters determination. In this case, broadening caused by resolution or $v \sin i$, as well as low S/N of the spectra must play a more important role on the determination than the NLTE effects.

In conclusion, with our line mask, developed for the analysis of GIRAFFE HR15N, SME can derive reasonably accurate and precise parameters for stars within the following range: $T_{\text{eff}} = [4000, 5500]$ K, $\log g = [3.5, 4.5]$ dex, $[\text{Fe}/\text{H}] = [-0.5, 0.5]$ dex and $v \sin i = [7, 40]$ km s⁻¹ (if $v \sin i$ is set as free parameter, otherwise the setup can be used for stars with $v \sin i \leq 7$ km s⁻¹).

If we compute the weighted average of the differences between the reference values and the SME results for the SME_A.1, BenS and FGK samples we obtain $\langle \Delta T_{\text{eff}} \rangle = 48$ K, $\langle \Delta \log g \rangle = 0.04$ dex and $\langle \Delta [\text{Fe}/\text{H}] \rangle = 0.02$ dex. The accuracy of our results is comparable

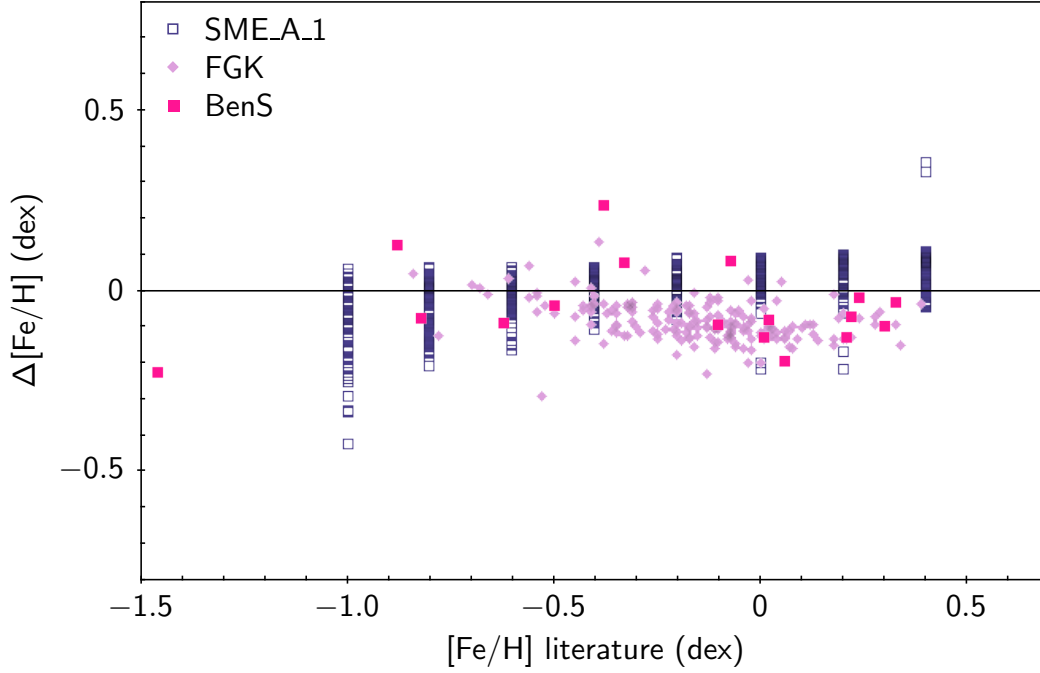


Figure 3.11: Compilation of SME $[\text{Fe}/\text{H}]$ results for SME_A.1, BenS and FGK samples. The plots show the difference between the reference value and the SME results ($\Delta = \text{reference} - \text{SME}$) versus $[\text{Fe}/\text{H}]$ reference values.

to that derived by other methods. In average, the uncertainty in a determination is of ~ 100 K for T_{eff} , ~ 0.2 dex for $[\text{Fe}/\text{H}]$ and ~ 0.5 dex for $\log g$.

3.5 Analysis of wTTS from NGC 2264

3.5.1 SME results

The analysis of the wTTS sample was done with the SME setup described in section 3.3. The parameters were obtained by the analysis of the 20 spectra available for each star. The final results, presented in Table 3.14, are the average of the results and the associated uncertainty is the standard deviation.

In Figures 3.12 and 3.13 we compare our determinations with those available in the literature: Venuti et al. (2014), Bouvier et al. (2016) and Spina et al. (2017). Besides being determined by other methods and codes, the parameters derived from spectroscopy (Bouvier et al. (2016) and Spina et al. (2017)) are from the analysis of spectra with higher S/N, but for each star only one spectrum was available.

In terms of T_{eff} , our results agree the best with those derived from spectroscopy (Bouvier et al., 2016; Spina et al., 2017) (Figure 3.12). There are only few stars for which SME estimated lower values of temperature. On the other hand, our T_{eff} results, as well

Table 3.14: SME results for the wTTS sample.

Star	T_{eff} (K)	$\log g$ (dex)	[Fe/H] (dex)	$v \sin i$ (km s ⁻¹)
223989989	4034 ± 250	3.12 ± 0.40	-1.07 ± 0.27	12.32 ± 1.83
500007458	4496 ± 380	2.96 ± 0.54	-0.78 ± 0.36	21.44 ± 2.24
223985176	4520 ± 206	3.14 ± 0.36	-0.81 ± 0.27	14.60 ± 1.16
223976494	4772 ± 134	3.80 ± 0.18	-0.42 ± 0.09	26.05 ± 1.52
223971984	4266 ± 317	3.27 ± 0.27	-0.77 ± 0.27	26.32 ± 1.88
500007276	4445 ± 121	3.29 ± 0.22	-0.68 ± 0.09	17.11 ± 1.56
223973692	4491 ± 156	3.20 ± 0.40	-0.82 ± 0.13	26.77 ± 3.04
500007330	4260 ± 250	3.43 ± 0.27	-0.78 ± 0.27	21.59 ± 2.15
223972691	4379 ± 206	3.43 ± 0.22	-0.67 ± 0.13	14.48 ± 1.03
223992383	4625 ± 206	3.40 ± 0.45	-0.52 ± 0.18	12.63 ± 1.39
500007366	4108 ± 232	2.90 ± 0.18	-1.31 ± 0.18	26.88 ± 0.98
500007298	4327 ± 85	3.37 ± 0.13	-0.86 ± 0.09	11.04 ± 1.07
223991789	4557 ± 94	3.57 ± 0.18	-0.61 ± 0.09	19.97 ± 1.30
500007248	4602 ± 139	3.70 ± 0.22	-0.38 ± 0.13	10.72 ± 1.39
223988965	4803 ± 179	3.66 ± 0.31	-0.36 ± 0.13	14.23 ± 2.24
223985845	4980 ± 139	3.78 ± 0.40	-0.14 ± 0.13	25.72 ± 0.89
223988742	4827 ± 125	3.75 ± 0.13	-0.24 ± 0.09	20.44 ± 1.65
500007176	4721 ± 112	4.07 ± 0.18	-0.15 ± 0.09	14.84 ± 1.52
223972960	4735 ± 40	3.99 ± 0.04	-0.22 ± 0.04	8.97 ± 0.89
223980989	4528 ± 148	3.75 ± 0.13	-0.40 ± 0.13	22.45 ± 1.25
223982535	5398 ± 80	4.26 ± 0.36	-0.02 ± 0.09	14.63 ± 1.83
223986498	5366 ± 116	4.00 ± 0.22	-0.14 ± 0.09	35.64 ± 0.67
223988099	5383 ± 98	4.10 ± 0.13	-0.13 ± 0.09	17.86 ± 0.40
500007051	5366 ± 80	4.11 ± 0.09	-0.10 ± 0.04	11.34 ± 1.07

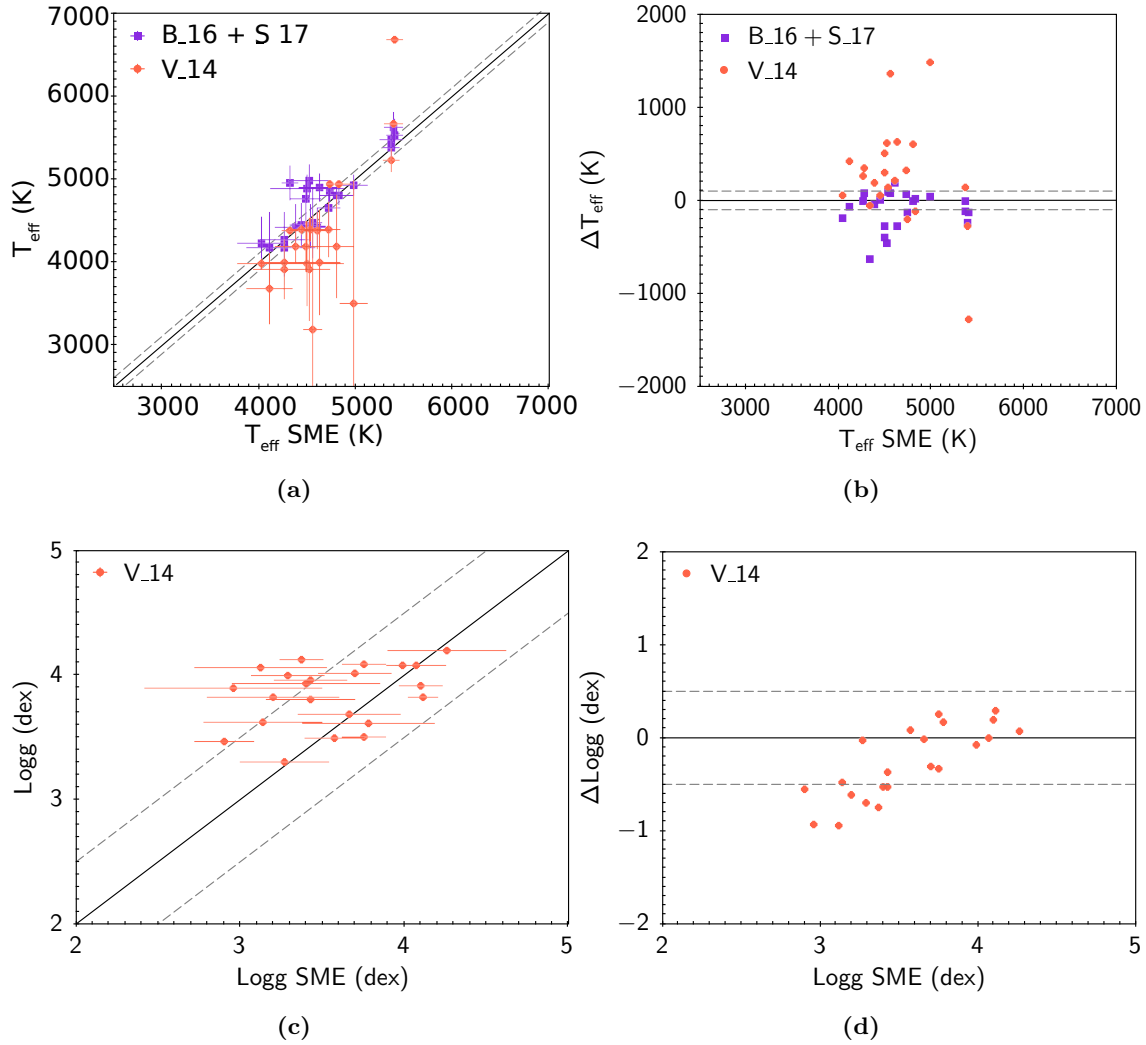


Figure 3.12: SME determinations versus literature values for T_{eff} and $\log g$ ($\Delta = \text{SME} - \text{literature}$). The dashed gray lines indicate the uncertainties obtained from the SME analysis to the test samples: $\sigma(T_{\text{eff}}) = \pm 100$ K and $\sigma(\log g) = \pm 0.5$ dex. The literature results were extracted from Venuti et al. (2014) (V.14), Bouvier et al. (2016) (B.16) and Spina et al. (2017) (S.17).

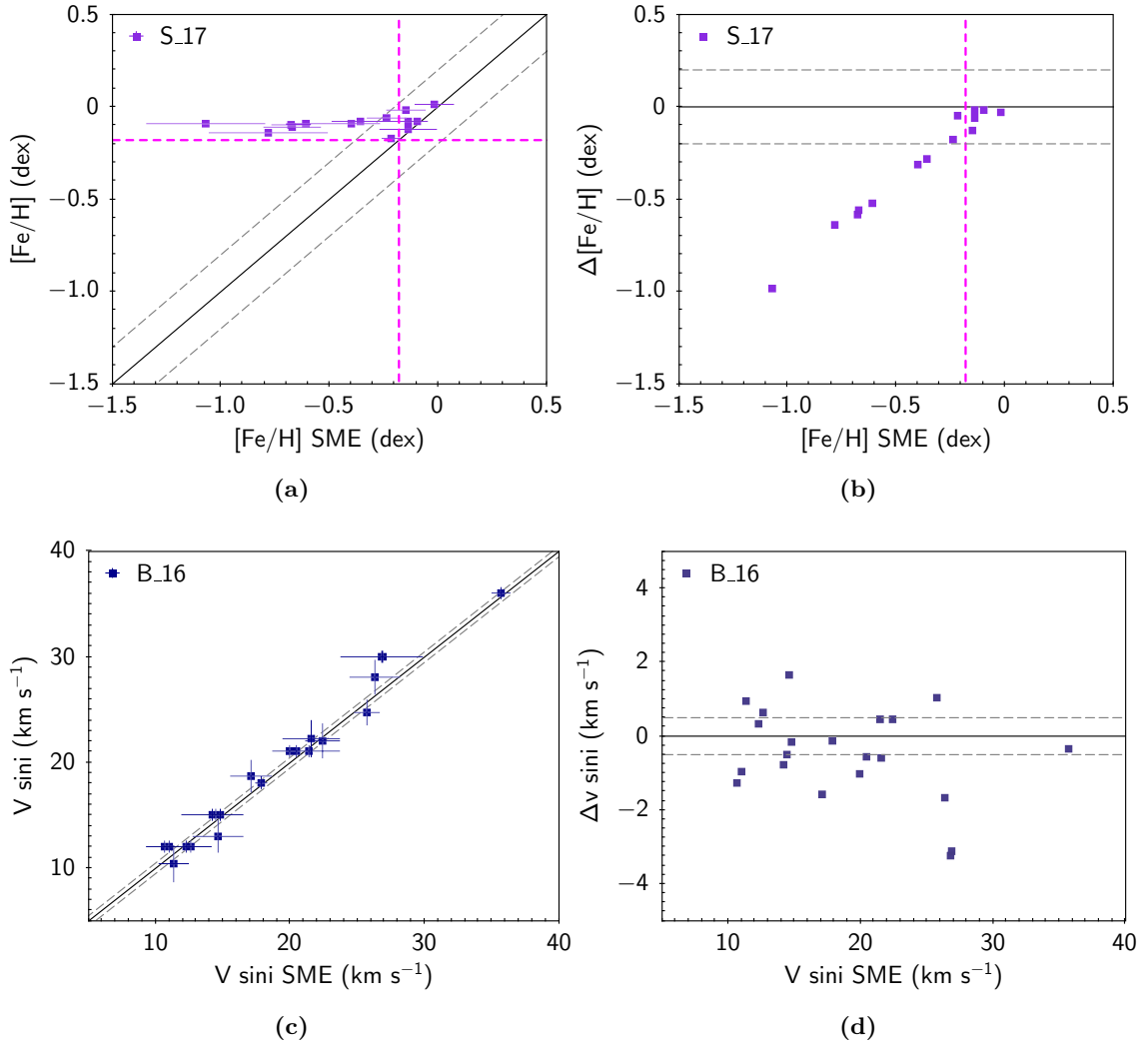


Figure 3.13: SME determinations versus literature values for T_{eff} and $\log g$ ($\Delta = \text{SME} - \text{literature}$). The dashed gray lines indicate the uncertainties obtained from the SME analysis to the test samples: $\sigma([\text{Fe}/\text{H}]) = \pm 0.2$ dex and $\sigma(v \sin i) = \pm 0.5$ km s⁻¹. The dashed pink lines in the [Fe/H] plots indicate the lowest [Fe/H] value found in literature for the NGC 2264 cluster: -0.18 dex (King et al., 2000). The literature results were extracted from Bouvier et al. (2016) (B_16) and Spina et al. (2017) (S_17).

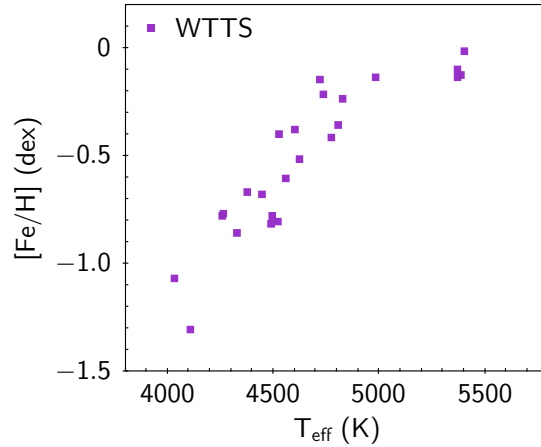


Figure 3.14: WTTS T_{eff} versus $[\text{Fe}/\text{H}]$ SME results. There is a clear correlation between temperature and metallicity derived by SME for the wTTS. The lower the temperature, the lower the value of $[\text{Fe}/\text{H}]$.

as the others derived from spectroscopy, show a poor agreement with parameters derived from photometry data (Venuti et al., 2014). This shows that from photometry we have an underestimation of temperature in relation to the values derived from spectroscopy observations.

However, we only have $\log g$ values derived from the photometry data. The comparison of the SME results with those from Venuti et al. (2014) (Figure 3.12) show a high discrepancy between both determinations. We know *a priori* that $\log g$ is affected by high uncertainties, since the GIRAFFE HR15N wavelength band lacks proper lines to measure this parameter. We do expect a poor $\log g$ determination, but since spectroscopy T_{eff} values also do not agree well with those derived from photometry data, we can not conclude much about our $\log g$ estimates for the wTTS.

Our results for the $v \sin i$ parameter show a good agreement with those from Bouvier et al. (2016) (Figure 3.13). On the other hand, the $[\text{Fe}/\text{H}]$ results that we derived for the wTTS are not what we expected (Figure 3.13). We saw during the tests done to the SME setup with the synthetic spectra and real stars that the $[\text{Fe}/\text{H}]$ parameter had relatively low uncertainties for intermediate resolution spectra (in average inferior to 0.2 dex). Some of the earlier $[\text{Fe}/\text{H}]$ estimations for the NGC 2264 cluster were of -0.15 dex (Barry et al., 1979) and -0.18 dex (King et al., 2000), while some of the latest results bring that metallicity value closer to that of the Sun (Spina et al., 2017): -0.06 dex. So we expected that the average of SME $[\text{Fe}/\text{H}]$ results would be somewhere between 0 and -0.2 dex.

Our SME results are, in fact, very different from these values for more than half of our sample. When we compare our results with those from Spina et al. (2017) we can clearly

see the discrepancy of the results. For several stars, the SME determinations indicate that these stars have $[\text{Fe}/\text{H}]$ values that are much lower than what was supposed ($[\text{Fe}/\text{H}] \leq -0.5$ dex). In fact, there is a clear trend between the T_{eff} and $[\text{Fe}/\text{H}]$, with the stars with lower values of T_{eff} displaying also the lower values of $[\text{Fe}/\text{H}]$ (Figure 3.14). The cause of this effects is unknown, but is it possible that the models do not work well at temperatures lower than 4700 K. We explore some possibilities in section 3.5.6.

3.5.2 The Spectral Indices method results

At the beginning of the analysis of GES GIRAFFE HR15N spectra, Damiani et al. (2014) came up with a method based on spectral indices. This method tries to provide a way to the determination of fundamental stellar parameters for PMS stars observed with the GIRAFFE HR15N setup, based on spectral indicators. It makes use of several young clusters to produce calibrations for the computation of several indices. We followed the instructions described in Damiani et al. (2014) and build an IDL routine with the spectral indices method to analyse our wTTS spectra. The results are the average of the 20 spectra available for each star and the uncertainty is given by the standard deviation. In Table 3.15 we present the results and in Figure 3.15 we plot the spectral indices method versus the SME determinations.

The spectral indices method computes lower values of T_{eff} than those obtained with SME, while the derived values of $\log g$ are very similar to those obtained from photometry data. The $[\text{Fe}/\text{H}]$ results using the spectral indices method still show a high discrepancy of values, but are more in agreement with the values from Spina et al. (2017).

The $[\text{Fe}/\text{H}]$ estimates reported in Spina et al. (2017) work were done by the several GES consortium working groups, which also includes the group using the spectral indices method to derive stellar parameters. It is possible that some, if not all, of the Spina et al. (2017) $[\text{Fe}/\text{H}]$ measurements were done using this method. The differences between our spectral indices results and those from Spina et al. (2017) might result from the fact that we are analysing spectra with different quality and different S/N.

3.5.3 Influence of v_{mic} and v_{mac} on the results

To derive the stellar parameters for the wTTS we fixed v_{mic} and v_{mac} at 0.85 km s^{-1} and 2.8 km s^{-1} , respectively. Although the fixed values are similar to those normally adopted for cool stars and wTTS (e.g. Padgett, 1996; Valenti & Fischer, 2005; Rojas et al., 2008; Taguchi et al., 2009), we tested the impact that different values than the fixed ones would

Table 3.15: WTTS parameters determination using the Spectral Indices method.

Star	T_{eff} (K)	$\log g$ (dex)	[Fe/H] (dex)
223989989	4126 ± 451	4.27 ± 1.07	-0.47 ± 0.31
500007458	4092 ± 224	3.85 ± 0.40	-0.48 ± 0.33
223985176	4109 ± 331	3.59 ± 1.56	-0.32 ± 0.40
223976494	4703 ± 577	4.45 ± 1.48	-0.16 ± 0.25
223971984	4007 ± 335	3.44 ± 1.25	-0.53 ± 0.26
500007276	4294 ± 179	3.94 ± 1.03	-0.32 ± 0.17
223973692	4081 ± 174	3.74 ± 0.45	-0.45 ± 0.89
500007330	4114 ± 179	3.94 ± 0.40	-0.39 ± 0.23
223972691	4252 ± 170	4.01 ± 0.31	-0.33 ± 0.17
223992383	4231 ± 215	3.75 ± 0.54	-0.28 ± 0.26
500007366	4036 ± 156	3.92 ± 0.22	-0.64 ± 0.17
500007298	4355 ± 192	3.92 ± 0.49	-0.59 ± 0.18
223991789	4180 ± 443	3.91 ± 0.58	-0.18 ± 0.17
500007248	4307 ± 161	3.96 ± 0.27	-0.18 ± 0.12
223988965	4273 ± 130	3.91 ± 0.36	-0.21 ± 0.16
223985845	4616 ± 165	4.33 ± 0.31	-0.13 ± 0.08
223988742	4368 ± 255	3.97 ± 0.49	-0.11 ± 0.14
500007176	4427 ± 384	4.24 ± 1.39	-0.03 ± 0.08
223972960	4619 ± 165	4.11 ± 0.31	-0.20 ± 0.12
223980989	4223 ± 54	3.82 ± 0.09	-0.14 ± 0.15
223982535	5239 ± 179	4.13 ± 0.18	-0.12 ± 0.08
223986498	5001 ± 264	3.87 ± 1.43	-0.25 ± 0.27
223988099	4943 ± 130	4.09 ± 0.13	-0.25 ± 0.04
500007051	4950 ± 125	3.92 ± 0.18	-0.22 ± 0.04

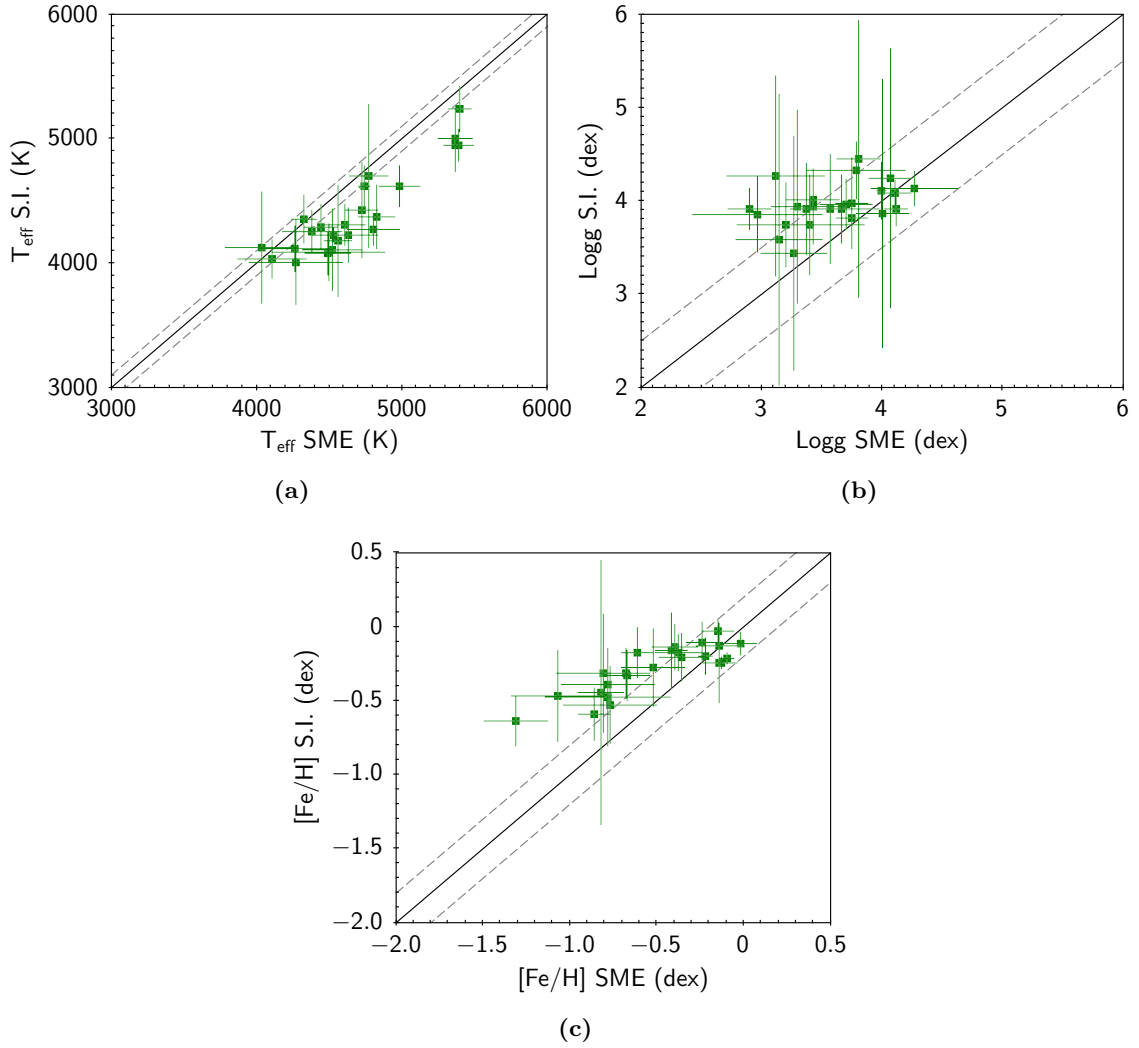


Figure 3.15: Spectral Indices method (SI) results versus SME results for the wTTS for T_{eff} (a), $\log g$ (b) and $[\text{Fe}/\text{H}]$ (c). The dashed gray lines indicate the uncertainties obtained from the SME analysis to the test samples: $\sigma([\text{Fe}/\text{H}]) = \pm 0.2$ dex and $\sigma(v \sin i) = \pm 0.5$ km s $^{-1}$. The dashed pink lines in the $[\text{Fe}/\text{H}]$ plots indicate the lowest $[\text{Fe}/\text{H}]$ value found in literature for the NGC 2264 cluster: -0.18 dex (King et al., 2000).

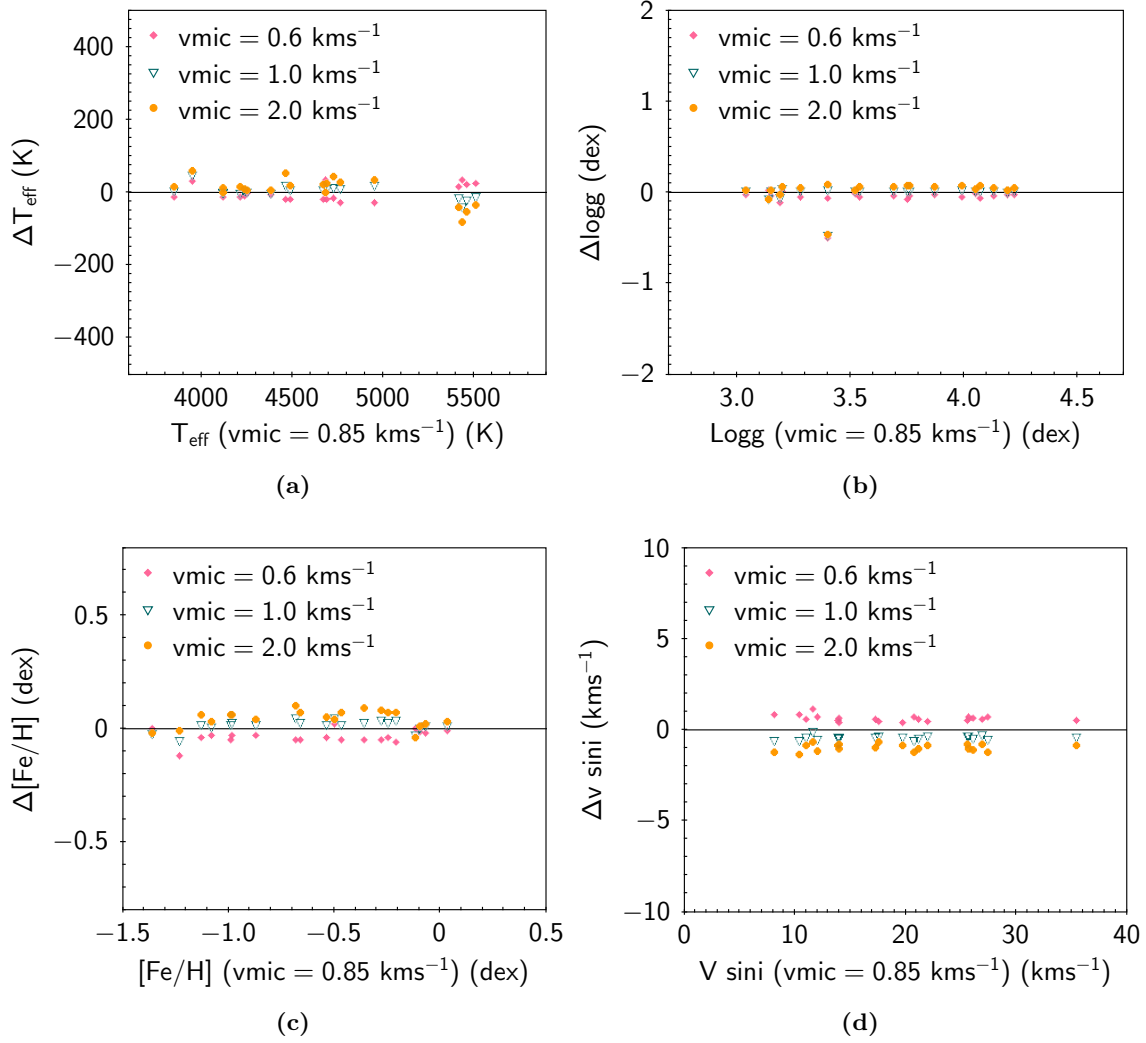


Figure 3.16: SME results for the wTTS with different values of v_{mic} . The plots show the difference between the SME result derived with v_{mic} fixed for 0.85 km s^{-1} and with 3 other values of v_{mic} versus the SME result derived with v_{mic} fixed for 0.85 km s^{-1} for T_{eff} (a), $\log g$ (b), $[\text{Fe}/\text{H}]$ (c) and $v \sin i$ (d).

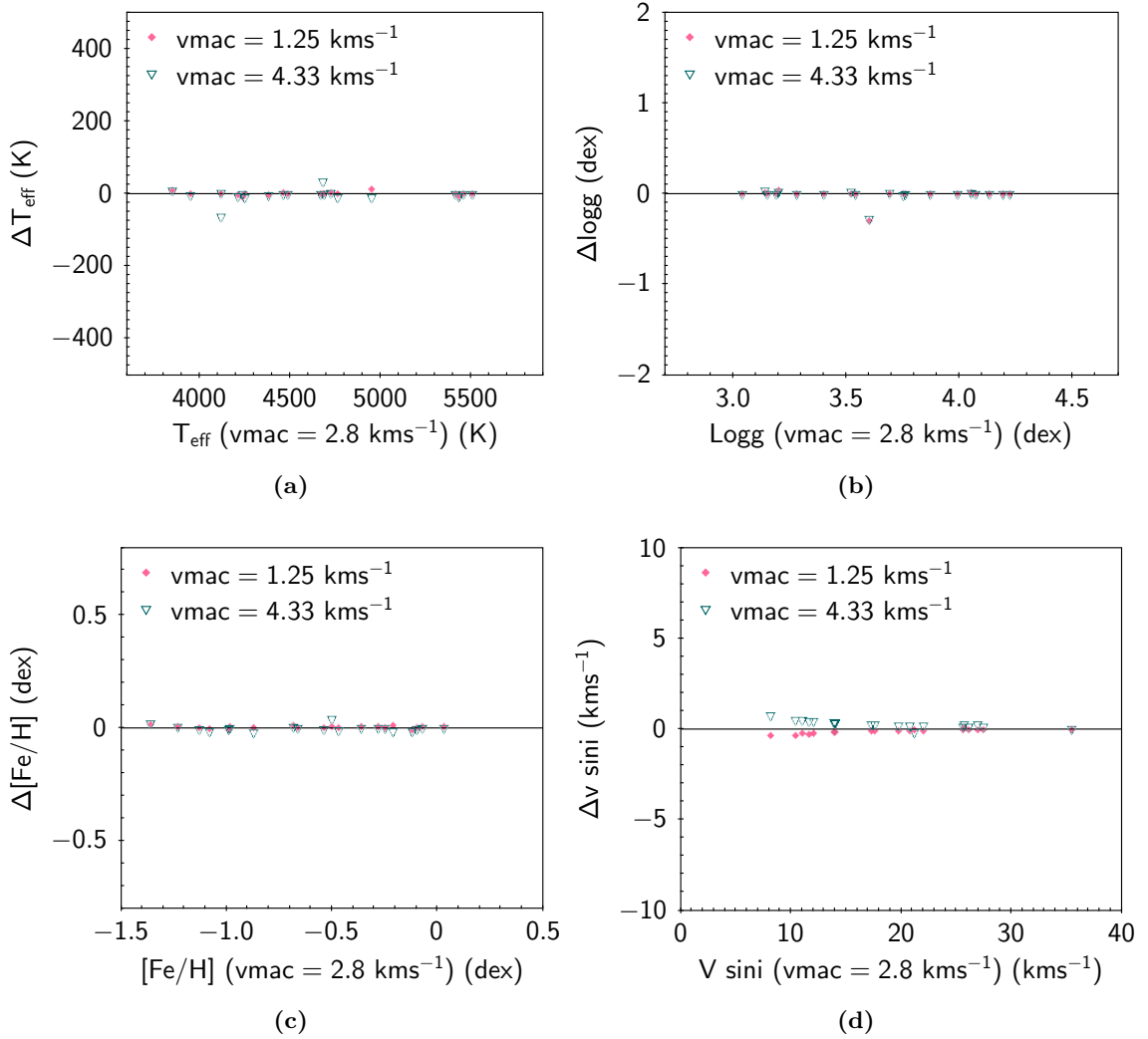


Figure 3.17: SME results for the wTTS with different values of v_{mac} . The plots show the difference between the SME result derived with v_{mac} fixed for 2.8 km s^{-1} and with 3 other values of v_{mac} versus the SME result derived with v_{mac} fixed for 2.8 km s^{-1} for T_{eff} (a), $\log g$ (b), $[\text{Fe}/\text{H}]$ (c) and $v \sin i$ (d).

have in the final parameters determination for the wTTS.

This time we used the median spectra of our wTTS and gave as input different values of v_{mic} and v_{mac} . For v_{mic} we choose to test the values 0.6, 1.0 and 2 km s⁻¹. In this case we are testing a value that is smaller, one that is similar and considered as a typical value for wTTS, and a value that is much higher than the chosen one. As for v_{mac} we chose to test the values associated with the minimum and maximum values of T_{eff} tested in this work: 1.25 km s⁻¹ for 4000 K and 4.33 km s⁻¹ for 6000 K. These values were deduced using equation 1 from Valenti & Fischer (2005).

The results are shown in Figure 3.16 and 3.17. The average difference between results is in general very small if compared with the SME setup uncertainties derived previously. For the case of v_{mac} , the maximum errors obtained if a wrong value of v_{mac} is used are inferior to 20 K for T_{eff} , 0.1 dex for $\log g$, 0.05 dex for [Fe/H] and up to 1 km s⁻¹ for $v \sin i$. For the case of v_{mic} , the error obtained is also small. The maximum errors are inferior to 30 K for T_{eff} , 0.2 dex for $\log g$, 0.1 dex for [Fe/H] and up to 2 km s⁻¹ for $v \sin i$. Nevertheless, our $v \sin i$ results agree well with those of Bouvier et al. (2016). This means, at least, that we are assuming similar values of v_{mic} when determining $v \sin i$.

3.5.4 Mass and age determination

Even though our SME results for the $\log g$ parameter might not be as reliable as the T_{eff} determinations, when compared with others from literature, we used the obtained values of T_{eff} and $\log g$ to roughly estimate mass and age for each star. We made use of a grid of Siess PMS evolutionary tracks (Siess et al., 2000) to obtain an estimate for mass and age⁴ (Table 3.16).

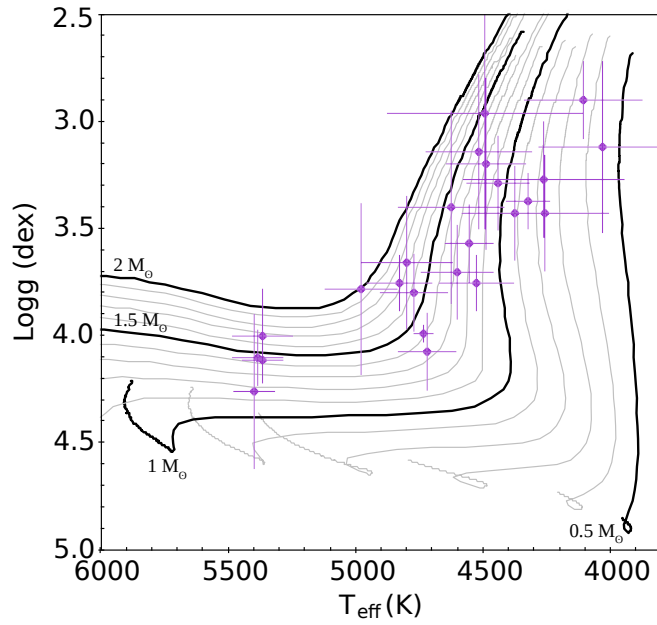
From the two, the determination of age is the parameter most affected by the uncertainties in $\log g$, specially for stars that are still placed along the Hayashi track. In Figure 3.18 we plot the diagram T_{eff} versus $\log g$, with the Siess PMS tracks, from 0.5 to 2 M_{\odot} . Our SME determinations place the wTTS mostly along the Hayashi part of the track, indicating very young stars (≤ 1 Myr) still ongoing gravitational contraction. Also, most of the stars have masses between 1 and 2 M_{\odot} . This is within the expected mass values for the TTS population (e.g. Petrov (2003)).

On the other hand, we are obtaining ages that are lower than the estimated mean

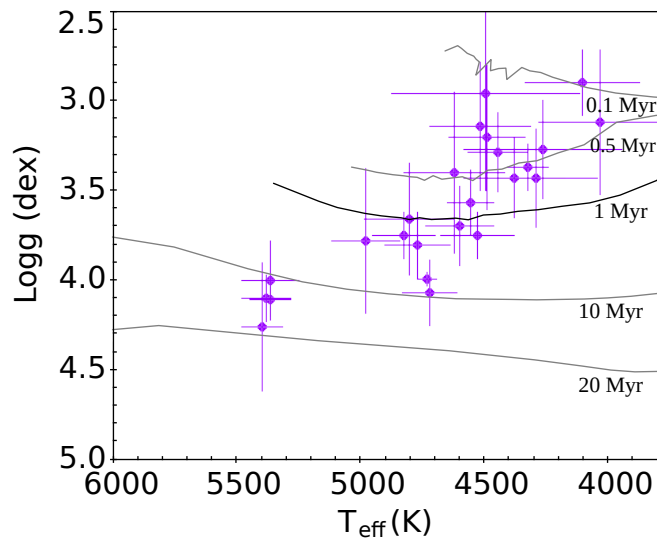
⁴We considered all the tracks with parameters within the error bars of T_{eff} and $\log g$ for each star to estimate the uncertainty in mass and age. The track that passed closer to the location of the star in the T_{eff} vs $\log g$ diagram (Figure 3.18) was chosen and both mass and age were estimated from the point in that tracks that passed closer to the star point.

Table 3.16: WTTS mass and age estimates.

Star	Mass (M_{\odot})	Age (Myrs)
223989989	0.55 ± 0.12	0.44 ± 0.17
500007458	1.40 ± 0.40	0.24 ± 0.12
223985176	1.30 ± 0.32	0.31 ± 0.09
223976494	1.55 ± 0.17	1.10 ± 0.55
223971984	0.80 ± 0.28	0.34 ± 0.12
500007276	1.10 ± 0.16	0.32 ± 0.10
223973692	1.20 ± 0.31	0.33 ± 0.10
500007330	0.75 ± 0.19	0.60 ± 0.21
223972691	0.95 ± 0.20	0.58 ± 0.18
223992383	1.40 ± 0.25	0.50 ± 0.32
500007366	0.65 ± 0.16	0.10 ± 0.13
500007298	0.90 ± 0.07	0.50 ± 0.09
223991789	1.20 ± 0.10	0.92 ± 0.24
500007248	1.30 ± 0.15	1.11 ± 0.44
223988965	1.75 ± 0.21	0.70 ± 0.64
223985845	1.95 ± 0.19	1.46 ± 1.50
223988742	1.70 ± 0.16	1.30 ± 0.34
500007176	1.45 ± 0.11	2.90 ± 1.69
223972960	1.40 ± 0.00	2.90 ± 0.43
223980989	1.15 ± 0.34	1.40 ± 0.32
223982535	1.19 ± 0.13	16.8 ± 0.32
223986498	1.80 ± 0.22	10.2 ± 2.25
223988099	1.30 ± 0.14	13.0 ± 1.80
500007051	1.40 ± 0.13	13.0 ± 2.00



(a)



(b)

Figure 3.18: WTTS placed in T_{eff} versus $\log g$ diagram with Siess PMS evolutionary tracks (Siess et al., 2000) (a) and isochrones (b)). The SME results place the majority of the wTTS along the Hayashi track, indicating that these wTTS are very young stars.

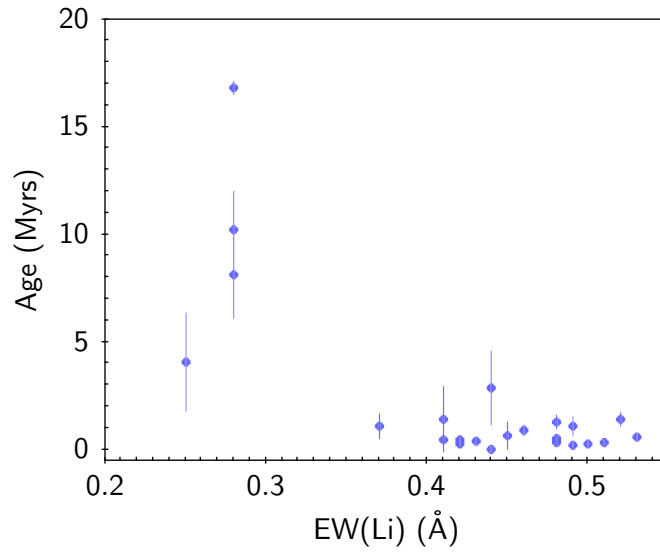


Figure 3.19: EW(Li) versus age for the wTTS sample. Those stars with the higher values of EW(Li) are also the youngest stars.

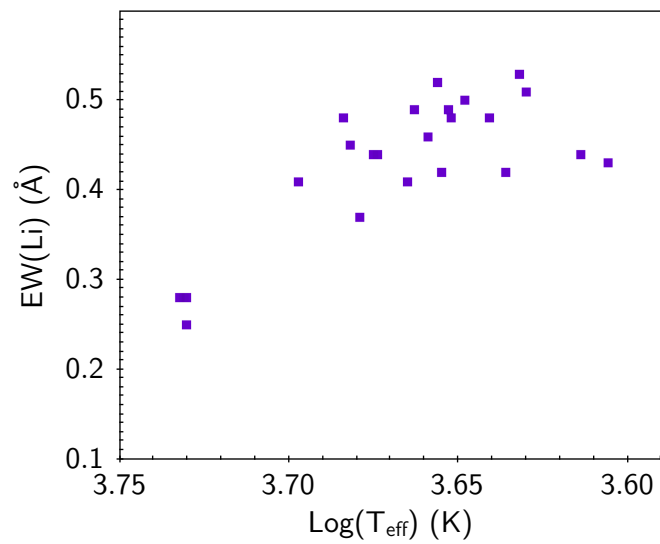


Figure 3.20: T_{eff} versus EW(Li) for the wTTS sample. There is a tendency for stars with the lower values of T_{eff} to also have the higher values of EW(Li).

age of the cluster: 3 Myrs (Dahm & Simon, 2005). If we estimate the median age of our wTTS sample of 24 stars we obtain 0.8 ± 3.4 Myrs, indicating that most stars are very young, but within the average age of the cluster. Again, $\log g$ has a high influence in the age determination, so its high uncertainty also indicates that our age determinations are highly uncertain.

PMS stars are still young and did not had enough time to consume all the lithium content present in the cloud material from which they are forming. It is expected that these stars show a relatively strong lithium abundance. In Figure 3.19 we plot the equivalent width of the lithium line ($EW(\text{Li})$) versus the age estimated for these stars. The stars with the lower values of age have the highest lithium equivalent widths.

The wTTS with the highest equivalent widths of the Li line are also the ones with the lowest values of T_{eff} (Figure 3.20). The plots $EW(\text{Li})$ versus T_{eff} has been widely used to confirm the TTS nature of young stellar objects, by comparison with older objects (e.g. Alcalá et al. (2000)). Figure 3.20 ensures the TTS nature of the wTTS in our sample.

3.5.5 Fixing $[\text{Fe}/\text{H}]$

The determinations of $[\text{Fe}/\text{H}]$ done by the SME setup for the wTTS have been the most challenging issue that we encountered in this work. The intense testing of the SME setup for the analysis of the GIRAFFE HR15N spectra has shown that those results must not be directly associated with our line mask.

After encountering this issue, we decided to fix the $[\text{Fe}/\text{H}]$ parameter, since it is expected that this parameter would be similar for all the analysed wTTS, assuming that the cloud is rather homogeneous. We assumed $[\text{Fe}/\text{H}] = -0.15$ dex (Barry et al., 1979) for the NGC 2264 cluster. This alternate determination of parameters for the wTTS was performed before the recent GES-consortium determinations of $[\text{Fe}/\text{H}]$ for the NGC 2264 cluster (Spina et al., 2017), that indicate a more solar-like metallicity for these stars.

With $[\text{Fe}/\text{H}]$ fixed, we used our SME setup to compute T_{eff} , $\log g$ and $v \sin i$ for our sample. The results are plotted in Figure 3.21. While both $\log g$ and $v \sin i$ parameters do not change significantly from the values derived with the original setup, the same is not true for the T_{eff} parameter. If we keep $[\text{Fe}/\text{H}]$ fixed to -0.15 dex, the derived values of T_{eff} are all above 4500 K. In a diagram T_{eff} versus $\log g$ (Figure 3.22) we can see that fixing $[\text{Fe}/\text{H}]$ significantly influences the mass and age of these stars, since it is clear that the T_{eff} determination is influenced by the $[\text{Fe}/\text{H}]$ determination. In some cases these stars are no longer TTS, but rather young intermediate-mass stars, with masses above $2 M_{\odot}$.

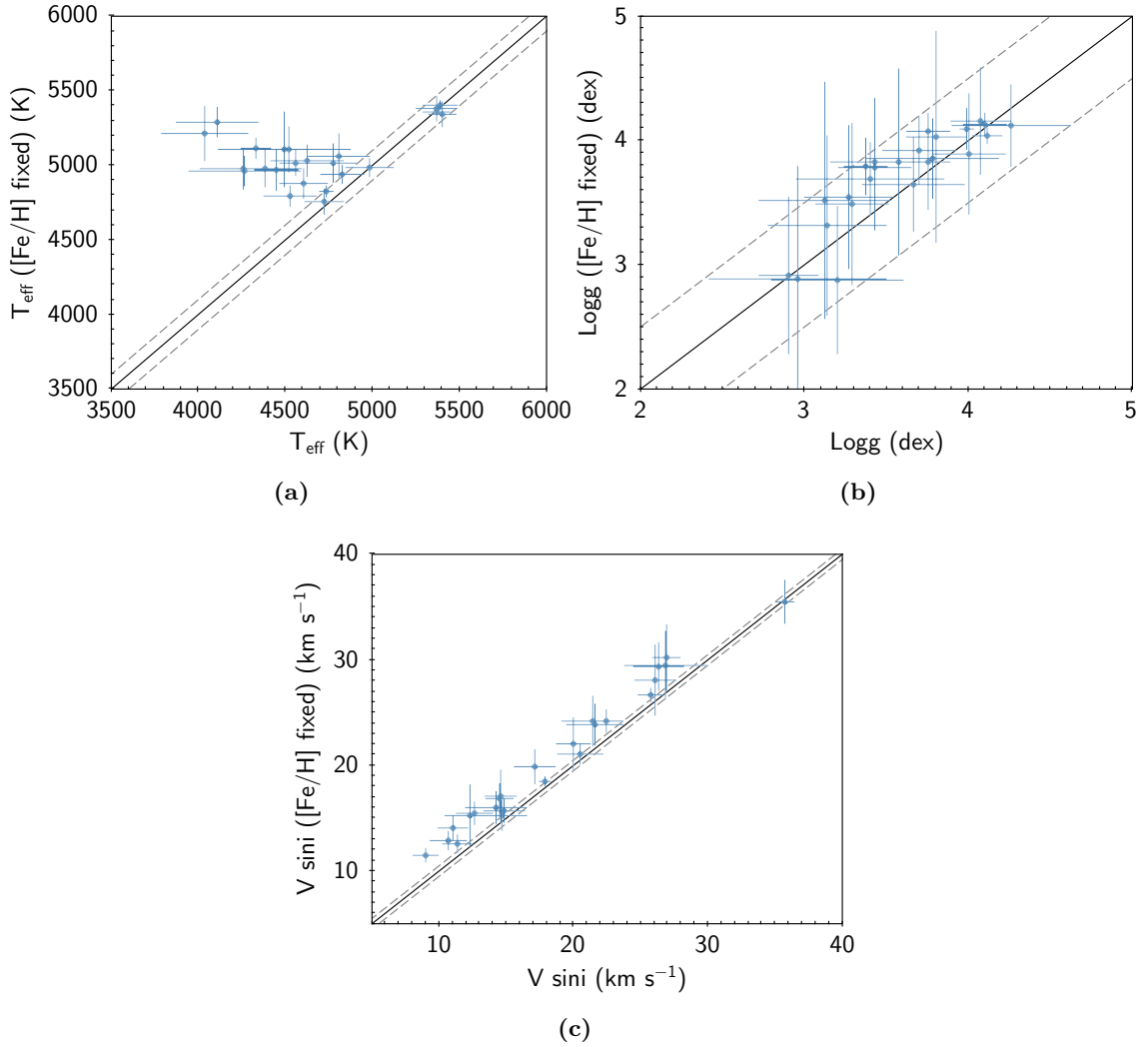


Figure 3.21: SME results for T_{eff} (a), $\log g$ (b) and $v \sin i$ (c), while fixing the $[\text{Fe}/\text{H}]$ parameter to the value -0.15 dex during the parameters computation. The dashed gray lines indicate the uncertainties obtained from the SME analysis to the test samples: $\sigma(T_{\text{eff}}) = \pm 100$ K, $\sigma(\log g) = \pm 0.5$ dex and $\sigma(v \sin i) = \pm 0.5$ km s^{-1} .

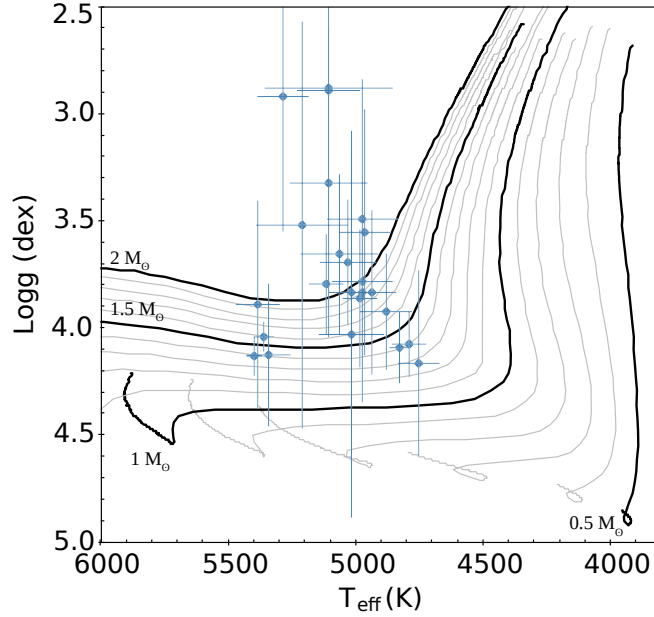


Figure 3.22: WTTS placed in T_{eff} versus $\log g$ diagram with Siess PMS evolutionary tracks (Siess et al., 2000). In this case $[\text{Fe}/\text{H}]$ was kept as a fixed parameter ($[\text{Fe}/\text{H}] = -0.15$ dex) while computing T_{eff} , $\log g$ and $v \sin i$ with SME. It is noticeable the differences in terms of mass estimation for these stars. By fixing $[\text{Fe}/\text{H}]$, SME results for T_{eff} implies that some of the stars are in fact intermediate to high mass young stars.

We saw previously that our results for T_{eff} (derived with $[\text{Fe}/\text{H}]$ as a free parameter) do agree reasonably well with those derived from spectroscopy by Bouvier et al. (2016) and Spina et al. (2017). So fixing the metallicity of these stars to a same value, while using our SME setup, introduces a major error in the determination of temperature.

3.5.6 WTTS metallicity issue

We were not able to solve the $[\text{Fe}/\text{H}]$ underestimation by fixing this parameter while computing T_{eff} , $\log g$ and $v \sin i$. At the same time the several tests performed to our SME setup do not indicate any problem with the $[\text{Fe}/\text{H}]$ determination for both real (MS stars) and synthetic spectra.

The stars with the lower values of T_{eff} are also the ones showing the most discrepant values of $[\text{Fe}/\text{H}]$. It is clear that there is an inter-dependency between T_{eff} and $[\text{Fe}/\text{H}]$, that is probably more notorious since the lines used in our line mask are more sensitive to T_{eff} and not so sensitive to $\log g$.

The stars with the lower values of $[\text{Fe}/\text{H}]$ are also the ones with the highest values of equivalent width of the $\text{H}\alpha$ line. For those stars with $\text{H}\alpha$ line in emission it is possible that a higher value of $\text{EW}(\text{H}\alpha)$ indicates some chromospheric activity or even some accretion

with low accretion rates. At the same time, the $H\alpha$ line in emission can be residual nebular emission. Sadly, for the GIRAFFE HR15N wavelength band the $H\alpha$ line is the only activity indicator that we have available and so it is not possible to further explore this matter.

A stronger possibility for the cause of this issue is the line list used in our analysis. As pointed out by Tsantaki et al. (2018), even the calibration done to the atomic data using the Sun's spectrum may introduce uncertainties in the determination of parameters, if the stars have parameters too different from the Sun. Although these stars can be considered solar-type stars, it is for the ones with T_{eff} values further from that of the Sun that the $[\text{Fe}/\text{H}]$ values are more discrepant. Besides, these stars are not MS stars. The empirical corrections done to the line lists try to minimize the differences between the real stars and the theoretical atmospheric models, that are made for MS stars. The combination of inadequate atmospheric models and inadequate line list and atomic data calibration for the PMS stars can be the reason for which we obtain such values of $[\text{Fe}/\text{H}]$.

3.5.7 NGC 2264 cluster metallicity

The metallicity of the NGC 2264 cluster is still under debate. Early high resolution spectroscopy studies of small samples of selected stars estimated a cluster metallicity of -0.15 dex (Barry et al., 1979) and -0.18 ± 0.09 dex (King et al., 2000). More recently, the GES consortium estimated a solar-like metallicity for this cluster: -0.060 ± 0.006 dex from both GIRAFFE and UVES observations (Spina et al., 2017). From our sample of 24 wTTS we estimate an average value for the metallicity of -0.51 ± 0.34 dex.

3.6 Discussion

The aim of this work was the determination of fundamental stellar parameters, mainly T_{eff} , $\log g$, $[\text{Fe}/\text{H}]$ and $v \sin i$, for a small sample of wTTS. The spectra was obtained with the VLT/GIRAFFE spectrograph in the multi-mode Medusa and are of intermediate resolution ($R \sim 17000$). The observational setup, the HR15N, produces narrow wavelength spectra between around 6450 and 6820 Å. This wavelength range is of special importance for the identification and classification of TTS, due to the presence of the $H\alpha$ line and Li line at 6708 Å, but lacks proper photospheric lines for the accurate stellar parameters determination.

We decided to use the spectral synthesis method to analyse the wTTS spectral sample.

3.6.1 The method

One of the advantages of SME is its adaptability to almost any spectral resolution, so that it can be used to analyse the GIRAFFE HR15N spectra. Although this type of method requires an indication for a starting point of each computation (initial guess parameters), it is possible to use it to analyse large samples of unknown stars in a rather homogeneous way.

We started our work by defining wavelength intervals with well defined line profiles, mainly of iron lines, as well as by defining the variable and fixed parameters while using SME. After that, we executed several tests with both synthetic spectra and real stars spectra (benchmark stars and a sample of MS FGK stars). One of the major advantages of using synthetic spectra is the fact that all parameters are rigorously controlled. Instead, real stars only have an estimation for their stellar parameters and their spectra can be affected by activity or other spectral peculiarities that are difficult to control and identify.

For the analysis of the synthetic spectra we created a grid of spectra with SME, using the same line list used in the computation of the parameters (sample SME_A). This line list was extracted from VALD, for a temperature of 5770 K and $\log g = 4.44$ dex, and the $\log gf$ and van der Waals damping parameters of the lines (analysed in our work) were corrected, using a high resolution spectrum of the Sun. This correction improves mainly the determination of $\log g$ and $[\text{Fe}/\text{H}]$.

The analysis of the SME_A sample revealed a problem with the determination of T_{eff} for the spectra with values of temperature below 5000 K. We concluded that the observed underestimation, of around 70 K, was due to the fact that we are using a line list extracted for 5770 K while creating these synthetic spectra with SME. SME_B sample unveiled the origin of that underestimation, at the same time showing the importance of the $\log gf$ and van der Waals damping parameters correction for the $\log g$ and $[\text{Fe}/\text{H}]$ determination. Since neither benchmark stars nor FGK stars have shown any problem of the sort, we decided to use the SME_A sample results to constrain both accuracy and precision of our method.

As for the real stars we were able to derive stellar parameters values with similar accuracy and precision as other works. In general, the results of our testing allows the determination of T_{eff} , $\log g$, $[\text{Fe}/\text{H}]$ and $v \sin i$ for stars within the range: $T_{\text{eff}} = [4000, 6000]$ K, $\log g = [3.0, 4.5]$ dex, $[\text{Fe}/\text{H}] = [-1.0, +0.5]$ dex and for stars with $v \sin i \geq 7$ km s⁻¹, up to 40 km s⁻¹. For stars with $v \sin i \leq 7$ km s⁻¹ it is recommended to fix this parameter to a certain value, between 1 to 5/6 km s⁻¹, and compute only T_{eff} , $\log g$ and

[Fe/H]. This recommendation is due to the spectral resolution limitations of the GIRAFFE spectra (Frasca et al., 2015).

Our estimates for the accuracy and precision of the method are comparable to those derived by Lanzafame et al. (2015) for the GES GIRAFFE spectra, while using other methods, as well as those from Blanco-Cuaresma et al. (2014) and Smiljanic et al. (2014).

From the four parameters, $\log g$ is the one with the least reliable results, as expected from the lack of photospheric lines, mainly of ionized states. Also, the higher dispersion observed are for the values closer to the SME setup limitations. When using this methodology we recommend a minimum S/N of 50 for the GIRAFFE spectra, in order to get enough accuracy and precision of the results.

Uncertainties of T_{eff} and $\log g$ parameters can translate into high uncertainties regarding the age and mass of the wTTS. It is important to have this in mind when using this SME setup results for the estimation of mass and age. This was clearly seen in Figures 3.18 and 3.22, where we place our results with and without [Fe/H] fixed in a T_{eff} versus $\log g$ diagram. Just by constraining one parameter to a certain value we are dramatically affecting others. In this case, fixing [Fe/H] is altering the values of T_{eff} in a way that some stars fall into a mass range that exclude them from the TTS category.

3.6.2 NGC 2264 wTTS

From a sample of around 160 stars (including TTS, other PMS stars and MS stars) observed in two fields, we selected 24 wTTS. The selected stars obey the criteria defined by White & Basri (2003), for the empirical classification of TTS into wTTS and cTTS. Only wTTS with S/N above 30 were used in this work. Below this value there is a significant decrease of accuracy and precision in the determination of stellar parameters. Besides, we were also faced with computational difficulties for the spectra with the lowest S/N. In some cases the program was not able to finish the computation of parameters.

The SME intervals used in the analysis were chosen in order to avoid spectral peculiarities found in these spectra, like the H α line in emission, the Li line in absorption and residual nebular emission. Since the stars in our sample show rotation at relatively high speeds (above 10 km s $^{-1}$), we also restricted our lines choice to those lines profiles that were relatively isolated.

Measurements of the radial velocity for our sample of 24 wTTS are consistent with the values measured for the NGC 2264 cluster members by Jackson et al. (2015). Although the v_{rad} values are not the same for all sample members, we are positive that all the

analysed stars belong to the NGC 2264 cluster and are not field stars. This argument is reinforced by the fact that all stars have equivalent widths of the Li line (at 6708 Å) above 100 mÅ (Bertout, 1989)⁵, indicating that these stars are young.

Five of our wTTS have H α line in absorption, while the rest of the sample have the H α line in emission. The highest equivalent width of the H α line does not exceed 4 Å. Also, the largest width at 10% peak of the H α line does not exceed 140 km s⁻¹. These two factors together confirm the wTTS classification of the stars in our sample, according to White & Basri (2003). An analysis of the H α variance, using the information provided by the 20 spectra of each star, does not show significant variability of this line during the course of two months.

The obtained results by SME for the wTTS challenged us with an enigma: the results for the [Fe/H] parameter are far from what we expected. On the other hand, both our T_{eff} and $v \sin i$ results agree within the errors with the recent works of Bouvier et al. (2016) and Spina et al. (2017).

From the literature, we only have $\log g$ values derived from photometry data (Venuti et al., 2014) to compare with our results. At the same time, we can also compare the SME determinations with those derived by the Spectral Indices method, when applied to our spectra. Since the determination of T_{eff} done from spectroscopy does not agree well with the photometry derived values of T_{eff} , it is possible that the $\log g$ values derived from photometry data might not be accurate. Nevertheless, we do not expect our $\log g$ results to be enough accurate and precise either, as explained before. But even with a high error we can get an idea about the age and mass of the wTTS in our sample.

The T_{eff} results indicate that these stars have spectral classes between late G and early M, being mostly K type stars, and masses that do not exceed 2 M_{\odot} .

A pronounced underestimation of [Fe/H] is observed for the stars with lower values of T_{eff} . These stars are also the ones with the higher values of equivalent widths of the H α line. There seems to be a clear inter-dependency between T_{eff} and [Fe/H]. Since all these stars are forming from the same cloud material and assuming cloud homogeneity, we expected that, apart from few exceptions, our [Fe/H] results would be similar for the vast majority of the stars and similar to the values previously estimated by Barry et al. (1979), King et al. (2000) and Spina et al. (2017). In fact, only 9 wTTS have [Fe/H] above -0.3 dex, that is the lowest value reported for [Fe/H] for the NGC 2264 cluster in Spina et al. (2017). This corresponds to around one third of our wTTS sample. The other 15

⁵Although this depends on spectral type and might not be true for most massive stars.

stars have values determined by SME below -0.3 dex, down to -1.31 dex. These stars also show lower values of $\log g$, between 2.9 and 3.75 dex, leading to the estimation of much younger ages for these wTTS.

We decided to fix the only parameter from the four for which we can have a more confident guess: $[\text{Fe}/\text{H}]$. This parameter is the one that should be similar for the majority of the wTTS in our sample. Then we obtained T_{eff} , $\log g$ and $v \sin i$, using the same value SME setup, but keeping $[\text{Fe}/\text{H}]$ fixed to the value -0.15 dex. Although there is a small change in $\log g$ towards higher values, the T_{eff} values are dramatically affected, with SME determining temperatures above 4700 K for all stars. This corresponds to a drastic change in mass and age for the stars, even tossing out some stars from the TTS classification. But we saw before that our T_{eff} values, with $[\text{Fe}/\text{H}]$ set as a free parameter (the original setup), were in accordance with those from the most recent works. This small test also shows how fixing a parameter can severely influence the results, mainly if the parameters show inter-dependency.

It is possible that both line list and empirical calibration done to the atomic data are not the best for the wTTS. Together with the used atmospheric models, that are for MS stars, might cause the strong underestimation of $[\text{Fe}/\text{H}]$, that might also be affecting the $\log g$ determinations and hence the age estimates.

Observations in other wavelength bands and with higher resolution and S/N are required to understand why we are not able to use the spectral synthesis method to properly determine $[\text{Fe}/\text{H}]$ and $\log g$ for these wTTS.

Chapter 4

Conclusion

When life on Earth first appeared, the closest star to our planet, the Sun, was already there, shining in the sky, day after day. When the human race started studying the Sun, one thing was certain: that brilliant sphere in the sky is the most reliable thing in our existence. But how did it first appear? Was the Sun always there? Are stars eternal?

Although this first paragraph looks more like one from a novel, the truth is that few centuries ago, philosophers of the nature made those same questions. It was human curiosity and creativity that led us to the knowledge that we have today. Now we know that stars, like any biological being in the planet, also have a life cycle: they form in giant molecular clouds, live and die. But the way a star is born is also determinant for the existence of life as we know it.

In the end, our Sun is just an ordinary low-mass star and we are here because of that. For the stars, being ordinary also means having a long and relatively quiet life. This stability is fundamental for life. Since we are not able to do time traveling (yet!), we are only able to know how our solar system formed if we observe and study how stars like the Sun are formed. Luckily for us, low-mass star formation is very common in any star forming region. The study of T Tauri stars is the key to unlock the secrets of our solar system formation.

At the same time, T Tauri stars themselves are amazing objects, since they show different ranges of activity, due to the interaction between star and disk. The degree of activity marks the distinction between classical T Tauri stars and weak-line T Tauri stars. In this work, we studied different topics of both T Tauri stars flavours.

4.1 Activity: classical T Tauri Stars

Our studies on the activity were focused on one key feature of cTTS that distinguishes these stars from MS stars: the excess of continuum emission. At first, it was believed

that the veiling was only caused by the hot spot region at the base of the accretion column, where the material coming from the disk hits the stellar atmosphere. This region radiates high energy continuum emission that superposes that of the stellar photosphere. As a result, the photospheric lines become shallower, some even disappear, making the determination of fundamental stellar parameters for these stars a very hard task.

Recent studies, like those from Sicilia-Aguilar et al. (2015) and Gahm et al. (2008) have shown that the observed veiling might have other sources of radiation contributing with extra emission to the total veiling.

These sources do seem to produce radiation that only affects some lines. This line-dependent emission filling-in the photospheric lines is believed to be related with both broad emission, radiated from the in-falling gas at the pre-shock region, and narrow emission, radiated from the post-shock region. Recently, Petrov et al. (2011, 2014) have shown that in the case of stars with high mass accretion rates, the line-dependent veiling correlated with line strength of the template. In these stars, no narrow emission peaks inside absorption lines are observed, and photospheric lines are observed at the top of the broad emission lines (these lines do seem to be optically thin or might have origin at the disk wind). So the observed veiling must have another origin.

To further unveil the origin of this line-dependent veiling we analysed three stars with P-Cygni profiles in the Balmer lines. Powerful mass-loss processes do seem to be connected to high mass accretion rates, making LkH α 321, AS 353A and V1331 Cyg excellent case studies. For all three stars, the equivalent widths of the several photospheric lines were measured and compared with those of appropriated synthetic templates. We obtained the same result for the three stars: the veiling is higher for the lines with higher equivalent widths on the template. In the case of V1331 Cyg, we were able to reproduce the results from Petrov et al. (2014), and this star is also the one for which the dependency of veiling on line strength is stronger.

We estimated high mass accretion rates for these stars, which are in accordance with the indications of powerful mass-loss processes. We also estimated the veiling continuum from weak lines. Interestingly, the veiling continuum for the three stars is low (veiling factor inferior to 1), showing that in these cases the veiling continuum contribution for the observed veiling is very small.

During the measurement of the equivalent widths of the photospheric lines we did not notice any narrow emission core. Also, the photospheric lines can be easily observed on top of the broad emission lines, affected by the veiling in the same way as those at continuum level. This shows that the veiling in these stars have other origin than the hot

spot, pre and post-shock regions. Petrov et al. (2011, 2014) advanced with the possibility of an enhanced chromosphere due to the accretion processes. Since stronger lines are formed at the top layers of the stellar atmosphere, they should also be more affected by the accretion phenomenon.

In fact, for stars with high mass accretion rates, the emitted radiation at the shock region must affect the star's atmosphere at a much more extended region than what is predicted by the simple magnetospheric accretion models. The involved energies might cause changes in the structure of the stellar atmosphere, like creating an enhanced chromosphere, that can lead to the production of emission lines from a larger atmospheric extension.

Weaker lines, formed deeper in the stellar atmosphere, are least affected by the accretion and so do not display the same decrease of line strength. Veiling observed in weak lines must be only due to the veiling continuum.

The optical veiling continuum is extensively used in the literature as a way to estimate the mass accretion rates. If other sources of veiling are not taken into account when measuring the veiling in a cTTS spectrum, we might be overestimating the mass accretion rates. This alone can have implications on modelling the mass-accretion.

4.2 Evolution: weak-line T Tauri Stars

The study of wTTS is important for several reasons. One of this reasons is the comprehension of the star-disk system evolution and the relationship between wTTS and cTTS. And to do this we must have, as accurate as possible, information about their fundamental stellar parameters, like T_{eff} , $\log g$, $v \sin i$ and $[\text{Fe}/\text{H}]$, in order to get a good estimate of mass and age.

NGC 2264 is one of the star forming regions being observed in the context of the Gaia-ESO Survey. Millions of young stars are being observed with the VLT/GIRAFFE spectrograph, with the multi-mode MEDUSA in the configuration HR15N. This setup produces spectra with intermediate resolution in a narrow wavelength region, that includes the $\text{H}\alpha$ line and the Li line at 6708 Å. Though this region is crucial for the identification of young low-mass stars and distinguish the wTTS from cTTS, it is not the best for fundamental stellar parameters determination, since it lacks enough lines to accurately determine these parameters. There are only few methods being used for the analysis of these spectra and in this thesis we present an alternative method, via adaptation of an already existing tool used for the analysis of MS stars spectra: Spectroscopy Made Easy.

From a sample of more than 150 stars from NGC 2264, observed with GIRAFFE spectrograph to complement COROT observations, we selected 24 stars that obey the criteria to be a wTTS, as described in Chapter 3.

The methodology, used to determined T_{eff} , $\log g$, $[\text{Fe}/\text{H}]$ and $v \sin i$ for the selected sample, was able to produce results for T_{eff} and $v \sin i$ similar to those already derived in the literature. On the other hand, the expected results for the $[\text{Fe}/\text{H}]$ results were not obtained. Instead, only for few stars, mainly those with $\text{H}\alpha$ line not in emission, we were able to obtain $[\text{Fe}/\text{H}]$ values within the expected values for the NGC 2264 cluster. Those wTTS with $\text{H}\alpha$ in emission and lower values of T_{eff} have shown an underestimation of $[\text{Fe}/\text{H}]$, that is lower for the stars with higher values of equivalent width of the $\text{H}\alpha$ line, as well as lower values of T_{eff} . Even though we performed several tests to our methodology, we did not come to a conclusion regarding the cause of the observed underestimation of $[\text{Fe}/\text{H}]$ for the wTTS.

Both T_{eff} and $\log g$ are relevant parameters to estimate mass and age for these stars. While the error obtained on the mass determination is not as large as the one on the age, we can still see that these stars are very young, with some still ongoing contraction.

In the end, the intermediate-resolution and wavelength range of the GIRAFFE HR15N spectra lacks photospheric lines appropriated for accurate $[\text{Fe}/\text{H}]$ and $\log g$ determinations.

4.3 Activity is linked to evolution

Although both works developed in this thesis might seem disconnected, they are not. Methodologies are very different between both, as well as each goal. But while both are fundamental for the general understanding of TTS, they are also necessary to each other.

Studies related with the activity on cTTS are fundamental to unveil how the mass-accretion and mass-loss processes are regulated. They are also important for our comprehension about the changes that accretion produces on the star. But veiling, as well as emission lines, makes the estimation of stellar parameters, like T_{eff} , $\log g$ and $[\text{Fe}/\text{H}]$, extremely difficult. So we need to use templates to the spectral types of these stars, by comparison of weak-lines ratios between template and star.

Both MS stars, sub-giant stars and even synthetic spectra can be used as templates. But none is as adequate as the spectrum of a diskless young star, formed from the same star forming cloud as the cTTS, and whose physical parameters can be measured with reasonable accuracy. This is one of the reasons that makes the determination of fundamental stellar parameters of wTTS so important. In a same star forming region they share

similar growing conditions and must be formed with similar metallic content. WTTS also exist in different sets of T_{eff} and $\log g$, so if a grid of wTTS spectra is available, they can be easily used as templates for most cTTS with spectral types earlier than M (for later types than K7 is difficult to accurately estimate fundamental stellar parameters with more traditional methods due to the increasing presence of molecular lines in the spectrum).

The construction of this type of grid is now possible, with all the data that is being released by the Gaia-ESO Survey. Most of the young low-mass stars are being observed for the first time. Fundamental stellar parameters are being obtained for hundreds of wTTS in several star forming regions. But while the available methods are able to determine the stellar parameters with high accuracy for high resolution spectra, the stars with intermediate resolution spectra might have their parameters determination affected by higher uncertainties. The main problem is the GIRAFFE HR15N observation band: necessary to confirm the youth of a star and differentiate between cTTS and wTTS, but not adequate to determine fundamental stellar parameters, in particular $\log g$. Spectra in other wavelength regions are necessary to accurate determinations of atmospheric stellar parameters.

Nevertheless, for the analysis of cTTS the most relevant atmospheric parameter is T_{eff} , that is necessary for the spectral type classification. So, despite our problems with the determination of $\log g$ and $[\text{Fe}/\text{H}]$ for our sample of wTTS from NGC 2264, our methodology, described in Chapter 3, can be of great use to derive T_{eff} and $v \sin i$ for hundreds of wTTS in several star forming regions. Those wTTS spectra can then form a nice grid of template spectra for cTTS forming from the same material.

4.4 Questions answered?

In the introduction we pointed out questions that we wanted to try to provide answers:

- How does the accretion process affect the stellar atmosphere?
- What information about the PMS evolution can wTTS give us? Can we improve the cTTS studies from wTTS spectral analysis?

We were not really able to provide any definite answer to each question. Instead we opened up the door to more questions than the ones previously asked. With the analysis of LkH α 321, AS 353 A and V1331 Cyg we were able to show that the accretion process does seem to affect the atmosphere of a star at a larger and in a more complex way than what the simple hot spot, pre- and post-shock regions model predicts. In more active star-disk

systems there seems to be other sources of veiling with higher contributions to the total veiling than the veiling continuum. But, up to what extension does the accretion process affect the stellar atmosphere? How does it alter the atmosphere structure? How does the accretion column interact with the stellar magnetic fields in the stellar atmosphere and what implications does it have to our determinations of mass-accretion rates and filling factors?

At the same time, today we believe that wTTS are the evolution of cTTS, no longer accreting from the circumstellar disk. But while some studies indicate that wTTS are slightly older than cTTS, they still coexist for the same masses and ages, being placed at the same locations in the H-R diagram as cTTS. So the study of wTTS alone is very important to constrain the star-disk evolution. The relationship between stellar and activity parameters is important to understand the dichotomy cTTS/wTTS.

4.5 What lies in the future?

Regarding the study about the veiling nature there is still a long way to go. In the next steps we must analyse the spectra of other high mass accretion cTTS and see if we can obtain similar results to LkH α 321, AS 353A and V1331 Cyg. Then, it is important to see what are the limits (lower) of the line-dependent veiling, with extended studies to more moderate cTTS. High resolution multi-wavelength spectra is the best to perform these, since it is important to see the behavior of the observed veiling with wavelength. It would also be interesting to have time-series observations of these active objects, so that we could study the time variability of the line-depending veiling, as well as its direct relationship with mass-accretion rate variations.

On the wTTS side, it would be important to clarify this sample [Fe/H] issues, with the analysis of observations of these stars in other wavelength regions using the same methodology. That way we could clarify if the problem may lie with the lines available in the GIRAFFE HR15N setup, with the line list used or with other reasons.

Bibliography

- Abramenko, V. I. 2008, *Solar Physics Research Trends*, Edited by Pingzhi Wang. ISBN 1-60021-987-x. Nova Publishers, 2008, p. 95-136, 95
- Alcalá, J. M., Covino, E., Torres, G., et al. 2000, *A&A*, 353, 186
- Alcalá, J. M., Natta, A., Manara, C. F., et al. 2014, *A&A*, 561, A2
- Alcalá, J. M., Manara, C. F., Natta, A., et al. 2017, *A&A*, 600, A20
- Alencar, S. H. P., & Basri, G. 2000, *ApJ*, 119, 1881
- Alencar, S. H. P., Teixeira, P. S., Guimarães, M. M., et al. 2010, *A&A*, 519, A88
- Alencar, S. H. P., Bouvier, J., Walter, F. M., et al. 2012, *A&A*, 541, A116
- Ambartsumian, V. A., 1947, *Stellar evolution and Astrophysics*, Acad. Sci. ArmSSR, Erevan
- Bally, J., & Devine, D. 1994, *APJL&A*, 428, L65
- Basri, G., & Batalha, C. 1990, *ApJ*, 363, 654
- Basri, G., Martin, E. L., & Bertout, C. 1991, *A&A*, 252, 625
- Barry, D.C., Cromwell, R.H. & Schoolman, S.A., 1979, *ApJSS*, Vol. 41, 119-130
- Batalha, C. C., Stout-Batalha, N. M., Basri, G., & Terra, M. A. O. 1996, *ApJS*, 103,211
- Barsunova, O. Y., Grinin, V. P., Arharov, A. A., et al. 2016, *Astrophysics*, 59, 147
- Bertout, C., Basri, G., & Bouvier, J. 1988, *ApJ*, 330, 350
- Bertout, C., 1989, *ARAA*, 27:351-395
- Blanco-Cuaresma, S., Soubiran, C., Heiter, U., & Jofré, P. 2014, *A&A*, 569, A111
- Bodman, E. H. L., Quillen, A. C., Ansdell, M., et al. 2017, *MNRAS*, 470, 202

- Bouvier, J., Bertout, C., Benz, W., & Mayor, M. 1986, *A&A*, 165, 110
- Bouvier, J. 1990, *ApJ*, 99, 948
- Bouvier, J. 1993, *The Messenger*, 71, 21
- Bouvier, J., Alencar, S. H. P., Harries, T. J., Johns-Krull, C. M., & Romanova, M. M. 2007, *Protostars and Planets V*, 479
- Bouvier, J., Lanzafame, A. C., Venuti, L., et al. 2016, *A&A*, 590, A78
- Calvet, N., & Gullbring, E. 1998, *ApJ*, 509, 802
- Calvet, N., Muzerolle, J., Briceño, C., et al. 2004, *ApJ*, 128, 1294
- Chavarria, C. 1981, *A&A*, 101, 105
- Castelli, F., & Kurucz, R. L. 2003, *Modelling of Stellar Atmospheres*, 210, A20
- Choudhary, A., Stecklum, B., & Linz, H. 2016, *A&A*, 590, A106
- Cody, A. M., Stauffer, J., Baglin, A., et al. 2014, *AJ*, 147, 82
- Cohen, M. & Kuhi, L.V. 1979, *ApJ*, 41, 743
- Dahm, S.E. & Simon, T., 2005, *ApJ*, 129:829-855
- Dahm, S. E. 2008, *ApJ*, 136, 521-547
- Damiani, F., Prisinzano, L., Micela, G., et al. 2014, *A&A*, 566, A50
- De Pascale, M., Worley, C. C., de Laverny, P., et al. 2014, *A&A*, 570, A68
- Dodin, A. V., & Lamzin, S. A. 2012, *Astronomy Letters*, 38, 649
- Donati, J.-F., Gregory, S. G., Alencar, S. H. P., et al. 2013, *MNRAS*, 436, 881
- Dyda, S., Lovelace, R. V. E., Ustyugova, G. V., et al. 2015, *MNRAS*, 450, 481
- Edwards, S., Fischer, W., Hillenbrand, L., & Kwan, J. 2006, *ApJ*, 646, 319
- Edwards, S., Kwan, J., Fischer, W., et al. 2013, *ApJ*, 778, 148
- Eisloffel, J., Solf, J., & Boehm, K. H. 1990, *A&A*, 237, 369
- Fang, M., van Boekel, R., Wang, W., et al. 2009, *A&A*, 504, 461
- Fernandez, M., & Eiroa, C. 1996, *A&A*, 310, 143

- Ferreira, J., Dougados, C., & Cabrit, S. 2006, *A&A*, 453, 785
- Finkenzeller, U., & Basri, G. 1987, *ApJ*, 318, 823
- Frasca, A., Biazzo, K., Lanzafame, A. C., et al. 2015, *A&A*, 575, A4
- Gahm, G. F., Fischerstrom, C., Lindroos, K. P., & Liseau, R. 1989, *A&A*, 211, 115
- Gahm, G. F., Walter, F. M., Stempels, H. C., Petrov, P. P., & Herczeg, G. J. 2008, *A&A*, 482, L35
- Gameiro, J. F., Folha, D. F. M., & Petrov, P. P. 2006, *A&A*, 445, 323
- Galli, P.A.B., Bertout, C., Teixeira, R., Ducourant, C. 2015, *A&A*, 580, A26
- Gramajo, L. V., Rodón, J. A., & Gómez, M. 2014, *AJ*, 147, 140
- Gray, D. F. 2005, “The Observation and Analysis of Stellar Photospheres, 3rd Edition, by D.F. Gray.
- Grankin, K. N., Melnikov, S. Y., Bouvier, J., Herbst, W., & Shevchenko, V. S. 2007, *A&A*, 461, 183
- Gullbring, E., Hartmann, L., Briceño, C., & Calvet, N. 1998, *ApJ*, 492, 323
- Gurtovenko, E. A., & Sheminova, V. A. 2015, arXiv:1505.00975
- Hamann, F., & Persson, S. E. 1992, *ApJ*, 394, 628
- Hartigan, P., Hartmann, L., Kenyon, S., Hewett, R., & Stauffer, J. 1989, *ApJS*, 70, 899
- Hartigan, P., Kenyon, S. J., Hartmann, L., et al. 1991, *ApJ*, 382, 617
- Hartigan, P., Edwards, S., & Ghandour, L. 1995, *ApJ*, 452, 736
- Hartmann, L., & Kenyon, S. J. 1985, *ApJ*, 299, 462
- Hartmann, L., & Stauffer, J. R. 1989, *AJ*, 97, 873
- Hartmann, L. 2009, *Accretion Processes in Star Formation: Second Edition*, by Lee Hartmann. ISBN 978-0-521-53199-3. Published by Cambridge University Press, Cambridge, UK, 2009
- Hartmann, L., Herczeg, G., & Calvet, N. 2016, *Annual Review of Astronomy and Astrophysics*, 54, 135

- Hayashi, C. 1961, PASJ, 13
- Heiter, U., Jofré, P., Gustafsson, B., et al. 2015, A&A, 582, A49
- Heney, L. G., Lelevier, R., & Levée, R. D. 1955, PASP, 67, 154
- Herbig, G. H. 1962, *Advances in Astronomy and Astrophysics*, 1, 47
- Herbig, G. H. 1977, ApJ, 214, 747
- Herbig, G. H., & Jones, B. F. 1983, ApJ, 88, 1040
- Herbig, G. H., Petrov, P. P., & Duemmler, R. 2003, ApJ, 595, 384
- Herbig, G. H. 2009, AJ, 138, 448
- Herczeg, G. J., & Hillenbrand, L. A. 2008, ApJ, 681, 594-625
- Ingleby, L., Calvet, N., Herczeg, G., et al. 2013, ApJ, 767, 112
- Jackson, R. J., Jeffries, R. D., Lewis, J., et al. 2015, A&A, 580, A75
- James, D. J., Melo, C., Santos, N. C., & Bouvier, J. 2006, A&A, 446, 971
- Jofré, P., Heiter, U., Soubiran, C., et al. 2014, A&A, 564, A133
- Johns, C. M., & Basri, G. 1995, AJ, 109, 2800
- Johns-Krull, C. M., Valenti, J. A., & Koresko, C. 1999, ApJ, 516, 900
- Johnstone, C. P., Jardine, M., Gregory, S. G., Donati, J.-F., & Hussain, G. 2014, MNRAS, 437, 3202
- Jones, B. F., & Herbig, G. H. 1979, *Astronomical Journal*, 84, 1872
- Joy, A. H. 1945, ApJ, 102, 168
- Joy, A. H. 1949, ApJ, 110, 424
- King, J.R., Soderblom, D., Fischer, D., Jones, B.F., 2000, ApJ, 533:944-958
- Kolotilov, E. A. 1983, *Soviet Astronomy Letters*, V. 9, P. 289
- Kuhi, L.V. ApJ, 140, 1409
- Kupka, F., Piskunov, N., Ryabchikova, T. A., Stempels, H. C., & Weiss, W. W. 1999, A&A, 138, 119

- Kurosawa, R., Harries, T. J., & Symington, N. H. 2006, *MNRAS*, 370, 580
- Kurucz, R. 1993, *ATLAS9 Stellar Atmosphere Programs and 2 km/s grid*. Kurucz CD-ROM No. 13. Cambridge, Mass.: Smithsonian Astrophysical Observatory, 1993., 13
- Kwan, J., & Fischer, W. 2011, *MNRAS*, 411, 2383
- Lada, C. J. 1987, *Star Forming Regions*, 115, 1
- Lanzafame, A.C., Frasca, A., Damiani, F., et al. 2015, *A&A*, 576, A80
- Laverny, P., Recio-Blanco, A., Worley, C.C., Plez, B. 2012, *A&A* (arxiv:1205.2270v1)
- Lorenzetti, D., Antonucci, S., Giannini, T., et al. 2012, *ApJ*, 749, 188
- Magrini, L., Randich, S., Friel, E., et al. 2014, *Astrophysics Source Code Library*, 1402.016
- Matt, S., & Pudritz, R. E. 2005, *The Astrophysical Journal*, 632, L135
- McGinnis, P. T., Alencar, S. H. P., Guimarães, M. M., et al. 2015, *A&A*, 577, A11
- Mendigutía, I., Oudmaijer, R. D., Rigliaco, E., et al. 2015, *MNRAS*, 452, 2837
- Mundt, R., & Eislöffel, J. 1998, *ApJ*, 116, 860
- Muzerolle, J., Calvet, N., & Hartmann, L. 1998, *ApJ*, 492, 743
- Nisini, B., Antonucci, S., Alcalá, J. M., et al. 2018, *A&A*, 609, A87
- Padgett, D. L. 1996, *ApJ*, 471, 847
- Palacios, A., Gebran, M., Josselin, E., et al. 2010, *A&A*, 516, A13
- Petrov, P. P., Gahm, G. F., Gameiro, J. F., et al. 2001, *A&A*, 369, 993
- Petrov, P.P., 2003, *Astrophysics*, Vol. 46, N.º4
- Petrov, P. P., & Herbig, G. H. 2008, *AJ*, 136, 676
- Petrov, P. P., Gahm, G. F., Stempels, H. C., Walter, F. M., & Artemenko, S. A. 2011, *A&A*, 535, A6
- Petrov, P. P., & Babina, E. V. 2014, *Bulletin Crimean Astrophysical Observatory*, 110, 1
- Petrov, P. P., Kurosawa, R., Romanova, M. M., et al. 2014, *MNRAS*, 442, 3643
- Pickles, A. J. 1998, *The Publications of the Astronomical Society of the Pacific*, 110, 863

- Piskunov, N. E., Kupka, F., Ryabchikova, T. A., Weiss, W. W., & Jeffery, C. S. 1995, *A&AS*, 112, 525
- Prato, L., Greene, T. P., & Simon, M. 2003, *ApJ*, 584, 853
- Quanz, S.P., Apai, D., Henning, Th. 2007, *ApJ*, 656, 287
- Randich, S., Gilmore, G., & Gaia-ESO Consortium 2013, *The Messenger*, 154, 47
- Rei, A. C. S., Petrov, P. P., & Gameiro, J. F. 2018, *A&A*, 610, A40
- Reipurth, B., Pedrosa, A., & Lago, M. T. V. T. 1996, *Astronomy and Astrophysics Supplement*, 120, 229
- Reiter, M., Kiminki, M. M., Smith, N., & Bally, J. 2017, *MNRAS*, 467, 4441
- Rice, E. L., Prato, L., & McLean, I. S. 2006, *ApJ*, 647, 432
- Rice, T. S., Reipurth, B., Wolk, S. J., Vaz, L. P., & Cross, N. J. G. 2015, *AJ*, 150, 132
- Rigliaco, E., Natta, A., Testi, L., et al. 2012, *A&A*, 548, A56
- Rojas, G., Gregorio-Hetem, J., & Hetem, A. 2008, *MNRAS*, 387, 1335
- Romanova, M. M., Ustyugova, G. V., Koldoba, A. V., & Lovelace, R. V. E. 2012, *MNRAS*, 421, 63
- Ryabchikova, T., Piskunov, N., Kurucz, R. L., et al. 2015, *Physica Scripta*, 90, 054005
- Shevchenko, V. S., Yakulov, S. D., Hambarian, V. V., & Garibjanian, A. T. 1991, *Soviet Astronomy*, 68, 275
- Shu, F., Najita, J., Ostriker, E., et al. 1994, *ApJ*, 429, 781
- Sicilia-Aguilar, A., Fang, M., Roccatagliata, V., et al. 2015, *A&A*, 580, A82
- Siess L., Dufour E., Forestini M. 2000, *A&A*, 358, 593
- Smiljanic, R., Korn, A. J., Bergemann, M., et al. 2014, *A&A*, 570, A122
- Snedden, C. A. 1973, Ph.D. Thesis,
- Soderblom, D. R. 2010, *ARA&A*, 48, 581
- Sousa, S.G., Santos, N.C., Israelian, G., Mayor, M., Monteiro, M.J.P.F.G., 2007, *A&A*, 469, 783

- Sousa, S. G., Santos, N. C., Mayor, M., et al. 2008, *A&A*, 487, 373
- Sousa, S.G., Santos, N.C., Israelian, G., 2012, 159:141-166
- Sousa, A., Alencar, S., Bouvier, J., et al. 2015, arXiv:1509.05354
- Spina, L., Randich, S., Magrini, L., et al. 2017, *A&A*, 601, A70
- Stempels, H. C., & Piskunov, N. 2002, *A&A*, 391, 595
- Stempels, H. C., & Piskunov, N. 2003, *A&A*, 408, 693
- Taguchi, Y., Itoh, Y., & Mukai, T. 2009, *PASJ*, 61, 251
- Teixeira, G. D. C., Sousa, S. G., Tsantaki, M., et al. 2016, *A&A*, 595, A15
- Tokunaga, A. T., Reipurth, B., Gässler, W., et al. 2004, *ApJ*, 127, 444
- Tsantaki, M., Sousa, S. G., Adibekyan, V. Z., et al. 2013, *A&A*, 555, A150
- Tsantaki, M., Sousa, S.G., Santos, N.C. et al., 2014, *A&A*, 570, A80
- Tsantaki, M., Andreasen, D. T., Teixeira, G. D. C., et al. 2018, *MNRAS*, 473, 5066
- Valenti, J. A. & Piskunov, N. 1996, *A&AS*, 118, 595
- Valenti, J. A., Basri, G., & Johns, C. M. 1993, *ApJ*, 106, 2024
- Valenti, J. A. & Fischer, D. A. 2005, *ApJS*, 159, 141
- Venuti, L., Bouvier, J., Flaccomio, E., et al. 2014, *A&A*, 570, A82
- Vogt, S. S., Allen, S. L., Bigelow, B. C., et al. 1994, *Proc. SPIE Instrumentation in Astronomy VIII*, 2198, 362
- Walter, F. M., Brown, A., Linsky, J. L., et al. 1987, *ApJ*, 314, 297
- Welin, G. 1976, *A&A*, 49, 145
- Wenger, M., Ochsenbein, F., Egret, D., et al. 2000, *Astronomy and Astrophysics Supplement*, 143, 9
- White, R.J. & Basri, G. 2003, *ApJ*, 582:1109-1122
- Zanni, C., & Ferreira, J. 2013, *A&A*, 550, A99

Appendix A

WTTS H α plots

Plots of the H α line for those wTTS with H α line in emission. We plot the median spectrum H α line and the standard deviation (σ).

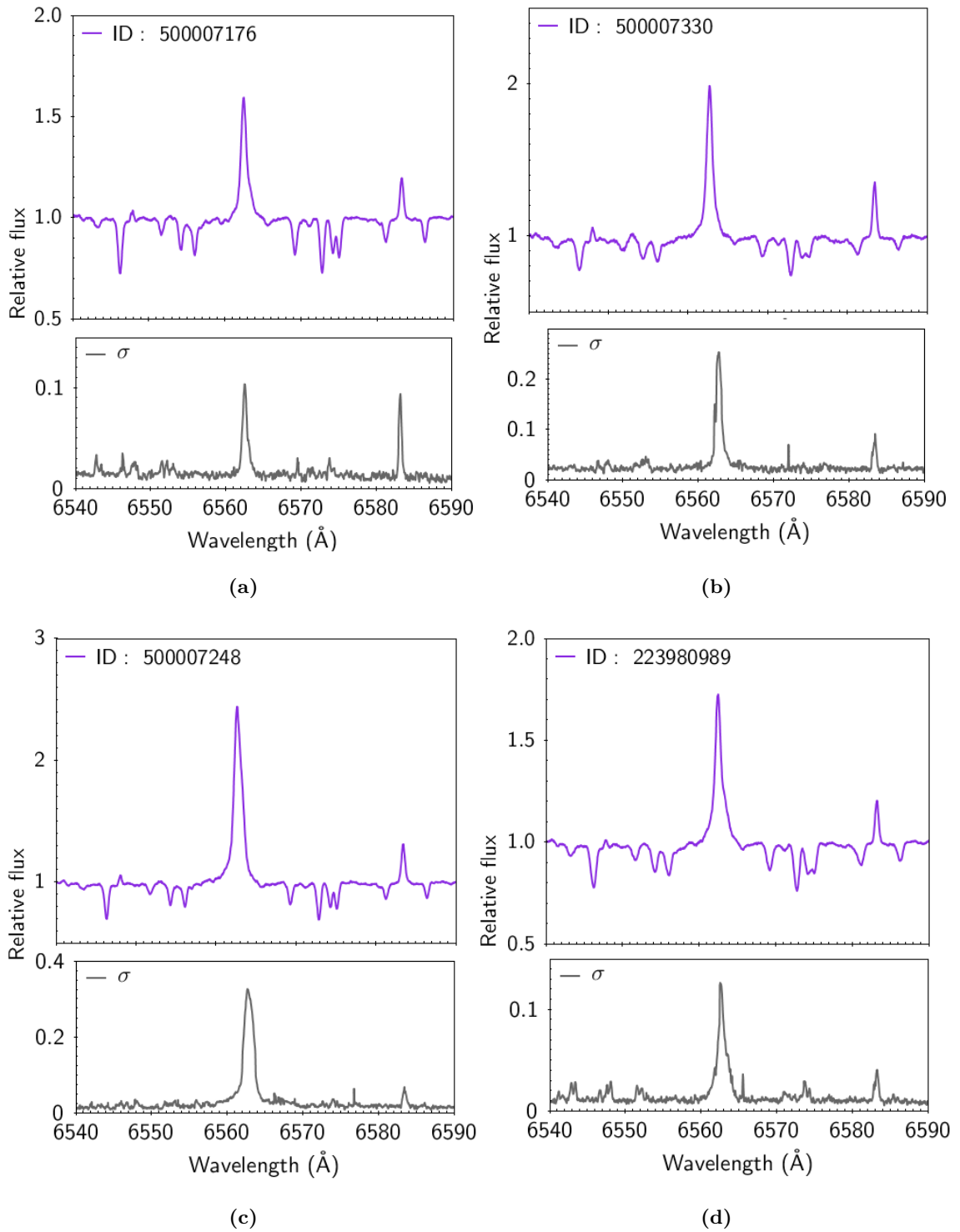


Figure A.1: WTS H α line and σ .

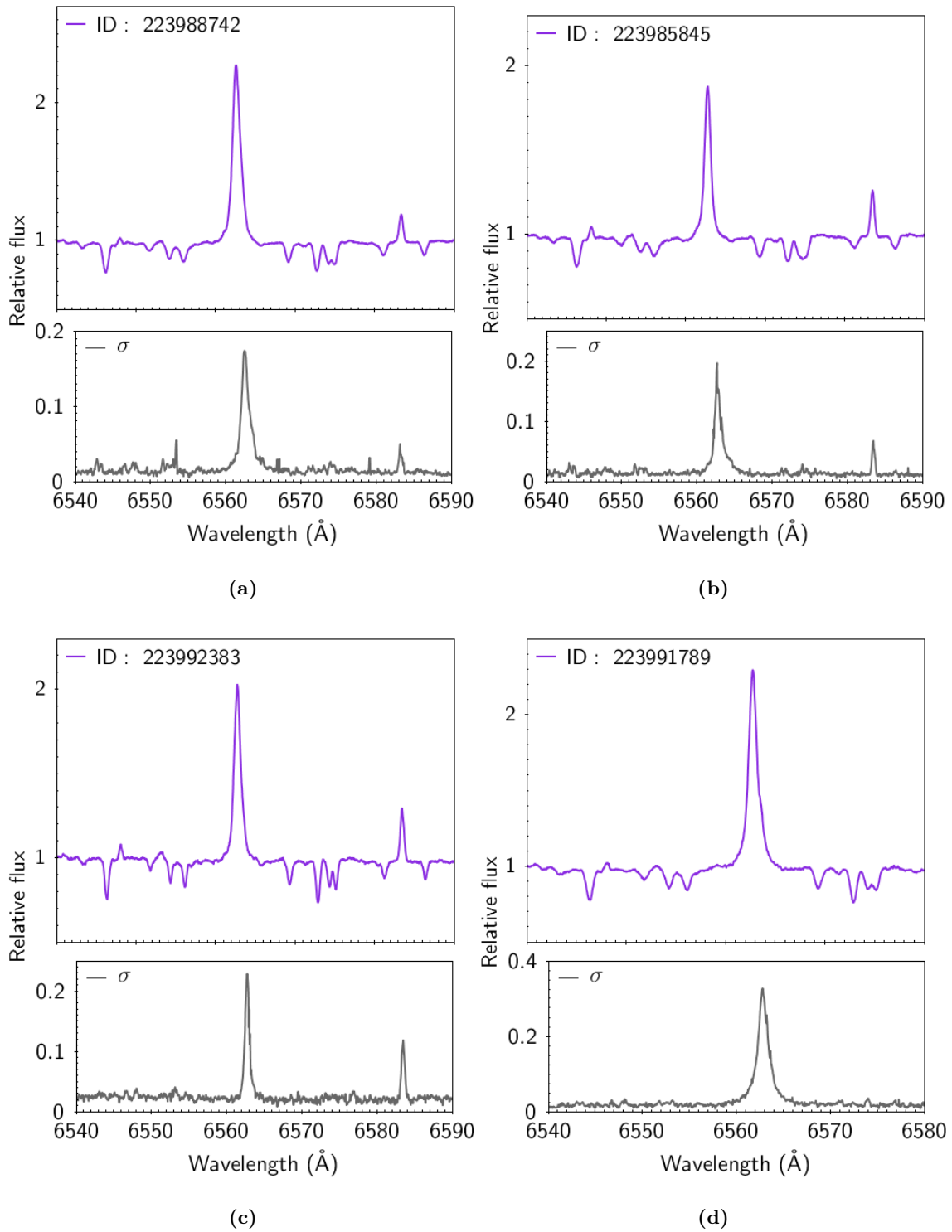


Figure A.2: WTTS H α line and σ (cont.).

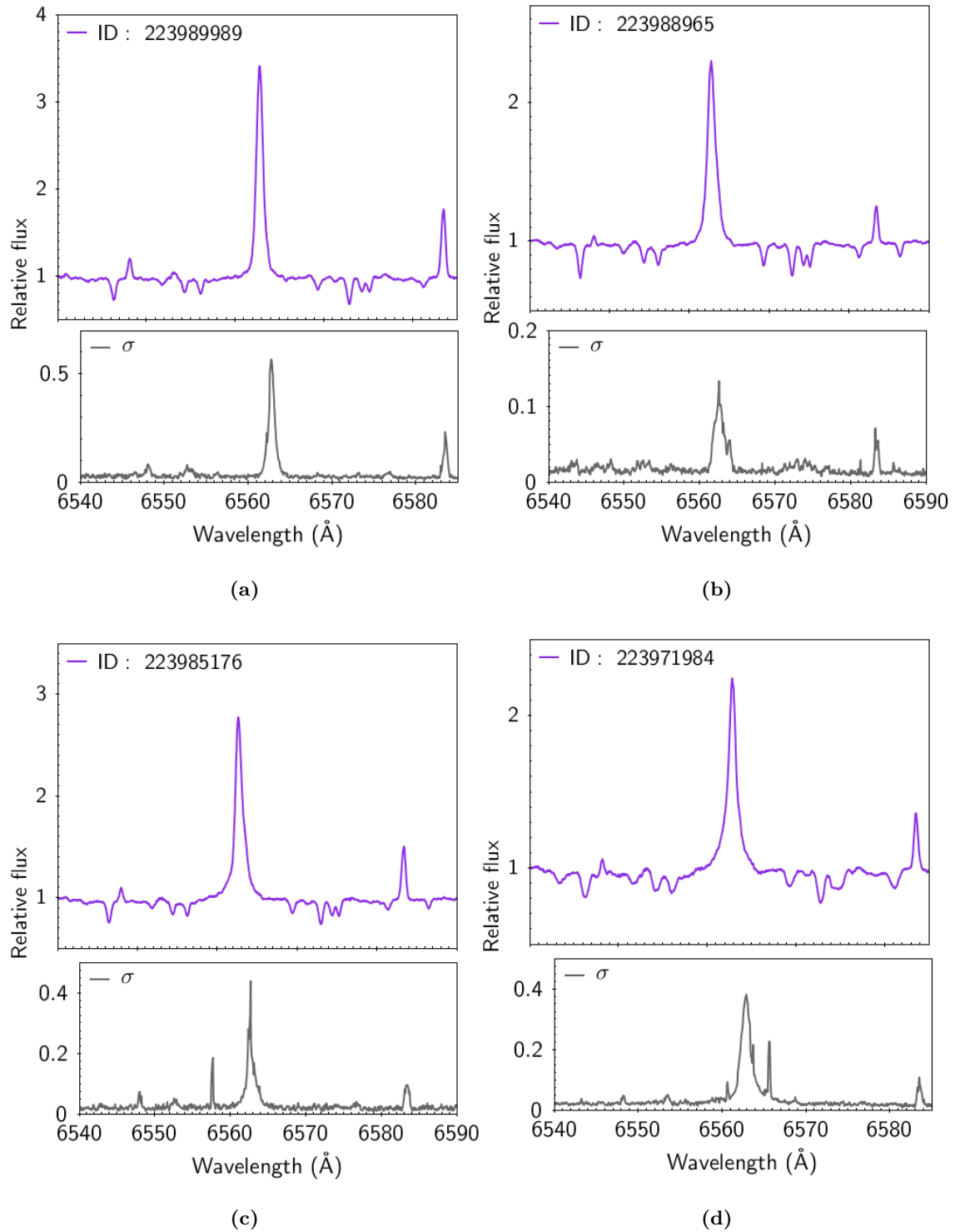


Figure A.3: WTTs $H\alpha$ line and σ (cont.).

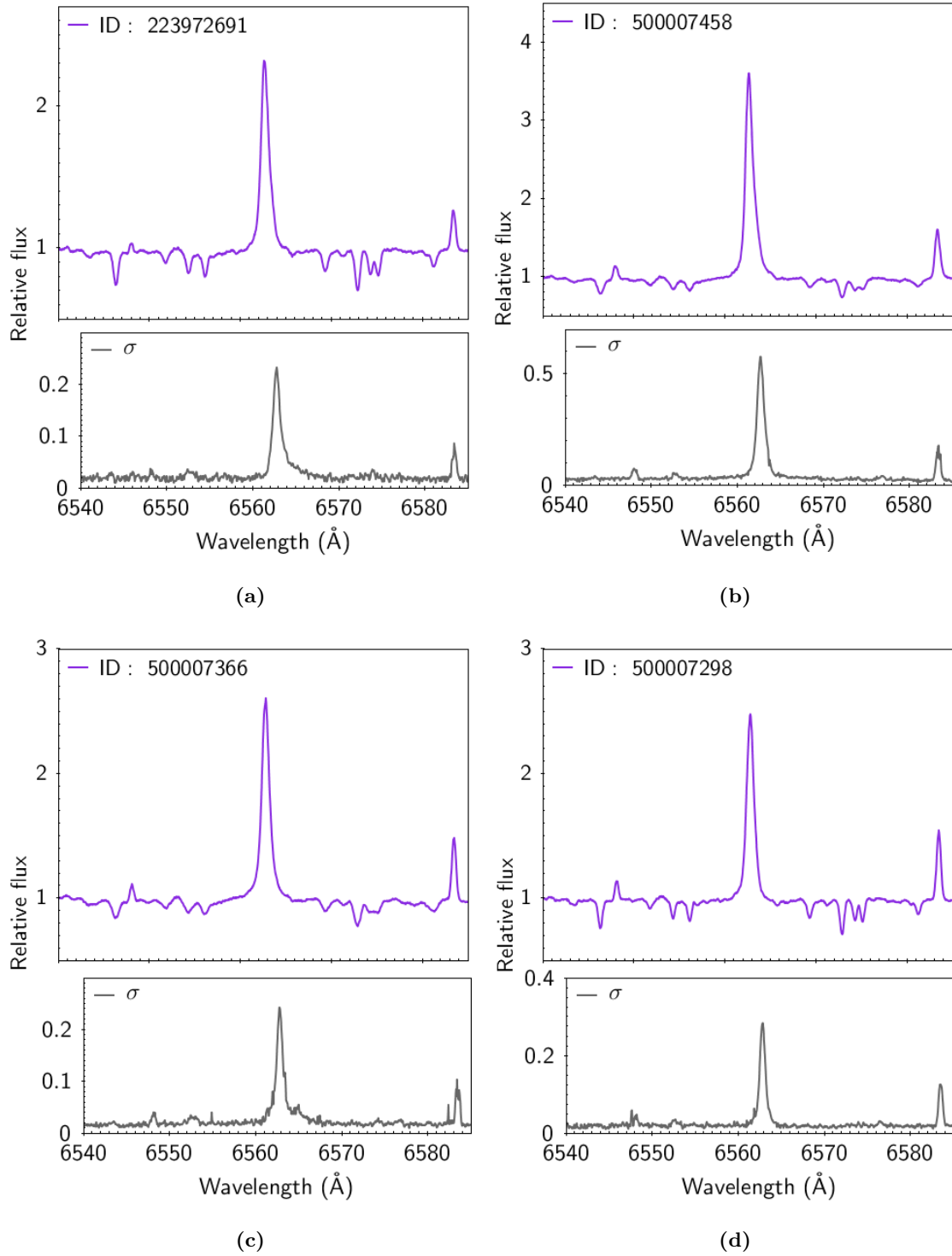


Figure A.4: WTTS H α line and σ (cont.).

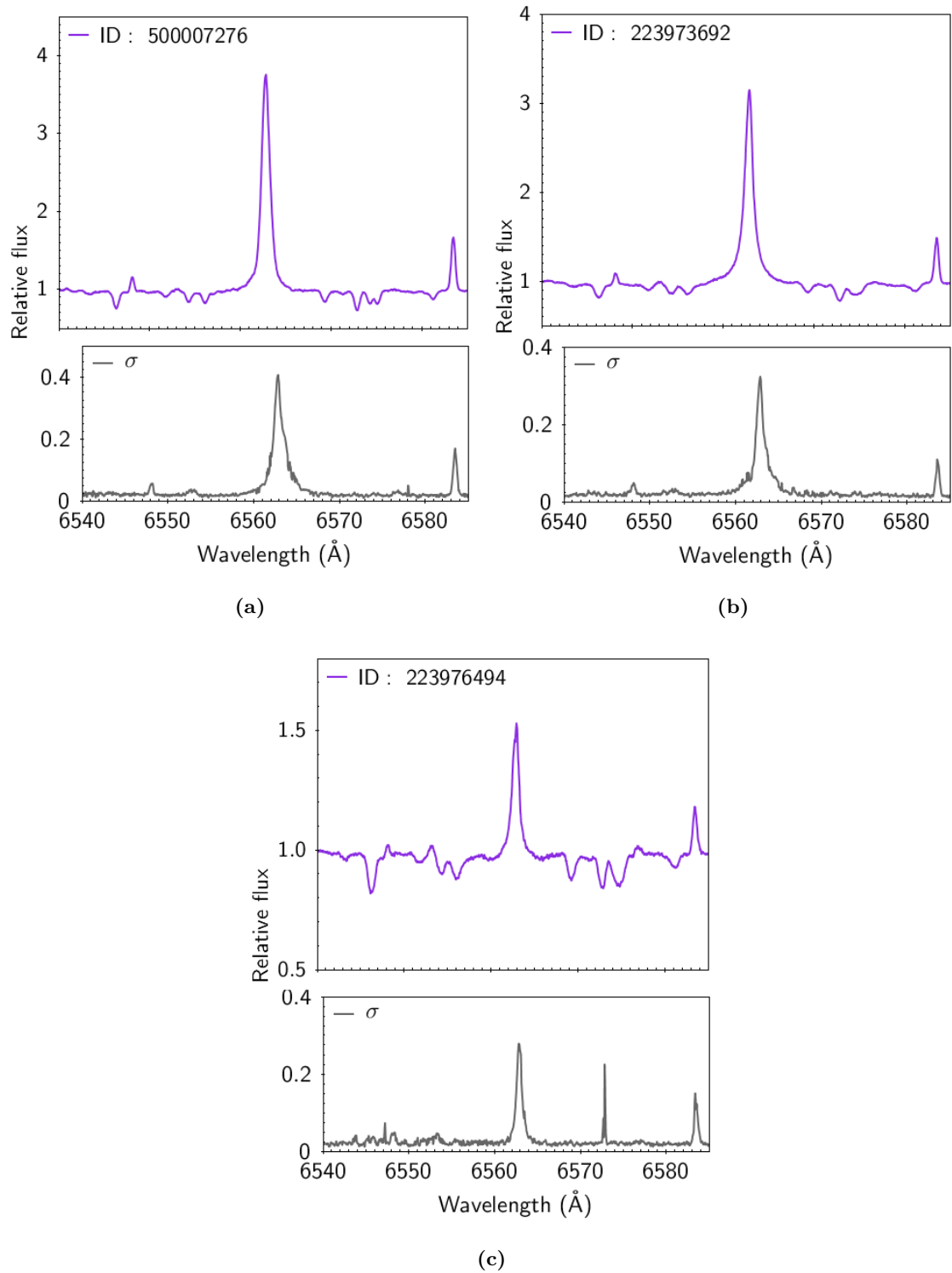


Figure A.5: WTTs H α line and σ (cont.).

Appendix B

Publications

- **Line-dependent veiling in very active classical T Tauri stars**, A.C.S. Rei, P.P. Petrov, J.F. Gameiro, published in *Astronomy & Astrophysics*, Volume 610, id.A40, 02/2018;
- **Fundamental stellar parameters of wTTS in NGC 2264. The GIRAFFE HR15N spectra.**, A.C.S. Rei, G. Teixeira, J.F. Gameiro, S.H.P. Alencar, submitted to *Astronomy & Astrophysics*.

Line-dependent veiling in very active classical T Tauri stars

A. C. S. Rei^{1,2}, P. P. Petrov³, and J. F. Gameiro^{1,2}

¹ Instituto de Astrofísica e Ciências do Espaço, CAUP, Rua das Estrelas, 4150-762 Porto, Portugal
e-mail: ana.rei@astro.up.pt

² Departamento de Física e Astronomia, Faculdade de Ciências, Universidade do Porto, Rua do Campo Alegre, 4150-762 Porto, Portugal

³ Crimean Astrophysical Observatory of Russian Academy of Sciences, p/o Nauchny, 298409, Crimea

Received 26 June 2017 / Accepted 22 November 2017

ABSTRACT

Context. The T Tauri stars with active accretion disks show veiled photospheric spectra. This is supposedly due to non-photospheric continuum radiated by hot spots beneath the accretion shocks at stellar surface and/or chromospheric emission lines radiated by the post-shocked gas. The amount of veiling is often considered as a measure of the mass-accretion rate.

Aims. We analysed high-resolution photospheric spectra of accreting T Tauri stars LkH α 321, V1331 Cyg, and AS 353A with the aim of clarifying the nature of the line-dependent veiling. Each of these objects shows a strong emission line spectrum and powerful wind features indicating high rates of accretion and mass loss.

Methods. Equivalent widths of hundreds of weak photospheric lines were measured in the observed spectra of high quality and compared with those in synthetic spectra of appropriate models of stellar atmospheres.

Results. The photospheric spectra of the three T Tauri stars are highly veiled. We found that the veiling is strongly line-dependent: larger in stronger photospheric lines and weak or absent in the weakest ones. No dependence of veiling on excitation potential within 0 to 5 eV was found. Different physical processes responsible for these unusual veiling effects are discussed in the framework of the magnetospheric accretion model.

Conclusions. The observed veiling has two origins: (1) an abnormal structure of stellar atmosphere heated up by the accreting matter, and (2) a non-photospheric continuum radiated by a hot spot with temperature lower than 10 000 K. The true level of the veiling continuum can be derived by measuring the weakest photospheric lines with equivalent widths down to ≈ 10 mÅ. A limited spectral resolution and/or low signal-to-noise ratio results in overestimation of the veiling continuum. In the three very active stars, the veiling continuum is a minor contributor to the observed veiling, while the major contribution comes from the line-dependent veiling.

Key words. stars: activity – stars: pre-main sequence – stars: variables: T Tauri, Herbig Ae/Be – stars: individual: LkH α 321 – stars: individual: V1331 Cyg – stars: individual: AS 353A

1. Introduction

The T Tauri stars are late-type stars at the pre-main sequence (PMS) phase of evolution. These stars are in fact star-disk systems and their spectra show several features associated with the interaction between star and disk. There are two classes of T Tauri stars, based on the degree of activity of the star-disk system: classical T Tauri stars (cTTS) and weak-line T Tauri stars (wTTS). The rich emission spectrum of cTTS is related to magnetospheric accretion of matter from the inner disk regions onto the star. Yet in the early studies of cTTS it was found that the strength of the photospheric lines is reduced as compared to a main-sequence (MS) star of the corresponding spectral type. Joy (1949) noted that this may be due to emission within the lines and due to veiling of the spectrum by an overlying continuous radiation.

In the concept of magnetospheric accretion, the veiling continuum is attributed to a shock-heated gas (a hot spot) at the stellar surface below the accretion stream. The veiling was often considered as a measure of accretion rate (e.g. Basri & Batalha 1990; Hartigan et al. 1991, 1995; Valenti et al. 1993; Calvet et al. 2004) along with other indicators, like the luminosity in H α and other emission lines (e.g. Muzerolle et al. 1998;

Herczeg & Hillenbrand 2008; Dahm 2008; Fang et al. 2009; Rigliaco et al. 2012; Mendigutía et al. 2015).

As more data were accumulated, some doubts appeared about the interpretation of the veiling origin. The expected correlation between the veiling in the optical spectrum and the brightness of the star was not found in some cTTS. For example, in RW Aur A the veiling is highly variable from night to night. However, no correlation has been found with the stellar brightness in the V band from the photometric and spectroscopic monitoring of the star (Petrov et al. 2001). No rotational modulation of the veiling was reported for the star.

Gahm et al. (2008) showed that in RU Lup and S CrA SE large veiling factors correlate only weakly with brightness. In the case of S CrA SE a narrow emission core appears at the bottom of photospheric absorptions at moments of enhanced accretion. Furthermore, when the veiling is measured carefully in every single spectral line within a narrow wavelength range, it turns out that the veiling depends on the line strength in a template of the corresponding spectral type. Stronger lines can be veiled considerably, while the weakest lines remain about normal for the spectral type. So far, line-dependent veiling has been found in DR Tau (Petrov et al. 2011) and V1331 Cyg (Petrov et al. 2014). A similar effect was noticed earlier in

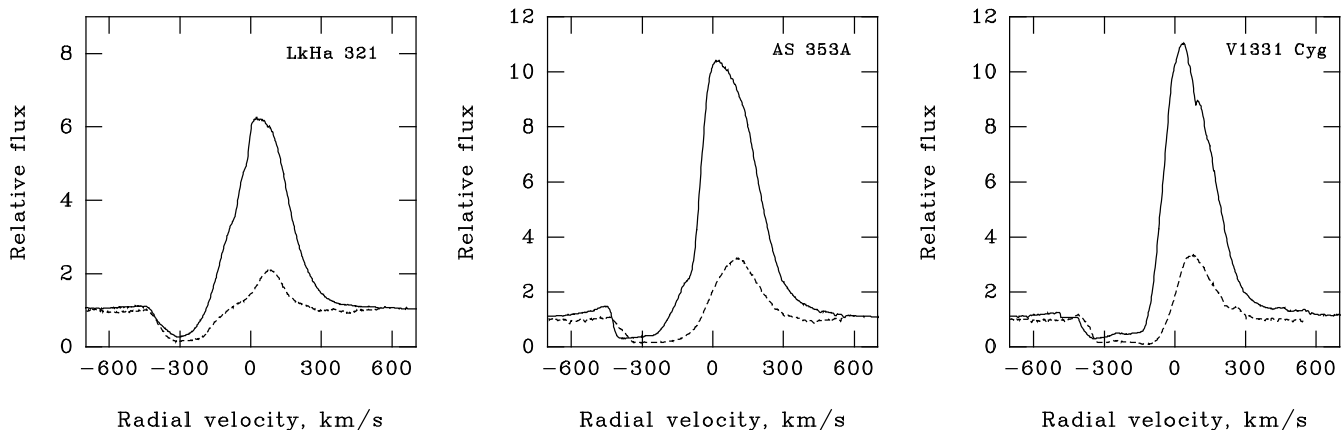


Fig. 1. $H\alpha$ (solid line) and $H\beta$ (dashed line) profiles.

DI Cep (Gameiro et al. 2006). Line-dependent veiling was found in spectra of EX Lup in quiescent state, when the accretion rate was relatively low (Sicilia-Aguilar et al. 2015). The authors concluded that photospheric lines in EX Lup are veiled by the broad emission lines from the extended pre-shock material.

In order to clarify the nature of line-dependent veiling, we undertake detailed inspection of photospheric lines in cTTS with high accretion rates. In this work we investigate the veiling effect in spectra of three cTTS: LkHa 321 (=V1980 Cyg), AS 353A (=V1352 Aql), and V1313 Cyg.

2. Observational data

In this research we use spectra obtained by George Herbig with the High Resolution Echelle Spectrometer (HIRES) at Keck-1¹ (Vogt et al. 1994). We estimated a spectral resolution of $R \sim 50\,000$ near 6300 \AA from the weakest telluric lines in this region.

The spectra were obtained on 2002 December 16 (LkHa 321), 2003 July 6 (AS 353A), and 2004 July 24 (V1331 Cyg). The wavelength coverage was $4350\text{--}6750 \text{ \AA}$ with some gaps between spectral orders in the region $>5000 \text{ \AA}$. One more spectrum of V1331 Cyg was taken on 2007 November 23 with the same spectrograph and a mosaic of three CCDs covering the spectral range $4750\text{--}8690 \text{ \AA}$. In the spectra of LkHa 321 and V1331 Cyg, the signal-to-noise (S/N) ratio per resolution element is 170 at 5000 \AA and rises to 400 at 6500 \AA . The spectrum of AS 353A has a S/N of 200 at 5000 \AA and 350 at 6500 \AA .

The spectra analysed belong to three cTTS with high accretion rates, whose stellar parameters are difficult to estimate. A summary of previous and current estimations of some stellar parameters for these stars can be found in Table 1. The estimations of spectral type, effective temperature (T_{eff}), projected rotational velocity ($v \sin i$), radial velocity (v_{rad}), and equivalent widths of the $H\alpha$ ($\text{EW}(H\alpha)$) and He I 5875 \AA ($\text{EW}(\text{HeI})$) lines for each star are described in Sect. 3.

Utrecht Echelle Spectrograph (UES) spectra of each star were also available, from observations done in November of 1998. The UES spectra have a similar resolution to those of HIRES, but with a $S/N < 100$. Although the S/N is not high

enough to perform the same type of study done with the HIRES spectra, it is possible to check for a change in radial velocity of the stars from spectra taken in different epochs.

The three objects show strong emission line spectra, powerful wind features, and highly veiled photospheric spectra. Typically, in spectra of cTTS the emission lines of neutral and ionized metals exhibit a composite profile: a broad component formed in the accretion funnel and a narrow component consistent with an origin in the post-shocked gas near the stellar surface (e.g. Beristain et al. 1998). This is the case of LkHa 321 and AS 353A, where the broad component is dominant with full width at half maximum ($FWHM$) $\approx 140 \text{ km s}^{-1}$. On the contrary, in V1331 Cyg the numerous emission lines of metals show only a single moderately broad profile with $FWHM = 40\text{--}60 \text{ km s}^{-1}$ (see Sect. 7.1).

The most prominent lines are the hydrogen Balmer and Paschen lines, the Ca II, Na I D, and O I 8446 \AA lines with $FWHM \approx 200 \text{ km s}^{-1}$. These broad lines are supposedly formed in the high velocity infalling gas at the base of the accretion column, before the shock (pre-shocked gas), within the stellar magnetosphere. The P Cyg type of the profiles of $H\alpha$ and $H\beta$ lines indicates an extensive mass-loss (Fig. 1).

Figure 2 compares two spectral fragments of the stars to show the differences in strength and width between the photospheric and emission lines. In all three objects the narrow forbidden emissions of [O I] 6300.3 and 6363.7 \AA are present.

3. Data analysis

Template spectra of non-active main-sequence (MS) stars, wTTS, or synthetic spectra are needed to perform the analysis of cTTS. In this investigation we analyse rather weak spectral lines, with equivalent width (EW) of about 10 m\AA , so we need high-resolution, high S/N spectra of template stars of different spectral type. In order to minimize the errors of measurements, we prefer to use a grid of synthetic spectra. This way we avoid possible spectral peculiarities from the real stars that could affect our results.

3.1. Template synthetic spectra

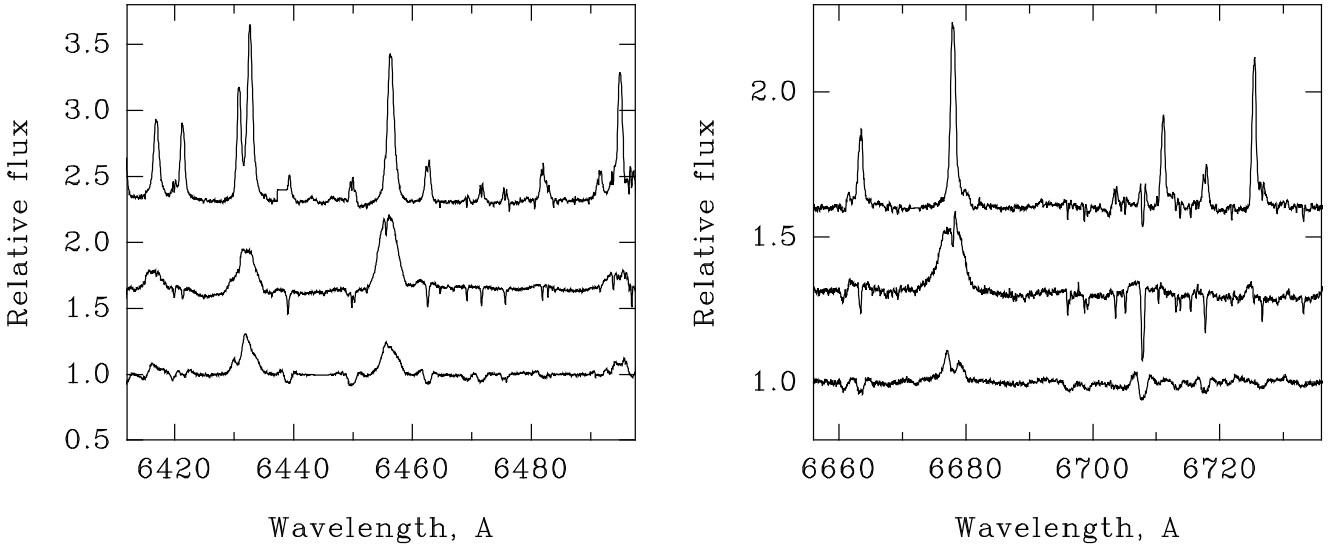
The synthetic spectra were produced by the software package Spectroscopy Made Easy (SME; Valenti & Piskunov 1996). It was initially used to confirm the spectral type of each cTTS, with the estimation of T_{eff} , as well as for the determination of $v \sin i$ and v_{rad} .

¹ The W. M. Keck Observatory is operated as a scientific partnership between the California Institute of Technology, the University of California, and the National Aeronautics and Space Administration. The Observatory was made possible by the generous financial support of the W. M. Keck Foundation.

Table 1. Stellar parameters.

Star	Sp.type	T_{eff} (K)	$\log L_*$ (L_{\odot})	M_*^d (M_{\odot})	R_*^d (R_{\odot})	$\log g^d$ (dex)	$v \sin i$ (km s $^{-1}$)	v_{rad} (HIRES) (km s $^{-1}$)	EW(H α) (\AA)	EW(HeI) (\AA)
LkH α 321	G5–G7	5500–5250	1.42 ^a	2.9	5.3	3.5	32	-16.0 ± 0.5	30	0.08
V1331 Cyg	G7–K1	5250–5000	1.32 ^b	2.9	5.5	3.5	<6	-15.0 ± 0.3	53	0.22
AS 353A	K0–K1	5100–4900	0.4 ^c	1.6	2.1	4.0	<6	-10.4 ± 0.2	58	1.30

Notes. Sp.type, T_{eff} , $v \sin i$, v_{rad} , EW(H α), and EW(HeI) are from this paper. ^(a) Cohen & Kuhi (1979), ^(b) Tokunaga et al. (2004), ^(c) Hamann & Persson (1992), ^(d) Obtained from T_{eff} and L_* and using the PMS models by Siess et al. (2000).


Fig. 2. Fragments of spectra: LkH α 321 (*lower*), AS 353A (*middle*), and V1331 Cyg (*upper*).

Two sets of synthetic spectra with spectral resolution $R = 50\,000$ were produced. The first set corresponds to a grid of narrow-band spectra with several values of stellar parameters, which was used in the determination of spectral type, as well as $v \sin i$ and v_{rad} . Then, specific spectra for each star in a wider wavelength band between 4500 and 7000 \AA were produced. This second set of synthetic spectra corresponds to our templates and was used to measure EWs of hundreds of spectral lines for comparison with the same lines in the spectra of cTTS.

The spectral type determination, described in detail in Sect. 3.2, allowed us to gather information mainly about T_{eff} . The usual criteria of surface gravity ($\log g$) can hardly be used in the case of highly veiled spectra with strong lines in emission. Due to that we are assuming the value $\log g = 3.75$ dex for these stars (see Sect. 3.2). We also assume a priori a solar-like metallicity ($[M/H] = 0.0$).

Besides the mentioned stellar parameters, SME also needs input information about the microturbulence velocity (v_{mic}) and macroturbulence velocity (v_{mac}), as well as the instrumental resolution. For the v_{mic} parameter we assume a value that is typical for cool stars and wTTS (e.g. Padgett 1996; Rojas et al. 2008; James et al. 2006; Taguchi et al. 2009): $v_{\text{mic}} = 1.0$ km s $^{-1}$. For the v_{mac} value we assume a value based on the T_{eff} value, as reported by Valenti & Fischer (2005). The three stars have spectral types between K1 and G5 corresponding to temperatures between 4900 and 5500 K for sub-giant stars (Table 1). For this range of temperatures we assume a value of $v_{\text{mac}} = 2.8$ km s $^{-1}$, consonant to an average $T_{\text{eff}} = 5000$ K.

To create the synthetic spectra we use the Kurucz grids of stellar atmospheric models, considering local thermodynamic

equilibrium (LTE) conditions. The line list used by SME to create the synthetic spectra was extracted from the Vienna Atomic Line Database (VALD) database using the ‘‘Extract stellar’’ option (Ryabchikova et al. 2015). Since we measured several hundred spectral lines, we did not apply any corrections to the $\log gf$ and Van der Waals damping parameters.

3.2. Spectral type determination

The spectral types of our targets were determined by using a grid of synthetic spectra with several values of T_{eff} and $\log g$. Determination of the spectral type of cTTS is hampered by the veiling effect. As will be shown below, the stronger lines are most affected by the veiling, therefore the use of strong lines in the spectral classification should be avoided. To perform this task we identified the less blended photospheric lines on several spectral fragments throughout the whole spectrum.

To find the value of T_{eff} for each star, we identified several pairs of weak lines with ratios sensitive to temperature changes in the synthetic spectra grid. The synthetic spectra with the ratios of lines similar to those of the cTTS were chosen as the appropriate templates. Typically, the cTTS spectra drop in between two synthetic templates with 250 K difference. The pairs of photospheric lines used to determine the spectral type of each cTTS are listed in Table 2.

Due to the numerous emission lines and the veiling of photospheric lines, it is problematic to derive the $\log g$ parameter directly from the spectra of very active cTTS. It can be estimated from the grid of models of PMS stars (Siess et al. 2000) with input parameters T_{eff} and L_* (see Table 1). For the synthetic

Table 2. Photospheric line pairs used in the spectral type determination.

Star	Line 1			Line 2		
	λ (Å)	Ele.	Exc. pot. (eV)	λ (Å)	Ele.	Exc. pot. (eV)
LkH α 321	6013.416	Ti I	1.07	6016.605	Fe I	3.55
	6039.729	V I	1.06	6041.950	Fe I	4.96
	6325.164	Ti I	0.02	6327.599	Ni I	1.68
	6469.193	Fe I	4.48	6471.662	Ca I	2.53
V1331 Cyg	5054.074	Ti I	2.68	5054.642	Fe I	3.64
	5289.269	Ti I	0.84	5289.817	Y II	1.03
	5295.312	Fe I	4.42	5295.776	Ti I	1.07
	5376.599	Ti I	0.00	5376.830	Fe I	4.29
	5384.630	Ti I	0.83	5385.575	Fe I	3.69
	5385.133	V I	2.61	5385.575	Fe I	3.69
	5440.509	Ti I	1.43	5441.339	Fe I	4.31
	5460.499	Ti I	0.05	5461.549	Fe I	4.45
AS 353A	5465.773	Ti I	1.07	5466.987	Fe I	3.57
	6111.070	Ni I	4.09	6111.651	V I	1.04
	6116.180	Ni I	4.27	6116.990	Co I	1.79
	6116.180	Ni I	4.27	6119.528	V I	1.06
	6146.207	Ti I	1.87	6147.834	Fe I	4.08
	6151.617	Fe I	2.18	6152.292	Si I	5.96
	6154.225	Na I	2.10	6155.134	Si I	5.62
6156.023	Ca I	2.52	6157.727	Fe I	4.08	

Notes. Some of the lines listed in this table are blends, particularly for the LkH α 321 spectrum.

Table 3. Template synthetic spectra parameters for each star.

Template for	T_{eff} (K)	$\log g$ (dex)	[M/H] (dex)	$v \sin i$ (km s $^{-1}$)	v_{mic} (km s $^{-1}$)	v_{mac} (km s $^{-1}$)
LkH α 321	5250	3.75	0.0	32	1.0	2.8
V1331 Cyg	5000	3.75	0.0	1	1.0	2.8
AS 353A	5000	3.75	0.0	1	1.0	2.8

templates we adopted $\log g = 3.75$ dex. A simple test with the templates showed that differences of 0.25 dex in this parameter are not critical for our analysis of equivalent widths.

For the determination of the $v \sin i$ value, artificial veiling must be added to the synthetic spectra in order to mimic the real spectra. Because the estimation of veiling also depends on the $v \sin i$ value, this process must be done in an iterative way, until the synthetic spectra lines have a good match with the real ones.

The information regarding the synthetic templates for each cTTS, based on the previous estimation of stellar parameters, is summarized in Table 3. Details on the individual spectrum of each star can be found in Sects. 4–6.

3.3. Equivalent widths measurements

Our study is based on the comparison of EWs of several hundred photospheric lines of cTTS with those of synthetic templates. To measure the EWs we used IRAF². Due to the presence of strong veiling and emission in these stars' spectra, only lines that could be clearly identified with their counterparts in the

synthetic templates were measured. Regions with broad emission were avoided. In total, we measured the EWs of more than 500 photospheric lines, except for LkH α 321, where many lines are blended because of the large $v \sin i$. We measured EWs of the less blended lines in LkH α 321 and in the corresponding template with the same $v \sin i$.

Although the precision of the measurements is limited by S/N, the main source of errors is the uncertainty in the local continuum level, caused by the line blends of both photospheric absorptions and broad emissions. We use the synthetic template to find the adjacent points of the continuum for each photospheric line, and select the spectral intervals where the broad emissions are relatively small, not exceeding a few percent above the continuum level. The relative error in the EW of photospheric lines was found to be within 5–12%.

3.4. Equivalent widths ratio as a measure of veiling

Traditionally, on cTTS the veiling factor (VF) is expressed as $VF = EW(\text{template})/EW(\text{ts}) - 1$. In this expression it is assumed that $EW(\text{ts})$ is reduced by an additional (non-photospheric) continuum, and the VF is a measure of this non-photospheric continuum in units of the photospheric continuum. Since we do not know a priori the nature of the veiling,

² IRAF is distributed by the National Optical Astronomy Observatories, which are operated by the Association of Universities for Research in Astronomy, Inc., under cooperative agreement with the National Science Foundation.

we will use in the following analysis only the ratio of EWs: $EW(\text{template})/EW(\text{tts})$. In the veiled spectrum of cTTS, for most of the photospheric lines this ratio is larger than unity, although for the weakest lines it may be less than unity because of the measurement errors. The error in spectral type may also result in some bias. In the optical spectrum of cTTS, the veiling usually rises towards the blue region, which indicates the presence of a hot continuum (Basri & Batalha 1990; Calvet & Gullbring 1998). In this study we also analyse how the veiling changes with wavelength.

We used real spectra of the Sun and a G7IV star (HD190248) to evaluate how large the scatter of the $EW(\text{synthetic})/EW(\text{real})$ is along the spectrum. The Sun spectrum³ was obtained by High Accuracy Radial velocity Planet Searcher (HARPS) and has a $S/N > 500$ (Blanco-Cuaresma et al. 2014). The G7IV star spectrum was extracted from the ESO Archive. We assigned a synthetic template with $T_{\text{eff}} = 5000$ K and $\log g = 3.75$ dex to the G7IV star and a template with $T_{\text{eff}} = 5750$ K and $\log g = 4.4$ dex to the Sun, both with solar metallicity. The EWs of the same lines were measured on both real and synthetic spectra and the ratio $EW(\text{synthetic})/EW(\text{real})$ was analysed.

We found that the $EW(\text{synthetic})/EW(\text{real})$ ratio does not depend on wavelength, line strength, and excitation potential of low level of the transition. Other atomic parameters, like excitation potential of the upper level and total excitation energy, have also been tested and no dependence with $EW(\text{synthetic})/EW(\text{real})$ ratio was found. The line-to-line scatter of this ratio can be quantified with a standard deviation from the average. We found that the sample standard deviation is about 0.2–0.3 dex for the weakest lines with $EW < 50$ mÅ and 0.1–0.2 dex for stronger lines. There are two possible causes for the dispersion of values: one is due to the error in measurement and determination of continuum level, and another is due to the lack of correction for the $\log gf$ and Van der Waals damping parameters in the synthetic templates. Although the line-to-line scatter of the $EW(\text{synthetic})/EW(\text{real})$ ratio is relatively large, it does not affect our results due to the large number of lines used in the analysis.

4. LkH α 321

Two of our objects, LkH α 321 and V1331 Cyg, are located in a dark cloud in Cygnus, a few degrees north from the star forming region NGC7000/IC5070. The distance to these two objects was previously estimated as 700 pc (Chavarría 1981) but later revised to 550 ± 50 pc (Shevchenko et al. 1991).

The star LkH α 321 permanently shows strong wind features in the P Cyg profiles of the Balmer lines. The [S II] images show a knotty jet extending 22 arcsec (Mundt & Eisloffel 1998). The forbidden line of [O I] 6300 Å has the central peak and the blue-shifted emission component at a radial velocity of about -376 km s⁻¹ with respect to the star.

This star shows low photometric variability, within visual magnitude $V = 12.25$ – 12.44 (Grankin et al. 2007). To date, no period of axial rotation has been reported. According to Cohen & Kuhi (1979), this star has spectral type G1 and an interstellar extinction $A_V = 2.23 \pm 0.3$ mag. The stellar bolometric luminosity estimated from these photometric data, assuming a distance $d = 550 \pm 50$ pc, is: $\log(L_*/L_\odot) = 1.42 \pm 0.12$.

Figures 3 and 4 show fragments of the spectrum of LkH α 321, including emission and photospheric absorption lines. The

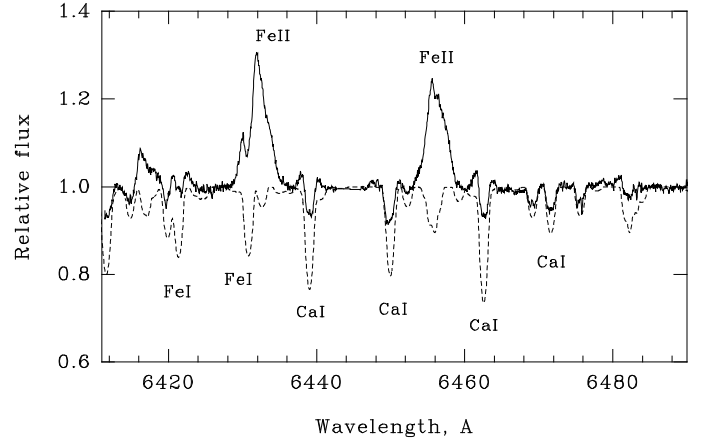


Fig. 3. Fragment of spectra of LkH α 321 (solid line) and the synthetic template $T_{\text{eff}} = 5250$ K, $\log g = 3.75$ dex, $v \sin i = 32$ km s⁻¹ (dotted line). The two broad emissions belong to Fe II. The weak broad emission wings can be noticed in the strongest Ca I lines.

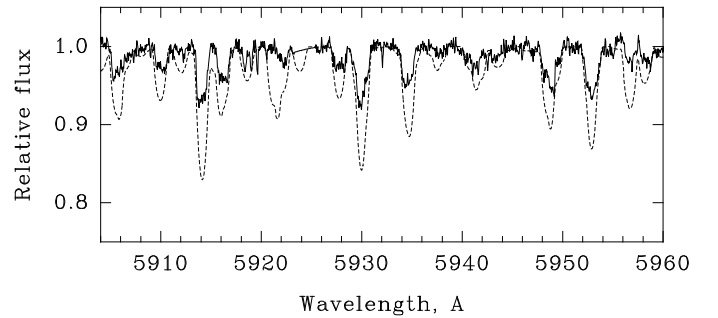


Fig. 4. Comparison of the photospheric lines in LkH α 321 and in the synthetic template. Most of the lines are of Fe I. No broad emissions in this region, but the photospheric lines are veiled considerably.

emission component of neutral metals is broader than the photospheric absorptions and becomes more noticeable in relatively strong transitions, where the photospheric counterparts have $EW \geq 100$ mÅ. In even stronger lines the broad emission is well above continuum, with the photospheric absorption on top of it. The emission lines of ions have no photospheric counterpart and display a triangular profile.

The comparison of the LkH α 321 spectrum with the grid of synthetic templates results in the best fit to $T_{\text{eff}} = 5250$ K and $v \sin i = 32$ km s⁻¹ as reported in Table 3. No significant change was observed between the radial velocities measured in UES spectra, $v_{\text{rad}} = -14.4 \pm 1.0$ km s⁻¹ and in the HIRES spectra (Table 1).

After the construction of the synthetic template we were able to measure EWs of photospheric lines on both LkH α 321 and template spectrum, as described in Sect. 3.3. We investigate the dependence of the ratio $EW(\text{template})/EW(\text{tts})$ on the line strength, wavelength, and excitation potential of the lower level of the transition.

Figure 5 shows that the amount of veiling in a photospheric line is dependent on the strength of the line in the template spectrum (corresponding to a spectral type G8). The dependence remains even if we adopt an earlier spectral type, G0. In this case the average level of veiling becomes lower. However, some lines in LkH α 321 are stronger than in a G0 template, which results in a false negative veiling and indicates that an inappropriate template star has been chosen. On the other hand, the

³ Source: <http://www.blancocuaresma.com/s/benchmarkstars>

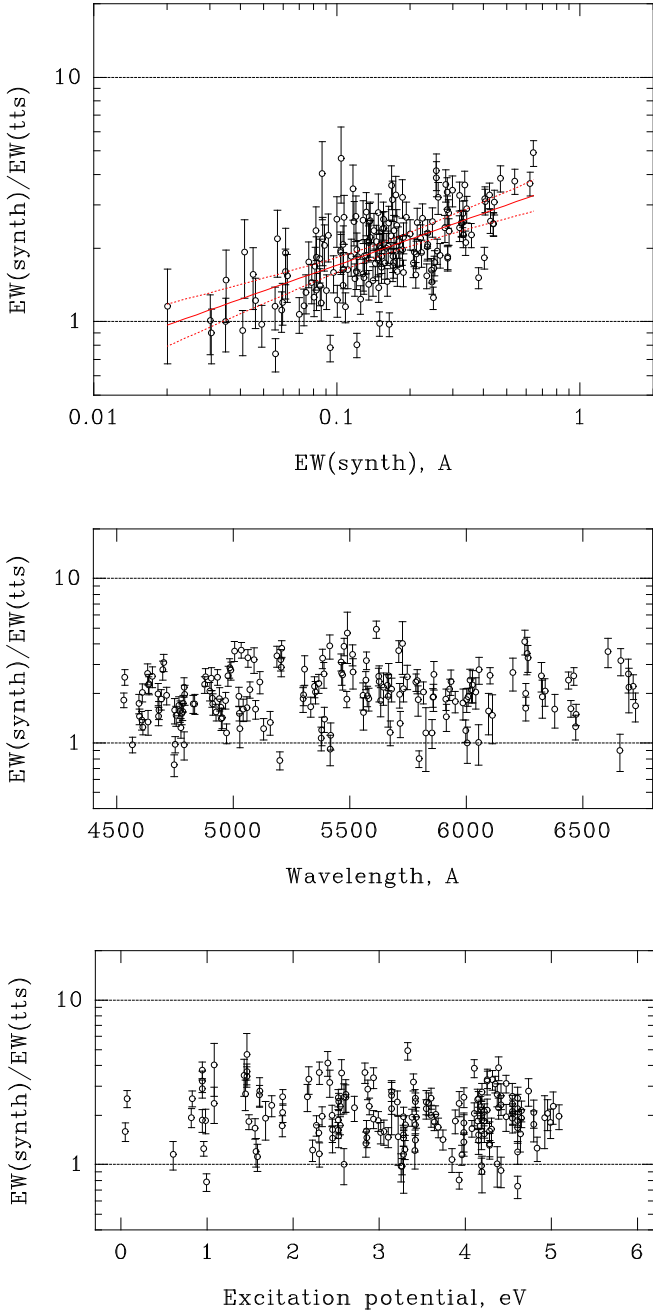


Fig. 5. Comparison of LkH α 321 with template $T_{\text{eff}} = 5250$ K. Veiling as a function of line strength (*upper*), wavelength (*middle*), and excitation potential (*lower*). The line of linear regression and the 99% confidence interval are indicated on the *top panel*.

lower limit of the spectral type is K1, because the low-excitation (0–1 eV) lines of neutrals are absent in the observed spectrum. Therefore, the dependence of veiling on line strength, shown in Fig. 5, is quite robust against any inappropriate spectral type determination.

The main result is that the strongest transitions are most affected by the veiling. We do not find any veiling dependence either on excitation potential or wavelength (Fig. 5). In this spectrum, the broad emission lines are unlikely to cause the line-dependent veiling. The weak broad emission can be noticed starting from EW of about 100 mÅ in the template spectrum, while the veiling is already strong in these lines. There must be another cause of the veiling. Although the photospheric line width is relatively large ($v \sin i = 32$ km s $^{-1}$), we do not see

narrow emission cores there, like those observed in S CrA SE (Gahm et al. 2008) and modelled by Dodin & Lamzin (2012).

5. V1331 Cyg

The unusually strong emission and wind features in V1331 Cyg make it similar to the pre-outburst spectrum of the FU Orionis type star (FUor) V1057 Cyg. For that reason, V1331 Cyg was considered as a possible pre-outburst FUor (Welin 1976). The star is viewed pole-on with a collimated outflow (jet) towards the observer (Mundt 1984; Mundt & Eisloffel 1998). Furthermore, the star is surrounded by ring-like nebulae, which might be made up of remnants of powerful mass-loss events in the past (Kuhi 1964; Mundt & Eisloffel 1998; Quanz et al. 2007; Choudhary et al. 2016).

The Keck spectra of V1331 Cyg, used in our research, was previously analysed by Petrov & Babina (2014) and Petrov et al. (2014), where the presence of the line-dependent veiling was demonstrated. In addition, the spectral type of G7–K0IV, $\log g \sim 3.5$ dex, radial velocity $v_{\text{rad}} = -15.0$ km s $^{-1}$ and a small $v \sin i < 6$ km s $^{-1}$ were derived from the photospheric lines. From the analysis of the forbidden line profiles and the blue-shifted “shell” components of strong permitted lines, it was proved that the star is viewed through the jet (Petrov et al. 2014). The forbidden line of [O I] 6300 Å has a strong central peak and a blue-shifted one at -235 km s $^{-1}$.

The star varies in brightness within $V = 11.7$ – 12.5 (Kolotilov 1983; Shevchenko et al. 1991) and to the best of our knowledge no period related with rotation has been reported. Hamann & Persson (1992) estimated a stellar bolometric luminosity of $L = 21 L_{\odot}$, with interstellar extinction $A_V = 1.4$ mag. The two spectra of 2004 and 2007 show no difference in strength of photosphere lines. The radial velocity of the star is the same in both spectra and slightly smaller in the UES spectra obtained in 1998, $v_{\text{rad}} = -16.8 \pm 0.3$ km s $^{-1}$.

Spectral type analysis for V1331 Cyg places this star between the synthetic spectra with $T_{\text{eff}} = 5250$ and 5000 K, making it a G7IV–K1IV star (Table 1). This result is consistent with previous determinations by Petrov & Babina (2014). The complete set of parameters for the V1331 Cyg synthetic template are listed in Table 3.

In Fig. 6 we present the dependence of the ratio $\text{EW}(\text{template})/\text{EW}(\text{tts})$ on the line strength, wavelength, and excitation potential of the lower level of the transition for V1331 Cyg. The top panel in Fig. 6 is similar to that obtained by Petrov et al. (2014), where spectra of real stars were used as templates. Also, there is no dependence of the ratio $\text{EW}(\text{template})/\text{EW}(\text{tts})$ on wavelength or excitation potential. The gaps along the wavelength scale on the middle panel of Fig. 6 reflect the regions of intense emission lines and gaps between spectral orders.

6. AS 353A

The star AS 353A belongs to the Aquila star forming region. The distance is estimated as $d = 150 \pm 50$ pc (Prato et al. 2003; Rice et al. 2006). It is a mixed system with a primary cTTS, AS 353A, and a secondary wTTS, AS 353B. The secondary, located at $5.6''$ of the primary, is resolved into a subarcsecond binary, AS 353Ba and Bb, separated by $0.24''$ (Tokunaga et al. 2004).

The star AS 353A has a rich emission line spectrum with strong blue-shifted absorptions in all the Balmer lines, indicating a powerful outflow (Herbig & Jones 1983; Eisloffel et al. 1990; Hamann & Persson 1992; Alencar & Basri 2000). The star

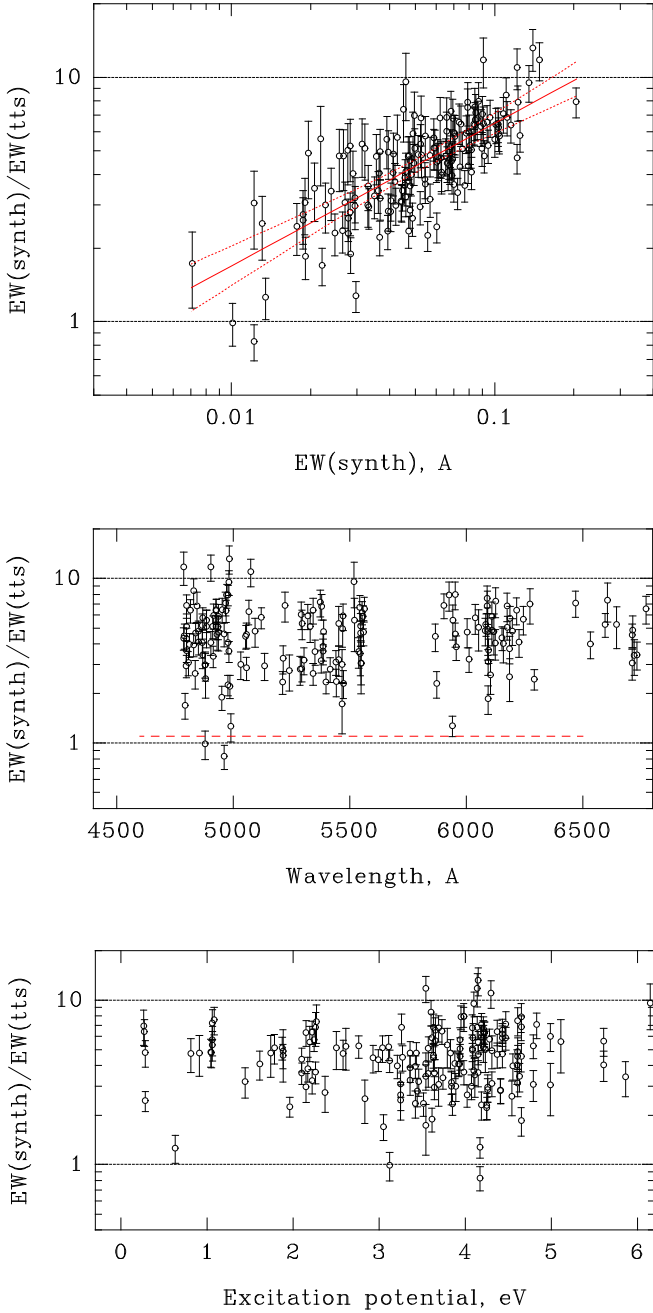


Fig. 6. Comparison of V1331 Cyg with template $T_{\text{eff}} = 5000$ K. Veiling as a function of line strength (*upper*), wavelength (*middle*), and excitation potential (*lower*). The line of linear regression and the 99% confidence interval are indicated on the *top panel*. Approximate level of the veiling continuum is indicated with the dashed line in the *middle panel*.

drives the Herbig-Haro object HH-32 (Herbig & Jones 1983). The forbidden line of [O I] 6300 Å has the central peak and two components at -270 and $+250$ km s $^{-1}$.

Basri & Batalha (1990) estimated the spectral type K2 from the optical spectroscopy. This was later confirmed from the K -band spectroscopy (Tokunaga et al. 2004). From the H -band spectroscopy, Rice et al. (2006) derived the following parameters for AS 353A: spectral type K5, $v \sin i = 10$ km s $^{-1}$, and stellar radial velocity $v_{\text{rad}} = -11.4 \pm 1.1$ km s $^{-1}$. The stellar bolometric luminosity is $\log(L_*/L_{\odot}) = 0.4$ (Tokunaga et al. 2004). Photometric variability within 0.86 mag in V was observed

by Fernandez & Eiroa (1996). No periodicity related to stellar rotation was reported.

Our spectral type analysis placed AS 353A between the synthetic templates with $T_{\text{eff}} = 4900$ and 5100 K, corresponding to a K0IV–K1IV star. The complete information about the AS 353A synthetic template can be found in Table 3. From the HIRES spectra we measured similar radial velocity to that given by Rice et al. (2006) (see Table 1), but in the UES spectra we found higher velocity, $v_{\text{rad}} = -8.0 \pm 0.2$ km s $^{-1}$. This star also shows dependence of the ratio $\text{EW}(\text{template})/\text{EW}(\text{tts})$ on the line strength (Fig. 7). Again, we found no correlation between the ratio $\text{EW}(\text{template})/\text{EW}(\text{tts})$ with wavelength and excitation potential of the lower level of the transition. The spectrum of AS 353A is remarkable in the combination of the narrow photospheric lines, $v \sin i < 6$ km s $^{-1}$, and the broad emissions of metals, $FWHM \sim 150$ km s $^{-1}$ (Fig. 9). This makes clear the presence of the photospheric lines on top of the broad emissions.

7. Discussion

Three possible sources of veiling were considered in the literature: (1) the veiling continuum radiated by a hot spot(s) at the base of accretion funnel(s) (e.g. Basri & Batalha 1990), (2) narrow emission lines originating from the post-shocked gas (Dodin & Lamzin 2012), and (3) broad emission lines originating in the infalling pre-shocked gas within the magnetosphere (Sicilia-Aguilar et al. 2015).

In all of our objects the different spectral lines show different veiling, with a clear dependence of veiling on the strength of transition. This cannot be explained entirely with the traditional model of a hot spot radiating the veiling continuum. The three cTTS discussed here are outstanding due to their high luminosity and high accretion rates, therefore the origin of the veiling may not be necessarily the same as in a moderately accreting cTTS. In the following we consider in more detail the possible sources of veiling.

7.1. Broad emission

Line-dependent veiling was investigated by Sicilia-Aguilar et al. (2015) from the spectral analysis of the EXor EX Lup in quiescence time. The authors suggested that broad emission lines, originating from the pre-shocked material, can fill in the photospheric absorptions, thus resulting in line-dependent veiling. We examined whether this interpretation may be applied for our three stars.

In AS 353A and LkH α 321, the broad emission lines of metals are much broader than the corresponding photospheric lines (see Figs. 8 and 9). The photospheric counterparts of the broad emissions of neutral metals (mostly Fe I) are well seen on top of the emissions and are reduced in depth by about the same factor as the other strong photospheric lines without the broad emission component. It means that the broad emission component does not contribute considerably to the line-dependent veiling. The observed profile is just a sum of the optically thin broad emission and the underlying photospheric absorption. The only way the broad emission can affect the photospheric lines is that blends of the broad emissions may form an additional local pseudo continuum. In our analysis of the veiled photospheric lines, we avoided those lines which might be contaminated by such blends.

The third of our objects, V1331 Cyg, is remarkable for its pole-on orientation towards the observer. The low excitation emission lines of neutral and ionized metals appear at stellar

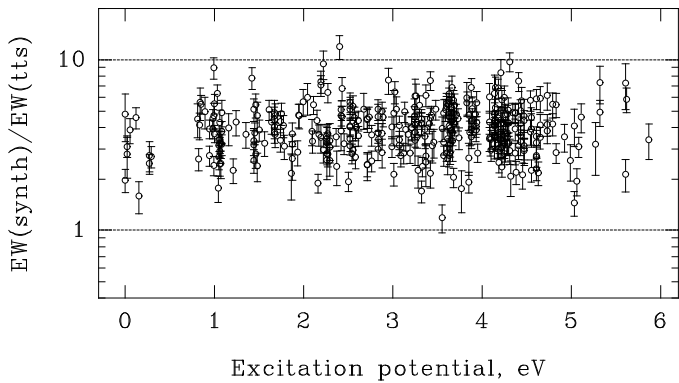
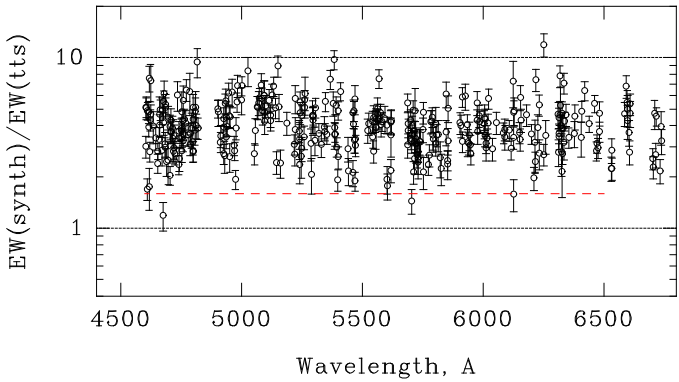
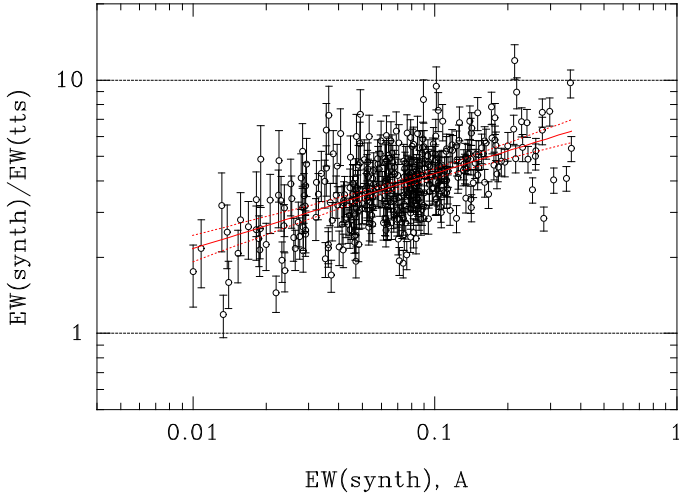


Fig. 7. Comparison of AS 353A with template $T_{\text{eff}} = 5000$ K. Veiling as a function of line strength (*upper*), wavelength (*middle*), and excitation potential (*lower*). The line of linear regression and the 99% confidence interval are indicated on the *top panel*. Approximate level of the veiling continuum is indicated with the dashed line in the *middle panel*.

velocity, and look similar in the three spectra taken in 2002, 2004, and 2007 (Fig. 10). The emission lines appear as not broadened by the flows within the stellar magnetosphere, probably because of the pole-on orientation of the star.

7.2. Photospheric hot spot

Our results, presented above, show that the veiling continuum can be quantified only by the weak photospheric lines. Measuring the weakest lines, we probed the deepest layers

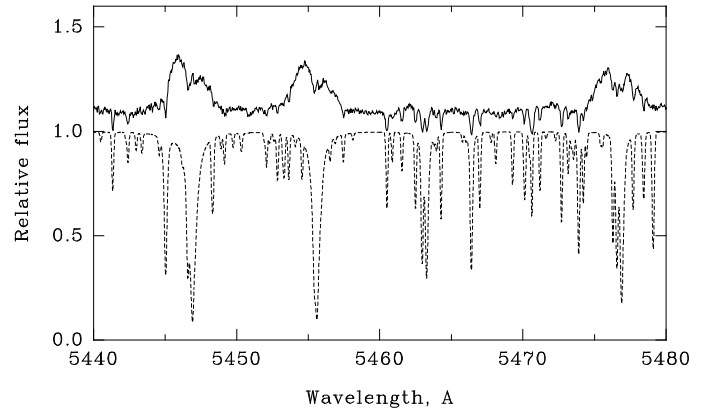


Fig. 8. Spectral fragments of AS 353A and the corresponding synthetic template (dashed line). We note the photospheric absorption lines on top of the broad emissions of Fe I.

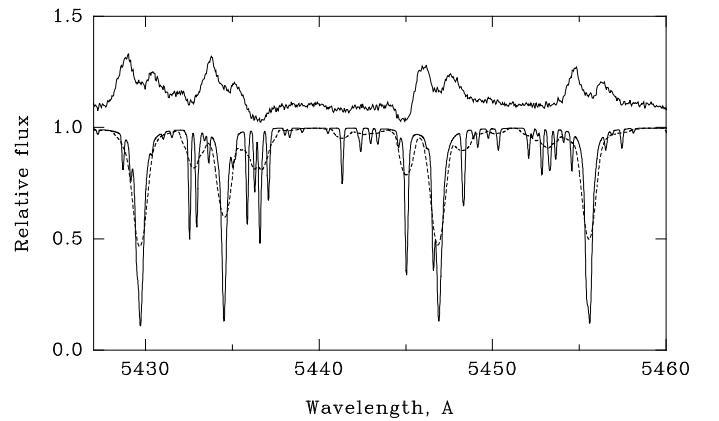


Fig. 9. Spectral fragments of LkH α 321 and the corresponding synthetic template (thin line). The template broadened to $v \sin i = 32$ km s $^{-1}$ is overplotted with dashed line. We note the photospheric absorption lines on top of the broad emissions of Fe I.

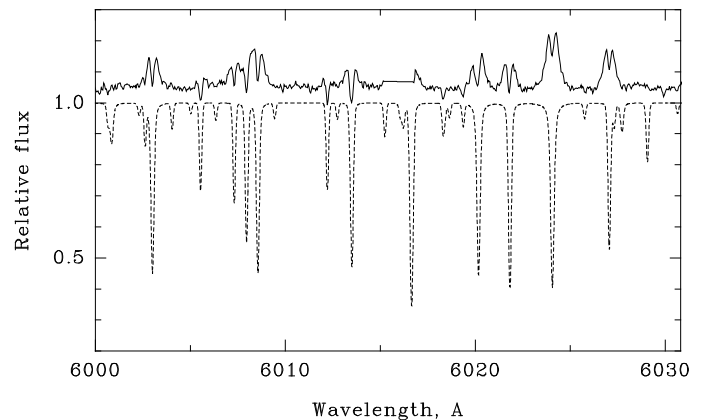


Fig. 10. Spectral fragment of V1331 Cyg and the corresponding synthetic template (dashed line). We note the photospheric absorption dips on top of the emission lines of Fe I and Mn I.

of line formation. We also found that the veiling continuum determination is affected by the spectral resolution and S/N level. The spectra with lower resolution and/or poor S/N ratio lead to an overestimation of the veiling continuum.

The hot spot hypothesis assumes that the accretion luminosity and the veiling continuum can be explained as being due to

radiation of a hot spot, with temperature T_{spot} , and a filling factor, f , representing the relative size of hot spot region with respect to the stellar surface. The accretion luminosity can be estimated from the observed emission lines. It has been shown that L_{acc} is well correlated with the line luminosity, L_{line} , of several emission lines, though the uncertainties in the empirical relations are in some cases high (e.g. Fang et al. 2009; Rigliaco et al. 2012; Alcalá et al. 2014 and references therein). In our study we opted for the empirical relations $L_{\text{acc}} - L_{\text{line}}$ obtained by Alcalá et al. (2014), which span a larger range in mass. In our sample of very active cTTS, the $H\alpha$ and $H\beta$ emissions are not good indicators because of the large optical depth and strong P Cygni profiles, which remove the blue emission wings of those lines (as seen in Fig. 1). Therefore, we assume that the He I 5876 Å line is more reliable to estimate the accretion luminosity.

We first determine the ratio $L_{\text{line}}/L_{\text{star}}$ through the equation

$$\frac{L_{\text{line}}}{L_{\text{star}}} = EW * (1 + VC) * \frac{F_{\text{cont}}}{L_{\text{star}}}, \quad (1)$$

where L_{star} is the stellar bolometric luminosity, F_{cont} is the stellar continuum flux density at the wavelength of the He I line, EW is the equivalent width of the He I emission, and VC is the veiling continuum near the He I line.

The ratio $F_{\text{cont}}/L_{\text{star}}$ is obtained using the adequate template spectra selected from the stellar spectral flux library by Pickles (1998). The library covers the spectral range 1150–25 000 Å, and a blackbody at the star temperature is added to simulate the continuum level at wavelengths longer than 2.5 μm for a better determination of L_{star} .

The ratio $L_{\text{line}}/L_{\text{star}}$ is converted to $L_{\text{acc}}/L_{\text{star}}$ using the relationship obtained by Alcalá et al. (2014) and the mass accretion rate determined from the equation

$$\dot{M}_{\text{acc}} = \frac{L_{\text{acc}}R_*}{GM_*}(1 - R_*/R_{\text{in}})^{-1}, \quad (2)$$

where R_* and M_* are the star radius and mass, respectively, reported in Table 1, and R_{in} is the inner disk radius taken as $3R_*$ in our calculation. Table 4 displays the final results, including the veiling continuum estimated from the plots EW/EW versus wavelength, the He I line, and accretion luminosities used for the mass accretion rate determination.

We have also checked that the accretion luminosities and the veiling continuum reported in Table 4 are consistent with the hot spot hypothesis. Within the used spectral range (4350–6750 Å), we do not see dependence of the veiling continuum on wavelength, which makes the estimation of the hot spot(s) temperature more difficult. We may only assert that temperatures higher than 10 000 K for the spots are not expected, otherwise the slope in the plots EW/EW versus wavelength would be more pronounced.

If we consider the typical spot temperatures for cTTS in the range 6000–8000 K (Calvet & Gullbring 1998) and assuming blackbody emission from the spot, we may infer the spot filling factor in our stars by using the equation:

$$\frac{L_{\text{acc}}}{L_{\text{star}}} \sim f \left(\frac{T_{\text{spot}}}{T_{\text{star}}} \right)^4, \quad (3)$$

where T_{star} is the effective temperature of the star.

We get filling factor values between 1% and 3% for V1331 Cyg 7, 20% for AS 353A, and below 1% for LkHα 321. The filling factor for AS 353A seems to be unusually large, which may be caused by an overestimated veiling continuum for this star.

7.3. Accretion-powered chromosphere

The dependence of veiling on the strength of transition indicates that the origin of this veiling is related to a drastic change in the stellar atmosphere structure due to accretion. The upper layers of the stellar atmosphere are most affected by the hard radiation of the shock wave located above. Therefore, at a given accreting mass flux the cores of strong lines will be mostly affected, while the weakest lines formed in the deeper layers remain still unchanged. In this situation, only the weakest lines may be used as a measure of the veiling continuum.

Dodin & Lamzin (2012) considered a model of veiling by lines, where the narrow emission lines, radiated in the post-shock region, contribute to the veiling along with the continuum radiation from the hot spot. The model showed that the veiling by lines prevails in cTTS with a moderate accretion flux, while with increasing accretion flux the veiling continuum becomes the most important. Our results do not contradict this prediction: the relative contribution of the veiling continuum is greater in AS 353A, where $L_{\text{acc}}/L_{\text{star}}$ is the largest of the three stars.

If the line-dependent veiling is caused by the emission lines radiated in a small post-shock region, which is hotter than the surrounding undisturbed photosphere, one would expect an emission core in the strongest lines and/or a dependence of veiling on the excitation potential. None of our objects reveals the dependence of veiling on excitation potential, probably because of the large scatter of points on the diagrams.

In AS 353A and V1331 Cyg, the $v \sin i$ is too small to resolve the details in a photospheric line profile. However, in the case of LkHα 321, the $v \sin i$ is larger and we can conclude from the absence of a narrow emission core in relatively broad photospheric lines that the line emission is not concentrated in a single spot but spread over a larger area above the visible stellar surface. A time series of spectral observations of this star would reveal probable variations in the photospheric line profiles. The mapping of magnetic field, cool spots, and emission line areas on the stellar surface was done for several cTTS (see Donati et al. 2013; Johnstone et al. 2014, and references therein). In all cases there is an axial asymmetry in the distribution of the emission line areas.

In LkHα 321 the line width is large enough to apply Doppler imaging. In V1331 Cyg and AS 353A, where the photospheric lines are so narrow, it is still possible to look for variations in radial velocity caused by a passage of the presumable hot spot(s) across the visible stellar surface. So far we can only assert that there is no change in the radial velocity of V1331 Cyg within $\pm 0.3 \text{ km s}^{-1}$ as derived from the HIRES spectra of 2004 and 2007. A significant change in radial velocity was noticed only in AS 353A: $v_{\text{rad}} = -8.0 \pm 0.2 \text{ km s}^{-1}$ in 1998 and $-10.4 \pm 0.2 \text{ km s}^{-1}$ in 2004.

The most intriguing is that of LkHα 321, where the veiling continuum is absent, but the line-dependent veiling is large. A similar effect was observed in DR Tau (Petrov et al. 2011). In that star both the veiling continuum and the line-dependent veiling vary from night to night. When the veiling continuum disappears, the line-dependent veiling remains, although at a reduced level. It was interpreted as an accretion-powered chromosphere. At a given infall velocity, the accretion energy flux is proportional to the density of infalling gas. At lower density the

Table 4. Determination of accretion luminosities and mass accretion rates.

Star	Template	VC	$\log(L_{\text{He}}/L_{\text{star}})$ (dex)	$\log(L_{\text{acc}}/L_{\text{star}})$ (dex)	$\log(\dot{M}_{\text{acc}})$ ($M_{\odot} \text{ yr}^{-1}$)
LkH α 321	G8V	0.0	-4.97	-1.72	-7.4
V1331 Cyg	K0V	0.1	-4.51	-1.21	-6.9
AS 353A	K0V	0.6	-3.6	-0.31	-7.1

Notes. VC is the veiling continuum at the wavelength of the He I line.

photosphere is not affected, while the upper layers of atmosphere are heated, thus giving rise to chromospheric-like emissions filling in the photospheric absorptions.

Yet one more consideration concerns the magnetic field structure. The Zeeman Doppler Imaging technique enables us to restore the large-scale topology of the stellar magnetic field in cTTS (e.g. [Johnstone et al. 2014](#)). So far, the Sun is the only star for which the small-scale (down to megameters) structures of magnetic fields have been investigated. It was found that the solar magnetic field has a fractal (scale-invariant) structure ([Abramenko 2008](#)). In fact, we expect that the local magnetic fields in cTTS within any small fraction of stellar surface may be as complex as in the Sun. In the framework of the magnetospheric accretion model, the shock front is supposed to be a confined area over a small fraction of the stellar surface. One can imagine that as the ionized infalling gas approaches the star, it meets more complicated magnetic structures and finally enters the stellar atmosphere at the dividing lines between the local closed fields. How would this alter the shock structure and the heating of the underlying photosphere? These small-scale processes may be important in the manifestation of the observed consequences of accretion.

8. Conclusions

The analysis of spectra of three very active cTTS of low to intermediate mass show that veiling consists of two components: a line-dependent veiling and the veiling continuum. Those two components are visible when the ratios of equivalent widths of nearby lines between template and TTS are plotted against the line strength on the template. Stronger lines are more veiled than weaker lines, regardless of wavelength and excitation potential. The veiling continuum was determined from the ratio of the weakest lines and the accretion luminosities from the He I line emission. In the three studied stars, we found that the photospheric line veiling is dominated by the line-dependent component, while the veiling continuum is a minor contributor. We conclude that the observed veiling on the photospheric lines of LkH α 321, AS 353A, and V1331 Cyg is composed of a line-dependent veiling with its origin in an abnormal structure of stellar atmosphere being heated up by the accreting matter and a veiling continuum radiated by a hot spot with temperature lower than 10 000 K.

Acknowledgements. This work was supported by Fundação para a Ciência e a Tecnologia (FCT) through national funds (UID/FIS/04434/2013) and by FEDER through COMPETE2020 (POCI-01-0145-FEDER-007672). A.C.S.R. acknowledges the support of an IA fellowship: CIAAUP-17/2015-BI in the context of the project (UID/FIS/04434/2013&POCI-01-0145-FEDER-007672). P.P.P. acknowledges the visitor's programme grant from Instituto de Astrofísica e Ciências do Espaço, Portugal. This work has made use of the VALD database, operated at Uppsala University, the Institute of Astronomy RAS in Moscow, and the University of Vienna.

References

- Abramenko, V. I. 2008, in *Solar Physics Research Trends*, ed. P. Wang (New York: Nova Publishers), 95
- Alcalá, J. M., Natta, A., Manara, C. F., et al. 2014, *A&A*, 561, A2
- Alencar, S. H. P., & Basri, G. 2000, *AJ*, 119, 1881
- Basri, G., & Batalha, C. 1990, *ApJ*, 363, 654
- Beristain, G., Edwards, S., & Kwan, J. 1998, *ApJ*, 499, 828
- Blanco-Cuaresma, S., Soubiran, C., Jofré, P., & Heiter, U. 2014, *A&A*, 566, A98
- Calvet, N., & Gullbring, E. 1998, *ApJ*, 509, 802
- Calvet, N., Muzerolle, J., Briceño, C., et al. 2004, *AJ*, 128, 1294
- Chavarría, C. 1981, *A&A*, 101, 105
- Choudhary, A., Stecklum, B., & Linz, H. 2016, *A&A*, 590, A106
- Cohen, M., & Kuhl, L. V. 1979, *ApJ*, 41, 743
- Dahm, S. E. 2008, *AJ*, 136, 521
- Dodin, A. V., & Lamzin, S. A. 2012, *Astron. Lett.*, 38, 649
- Donati, J.-F., Gregory, S. G., Alencar, S. H. P., et al. 2013, *MNRAS*, 436, 881
- Eisloffel, J., Solf, J., & Boehm, K. H. 1990, *A&A*, 237, 369
- Fang, M., van Boekel, R., Wang, W., et al. 2009, *A&A*, 504, 461
- Fernandez, M., & Eiroa, C. 1996, *A&A*, 310, 143
- Gahm, G. F., Walter, F. M., Stempels, H. C., Petrov, P. P., & Herczeg, G. J. 2008, *A&A*, 482, L35
- Gameiro, J. F., Folha, D. F. M., & Petrov, P. P. 2006, *A&A*, 445, 323
- Grankin, K. N., Melnikov, S. Y., Bouvier, J., Herbst, W., & Shevchenko, V. S. 2007, *A&A*, 461, 183
- Hamann, F., & Persson, S. E. 1992, *ApJ*, 394, 628
- Hartigan, P., Kenyon, S. J., Hartmann, L., et al. 1991, *ApJ*, 382, 617
- Hartigan, P., Edwards, S., & Ghandour, L. 1995, *ApJ*, 452, 736
- Herbig, G. H., & Jones, B. F. 1983, *AJ*, 88, 1040
- Herczeg, G. J., & Hillenbrand, L. A. 2008, *ApJ*, 681, 594
- James, D. J., Melo, C., Santos, N. C., & Bouvier, J. 2006, *A&A*, 446, 971
- Johnstone, C. P., Jardine, M., Gregory, S. G., Donati, J.-F., & Hussain, G. 2014, *MNRAS*, 437, 3202
- Joy, A. H. 1949, *ApJ*, 110, 424
- Kolotilov, E. A. 1983, *Sov. Astron. Lett.*, 9, 289
- Kuhl, L. V. *ApJ*, 140, 1409
- Mendigúta, I., Oudmaijer, R. D., Rigliaco, E., et al. 2015, *MNRAS*, 452, 2837
- Mundt, R. 1984, *ApJ*, 280, 749
- Mundt, R., & Eisloffel, J. 1998, *AJ*, 116, 860
- Muzerolle, J., Calvet, N., & Hartmann, L. 1998, *ApJ*, 492, 743
- Padgett, D. L. 1996, *ApJ*, 471, 847
- Petrov, P. P., & Babina, E. V. 2014, *Bull. Crim. Astrophys. Obs.*, 110, 1
- Petrov, P. P., Gahm, G. F., Gameiro, J. F., et al. 2001, *A&A*, 369, 993
- Petrov, P. P., Gahm, G. F., Stempels, H. C., Walter, F. M., & Artemenko, S. A. 2011, *A&A*, 535, A6
- Petrov, P. P., Kurosawa, R., Romanova, M. M., et al. 2014, *MNRAS*, 442, 3643
- Pickles, A. J. 1998, *PASP*, 110, 863
- Prato, L., Greene, T. P., & Simon, M. 2003, *ApJ*, 584, 853
- Quanz, S. P., Apai, D., Henning, Th. 2007, *ApJ*, 656, 287
- Rice, E. L., Prato, L., & McLean, I. S. 2006, *ApJ*, 647, 432
- Rigliaco, E., Natta, A., Testi, L., et al. 2012, *A&A*, 548, A56
- Rojas, G., Gregorio-Hetem, J., & Hetem, A. 2008, *MNRAS*, 387, 1335
- Ryabchikova, T., Piskunov, N., Kurucz, R. L., et al. 2015, *Phys. Scr.*, 90, 054005
- Shevchenko, V. S., Yakulov, S. D., Hambarian, V. V., & Garibjanian, A. T. 1991, *AZh*, 68, 275
- Sicilia-Aguilar, A., Fang, M., Roccatagliata, V., et al. 2015, *A&A*, 580, A82
- Siess, L., Dufour, E., & Forestini, M. 2000, *A&A*, 358, 593
- Taguchi, Y., Itoh, Y., & Mukai, T. 2009, *PASJ*, 61, 251
- Tokunaga, A. T., Reipurth, B., Gässler, W., et al. 2004, *AJ*, 127, 444
- Valenti, J. A., & Fischer, D. A. 2005, *ApJS*, 159, 141
- Valenti, J. A., & Piskunov, N. 1996, *A&AS*, 118, 595
- Valenti, J. A., Basri, G., & Johns, C. M. 1993, *AJ*, 106, 2024
- Vogt, S. S., Allen, S. L., Bigelow, B. C., et al. 1994, *Proc. SPIE*, 2198, 362
- Welin, G. 1976, *A&A*, 49, 145